TECHNISCHE UNIVERSITÄT MÜNCHEN

WALTHER-MEISSNER-INSTITUT

BAYERISCHE AKADEMIE DER WISSENSCHAFTEN

Remote State Preparation of Squeezed Microwave States

Dissertation

Stefan Pogorzalek

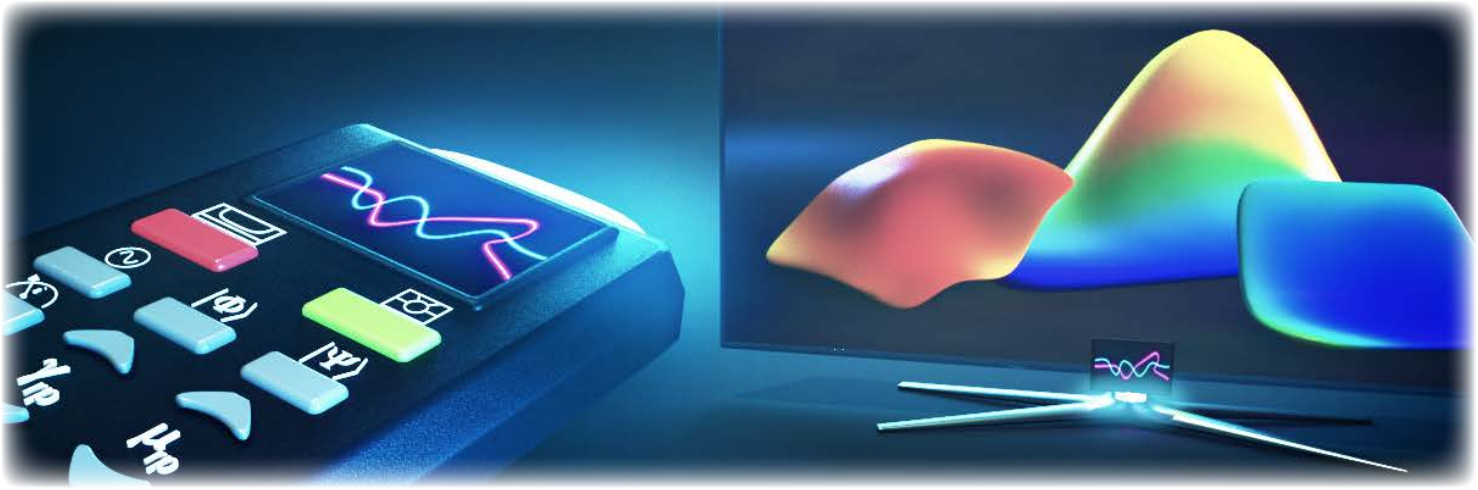

Cover image by Christoph Hohmann (MCQST/LMU)

TECHNISCHE UNIVERSITÄT MÜNCHEN

Lehrstuhl E23 für Technische Physik

Walther-Meißner-Institut für Tieftemperaturforschung
der Bayerischen Akademie der Wissenschaften

Remote State Preparation of Squeezed Microwave States

Stefan Pogorzalek

Vollständiger Abdruck der von der Fakultät für Physik der Technischen Universität München zur Erlangung des akademischen Grades eines

Doktors der Naturwissenschaften

genehmigten Dissertation.

Vorsitzender:	Prof. Dr. Frank Pollmann
Prüfer der Dissertation:	1. Prof. Dr. Rudolf Gross
	2. Prof. Jonathan J. Finley, Ph.D.

Die Dissertation wurde am 13.03.2020 bei der Technischen Universität München eingereicht und durch die Fakultät für Physik am 30.09.2020 angenommen.

Abstract

In quantum information science, efficient methods for communicating information play a central role. In particular, the secure exchange of information is of high practical relevance and can be realized with certain protocols by making use of fundamental quantum-mechanical properties. In this thesis, we present key developments towards the realization of quantum communication with propagating quantum microwaves. We employ superconducting Josephson parametric amplifiers as the central elements for the generation and manipulation of propagating quantum microwaves. As a first result, we demonstrate the generation of propagating two-mode squeezed (TMS) microwave states by superimposing two squeezed states at a microwave beam splitter. The resulting TMS states possess strong path entanglement, manifesting itself in nonlocal correlations between the signal quadratures in the different paths. Furthermore, we study fundamental properties of the TMS states against finite-time delays in one propagation path of these states and determine the maximally tolerable time delays until the entanglement disappears. We also investigate the influence of environmental noise on the propagating TMS states and observe, independent of the initial entanglement strength, a sudden death of entanglement upon injecting roughly one noise photon to one path of the TMS states. In addition, we study quantum discord, which describes quantum correlations beyond entanglement, and find an asymptotic robustness of quantum discord in TMS states against finite-time delays and injected noise. The knowledge gained from these investigations is crucial for the application of propagating microwaves in advanced quantum communication protocols.

As our main result, we realize deterministic remote state preparation (RSP) with continuous-variable microwaves. In this quantum communication protocol, the aim is to prepare a known quantum state at a distant location. For this task, we employ TMS states as an entangled resource and an additional Josephson parametric amplifier for the generation of a feedforward signal. We are able to remotely prepare squeezed states with a squeezing level below the vacuum limit and theoretically describe our results. Additionally, we investigate how the entanglement strength influences the preparable squeezed states. Finally, we relate the RSP scheme to an extension of the one-time pad cryptographic protocol in the quantum regime. Here, we implement close-to-perfectly secure communication of a quantum state in the vicinity of the optimal operation point of RSP.

Kurzzusammenfassung

In der Quanteninformationsverarbeitung spielt die effiziente Kommunikation von Information eine zentrale Rolle. Insbesondere ist eine abhörsichere Kommunikation von hoher praktischer Relevanz und kann für gewisse Quantenkommunikationsprotokolle durch Ausnutzen fundamentaler quantenmechanischer Eigenschaften realisiert werden. In dieser Arbeit stellen wir Schlüsselbeiträge zum Forschungsfeld der Quantenkommunikation mit propagierenden Quantenmikrowellen vor. Wir verwenden Josephson parametrische Verstärker als zentrale Elemente zur Erzeugung und Verarbeitung von propagierenden Quantenmikrowellen. Zuerst demonstrieren wir, dass wir zwei-Moden-gequetschte (TMS) Mikrowellenzustände erzeugen können, indem wir zwei gequetschte Zustände an einem Strahlteiler überlagern. Die dadurch erzeugten TMS-Zustände besitzen eine starke Pfadverschränkung, die sich in nichtlokalen Korrelationen zwischen den Signalquadraturen der verschiedenen Pfade manifestiert. Des Weiteren untersuchen wir fundamentale Eigenschaften der TMS-Zustände in Bezug auf eine Zeitverzögerung in einem der Propagationspfade und bestimmen die maximal tolerierbaren Zeitverzögerungen, ab denen die TMS-Zustände nicht mehr verschränkt sind. Zudem studieren wir den Einfluss von Rauschen auf die propagierenden TMS-Zustände und beobachten, dass die Verschränkung abrupt verschwindet, sobald ungefähr ein Rauschphoton in einen der Pfade injiziert wird. Dieser Effekt ist unabhängig von der ursprünglichen Stärke der Verschränkung. Außerdem diskutieren wir Quantendiscord, welcher Quantenkorrelationen jenseits von Verschränkung beschreibt, und beobachten eine asymptotische Robustheit von Quantendiscord gegenüber Zeitverzögerungen sowie der Anzahl der injizierten Rauschphotonen. Die Erkenntnisse aus diesen Studien sind essentiell für die Anwendung von propagierenden Mikrowellen in fortgeschrittenen Quantenkommunikationsprotokollen.

Das zentrale Ergebnis dieser Arbeit ist die Realisierung einer deterministischen nichtlokalen Erzeugung von Quantenzuständen (RSP) mit Mikrowellenzuständen der kontinuierlichen Variablen. Das Ziel in diesem Quantenkommunikationsprotokoll besteht darin, einen bekannten Quantenzustand an einem entfernten Ort zu erzeugen. Für diese Aufgabe nutzen wir die TMS-Zustände als Ressource für Verschränkung und einen zusätzlichen Josephson parametrischen Verstärker, um ein klassisches Kommunikationssignal zu erzeugen. Wir sind in der Lage, gequetsche Zustände zu erzeugen und unsere Ergebnisse theoretisch zu beschreiben. Außerdem untersuchen wir, wie die Stärke der Verschränkung die erzeugten Zustände beeinflusst. Schließlich verknüpfen wir RSP mit einer Erweiterung des kryptographischen One-Time-Pads in den Bereich der Quantenkommunikation. Hier zeigen wir eine sichere Übertragung von einem Quantenzustand mit nahezu perfekter Abhörsicherheit in der Umgebung des optimalen Arbeitspunktes von RSP.

Contents

List of Figures

List of Tables

Chapter 1

Introduction

Over the last century, quantum mechanics lead to various developments of new technologies and groundbreaking discoveries in fundamental science. However, only within the last few decades quantum mechanics was entering information science, leading to the highly active and prospering field of quantum information science. It encompasses various subjects such as quantum computing [1], quantum cryptography [2], quantum communication [3, 4], quantum simulation [5], and quantum sensing [6, 7]. In quantum information science, one exploits fundamental quantum mechanical properties such as superposition or quantum entanglement to achieve a quantum advantage in terms of security, efficiency, or computing power. Moreover, meanwhile key concepts of quantum information theory are successfully used for the description of many body systems and novel phenomena of quantum matter.

Until today, various physical platforms have been developed to implement concepts of quantum information science. Each of these platforms have certain advantages and disadvantages. A particularly promising approach utilizes superconducting circuits operating in the quantum regime [8]. Here, Josephson junctions serve as a key element and tool for building of such circuits. They provide a nonlinear, tunable and lossless inductance which can be exploited to build quantum circuits operating in the gigahertz regime and behaving as artificial atoms. Superconducting quantum circuits have been successfully used to study the fundamental interaction between light and matter in the field of circuit quantum electrodynamics. In particular, the large dipole moments of the artificial atoms in combination with the small mode volume and, in turn, an enhanced field strength of quasi one-dimensional transmission line resonators, enables strong [9] or even ultrastrong light-matter coupling [10]. Without any doubt, the large present interest in quantum information science in the microwave frequency regime is motivated by the ongoing progress in constructing a quantum computer based on superconducting quantum circuits [11].

In the framework of quantum computing with superconducting circuits, a major challenge consists within connecting multiple quantum processors in a quantum network. This goal requires an efficient method of communication between them. To this end, deterministic direct state transfer protocols between localized discrete-variable systems in the microwave regime have been reported [12, 13]. Another approach for such a task utilizes

continuous-variable systems where the information is encoded into variables with a continuum of observable eigenstates [14]. Quantum communication with continuous-variables is a flourishing field of intense research [15, 16] where, for optical systems, quantum teleportation [17, 18], quantum key distribution [19, 20], dense coding [21], and free-space quantum communication [22] have been experimentally achieved. However, continuous-variable quantum communication schemes in the microwave frequency regime, which are required to interlink superconducting quantum processors, are still lacking. To fill this gap, one promising approach focuses on propagating quantum microwaves where the communicated information is embedded into quadratures of the propagating electromagnetic field [16]. They are a natural choice since the frequency of the propagating quantum signals can be easily matched to those in superconducting quantum circuits. Furthermore, most communication and computational tasks are nowadays realized with highly developed technology operated in the microwave regime. These facts make propagating quantum microwaves a promising candidate for the realization of advanced quantum communication protocols.

The realization of quantum information processing tasks in the microwave regime is accompanied by several experimental challenges. First of all, the low photon energy of microwave photons in the gigahertz range requires cryogenic temperatures of a few tens of millikelvins to avoid excessive thermal noise. Additionally, the employed superconducting circuits require temperatures below their critical temperatures in order to become superconducting. Moreover, advanced experiments require micro- and nano-fabricated circuits combined with modern microwave technology. In particular, the detection and reconstruction of quantum microwaves poses a challenge since microwave single-photons detectors [23, 24] are not yet readily available for routine applications. Alternatively, weak quantum signals can be amplified by commercially available high-electron-mobility transistors and measured at room temperature. However, these amplifiers add a considerable amount of noise to the signal and, consequently, sophisticated signal recovery techniques [25, 26] are required for the control and measurement of the propagating quantum microwaves. Such techniques have been developed and pioneered at the Walther-Meißner-Institute over the past decade.

In our experiments, we employ superconducting circuits called Josephson parametric amplifiers (JPA) [27–30] which can be understood as weakly-nonlinear, tunable resonators. They can be used to produce or manipulate nonclassical states of light by utilizing parametric effects which are induced by the interaction of microwave fields with a nonlinear medium. In practice, the parametric effects are caused by modulating the Josephson inductance by an external microwave drive leading to a parametric modulation of the JPA resonance frequency. In this way, the JPA can generate squeezed states where the noise in one quadrature is reduced below the vacuum level, while the noise in the orthogonal quadrature is proportionally increased. Propagating quantum microwaves in the form of squeezed states are produced by letting the JPA intra-resonator field leak into a

transmission line coupled to the JPA. Squeezed states are an essential nonclassical resource for continuous-variable quantum information tasks as they allow for the generation of entanglement. Furthermore, their manipulation is straightforward and well-understood [16]. They have been employed for sideband cooling of mechanical oscillators [31], the enhanced detection of magnetic resonances [32], the stroboscopic readout of qubits [33], and the generation of path entanglement [25]. Alternatively, JPAs are routinely employed for, e.g., the efficient readout of qubits where they act as phase-insensitive amplifiers with a noise performance close to the quantum limit [33–35].

For the realization of quantum communication tasks, a quantum correlated resource is a necessary prerequisite. In continuous-variable systems, two-mode squeezed (TMS) states are commonly employed as such an entangled state [15]. The TMS states are in close analogy to the original notion of entanglement first discussed by Einstein, Podolsky and Rosen [36]. Here, a measurement of the position or momentum of one particle determines the corresponding quantity of the second particle with certainty. For entangled states of light, not the position and momentum are quantum correlated but the respective electromagnetic field quadratures in the two propagation paths. For an infinitely squeezed TMS state, knowledge about one quadrature in one path reveals full information on the corresponding quadrature in the other path. In quantum optics experiments, TMS states have been employed as entangled resource for quantum teleportation [17, 37], entanglement swapping [38], and dense coding [21]. However, in the microwave regime, TMS states have not yet been employed for quantum communication tasks. In this thesis, we utilize TMS states for the realization of a fundamental quantum communication protocol using continuous-variable microwaves. In order to employ these states for such a purpose, we require path-entangled TMS states where strong correlations exist between electromagnetic field quadratures in different propagation paths [16]. We achieve this goal by superimposing two squeezed states at a beam splitter. If correctly balanced, the TMS states at the two output ports of the beam splitter possess strong cross-correlations but no local correlations [39]. We characterize the balancing and quantum correlations in the TMS states by employing a previously established method for full state tomography based on the measured quadrature moments [25]. Furthermore, the effect of a finite time delay in one propagation path on the quantum correlations is interesting from a fundamental point of view as it provides insight into the dephasing of quantum correlations. In addition, the finite-time properties of the TMS states provide information on whether delay lines are required in application scenarios. We also investigate the effect of environmental noise on the quantum correlations in TMS states. The robustness of cross-correlations to noise is particularly relevant for quantum microwave states as the thermal population is negligible only at low temperatures around a few tens of millikelvins.

After characterizing the TMS states as an entangled resource, we employ them for the realization of the remote state preparation (RSP) protocol [40–43]. Here, a known quantum state is safely communicated from one party to another by employing similar tools

as in quantum teleportation [44]. Previously, only conditional schemes have been realized in quantum optics with continuous-variables [45, 46]. In the microwave regime, quantum communication has only been realized for discrete-variable systems in the form of quantum teleportation between on-chip superconducting qubits [4] or, more recently, direct state transfer schemes [12, 13]. We employ propagating TMS microwave states as entangled resource and a feedforward in order to realize deterministic RSP of squeezed states [47]. We present full tomography and the phase space of preparable states. Furthermore, we investigate how the initial entanglement strength affects the prepared states. Since entanglement is essential for RSP, we probe the quantum correlations in different steps of the protocol and explore the correlation consumption. Finally, we consider how one can safely transfer quantum states using RSP by connecting the latter to an extension of the one-time pad to the quantum regime.

The thesis is structured in the following way. In chapter 2, we present the theoretical foundations for this work. Here, we introduce important concepts in Gaussian quantum information and relevant quantum states. Furthermore, the operation principle and theoretical description of the employed JPAs are presented, which is followed by a detailed description of the RSP protocol. Chapter 3 describes the employed cryogenic and room temperature setups. Additionally, the data acquisition and processing as well as calibration procedures are presented. In chapter 4, we focus on the experimental generation of balanced TMS states by superimposing two squeezed microwave states at a 50:50 beam splitter. In addition, the effect of finite-time delays and environmental noise is experimentally investigated and theoretically described. The main results of this thesis are discussed in chapter 5, where we show the realization of deterministic RSP of squeezed states in the microwave regime. Furthermore, we investigate the quantum correlations in different parts of the protocol and study how one can safely transfer quantum states using our scheme. Finally, we summarize our work and provide an outlook in chapter 6.

Chapter 2

Propagating microwaves and superconducting circuits

In this chapter, we introduce the theoretical foundations relevant for this thesis. First, we discuss Gaussian states and their quantum mechanical description in Sec. 2.1. In addition, we introduce exemplary classes of quantum correlations, including entanglement and quantum discord. In Sec. 2.2, we describe the superconducting circuits used for building a flux-driven Josephson parametric amplifier (JPA), which serves as a source of nonclassical microwave radiation. Finally, we introduce the central quantum communication protocol experimentally implemented within this work, namely, remote state preparation (RSP) in Sec. 2.3 and compare it to related quantum communication protocols.

2.1 Gaussian quantum information

In Gaussian quantum information, one utilizes Gaussian states and Gaussian operations to perform various tasks in the framework of quantum communication [17], quantum information processing [15, 16] or quantum illumination [48, 49]. In this section, we introduce quantum mechanical representations and fundamental properties of continuous-variable Gaussian states. Gaussian states possess a Gaussian probability distribution of their field quadratures and can be conveniently described by their corresponding covariance matrix which represents an analog of the density matrix. A particular covariance matrix offers full knowledge about a given Gaussian state. It allows one to estimate various physical quantities of the state - such as expectation values of observables, entropic quantities, and entanglement estimators.

2.1.1 Representation of propagating quantum microwave states

In this work, we investigate the quantum properties of electromagnetic fields in the frequency range of $4 - 6\,\mathrm{GHz}$ which propagate along quasi one-dimensional structures such as coaxial cables or coplanar waveguides. Such signals $A(r,t)$ can be described classically by their in-phase and out-of-phase quadrature components, $I(t)$ and $Q(t)$. The

description of $A(r,t)$ in terms of the quadratures is, in particular, useful if one considers quasi single-mode signals with a small bandwidth compared to the mode frequency, $\delta f \ll f$. Then, an arbitrary signal $A(r,t)$ with a carrier frequency $f = \omega/2\pi$ at position r can be expressed as sinusoidal oscillations of the field quadratures $I(t)$ and $Q(t)$,

$$A(r,t) = I(t)\cos(\omega t - kr) + Q(t)\sin(\omega t - kr)\,, \tag{2.1}$$

where k is the wave vector. Here, the relevant information is fully encoded in the quadratures $I(t)$ and $Q(t)$ which represent the in-phase and out-of-phase instantaneous amplitudes.

A similar approach is useful for the description of propagating quantum-mechanical signals. However, for that, one needs to take into account additional effects imposed by quantum mechanics. The electrical field of a one-dimensional, single-mode signal is given by [50]

$$\hat{A}(r,t) = C\left[\hat{a}^\dagger e^{i(\omega t - kr)} + \hat{a}e^{-i(\omega t - kr)}\right] = 2C\left[\hat{q}\cos(\omega t - kr) + \hat{p}\sin(\omega t - kr)\right]\,, \tag{2.2}$$

where $\omega = 2\pi f$ is the angular frequency and C a constant chosen such that $\hat{A}(r,t)$ corresponds to the electrical field of the signal. Here, the creation and annihilation operators of the field, $\hat{a}$ and $\hat{a}^\dagger$, obey the usual bosonic commutation relation $[\hat{a},\,\hat{a}^\dagger] = 1$ and are related to the complementary quadrature operators $\hat{q}$ and $\hat{p}$ by

$$\hat{q} = \frac{\hat{a} + \hat{a}^\dagger}{2} \qquad \text{and} \qquad \hat{p} = \frac{\hat{a} - \hat{a}^\dagger}{2i}\,. \tag{2.3}$$

The quadrature operators obey the commutation relation $[\hat{q},\,\hat{p}] = i/2$ and are the quantum-mechanical counterparts of the classical quadratures I and Q. In general, $\hat{q}$ and $\hat{p}$ can be defined with a relative phase shift θ. Then, the generalized definition of the quadrature operators reads [51]

$$\hat{q_\theta} = \frac{\hat{a}e^{-i\theta} + \hat{a}^\dagger e^{i\theta}}{2} \qquad \text{and} \qquad \hat{p_\theta} = \frac{\hat{a}e^{-i\theta} - \hat{a}^\dagger e^{i\theta}}{2i}\,. \tag{2.4}$$

This means that a phase shift of θ of the chosen reference frame leads to a rotation of the axis spanned by $\hat{q}$ and $\hat{p}$ in a specific phase space.

In contrast to a classical scenario, $\hat{q}$ and $\hat{p}$ cannot be measured simultaneously with infinite accuracy due to the Heisenberg uncertainty relation [52]

$$\Delta q \Delta p \geq \frac{1}{4}\,, \tag{2.5}$$

where the standard deviation ΔO of an observable $\hat{O}$ is given by $(\Delta O)^2 = \langle(\Delta\hat{O})^2\rangle \equiv \langle\hat{O}^2\rangle - \langle\hat{O}\rangle^2$. The Heisenberg uncertainty stems from the fact that $\hat{q}$ and $\hat{p}$ are comple-

mentary observables with a non-zero commutator. From Eq. (2.5) it becomes evident that a full description of a general quantum state with just the expectation values of the quadrature components is not possible. There are multiple ways to fully describe a quantum state and we discuss the relevant ones for Gaussian quantum states below.

Density operator

A widespread method to describe a general quantum state is the density operator $\hat{\rho}$ which is particularly useful for mixed states. The density operator

$$\hat{\rho} = \sum_j p_j \left|\psi_j\right\rangle \left\langle\psi_j\right| \tag{2.6}$$

is defined as the sum of basis states $|\psi_j\rangle$ where p_j denotes the probability to be in state $|\psi_j\rangle$. The expectation value of an observable $\hat{O}$ can be calculated by using the trace $\langle\hat{O}\rangle = \mathrm{Tr}(\hat{O}\hat{\rho})$. For pure states, we have $\mathrm{Tr}(\hat{\rho}^2) = 1$, while for mixed states $\mathrm{Tr}(\hat{\rho}^2) < 1$. The description of Gaussian quantum states in terms of the density operator is possible but not very practical since one typically would need to consider a high-dimensional Hilbert space in this description.

Moments of signal operator

Another description of a single-mode quantum state is provided by the moments of the signal operators $\hat{a}$ and $\hat{a}^\dagger$. The signal moments $\langle(\hat{a}^\dagger)^m \hat{a}^n\rangle$ with $m, n \in \mathbb{N}_0$ contain the same information as the density operator and, thus, fully define a quantum state [53]. Even though an infinite number of signal moments exists, a finite number of them fully determines certain quantum states. For example, Gaussian states are fully defined by signal moments up to the second order, $m + n \leq 2$ [54]. If one considers a two-mode state, the signal operators of both modes needs to be taken into account, which results in the signal moments $\langle(\hat{a}_1^\dagger)^k (\hat{a}_2^\dagger)^l \hat{a}_1^m \hat{a}_2^n\rangle$ with $k, l, m, n \in \mathbb{N}_0$. Note that operators of different modes always commute $[\hat{a}_i, \hat{a}_j^\dagger] = \delta_{ij}$ where δ_{ij} is the Kronecker delta.

Statistical moments

The most natural description of an arbitrary N-mode Gaussian state is given by the statistical moments of the quadratures. The first statistical moment is the mean $\bar{\mathbf{r}} = \langle\mathbf{r}\rangle$ where $\hat{\mathbf{r}} = (\hat{q}_1, \hat{p}_1, ..., \hat{q}_N, \hat{p}_N)$ is a vector consisting of all quadratures of the N modes. Quadratures of different modes commute. The second statistical moment is given by the covariance matrix $\mathbf{V}$ which is a $2N \times 2N$ real symmetric matrix and is defined as

$$V_{ij} = \langle\hat{r}_i \hat{r}_j + \hat{r}_j \hat{r}_i\rangle/2 - \langle\hat{r}_i\rangle\langle\hat{r}_j\rangle\,, \tag{2.7}$$

for $i, j = 1, ..., 2N$. A Gaussian state is fully described by $\bar{\mathbf{r}}$ and $\mathbf{V}$ [15]. The purity of a Gaussian state is independent of $\bar{\mathbf{r}}$ and can be written as [55, 56]

$$\mu = \frac{1}{4^N \sqrt{\det \mathbf{V}}} . \tag{2.8}$$

Consequently, a Gaussian state is only pure if its covariance matrix fulfills $\det \mathbf{V} = 1/4^{2N}$.

In this work, we only consider Gaussian states with up to two modes. Then the covariance matrix can be expressed in the form

$$\mathbf{V} = \begin{pmatrix} \mathbf{A} & \mathbf{C} \\ \mathbf{C}^{\mathrm{T}} & \mathbf{B} \end{pmatrix} , \tag{2.9}$$

where $\mathbf{A}$, $\mathbf{B}$ and $\mathbf{C}$ are 2×2 matrices describing the local state A on the first mode, local state B on the second mode and cross-correlations between both parties, respectively. For a two-mode Gaussian state, it is useful to define the local symplectic invariants of the covariance matrix [55]

$$I_1 = \det \mathbf{A}, \quad I_2 = \det \mathbf{B}, \quad I_3 = \det \mathbf{C}, \quad I_4 = \det \mathbf{V} , \tag{2.10}$$

which do not change under local symplectic transformations, i.e., local unitary Gaussian transformations such as squeezing or displacement, which are defined in the next subsection. With the symplectic invariants, we can define the two symplectic eigenvalues of the bipartite Gaussian state

$$\nu_{\pm} = \sqrt{\frac{\Delta \pm \sqrt{\Delta^2 - 4I_4}}{2}} , \tag{2.11}$$

where $\Delta = I_1 + I_2 + 2I_3$. Importantly, $\nu_{\pm}$ can be used to calculate various essential quantities of the bipartite state. In particular, ν_- can be utilized to verify whether an experimentally reconstructed Gaussian state is physical, since the Heisenberg uncertainty relation can be written as [57]

$$\nu_- \geq \frac{1}{4} . \tag{2.12}$$

Wigner function

The description of quantum states as a quasi-probability distribution in the phase space is particularly useful for continuous-variable states. For a classical description, a well-defined probability to find a system at a particular coordinate (q, p) exists. In contrast, in quantum mechanics, the Heisenberg uncertainty prohibits precise knowledge of q and p at the same time. However, it is possible to extend the concept of classical probability distributions to quantum systems by introducing quasi-probability distributions such as the P-representation [58, 59] or Q-function [60]. The first quasi-probability distribution $W(\mathbf{r})$ was introduced by Wigner [61] and takes the following form for a N-mode Gaussian

state [16]

$$W(\mathbf{r}) = \frac{\exp\left[-\frac{1}{2}(\mathbf{r}-\bar{\mathbf{r}})\mathbf{V}^{-1}(\mathbf{r}-\bar{\mathbf{r}})^{\mathrm{T}}\right]}{(2\pi)^N\sqrt{\det\mathbf{V}}}, \tag{2.13}$$

where $\mathbf{r} = (q_1, p_1, ..., q_N, p_N)$. The Wigner function $W(\mathbf{r})$ is normalized $\int_{-\infty}^{\infty} W(\mathbf{r})\mathrm{d}\mathbf{r} = 1$. From Eq. (2.13) it can be seen that the Wigner function of a N-mode Gaussian state is always positive. For non-Gaussian quantum states, the Wigner function can take negative values which is a sufficient indicator for the nonclassicality of these states. However, also states with positively-valued Wigner functions, such as Gaussian states, can show quantum-mechanical properties.

For single-mode Gaussian states, the Wigner function can be expressed in terms of the signal moments up to the second order [54, 62]

$$\begin{aligned} W(q,\,p) = &\frac{1}{\pi\sqrt{(\nu+1/2)^2-|\mu|^2}} \\ &\times\exp\left[-\frac{(\nu+1/2)|\zeta-\langle\hat{a}\rangle|^2-(\mu^*/2)(\zeta-\langle\hat{a}\rangle)^2-(\mu/2)(\zeta^*-\langle\hat{a}^\dagger\rangle)^2}{(\nu+1/2)^2-|\mu|^2}\right], \end{aligned} \tag{2.14}$$

where $\zeta = q + ip$, $\mu = \langle\hat{a}^2\rangle - \langle\hat{a}\rangle^2$ and $\nu = \langle\hat{a}^\dagger\hat{a}\rangle - |\langle\hat{a}\rangle|^2$.

The observable probability distribution of a specific quadrature in an experiment can be obtained by integrating the Wigner function over the remaining quadratures. For example, for a single-mode Gaussian state, the probability distribution of the q-quadrature is given by $w(q) = \int_{-\infty}^{\infty} W(q,\,p)\mathrm{d}p$. In general, the marginal distribution of a N-mode Wigner function for specific quadratures is obtained by integration over the rest of the quadratures. For example, the local marginal distribution of mode 1 of a two-mode squeezed state is given by

$$W_{q_1p_1}(q_1,\,p_1) = \int_{-\infty}^{\infty}\int_{-\infty}^{\infty} W(q_1,\,p_1,\,q_2,\,p_2)\,\mathrm{d}q_2\,\mathrm{d}p_2\,. \tag{2.15}$$

2.1.2 Fundamental Gaussian quantum states

In this subsection, we introduce the Gaussian states which are relevant for our work and introduce their key properties. In particular, we discuss the three fundamental single-mode Gaussian states, namely, vacuum and thermal states, coherent or displaced states, and finally, squeezed states. We note that one could also describe any Gaussian state as a thermal squeezed displaced state which is a combination of the fundamental states.

Vacuum and thermal state

Due to the canonical quantization, even the lowest possible energy state possesses fluctuations in the electromagnetic field. This lowest energy state is typically referred to as a vacuum state $|0\rangle$. It is a minimum uncertainty state with equal variances in both quadratures $(\Delta q)^2 = (\Delta p)^2 = 1/4$. We note, that the particular value of the vacuum vari-

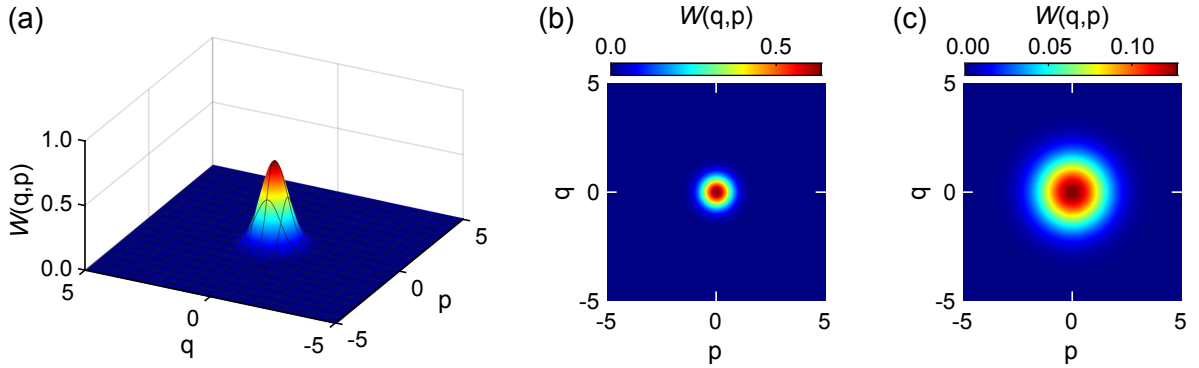

Figure 2.1: (a) 3D representation and (b) top view of the Wigner function of a vacuum state with $n_{\mathrm{th}} = 0$ corresponding to $(\Delta q)^2 = (\Delta p)^2 = 1/4$. (c) Top view of the Wigner function of a thermal state with $n_{\mathrm{th}} = 2$ corresponding to $(\Delta q)^2 = (\Delta p)^2 = 5/4$.

ance depends on the prefactor in the definition of the quadrature operators [see Eq. (2.3)], which can be chosen arbitrarily. Since the vacuum state is the lowest possible energy state, we can ascribe a zero equilibrium temperature, $T = 0$, to it. Even though it is impossible to realize $T = 0$ in our experiments, we can approximate our states as vacuum states if the condition $k_{\mathrm{B}}T \ll hf$ is fulfilled.

If one now considers a black body emitter with $T > 0$, the emitted mean photon number into a single mode with a frequency f follows the Bose-Einstein statistics [63]

$$n_{\mathrm{th}} \equiv \mathrm{Tr}(\hat{a}^\dagger \hat{a} \rho_{\mathrm{th}}) = \frac{1}{\exp\left(\frac{hf}{k_{\mathrm{B}}T}\right) - 1}, \tag{2.16}$$

where k_{B} is the Boltzmann constant and h is the Planck constant. The density matrix of a thermal state

$$\rho_{\mathrm{th}} = \sum_n \frac{n_{\mathrm{th}}^n}{(1 + n_{\mathrm{th}})^{n+1}} |n\rangle\langle n| \tag{2.17}$$

only depends on its mean photon number n_{th}. The mean and covariance matrix of a thermal state are

$$\bar{\mathbf{r}}_{\mathrm{th}} = 0 \qquad \text{and} \qquad \mathbf{V}_{\mathrm{th}} = (2n_{\mathrm{th}} + 1)\frac{\mathbb{I}_2}{4}, \tag{2.18}$$

where $\mathbb{I}_2$ is the 2×2 identity matrix. The signal moments of a thermal state can be calculated from the density matrix and are $\langle (\hat{a}^\dagger)^m \hat{a}^n \rangle_{\mathrm{th}} = \langle \hat{n} \rangle^n n! \delta_{mn}$. Figure 2.1 shows the Wigner functions of the vacuum state and a thermal state with $n_{\mathrm{th}} = 0$ and $n_{\mathrm{th}} = 2$, respectively.

Coherent state

Coherent states $|\alpha\rangle$, sometimes also called displaced states, are eigenstates of the annihilation operator, $\hat{a}\,|\alpha\rangle = \alpha\,|\alpha\rangle$. Since the oscillatory behavior of coherent states is very similar to the dynamics of a classical harmonic oscillator, they are often regarded as the

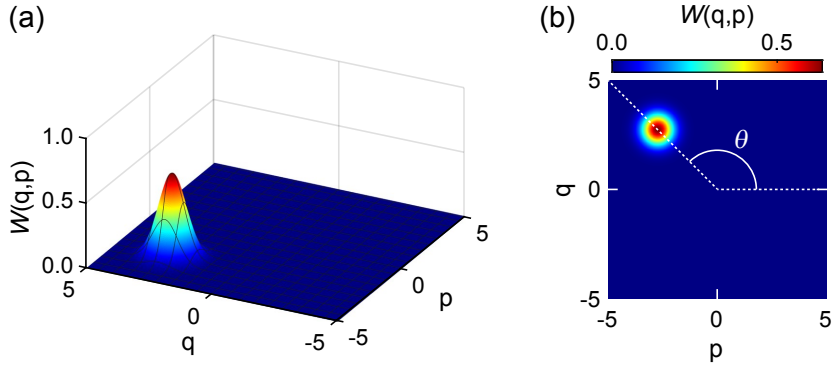

Figure 2.2: (a) 3D representation and (b) top view of the Wigner function of a coherent state with $|\alpha| = 15$ and $\theta = 3\pi/4$.

"most classical" states. Displaced states are the second class of states with equal minimum uncertainties in both quadratures aside from the vacuum state and are, consequently, pure states with $\mu = 1$. In fact, they can be theoretically described by displacing the vacuum state in the phase space $|\alpha\rangle = \hat{D}(\alpha)\,|0\rangle$ by using the displacement operator

$$\hat{D}(\alpha) = \exp\left(\alpha\hat{a}^\dagger - \alpha^*\hat{a}\right), \tag{2.19}$$

where $\alpha = |\alpha|e^{i(\pi/2-\theta)} = Q + iP$ is a complex number describing the displacement amplitude. We define the displacement angle θ as the angle between the displacement direction and the p-axis, as can be seen in Fig. 2.2. The center of the coherent state Wigner function is shifted to (Q, P) in the phase space leading to the following quadrature mean and covariance matrix

$$\bar{\mathbf{r}}_{\text{coh}} = (Q, P) = (\text{Re}\,\alpha,\ \text{Im}\,\alpha) \qquad \text{and} \qquad \mathbf{V}_{\text{coh}} = \frac{\mathbb{I}_2}{4}\,. \tag{2.20}$$

In our experiments, we implement the displacement operation $\hat{D}(\alpha)$ by utilizing a directional coupler acting as a highly asymmetric beam splitter in the microwave regime [64]. The to-be-displaced state $\hat{a}_{\text{in}}$ is incident at the port with high transmissivity τ while a strong coherent signal $\hat{b}_{\text{coh}}$ is applied to the weakly coupled port. The resulting signal takes the form [65]

$$\hat{a}_{\text{out}} = \sqrt{\tau}\hat{a}_{\text{in}} + \sqrt{1-\tau}\,\hat{b}_{\text{coh}}\,. \tag{2.21}$$

Since the strong coherent signal $\hat{b}_{\text{coh}}$ has a large amplitude $|\tilde{\alpha}| \gg 1$, we can treat it classically and use $\hat{b}_{\text{coh}}\,|\tilde{\alpha}\rangle = \tilde{\alpha}\,|\tilde{\alpha}\rangle$ to approximate it with $\tilde{\alpha}$. For $\tau \to 1$, we obtain $\hat{a}_{\text{out}} \approx \hat{a}_{\text{in}} + \sqrt{1-\tau}\,\tilde{\alpha} = \hat{a}_{\text{in}} + \alpha$ with $\alpha = \sqrt{1-\tau}\,\tilde{\alpha}$ [65].

Single-mode squeezed state

Single-mode squeezed (SMS) states are another class of minimum uncertainty states with unit purity. The name originates from the fact that the variances in different

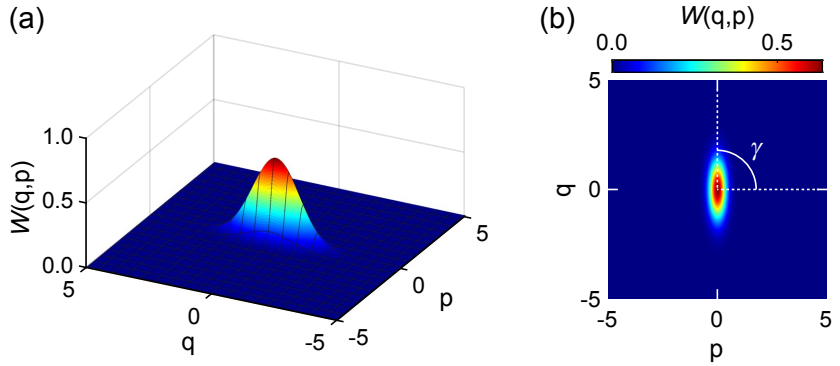

Figure 2.3: (a) 3D representation and (b) top view of the Wigner function of a single-mode squeezed state with $\gamma = \pi/2$ and $r = 0.6$ corresponding to a squeezing level $S = 5.2\,\mathrm{dB}$.

quadrature directions are different. Consequently, the Wigner function of a SMS state is not rotationally symmetric but has an ellipsoidal, i.e. a "squeezed", shape. For a SMS state, one variance along a certain quadrature direction is lower than the variance of a vacuum state. In this case, the Heisenberg uncertainty relation dictates that the variance of the orthogonal quadrature must be increased accordingly. Theoretically, squeezed states can be described by the application of the squeezing operator

$$\hat{S}(\xi) = \exp\left(\frac{1}{2}\xi^*\hat{a}^2 - \frac{1}{2}\xi(\hat{a}^\dagger)^2\right) \tag{2.22}$$

to the vacuum state $|\xi\rangle = \hat{S}(\xi)\,|0\rangle$. Here, $\xi = re^{i\varphi}$ is the complex squeezing amplitude. The phase φ defines the orientation of the squeezed state in the phase space. We define the squeezing angle $\gamma = -\varphi/2$ as the angle between the antisqueezed quadrature direction and the p-axis (see Fig. 2.3). The squeezing factor r determines the amount of squeezing and defines the variances along the squeezed quadrature and antisqueezed quadrature as $\sigma_\mathrm{s}^2 = e^{-2r}/4$ and $\sigma_\mathrm{a}^2 = e^{2r}/4$, respectively. In our experiments, we employ Josephson parametric amplifiers for the generation of squeezed microwave states (see Sec. 2.2). Also, in an experimental setting, we quantify the amount of squeezing and antisqueezing in decibel as

$$S = -10\log_{10}\left[\sigma_\mathrm{s}^2/0.25\right] \qquad \text{and} \qquad A = 10\log_{10}\left[\sigma_\mathrm{a}^2/0.25\right], \tag{2.23}$$

where 0.25 is the quadrature variance of the vacuum which originates from the non-commutation of the quadrature operators. Positive levels of S indicate squeezing below the vacuum limit and we expect $S = A = 20r\log_{10}(e)$ for an ideal squeezed state. Using the latter definitions of S and A, we can reformulate the Heisenberg uncertainty relation to $A - S \geq 0$. The quadrature mean and covariance matrix of a squeezed state are

$$\bar{\mathbf{r}}_\mathrm{sq} = 0 \qquad \text{and} \qquad \mathbf{V}_\mathrm{sq} = \frac{1}{4}\begin{pmatrix} e^{-2r}\cos^2\frac{\varphi}{2} + e^{2r}\sin^2\frac{\varphi}{2} & -\sinh 2r\sin\varphi \\ -\sinh 2r\sin\varphi & e^{2r}\cos^2\frac{\varphi}{2} + e^{-2r}\sin^2\frac{\varphi}{2} \end{pmatrix}. \tag{2.24}$$

The latter expression is obtained by using the definition of the quadratures in Eq. (2.3) and the transformation properties of the squeezing operator [60]

$$\hat{S}^\dagger(\xi)\hat{a}\hat{S}(\xi) = \hat{a}\cosh r - \hat{a}^\dagger e^{i\varphi}\sinh r\,, \tag{2.25}$$

$$\hat{S}^\dagger(\xi)\hat{a}^\dagger\hat{S}(\xi) = \hat{a}^\dagger\cosh r - \hat{a}e^{-i\varphi}\sinh r\,. \tag{2.26}$$

We note that these expressions have the form of a Bogoliubov transformation which originally appeared as a solution in the BCS theory of superconductivity [66, 67]. Since the Bogoliubov transformation is the most general linear transformation of $\hat{a}$ and $\hat{a}^\dagger$, it is used in various fields of physics [68–70].

2.1.3 Two-mode squeezed state

Until now, we only considered singe-mode Gaussian states which implies locality of these states. In continuous-variable quantum information, two-mode squeezed (TMS) states are an important nonlocal resource for various protocols. They possess entanglement and are closely related to the famous Einstein-Podolsky-Rosen (EPR) states [36] which are the first states connected with the notion of entanglement. A TMS state can be described by the two-mode squeezing operator [50]

$$\hat{S}_{1,2} = \exp\left(\xi^*\hat{a}_1\hat{a}_2 - \xi\hat{a}_1^\dagger\hat{a}_2^\dagger\right)\,, \tag{2.27}$$

where $\hat{a}_i$ is the annihilation operator of the i-th electromagnetic mode and $\xi = re^{i\varphi}$. Here, the amount of two-mode squeezing is given by r and the phase φ determines which quadratures on the two modes are correlated. For $\varphi = 0$, the quadrature mean and covariance matrix of a pure TMS state are [16]

$$\bar{\mathbf{r}}_{\text{tms}} = 0 \qquad \text{and} \qquad \mathbf{V}_{\text{tms}} = \frac{1}{4}\begin{pmatrix} \cosh 2r & 0 & \sinh 2r & 0 \\ 0 & \cosh 2r & 0 & -\sinh 2r \\ \sinh 2r & 0 & \cosh 2r & 0 \\ 0 & -\sinh 2r & 0 & \cosh 2r \end{pmatrix}\,, \tag{2.28}$$

where we now consider $\hat{\mathbf{r}} = (\hat{q}_1, \hat{p}_1, \hat{q}_2, \hat{p}_2)$ consisting of the quadratures of both modes. From Eq. (2.28) and Fig. 2.4, we can observe that locally the modes look like thermal states with a photon number $n_{\text{th}} = \sinh^2 r$. This means that there exist no local correlations or local squeezing in an ideal TMS state. The correlations between the modes are encoded in the off-diagonal 2×2 matrices, which becomes clearer if one considers the Wigner function [16]

$$W(\mathbf{x}) = \frac{4}{\pi^2}\exp\left\{-\frac{(q_1+q_2)^2+(p_1-p_2)^2}{e^{2r}} - \frac{(q_1-q_2)^2+(p_1+p_2)^2}{e^{-2r}}\right\}\,, \tag{2.29}$$

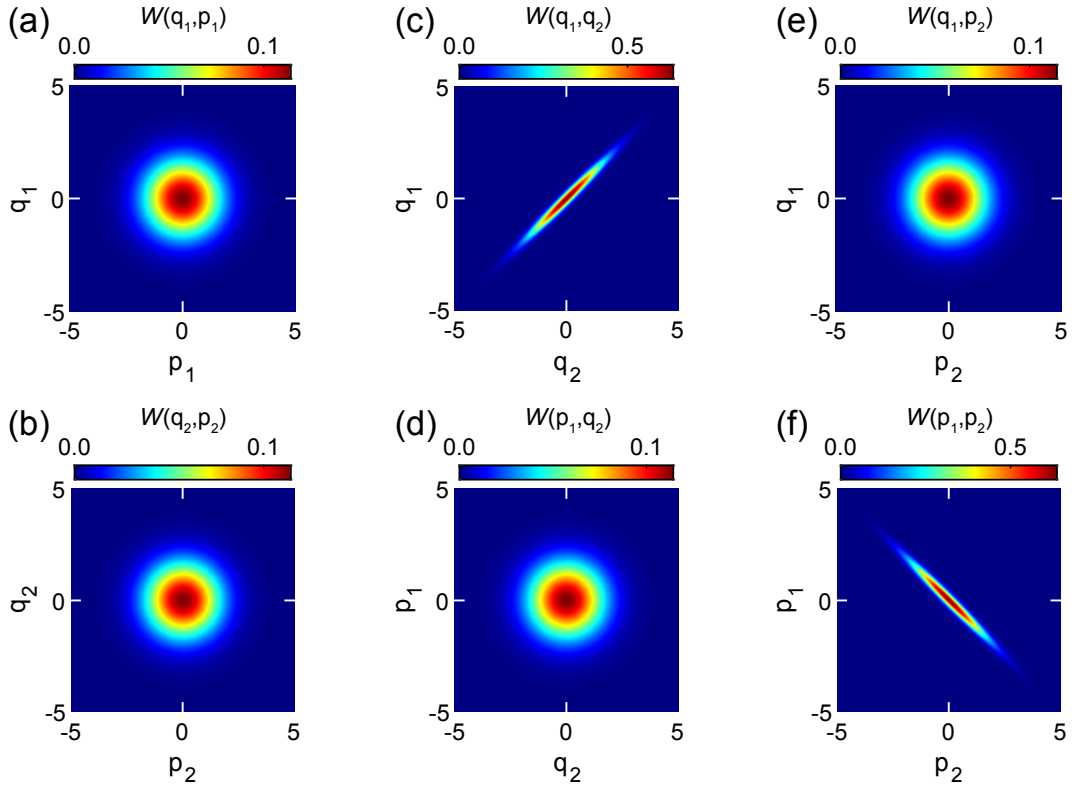

Figure 2.4: Marginal distributions of the Wigner function of a TMS state with $r = 1.2$ and $\varphi = 0$. Panels (a) and (b) are the local marginal distributions which are equivalent to thermal states. Panels (c-f) are the marginal distributions in the nonlocal phase spaces which reveal correlations in the quadrature pairs (q_1, q_2), (q_1, p_2), (p_1, q_2), and (p_1, p_2).

where $\mathbf{x} = (q_1, p_1, q_2, p_2)$. For $r \to \infty$, we obtain $W(\mathbf{x}) \propto \delta(q_1 - q_2)\delta(p_1 + p_2)$ which means that the pairs (q_1, q_2) and (p_1, p_2) are perfectly correlated and anti-correlated, respectively.

If one considers the sum and difference operators $\hat{q}_\pm = (\hat{q}_1 \pm \hat{q}_2)/\sqrt{2}$ and $\hat{p}_\pm = (\hat{p}_1 \pm \hat{p}_2)/\sqrt{2}$ of a TMS state with $\varphi = 0$, we obtain for the variances $(\Delta q_-)^2 = (\Delta p_+)^2 = e^{-2r}/4$ and $(\Delta q_+)^2 = (\Delta p_-)^2 = e^{2r}/4$. This is consistent with the Wigner function since the variance in $\hat{q}_-$ and $\hat{p}_+$ exponentially decreases with increasing r.

2.1.4 Entropy of quantum states

We now discuss various entropic quantities based on the von Neumann entropy. The latter is a useful information-theoretic tool for characterizing quantum states and can be calculated from the covariance matrix of Gaussian quantum states.

Classical information theory

In classical information theory, the Shannon entropy [71] is a basic quantity. Let us consider an ensemble X with elements x_i which occur with a probability p_i where $\sum_i p_i = 1$. Then,

the Shannon entropy is defined as [72]

$$H_{\mathrm{sh}}(X) = -\sum_i p_i \log p_i \,, \tag{2.30}$$

where the logarithm can be taken to different bases. Commonly, base two is used so that the entropy is measured in bits. However, for continuous variables, the information is often measured in nats where the natural logarithm is used for calculation of the entropies. The entropy can be interpreted in different ways. On the one hand, it quantifies the uncertainty, or the lack of information, in a system. This can be understood in the context of thermodynamics where the entropy increases for higher levels of disorder in the system. On the other hand, in information theory, the entropy quantifies the information required to fully describe the system. In fact, according to Shannon's noiseless coding theorem [71], the entropy provides the minimum number of classical bits encoding all information about the system.

Von Neumann entropy

The von Neumann entropy $H(X) = -\operatorname{Tr}(\hat{\rho}_x \log \hat{\rho}_x)$ of a quantum state X with density operator $\hat{\rho}_x$ is the quantum information analogue of the entropy used in thermodynamics (up to a factor of the Boltzmann constant k_{B}). In general, the von Neumann entropy is enclosed in the Shannon entropy, $H(X) \leq H_{\mathrm{sh}}(X)$ [72]. Furthermore, similar as for the Shannon entropy, one can find different interpretations of the von Neumann entropy. On the one hand, $H(X)$ measures the mixedness of a quantum state. On the other hand, $H(X)$ provides the optimal compression in quantum coding, i.e., the minimal number of qubits required to represent a quantum state X faithfully [73, 74].

For Gaussian states, $H(X)$ can be calculated from their covariance matrices $\mathbf{V}$ and, for single-mode Gaussian states, is given by [15]

$$H(X) = f\left(\sqrt{\det \mathbf{V}}\right) \,, \tag{2.31}$$

where $f(x) = \left(2x + \frac{1}{2}\right) \log\left(2x + \frac{1}{2}\right) - \left(2x - \frac{1}{2}\right) \log\left(2x - \frac{1}{2}\right)$. Here and in the rest of this work, we use the natural logarithms when calculating $H(X)$ and related quantities. The joint entropy of the whole bipartite state is given by [55]

$$H(A, B) = H(B, A) = f(\nu_+) + f(\nu_-) \,, \tag{2.32}$$

where $\nu_\pm$ are the symplectic eigenvalues defined in Eq. (2.11). For such a bipartite system, we also define the quantum mutual information which captures all correlations, quantum and classical, in the system [55]

$$I(A:B) = H(A) + H(B) - H(A, B) = f\left(\sqrt{I_1}\right) + f\left(\sqrt{I_2}\right) - f(\nu_+) - f(\nu_-) \,. \tag{2.33}$$

Finally, we introduce the quantum conditional entropies

$$H(A|B) = H(A,\, B) - H(B) = f(\nu_+) + f(\nu_-) - f\left(\sqrt{I_2}\right), \tag{2.34}$$

$$H(B|A) = H(A,\, B) - H(A) = f(\nu_+) + f(\nu_-) - f\left(\sqrt{I_1}\right), \tag{2.35}$$

which are the entropy of A conditioned on full knowledge about B or vice versa. If both parties are correlated, knowledge about B will reveal information about A, and thus, decrease its entropy, $H(A|B) < H(A)$. We want to note that $H(A|B) < 0$ and $H(B|A) < 0$ indicate entanglement between A and B which will be discussed in detail in the next subsection.

2.1.5 Quantum entanglement

One of the most intriguing properties a quantum-mechanical system may possess is quantum entanglement. We already mentioned entanglement in the context of TMS states in Sec. 2.1.2. The latter states are a prime example of entangled states in continuous variables. Whether a bipartite quantum state is entangled or not is defined via the separability of the density operator $\hat{\rho}_{AB}$ of the state. A quantum state is not entangled if $\hat{\rho}_{AB}$ is separable, meaning that $\hat{\rho}_{AB}$ can be expressed as a convex sum of product states [16]

$$\hat{\rho}_{AB} = \sum_i p_i \hat{\rho}_{i,A} \otimes \hat{\rho}_{i,B}\,. \tag{2.36}$$

In general, it is nontrivial to find quantitative measures of entanglement for arbitrary quantum states. However, for our case of bipartite Gaussian states, there exist multiple of such measures [57]. We will use negativity N which is based on the partial transpose of the density matrix and is an entanglement monotone. It reduces to [57]

$$N = \max\left[0,\, \frac{1 - 4\tilde{\nu}_-}{8\tilde{\nu}_-}\right] = \max[0,\, N_\mathrm{k}] \tag{2.37}$$

for bipartite Gaussian states. We note that Eq. (2.37) is written for our vacuum variance of $1/4$ whereas Ref. [57] uses a vacuum variance of 1. The quantity $\tilde{\nu}_-$ is one of the symplectic eigenvalues of the partially transposed density matrix defined as [75]

$$\tilde{\nu}_- = \sqrt{\frac{\tilde{\Delta} - \sqrt{\tilde{\Delta}^2 - 4I_4}}{2}}, \tag{2.38}$$

where $\tilde{\Delta} = I_1 + I_2 - 2I_3$. The state is separable if $\tilde{\nu}_- \geq 1/4$ and entangled otherwise. Consequently, a positive negativity kernel, $N_\mathrm{k} > 0$, indicates entanglement and for maximally entangled states $N_\mathrm{k} \to \infty$.

2.1.6 Quantum discord

In quantum mechanics, there exist quantum correlations which go beyond entanglement as illustrated in Fig. 2.5 (a). One quantity to gain insight into such quantum correlations is quantum discord. It is defined as the difference between two classically-equivalent definitions of the mutual information [76, 77] [see Fig. 2.5 (b)]. The first is the quantum mutual information $I(A:B)$, defined in Eq. (2.33), which captures all correlations (both classical and quantum) in the bipartite system. The second one is the one-way classical correlation J which depends on a measurement-based quantum analogue of the conditional entropy. Intuitively, quantum discord can be understood as a measure of "quantumness" of a state. In particular, non-zero quantum discord is only a necessary but not a sufficient condition for correlations in a bipartite state to surpass the classical limit [78].

Let us consider a bipartite quantum state $\hat{\rho}_{AB}$ under a local projective measurement on B. The measurement can be mathematically represented as a positive operator-valued measure (POVM) $\mathbf{\Pi}_B = \{\hat{\Pi}_i\}$ where the elements $\hat{\Pi}_i$ correspond to the measurement outcome i. The post-measurement state of A is given by $\hat{\rho}_{A|i} = 1/p_i \, \mathrm{Tr}_B(\hat{\rho}_{AB}\hat{\Pi}_i)$ and it occurs with the probability $p_i = \mathrm{Tr}_{AB}(\hat{\rho}_{AB}\hat{\Pi}_i)$ [79]. Here, Tr_B denotes the partial trace of the subsystem B. We can define the conditional entropy obtained under the measurement $\mathbf{\Pi}_B$ on B as $C_{\mathbf{\Pi}_B}(A|B) = \sum_i p_i H(\hat{\rho}_{A|i})$. The one-way classical correlation is defined as [79]

$$J(A|B) = H(A) - \inf_{\mathbf{\Pi}_B} C_{\mathbf{\Pi}_B}(A|B) = H(A) - C_{\min}(A|B)\,, \tag{2.39}$$

where $\inf_{\mathbf{\Pi}_B} C_{\mathbf{\Pi}_B}(A|B)$ denotes minimization of the conditional entropy over all possible measurements and $C_{\min}(A|B)$ is the minimized conditional entropy. With the above

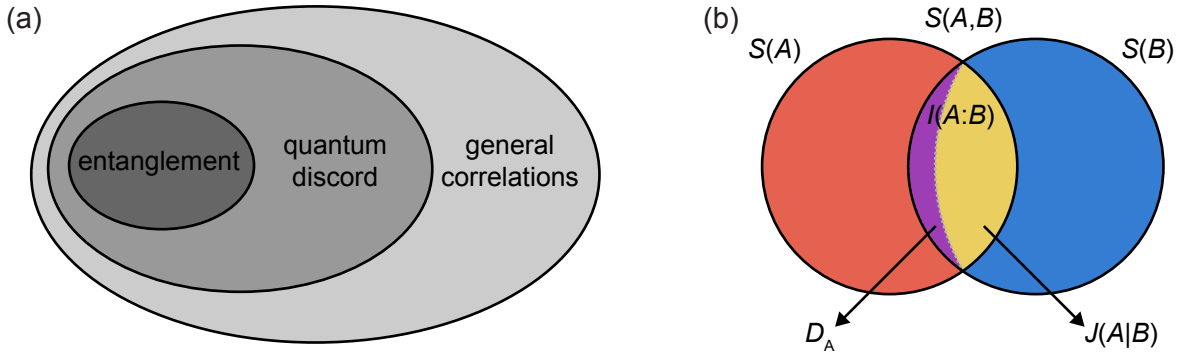

Figure 2.5: (a) Classification of different types of correlations. The grey shades indicate the strength of "quantumness" which is increasing with decreasing brightness of the grey shades. (b) Venn diagram for the description of quantum discord for mixed unentangled bipartite states which are correlated. The bipartite state has a joint entropy $S(A, B)$ (union of both circles) while the individual states have entropy $S(A)$ and $S(B)$ (left and right circle). The mutual information $I(A:B)$ (overlap of both circles) between A and B consists of the sum of quantum discord D_A (violet region) and one-way classical correlations $J(A|B)$ (yellow region).

quantities, we can define quantum discord as [76]

$$D_A = I(A:B) - J(A|B) = H(B) - H(A,\,B) + C_{\min}(A|B)\,. \tag{2.40}$$

In general, quantum discord is not symmetric, i.e., it matters if the measurements are considered to be performed on system A or system B. $D_B = I(A:B) - J(B|A)$ is obtained by swapping the roles of A and B. Interestingly, by using Eq. (2.34), quantum discord can also be expressed as the difference between the two conditional entropies

$$D_A = C_{\min}(A|B) - H(A|B)\,. \tag{2.41}$$

From an intuitive point of view, quantum discord can be linked to the indistinguishability of quantum states. For non-orthogonal states, it is not possible to perfectly distinguish two states with a single measurement. This means that a single measurement cannot, in general, reveal all information on the quantum state. Quantum discord is only non-zero for a bipartite state if at least one of the local states cannot be expressed in terms of an orthonormal basis. This is consistent with the fact that quantum discord D_B vanishes for classical-quantum states such as [80]

$$\hat{\rho}_{AB} = \sum_i p_i \left|i\right\rangle \left\langle i\right|_A \otimes \hat{\rho}_B^{(i)}\,, \tag{2.42}$$

where $\hat{\rho}_B^{(i)}$ is an arbitrary quantum state of B, p_i the probability for state $|i\rangle$, and $|i\rangle$ an orthonormal basis of A's state. Due to the orthonormal basis, the states on A are fully distinguishable and, thus, $D_B = 0$ while D_A may be non-zero [81].

For general quantum states, it is hard to find analytic expressions for quantum discord since one needs to find the optimal POVM which minimizes the conditional entropy. For our case of Gaussian states, it was shown that quantum discord can be calculated analytically [79, 82, 83]. For a bipartite Gaussian state, we can write the minimized conditional entropy as $C_{\min}(A|B) = f\left(\sqrt{E_{A|B}^{\min}}\right)$, where [82]

$$E_{A|B}^{\min} = \begin{cases} \left[\frac{|I_3| + \sqrt{I_3^2 - (I_1 - 16I_4)(I_2 - 1/16)}}{(4I_2 - 1/4)}\right]^2 & \text{if } \frac{(I_1 I_2 - I_4)^2}{(I_1 + 16I_4)(I_2 + 1/16)I_3^2} \leq 1, \\ \frac{I_1 I_2 + I_4 - I_3^2 - \sqrt{(I_1 I_2 + I_4 - I_3^2) - 4I_1 I_2 I_4}}{2I_2} & \text{otherwise.} \end{cases} \tag{2.43}$$

Here, we use the symplectic invariants from Eq. (2.10). Note that the expression for $E_{A|B}^{\min}$ is written for our definition of the quadratures and corresponds to the vacuum variance of 1/4. Finally, the quantum discord for a Gaussian state is given by

$$D_A = f\left(\sqrt{I_2}\right) - f\left(\nu_+\right) - f\left(\nu_-\right) + f\left(\sqrt{E_{A|B}^{\min}}\right)\,. \tag{2.44}$$

Again, one obtains D_B by exchanging $A \leftrightarrow B$.

We note that quantum discord can be related to entanglement of formation E_F which is an entanglement monotone [84]. For pure states, the mathematical definitions of quantum discord and E_F coincide, meaning that the entanglement encloses all quantum correlations in the absence of noise [82]. Only for mixed states, there is a difference between entanglement and quantum discord [85].

2.1.7 Second-order correlation function

Photon statistics provide important information on the properties of an electromagnetic field emitted from a light source. However, single photons might be hard to directly observe in an experiment. Nevertheless, one can gain information on the photon statistics by measuring the intensity correlations of the field. These correlations can be measured in configurations similar to the famous Hanbury-Brown-Twiss experiment [50, 86]. The second-order correlation function $g^{(2)}(\tau)$ for stationary fields is defined as [87]

$$g^{(2)}(\tau) = \frac{\langle \hat{a}^\dagger(0)\hat{a}^\dagger(\tau)\hat{a}(\tau)\hat{a}(0)\rangle}{\langle \hat{a}^\dagger(0)\hat{a}(0)\rangle^2}\,, \tag{2.45}$$

where τ is a time delay. The function $g^{(2)}(\tau)$ provides insight into the probability of finding photons at a time τ if a photon was present at time $\tau = 0$ [50]. For coherent light, the photons are evenly distributed in time and the second-order correlation function is constant, $g^{(2)}(\tau) = g^{(2)}(0)$. If it is likely to detect multiple photons in a short time interval, $g^{(2)}(\tau) < g^{(2)}(0)$, the light is called *bunched*. Thermal or squeezed states are examples from the class of Gaussian states for such bunched light. In the case of $g^{(2)}(\tau) > g^{(2)}(0)$, the light is called *antibunched*. Here, an important example are single photons emitted by e.g. a quantum two-level system. In Ref. [88], it was shown that antibunched light can be produced by combining squeezing and displacement in a certain parameter regime.

The second-order correlation function at $\tau = 0$ also provides direct insight into the photon statistics by reformulating it to [50]

$$g^{(2)}(0) = 1 + \frac{\mathrm{Var}(\hat{a}^\dagger\hat{a}) - \langle \hat{a}^\dagger\hat{a}\rangle}{\langle \hat{a}^\dagger\hat{a}\rangle^2}\,, \tag{2.46}$$

where $\mathrm{Var}(\hat{a}^\dagger\hat{a})$ is the photon number variance. For the cases of $g^{(2)}(0) = 1$, $g^{(2)}(0) > 1$ and $g^{(2)}(0) < 1$ we have Poissonian, super-Poissonian, and sub-Poissonian light, respectively [60]. We summarize the properties of different fundamental quantum states in Tab. 2.1. For a squeezed displaced state with photon number $|\alpha|^2 + \sinh^2 r$, one obtains [50]

$$g^{(2)}(0) = 1 + \frac{|\alpha|^2(\cosh 2r - \sinh 2r \cos 2\theta - 1) + \sinh^2 r \cosh 2r}{\left(|\alpha|^2 + \sinh^2 r\right)^2}\,. \tag{2.47}$$

Table 2.1: Photon number $\langle\hat{n}\rangle = \langle\hat{a}^\dagger\hat{a}\rangle$, photon number variance $\mathrm{Var}(\hat{a}^\dagger\hat{a})$ and $g^{(2)}(0)$ for different quantum states. The number of photons in a Fock state is denoted by N.

	$\langle\hat{n}\rangle$	$\mathrm{Var}(\hat{a}^\dagger\hat{a})$	$g^{(2)}(0)$	photon statistics
coherent state	$\lvert\alpha\rvert^2$	$\lvert\alpha\rvert^2$	1	Poissonian
thermal state	n_{th}	$n_{\mathrm{th}}^2 + n_{\mathrm{th}}$	2	super-Poissonian
squeezed state	$\sinh^2 r$	$2\sinh^2 r \cosh^2 r$	$3 + 1/\langle\hat{n}\rangle$	super-Poissonian
Fock state	N	0	$1 - 1/\langle\hat{n}\rangle$	sub-Poissonian

2.2 Josephson parametric amplifiers (JPA)

In the previous section, we have discussed general properties of Gaussian states of light. Now, we theoretically describe means of generating these states in the microwave regime with a flux-driven Josephson parametric amplifier (JPA). A flux-driven JPA is a superconducting circuit consisting of a coplanar waveguide (CPW) resonator which is short-circuited to ground through a direct-current superconducting quantum interference device (dc-SQUID). It is a parametric device which allows for amplification of microwave signals with a noise performance close to the standard quantum limit or generation of quantum signals in the form of squeezed light.

2.2.1 Superconductivity and Josephson junctions

One of the most important properties of a superconductor is the Meißner-Ochsenfeld effect, i.e., the expulsion of magnetic flux from the bulk of the superconductor (perfect diamagnetism) below a certain transition temperature. An important consequence of this effect is perfect conductivity which makes superconducting materials a good choice to minimize dissipative losses. Another intriguing phenomenon is the Josephson effect, first theoretically predicted by Josephson [89], which can be observed if two superconductors are weakly coupled to each other. The effect can be understood by considering that superconductivity is a quantum-mechanical phenomenon which manifests on macroscopic scales. The Josephson effect originates from the overlap of the wave functions of each superconductor $\Psi_i(\mathbf{r},t) = \sqrt{n_i^*(\mathbf{r},t)}\mathrm{e}^{i\theta_i(\mathbf{r},t)}$, where $i = 1, 2$ denotes superconductor 1 or 2 [90]. Here, $\sqrt{n_i^*(\mathbf{r},t)}$ is the density of superconducting Cooper pairs, and $\theta_i(\mathbf{r},t)$ is the global phase of the wave function for each superconductor. An overlap of the wave functions can be achieved by placing a thin layer of non-superconducting material, such as an insulator, between the two superconductors, as shown in Fig. 2.6 (a). Such a structure is referred to as a Josephson junction. Due to the weak coupling, there can be a finite phase difference across the Josephson junction which will be important to describe the Josephson effect. The gauge invariant phase difference across the Josephson junction is

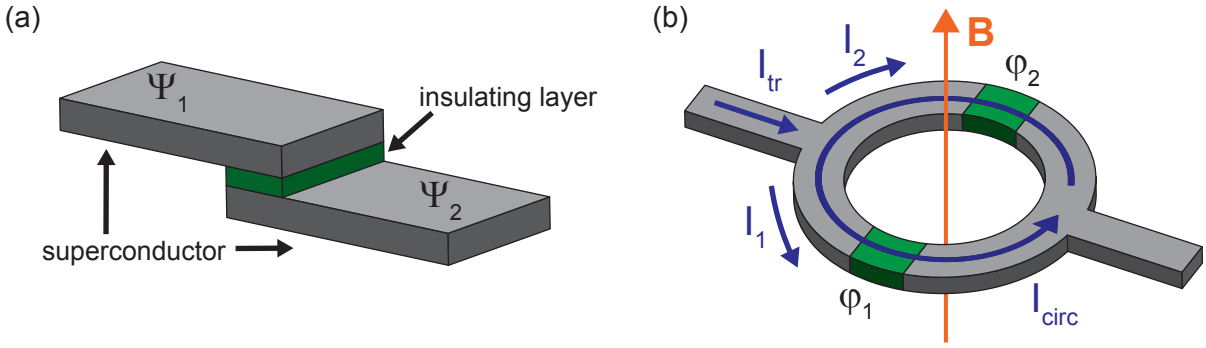

Figure 2.6: (a) Schematic of a Josephson junction with superconductors in gray and an insulating layer in green. (b) Schematic of dc-SQUID with one Josephson junction in each arm of the superconducting loop. Each Josephson junction is associated with a phase difference φ_i.

given by [91]

$$\varphi(\mathbf{r},t) = \theta_2(\mathbf{r},t) - \theta_1(\mathbf{r},t) - \frac{2\pi}{\Phi_0}\int_1^2 \mathbf{A}(\mathbf{r},t)\cdot d\mathbf{l}\,, \tag{2.48}$$

where $\Phi_0 = \frac{h}{2e}$ is the magnetic flux quantum and $\mathbf{A}(\mathbf{r},t)$ is a magnetic vector potential. The integration path is along a line from superconductor 1 to superconductor 2. In our experiments, we can neglect the spatial dependence of the Cooper pair density. The Josephson effect is commonly described by two equations, the first one being the current-phase relation [92]

$$I_\mathrm{s}(\varphi) = I_\mathrm{c}\sin(\varphi)\,, \tag{2.49}$$

where I_s is the supercurrent through the Josephson junction and I_c is the critical Josephson current.

The second Josephson equation, also called the voltage- or energy-phase relation, describes the time evolution of the phase difference in the presence of a finite energy difference $2eV = \hbar\omega = \hbar\partial\varphi/\partial t$ between the coupled superconductors. That is, it connects the voltage V across a Josephson junction to the time-derivative of the phase difference [92]

$$\frac{\partial\varphi}{\partial t} = \frac{2\pi}{\Phi_0}V(t)\,. \tag{2.50}$$

Consequently, a constant voltage across a Josephson junction leads to a linear evolution of φ in time which, in turn, causes a sinusoidal oscillation of the supercurrent I_s.

In this context, it is useful to define the nonlinear inductance of a Josephson junction [92]

$$L_\mathrm{s}(\varphi) = \frac{\Phi_0}{2\pi I_\mathrm{c}\cos\varphi} = L_\mathrm{c}\frac{1}{\cos\varphi}\,, \tag{2.51}$$

where $L_\mathrm{c} = \Phi_0/(2\pi I_\mathrm{c})$ corresponds to the minimal Josephson junction inductance. L_s can be derived by using the Josephson equations and definition of the inductance $V = L\frac{\mathrm{d}I_\mathrm{s}}{\mathrm{d}t}$. The nonlinear properties of a Josephson junction make it a central building block for

superconducting circuits where it is often utilized as a nonlinear, lossless inductance.

The dynamics of a Josephson junction can also be described using related energies and potentials. The Josephson coupling energy E_J originates from the finite overlap of the wave functions and is defined as [92]

$$E_\mathrm{J}(\varphi) = \frac{\Phi_0 I_\mathrm{c}}{2\pi}(1-\cos\varphi) = E_\mathrm{J0}(1-\cos\varphi)\,, \tag{2.52}$$

where $E_\mathrm{J0} = \Phi_0 I_\mathrm{c}/2\pi$.

If one drives a Josephson junction with an external current I, acting as a generalized force, the potential energy is given by the tilted washboard potential [92, 93]

$$E_\mathrm{pot}(\varphi) = E_\mathrm{J}(\varphi) - I\left(\frac{\Phi_0}{2\pi}\varphi\right) = E_\mathrm{J0}\left(1-\cos\varphi-\frac{I}{I_\mathrm{c}}\varphi\right)\,. \tag{2.53}$$

To gain an intuitive understanding of the dynamics under the external current I, one can imagine the phase difference φ as a classical particle moving inside this potential. The zero-voltage state and voltage state of a Josephson junction are related to the phase particle resting and moving in the potential, respectively. The first state can be obtained for $|I| < I_\mathrm{c}$, where the particle rests in a local minimum of the potential in the absence of noise sources. The second state corresponds to the phase particle rolling down the potential for $|I| > I_\mathrm{c}$, where no local minima exist anymore.

If we consider a Josephson junction with a finite capacitance C and normal resistance R, we can describe the Josephson junction dynamics with the Resistively and Capacitively Shunted Junction (RCSJ) model. This model is only an approximation since it does not consider the superconducting energy gap. The equation of motion within the RCSJ model reads [93, 94]

$$\frac{\ddot{\varphi}}{\omega_\mathrm{p}^2} + \frac{\dot{\varphi}}{\omega_\mathrm{c}} = j - \sin\varphi = -\frac{1}{E_\mathrm{J0}}\frac{\partial E_\mathrm{pot}(\varphi)}{\partial\varphi}\,, \tag{2.54}$$

where $\omega_\mathrm{p} = \sqrt{2\pi I_\mathrm{c}/\Phi_0 C}$ is the plasma frequency, $\omega_\mathrm{c} = 2\pi I_\mathrm{c} R/\Phi_0$ a characteristic frequency and $j = I/I_\mathrm{c}$ the normalized supercurrent through the Josephson junction.

Alternatively, the dynamics of a Josephson junction can be described with the corresponding Lagrangian. This approach will be useful when investigating more complex scenarios such as the response of JPAs to an applied magnetic flux. If we neglect the resistive term, we obtain the Lagrangian of a single Josephson junction,

$$\mathcal{L} = K(\dot{\varphi}) - E_\mathrm{pot}(\varphi) = \frac{\hbar^2\dot{\varphi}^2}{4E_\mathrm{c}} - E_\mathrm{J0}\left(1-\cos\varphi-j\varphi\right)\,, \tag{2.55}$$

where $E_\mathrm{c} = (2e)^2/2C$ is the charging energy of the capacitor with the charge of one Cooper pair and $K(\dot{\varphi})$ is the kinetic energy corresponding to the first term on the left hand side

of Eq. (2.54). The equation of motion can be obtained from the Lagrangian as

$$\frac{d}{dt}\frac{\partial \mathcal{L}}{\partial \dot{\varphi}} - \frac{\partial \mathcal{L}}{\partial \varphi} = 0\,. \tag{2.56}$$

We note that Eqs. (2.54) and (2.55) are a quasi-classical description of the Josephson junction dynamics. They describe the classical motion of a phase particle in the tilted washboard potential. For a description of superconducting qubits based on Josephson junctions, a full quantum mechanical description of the Josephson junctions is required. In particular, the commutation relation between the operators for the phase difference $\hat{\varphi}$ and the charge $\hat{Q}$ needs to be considered [95]. Depending on the relative magnitude of the Josephson energy E_J and the charging energy E_c, one obtains different types of superconducting qubits [96]. For the Josephson junctions used in the JPAs presented in this thesis, the Josephson energy strongly dominates over the charging energy, $E_\mathrm{J}/E_\mathrm{c} \simeq 10^3$. Furthermore, as discussed in Sec. 2.2.4, the Josephson nonlinearity in JPAs is diluted by galvanically connecting the Josephson junctions to a coplanar waveguide resonator. Consequently, the dynamics of the phase difference $\hat{\varphi}$ can be well described with the above quasi-classical model, and the charging energy of the Josephson junction and any uncertainty between the charge and phase degree of freedom can be neglected.

2.2.2 Dc-SQUID

A central building block of the JPA is a direct current superconducting quantum interference device (dc-SQUID). It consists of two Josephson junctions with critical currents I_c in a superconducting loop, as shown in Fig. 2.6 (b). For simplicity, we assume equal critical currents of the Josephson junctions but different I_c are also possible. An externally applied magnetic field $\mathbf{B}$ causes a magnetic flux Φ_ext through the loop. Due to boundary conditions, the total phase change along a closed contour C around the dc-SQUID loop is fixed to $\oint_C \nabla\theta = 2\pi n$ with $n \in \mathbb{Z}_0$. By using the gauge invariant phase difference in Eq. (2.48) and the phase gradient in the bulk superconductor, we can write [92]

$$\nabla\theta = \frac{2\pi}{\Phi_0}(\Lambda \mathbf{J}_s + \mathbf{A})\,, \tag{2.57}$$

where $\mathbf{J}_s$ is the supercurrent density, $\mathbf{A}$ is the vector potential and Λ is the London parameter. For simplicity, we choose an integration path inside the superconductor where the supercurrent density $\mathbf{J}_s$ is approximately zero and obtain

$$\varphi_2 - \varphi_1 = \frac{2\pi\Phi}{\Phi_0} + 2\pi n\,. \tag{2.58}$$

This equation provides us with a connection between the phase differences $\varphi_{1,2}$ across the Josephson junctions and the total magnetic flux Φ threading the loop. The total

magnetic flux $\Phi = \Phi_{\mathrm{ext}} + L_{\mathrm{loop}} I_{\mathrm{circ}}$ consists of the externally applied flux Φ_{ext} and the self-induced flux $L_{\mathrm{loop}} I_{\mathrm{circ}}$, where L_{loop} is the self-inductance of the superconducting loop. The circulating current is given by

$$I_{\mathrm{circ}} = \frac{I_1 - I_2}{2} = I_{\mathrm{c}} \cos\left(\frac{\varphi_1 + \varphi_2}{2}\right) \sin\left(\frac{\varphi_1 - \varphi_2}{2}\right) = -I_{\mathrm{c}} \cos\varphi_+ \sin\varphi_- \,, \tag{2.59}$$

where we introduced new phase differences

$$\varphi_+ \equiv \frac{\varphi_1 + \varphi_2}{2} \qquad \text{and} \qquad \varphi_- \equiv \frac{\varphi_2 - \varphi_1}{2} \,, \tag{2.60}$$

in order to simplify the notation. For example, the fluxoid quantization condition in terms of the new phase difference φ_- reads

$$\varphi_- = \pi \frac{\Phi}{\Phi_0} + \pi n \,. \tag{2.61}$$

Here, it is useful to define the total transport current through the dc-SQUID

$$I_{\mathrm{tr}} = I_1 + I_2 = 2 I_{\mathrm{c}} \sin\left(\frac{\varphi_1 + \varphi_2}{2}\right) \cos\left(\frac{\varphi_1 - \varphi_2}{2}\right) = 2 I_{\mathrm{c}} \sin\varphi_+ \cos\varphi_- \,, \tag{2.62}$$

which is given by the sum of the currents through each Josephson junction. The screening properties of the superconducting loop are summarized in the so-called screening parameter [97]

$$\beta_{\mathrm{L}} \equiv \frac{2 L_{\mathrm{loop}} I_{\mathrm{c}}}{\Phi_0} \,, \tag{2.63}$$

which relates the maximally induced flux $L_{\mathrm{loop}} I_{\mathrm{c}}$ to half of a flux quantum $\Phi_0/2$. With the above equations we can write the total flux through the dc-SQUID loop as

$$\frac{\Phi}{\Phi_0} = \frac{\Phi_{\mathrm{ext}}}{\Phi_0} - \frac{\beta_{\mathrm{L}}}{2} \cos\varphi_+ \sin\varphi_- \,, \tag{2.64}$$

If we now consider $\beta_{\mathrm{L}} \simeq 0$, the self-induced flux by the dc-SQUID can be neglected and, consequently, the total flux can be approximated by the externally applied flux, $\Phi \approx \Phi_{\mathrm{ext}}$. Then, in analogy to the critical current of a Josephson junction, one can define a maximum transport current of the dc-SQUID [93]

$$I_{\mathrm{s}}^{\mathrm{max}}(\Phi_{\mathrm{ext}}) = 2 I_{\mathrm{c}} \left| \cos\left(\pi \frac{\Phi_{\mathrm{ext}}}{\Phi_0}\right) \right| \,. \tag{2.65}$$

Consequently, for $\beta_{\mathrm{L}} \simeq 0$, the dc-SQUID can be considered as a single Josephson junction with a flux-modulated maximum supercurrent and, thus, in analogy to Eq. (2.51), a

flux-tunable inductance of the dc-SQUID can be defined as [98]

$$L_{\mathrm{s}}(\Phi_{\mathrm{ext}}) = \frac{\Phi_0}{2\pi I_{\mathrm{s}}^{\mathrm{max}}} = \frac{\Phi_0}{4\pi I_{\mathrm{c}} \left|\cos\left(\pi \frac{\Phi_{\mathrm{ext}}}{\Phi_0}\right)\right|} \,. \tag{2.66}$$

This equation nicely illustrates that the dc-SQUID can be applied both as an in-situ flux-tunable inductance as well as a nonlinear element in superconducting circuits.

For the case $\beta_{\mathrm{L}} > 0$, the self-inductance of the loop cannot be neglected anymore. Therefore, the behavior of the dc-SQUID is described by Eqs. (2.62) and (2.64). These two equations need to be solved self-consistently under the constraint of the fluxoid quantization condition in Eq. (2.58). For general cases, it is not possible to obtain an analytic expression but nevertheless one can define

$$I_{\mathrm{s}}^{\mathrm{max}}(\Phi_{\mathrm{ext}}) = 2I_{\mathrm{c}} \cdot j_{\mathrm{c}}(\Phi_{\mathrm{ext}}) \,, \tag{2.67}$$

$$L_{\mathrm{s}}(\Phi_{\mathrm{ext}}) = \frac{\Phi_0}{4\pi I_{\mathrm{c}} \cdot j_{\mathrm{c}}(\Phi_{\mathrm{ext}})} \,, \tag{2.68}$$

where $j_{\mathrm{c}}(\Phi_{\mathrm{ext}})$ is a dimensionless critical supercurrent through the dc-SQUID. We refer the reader to Sec. 2.2.5 and Sec. 2.2.4 for a detailed discussion on how we simulate and use $j_{\mathrm{c}}(\Phi_{\mathrm{ext}})$ in order to describe the flux dependence of a coplanar waveguide resonator short-circuited to ground by a dc-SQUID.

Similarly to the case of one Josephson junction, one can write Kirchhoff's law for both junctions [93]

$$\frac{\ddot{\varphi}_1}{\omega_{\mathrm{p1}}^2} + \frac{\dot{\varphi}_1}{\omega_{\mathrm{c1}}} = -\sin\varphi_1 + j_{\mathrm{tr}} + \frac{1}{\pi\beta_{\mathrm{L}}}\left(\varphi_2 - \varphi_1 - 2\pi\frac{\Phi_{\mathrm{ext}}}{\Phi_0}\right) \,, \tag{2.69}$$

$$\frac{\ddot{\varphi}_2}{\omega_{\mathrm{p2}}^2} + \frac{\dot{\varphi}_2}{\omega_{\mathrm{c2}}} = -\sin\varphi_2 + j_{\mathrm{tr}} - \frac{1}{\pi\beta_{\mathrm{L}}}\left(\varphi_2 - \varphi_1 - 2\pi\frac{\Phi_{\mathrm{ext}}}{\Phi_0}\right) \,, \tag{2.70}$$

where indices 1 and 2 denote the two Josephson junctions and $j_{\mathrm{tr}} = I_{\mathrm{tr}}/(2I_{\mathrm{c}})$. Finally, we neglected the dissipative terms and define the Lagrangian of a dc-SQUID [99]

$$\mathcal{L} = \frac{\hbar^2}{4E_{\mathrm{c}}}(\dot{\varphi}_1^2+\dot{\varphi}_2^2) - E_{\mathrm{J0}}\left(2 - \cos\varphi_1 - \cos\varphi_2 - j_{\mathrm{tr}}(\varphi_1+\varphi_2)\right) - \frac{E_{\mathrm{J0}}}{2\pi\beta_{\mathrm{L}}}\left(\varphi_2 - \varphi_1 - 2\pi\frac{\Phi_{\mathrm{ext}}}{\Phi_0}\right)^2 \,, \tag{2.71}$$

which can also be written in the form

$$\mathcal{L} = \frac{\hbar^2}{2E_{\mathrm{c}}}(\dot{\varphi}_+^2 + \dot{\varphi}_-^2) - E_{\mathrm{J0}}\left(2 - 2\cos\varphi_+\cos\varphi_- - 2j_{\mathrm{tr}}\varphi_+\right) - \frac{2E_{\mathrm{J0}}}{\pi\beta_{\mathrm{L}}}\left(\varphi_- - \pi\frac{\Phi_{\mathrm{ext}}}{\Phi_0}\right)^2 \,. \tag{2.72}$$

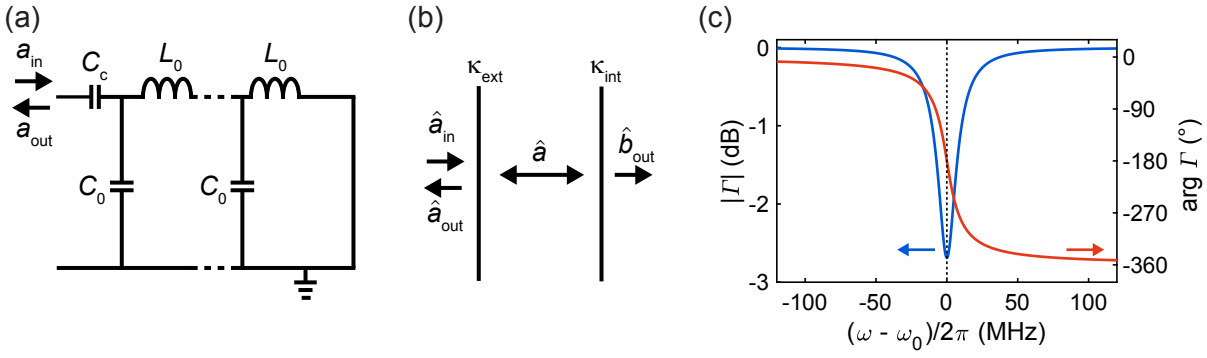

Figure 2.7: (a) Distributed element model of a CPW resonator. Here, L_0 and C_0 are the inductance and capacitance per unit length, and C_c is a coupling capacitance which allows an input signal a_{in} to enter and a signal a_{out} to leave the resonator. (b) Input-output model of a resonator with an internal mode $\hat{a}$ and internal loss rate κ_{int} which couples to a loss mode $\hat{b}_{out}$. Input-output coupling is expressed by an external coupling rate κ_{ext}. The operators $\hat{a}_{in}$, $\hat{a}_{out}$, $\hat{a}$, and $\hat{b}_{out}$ are treated quantum-mechanically. (c) Reflection magnitude $|\Gamma|$ and reflection angle Arg (Γ) versus readout frequency for $Q_{ext} = 300$, $Q_{int} = 1000$ and $\omega_0/2\pi = 5$ GHz.

2.2.3 Coplanar waveguide resonators

In circuit quantum electrodynamics, superconducting resonators have various purposes. For example, they can serve as quantum bus [100], quantum memory [101], or can be applied to study fundamental light-matter interactions [10]. Furthermore, they are an essential part of JPAs.

First, we consider a coplanar waveguide (CPW) which acts as a quasi one-dimensional transmission line. Since we are interested in frequencies in the gigahertz regime, the lateral dimensions of the CPW should be on the order of a few millimeters. Therefore, the CPW needs to be described with a distributed element model, where each circuit element is considered to be infinitesimally small. The wave propagation through such a system is generally described by the telegrapher's equations [102]. Since our CPW structures consist of a superconducting material, we can approximate the CPW with a lossless transmission line with a characteristic impedance [102]

$$Z = \sqrt{\frac{L_0}{C_0}}, \tag{2.73}$$

where L_0 and C_0 are the inductance and capacitance per unit length of the transmission line, respectively. In general, disregarding polarization, an infinite homogeneous transmission line does not have any mode restrictions due to the absence of boundary conditions.

In order to create a resonant structure, one needs to apply boundary conditions to the waves propagating through the transmission line. One way to realize such a boundary condition is to create a discontinuity in the transmission line by introducing a line break with a corresponding capacitance C_c. Simultaneously, this capacitor acts as an external

port to couple to the field inside the resonator. Alternatively, one can short-circuit the CPW to ground which creates a voltage node and current antinode. We focus on quarter-wavelength resonators where both of these boundary conditions are employed, namely, a coupling capacitance at one end of the resonator and a short to ground at the other end as shown in Fig. 2.7 (a). The fundamental resonance frequency of a quarter-wavelength resonator with length l is given by [103]

$$f_\mathrm{r} = \frac{c}{\sqrt{\epsilon_\mathrm{eff}}}\frac{1}{4l} = \frac{1}{4l\sqrt{L_0 C_0}}\,, \tag{2.74}$$

where $\epsilon_\mathrm{eff} = c^2/v_\mathrm{ph}^2$ is the effective permittivity of the CPW, c is the velocity of light in vacuum and $v_\mathrm{ph} = 1/\sqrt{L_0 C_0}$ is the phase velocity. The length of the resonator is connected to the wavelength of the fundamental mode as $l = \lambda/4$, hence the name quarter-wavelength resonator.

In order to probe the resonator, a microwave tone is applied and the reflected signal from the resonator is measured as depicted in Fig. 2.7 (b,c). The reflected signal can differ in amplitude and phase from the applied signal which is captured by the complex reflection coefficient [104]

$$\Gamma = \frac{(\omega-\omega_0)^2 + i\kappa_\mathrm{int}(\omega-\omega_0) + (\kappa_\mathrm{ext}^2 - \kappa_\mathrm{int}^2)/4}{\left[(\omega-\omega_0) + i(\kappa_\mathrm{ext}+\kappa_\mathrm{int})/2\right]^2}\,, \tag{2.75}$$

which is calculated using an input-output formalism. Here, κ_int and κ_ext are the internal and external loss rates, respectively, and ω_0 is the resonance frequency of the resonator in angular units.

The loss rates are related to the quality factor Q of the resonator which is an important quantity characterizing its performance. The quality factor is defined as [102]

$$Q = 2\pi\frac{\text{average energy stored}}{\text{energy loss/cycle}} = \frac{\omega_0}{\kappa_\mathrm{tot}}\,, \tag{2.76}$$

where $\kappa_\mathrm{tot} = \kappa_\mathrm{int} + \kappa_\mathrm{ext}$ defines the total loss rate. Consequently, the loaded quality factor Q_l is defined by the sum of loss rates

$$\frac{1}{Q_\mathrm{l}} = \frac{1}{Q_\mathrm{int}} + \frac{1}{Q_\mathrm{ext}} = \frac{\kappa_\mathrm{int}+\kappa_\mathrm{ext}}{\omega_0}\,, \tag{2.77}$$

where $Q_\mathrm{int} = \omega_0/\kappa_\mathrm{int}$ and $Q_\mathrm{ext} = \omega_0/\kappa_\mathrm{ext}$ are the internal and external quality factor, respectively. The external loss rate is mainly defined by the coupling capacitance and determines how well a probe tone couples to the resonator. The internal loss rate is a sum of various, typically unwanted, loss mechanisms such as loss from two-level fluctuators [105], surface resistance [106], or eddy currents [107].

2.2.4 Resonance frequency of the JPA

We now consider the flux-driven JPA [108] consisting of a quarter-wavelength CPW resonator which is short-circuited to ground by a dc-SQUID (see Fig. 2.8). Here, the dc-SQUID acts as a flux-tunable nonlinear inductor which contributes to the quasi-static resonance frequency ω_0 of the JPA. As discussed in Sec. 2.2.2, we can use a magnetic flux to tune the dc-SQUID inductance and, in this way, the resonance frequency of the whole JPA circuit. In order to induce parametric effects, an on-chip antenna couples inductively to the dc-SQUID loop via the loop inductance L_{loop} and is used to apply a strong coherent pump tone with an angular frequency $\omega_{\mathrm{p}} = 2\omega_0$.

In the following, we discuss how the resonance frequency of the JPA circuit depends on an external magnetic flux Φ_{ext} threading the dc-SQUID loop. The treatment is applicable for arbitrary flux-screening of the dc-SQUID which can be quantified by the dimensionless screening parameter β_{L}, as defined in Eq. (2.63). Based on the distributed element model for the quarter-wavelength resonator and a lumped element model for the dc-SQUID (see Fig. 2.8), one arrives at a transcendental equation for the resonance frequency ω_0 of the JPA [109–111]

$$\frac{\pi\omega_0}{2\omega_{\mathrm{r}}}\tan\left(\frac{\pi\omega_0}{2\omega_{\mathrm{r}}}\right) = \frac{(2\pi)^2}{\Phi_0^2}L_{\mathrm{r}}E_s(\Phi_{\mathrm{ext}}) - \frac{2C_{\mathrm{s}}}{C_{\mathrm{r}}}\left(\frac{\pi\omega_0}{2\omega_{\mathrm{r}}}\right)^2. \tag{2.78}$$

Here, L_{r}, C_{r}, and $\omega_{\mathrm{r}}/2\pi$ are the total inductance, the total capacitance and the resonance frequency of the bare resonator, respectively, $E_{\mathrm{s}}(\Phi_{\mathrm{ext}})$ is the flux-dependent energy of the dc-SQUID as defined below, and C_{s} is the capacitance of one Josephson junction. For the presented samples, the last term in Eq. (2.78) can be neglected, since the capacitance of the Josephson junctions is much smaller than the one of the resonator, $C_{\mathrm{s}} \ll C_{\mathrm{r}}$. For a vanishing transport current I_{tr} through the dc-SQUID, the normalized critical supercurrent $j_{\mathrm{c}}(\Phi_{\mathrm{ext}})$, used in Eqs. (2.67) and (2.68), only depends on φ_- and can be simplified to

$$j_{\mathrm{c}} = \left|\cos\varphi_-^{\min}(\Phi_{\mathrm{ext}})\right|, \tag{2.79}$$

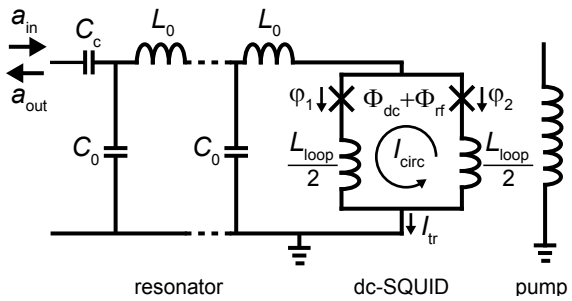

Figure 2.8: Circuit diagram of a JPA consisting of a CPW resonator which is short-circuited to ground by a dc-SQUID. The crosses indicate Josephson junctions. The dc-SQUID has a non-zero loop inductance L_{loop}, and thus, inductively couples to an external magnetic flux $\Phi_{\mathrm{dc}} + \Phi_{\mathrm{rf}}$. The flux Φ_{rf} is generated by an adjacent pump line.

where $\varphi_\pm \equiv (\varphi_1 \pm \varphi_2)/2$ are defined in Eq. (2.60). The superscript in $\varphi_\pm^{\min}(\Phi_{\text{ext}})$ denotes the steady-state phase differences for a given external flux Φ_{ext}. Thus, the Josephson inductance of the dc-SQUID reads

$$L_{\text{s}}(\Phi_{\text{ext}}) = \frac{\Phi_0}{4\pi I_{\text{c}} |\cos \varphi_-^{\min}(\Phi_{\text{ext}})|}\,, \tag{2.80}$$

where I_{c} is the critical current of a single Josephson junction. Using L_{s}, we can express the flux-dependent energy of the dc-SQUID as

$$E_{\text{s}}(\Phi_{\text{ext}}) = \frac{\Phi_0^2}{(2\pi)^2} \frac{1}{L_{\text{s}}(\Phi_{\text{ext}}) + L_{\text{loop}}/4}\,, \tag{2.81}$$

where the non-zero dc-SQUID loop inductance L_{loop} is split between both arms of the dc-SQUID [112].

The tangent in Eq. (2.78) can be expanded into a Laurent series near $\pi/2$ for $\omega_0/\omega_{\text{r}} \simeq 1$. Consequently, we obtain a simplified expression for the resonance frequency of the JPA in terms of inductances

$$\omega_0(\Phi_{\text{ext}}) = \omega_{\text{r}} \left[1 + \frac{L_{\text{s}}(\Phi_{\text{ext}}) + L_{\text{loop}}/4}{L_{\text{r}}}\right]^{-1}\,. \tag{2.82}$$

We now discuss the effect of flux-screening of the dc-SQUID depending on the screening parameter β_{L}. In general, $\varphi_-^{\min}(\Phi_{\text{ext}})$ exhibits a non-trivial dependence on the external magnetic flux. According to the fluxoid quantization, $\varphi_-^{\min}(\Phi_{\text{ext}})$ is related to the total flux $\Phi = \Phi_{\text{ext}} + L_{\text{loop}} I_{\text{circ}}$ threading the dc-SQUID according to $\varphi_-^{\min} = \pi(\Phi/\Phi_0)$. As already discussed in Sec. 2.2.2, we have $\Phi \approx \Phi_{\text{ext}}$ in the case of a vanishing screening parameter $\beta_{\text{L}} \simeq 0$. In this case, the phase of one Josephson junction relative to the other one is fixed by the fluxoid quantization, reducing the available degrees of freedom from two to one. This results in a single-valued dependence $\varphi_-^{\min} = \pi(\Phi_{\text{ext}}/\Phi_0)$. A mechanical analog of this situation are two strongly coupled pendula, where the system can be described by a single deflection angle, i.e., a single degree of freedom due to the rigid coupling. However, if the screening parameter β_{L} becomes non-zero, there is no analytic expression for $\varphi_-^{\min}(\Phi_{\text{ext}})$ anymore and the dependence has to be calculated numerically. Consequently, the JPA resonance frequency can exhibit a non-trivial behavior when varying the external flux.

The results presented in this subsection have been published by us in Ref. [113]. Parts of the text and figures are adapted from this reference.

2.2.5 Simulation of the dc-SQUID potential

In this subsection, we discuss hysteretic dc-SQUIDs for non-zero screening $\beta_{\text{L}} > 0$ under a varying external magnetic field. To describe the behavior of a dc-SQUID in equilibrium,

we consider a phase particle in the two-dimensional dc-SQUID potential [93, 99]

$$\frac{U(\varphi_+,\,\varphi_-)}{E_\mathrm{J}} = 2 - 2\cos\varphi_+\cos\varphi_- - 2j_\mathrm{tr}\varphi_+ + \frac{2}{\pi\beta_\mathrm{L}}\left(\varphi_- - \pi\frac{\Phi_\mathrm{ext}}{\Phi_0}\right)^2, \tag{2.83}$$

where $j_\mathrm{tr} \equiv I_\mathrm{tr}/2I_\mathrm{c}$ is the normalized dc-SQUID transport current and $E_\mathrm{J} \equiv I_\mathrm{c}\Phi_0/2\pi$ is the coupling energy of a single Josephson junction. The potential $U(\varphi_+,\,\varphi_-)$ can be derived from the Lagrangian in Eq. (2.72) by using $\mathcal{L} = K(\dot{\varphi}_+,\,\dot{\varphi}_-) - U(\varphi_+,\,\varphi_-)$. The dc-SQUID potential $U(\varphi_+,\,\varphi_-)$, calculated according to Eq. (2.83), for different values of the external flux Φ_ext and with a typical experimental value of $\beta_\mathrm{L} = 0.6$ as well as $j_\mathrm{tr} = 0$ is shown in Fig. 2.9. Note that there is no tilt of the potential landscape along the φ_+-direction for vanishing transport current, $j_\mathrm{tr} = 0$. In our simulations and experiments, j_tr is negligible at all times due to the small applied microwave signal which is in contrast to other works investigating hysteretic dc-SQUIDs [99, 114, 115]. Consequently, the possible equilibrium phase differences $(\varphi_+^\mathrm{min}, \varphi_-^\mathrm{min})$ of the dc-SQUID are given by the local minima shown in Fig. 2.9.

To get an intuition on the origin of the hysteretic behavior, we now consider a phase particle with coordinates $(\varphi_+^\mathrm{min}, \varphi_-^\mathrm{min})$ residing in one of the potential minima. Multiple equivalent local minima, which describe the same state of the dc-SQUID, exist due to the periodicity of the potential. For $\Phi_\mathrm{ext} = 0$, all local minima are degenerate and correspond to the same dc-SQUID state. However, for non-zero Φ_ext and β_L there exist at least two classes of minima corresponding to screening currents with a clockwise and counterclockwise direction. One is shifted downwards and the other one upwards in energy, therefore corresponding to a class of stable and metastable states, respectively.

In order to obtain $\varphi_-^\mathrm{min}(\Phi_\mathrm{ext})$, we record the equilibrium positions of the phase particle for a continuously varied external magnetic flux Φ_ext. Figure 2.9 depicts the behavior of the phase particle for increasing and decreasing Φ_ext. In our simulation, we neglect thermally activated switching and tunneling processes of the phase particle as well as the finite charging energy of the Josephson junctions. In other words, we assume that the phase particle resides in a specific minimum as long as the minimum exists. Only if this minimum vanishes due to a changed Φ_ext, the phase particle will perform transitions to one of the two adjacent minima. Since the adjacent minima always correspond to a different class of local minima, $\varphi_-^\mathrm{min}(\Phi_\mathrm{ext})$ exhibits a discontinuity. The magnetic flux at which the discontinuity appears depends on the magnitude of β_L. Since the dc-SQUID inductance $L_\mathrm{s}(\Phi_\mathrm{ext})$, and therefore the JPA resonance frequency $\omega_0(\Phi_\mathrm{ext})$, is dependent on $\varphi_-^\mathrm{min}(\Phi_\mathrm{ext})$, we can experimentally observe the discontinuity as a jump of $\omega_0(\Phi_\mathrm{ext})$, as discussed in Sec. 3.2.2. The flux dependence of the resonance frequency for the whole JPA circuit is obtained by evaluating Eq. (2.82) with the simulated $\varphi_-^\mathrm{min}(\Phi_\mathrm{ext})$ as shown in Fig. 2.9 (g).

The two-dimensional potential landscapes shown in Fig. 2.9 are calculated for $j_\mathrm{tr} = 0$. However, in our experiments discussed in Sec. 3.2.2, a finite microwave signal is applied to

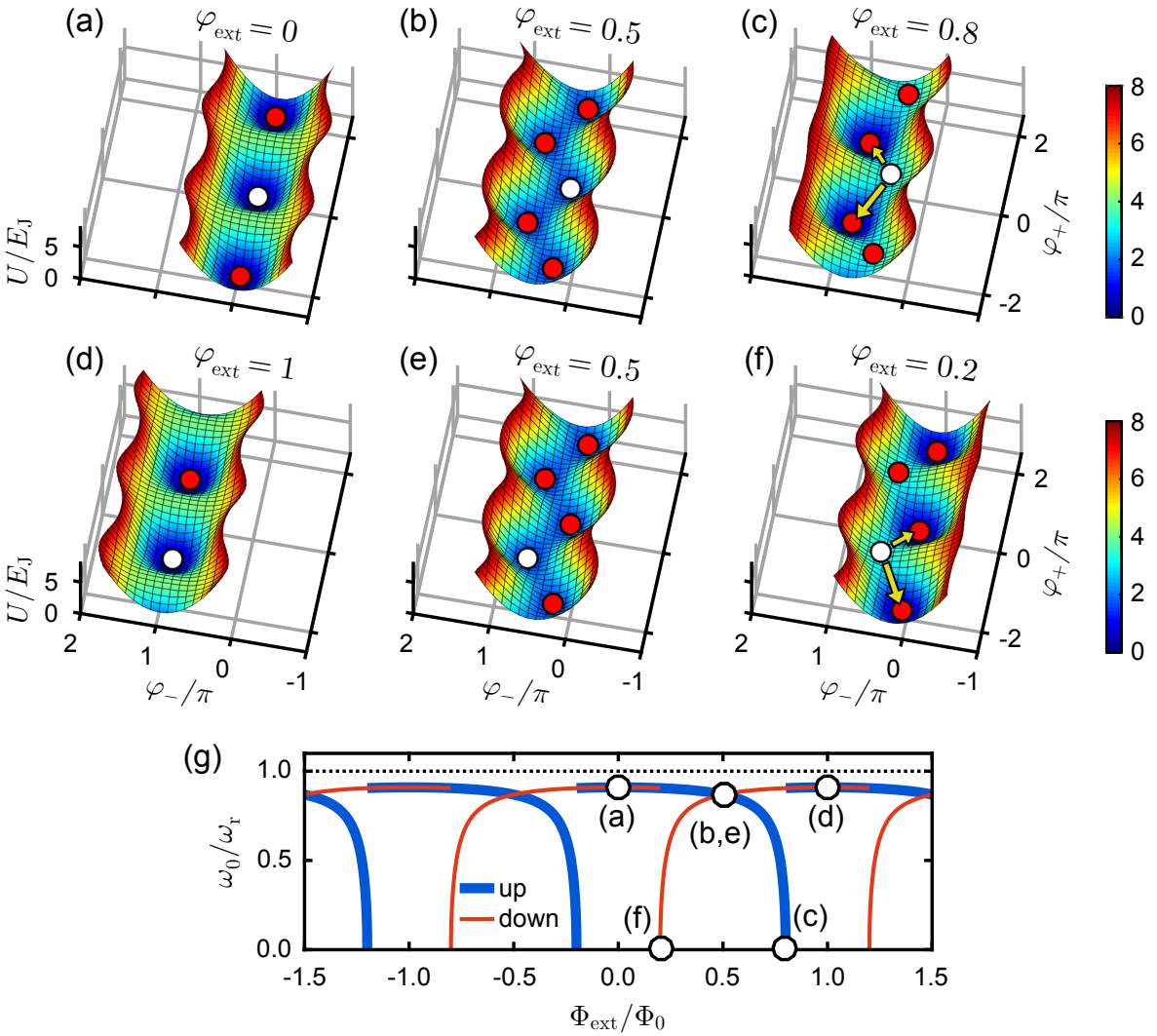

Figure 2.9: Two-dimensional dc-SQUID potential U for different normalized external flux values $\varphi_{ext} = \Phi_{ext}/\Phi_0$ with $\beta_L = 0.6$ and $j_{tr} = 0$. The position of the phase particle is marked by white dots, whereas red dotes denote the positions of other local minima. (a)-(d) and (e), (f) correspond to increasing and decreasing external flux Φ_{ext}, respectively. (g) JPA resonance frequency ω_0 as a function of external flux calculated from Eq. (2.82) for $L_r = 10L_{s,min}$, $L_{s,min} = \Phi_0/(4\pi I_c)$, and $L_{loop} = 0$. Furthermore, the white markers correspond to the position of the phase particle in panels (a)-(f).

the JPA. The microwave signal results in a finite microwave current across the dc-SQUID which resides in a current anti-node of the resonator. This finite microwave current results in a periodic tilt of the dc-SQUID potential along the φ_+-axis which affects the dynamics of the phase particle. However, in our experiments we apply only very weak microwave signals, resulting in small microwave currents inside the resonator. By taking into account the quality factors and inductance of the JPA resonators, we find that the microwave current, depending on the investigated JPA (see Sec. 3.2.2), is at least two orders of

magnitude smaller than the junction critical current. As a consequence, the negligible periodic tilt of the dc-SQUID potential along the φ_+-axis can be neglected when analyzing the phase dynamics. Note that the finite microwave current results in a smearing of the hysteretic $\varphi_-^{\min}$ versus Φ_{ext} dependence similar to thermal or other noise currents.

The results presented in this subsection have been published by us in Ref. [113]. Parts of the text and figures are adapted from this reference.

2.2.6 Parametric amplification with flux-driven JPAs

Amplification in JPAs is enabled by driving a parametric process with a pump tone. The pump tone typically varies one parameter of a system in a periodic fashion which gives rise to parametric effects [116, 117]. In general, such a system requires a nonlinear element. For superconducting circuits, Josephson junctions are routinely used for this purpose and a variety of parametric amplifiers have been realized based on them [27, 28, 118–122]. We focus on flux-driven JPAs [108] where the pump tone is inductively coupled to the JPA and has a frequency ω_p of twice the resonance frequency of the circuit. Here, the pump tone leads to a periodic modulation of the dc-SQUID inductance which, in turn, causes a periodic modulation of the resonance frequency ω_0 of the JPA circuit. Consequently, the induced parametric modulation enables a three-wave mixing process where an incident signal mode at frequency $\omega_\text{s} = \omega_\text{p}/2 + \delta\omega$ and detuning $\delta\omega$ is amplified, as depicted in Fig. 2.10. At the same time, an idler mode at frequency $\omega_\text{i} = \omega_\text{p}/2 - \delta\omega$ is created. One can imagine this process as a pump photon splitting into one signal photon and one idler photon such that the energy is conserved, $\omega_\text{p} = \omega_\text{s} + \omega_\text{i}$ [123].

In order to describe the flux-driven JPA analytically, we employ an input-output model for the JPA developed by Yamamoto *et al.* [104] and start with an unperturbed classical harmonic oscillator whose resonance frequency ω_0 is periodically modulated such that $\omega_0 \to \omega_0 \left[1 + \epsilon/2 \cos(\alpha\omega_0 t)\right]$, where $\epsilon/2$ and $\alpha\omega_0$ are the amplitude and frequency of the

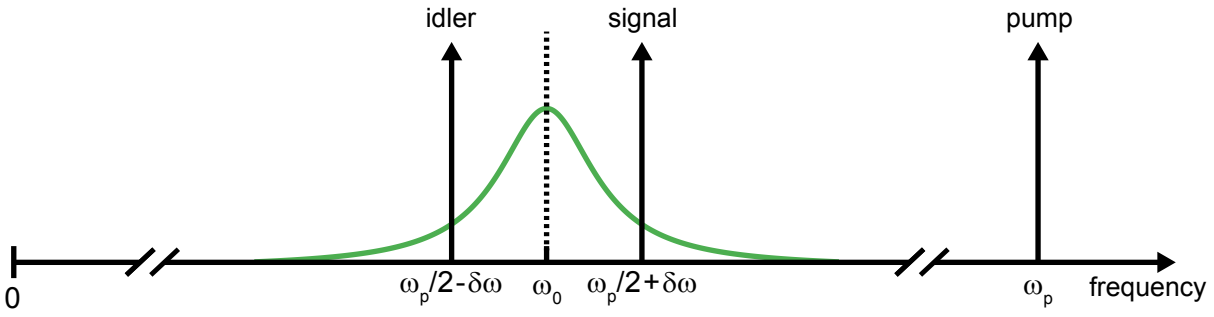

Figure 2.10: Scheme of relevant frequencies for parametric amplification with a flux-driven JPA. The pump frequency ω_p is at roughly twice the JPA resonance frequency ω_0. The signal mode at frequency $\omega_\text{p}/2 + \delta\omega$ is amplified and an idler mode at frequency $\omega_\text{p}/2 - \delta\omega$ is created.

modulation, respectively. Consequently, the classical equation of motion reads [104]

$$\frac{d^2x}{dt^2} + \omega_0^2 \left[1 + \epsilon \cos(\alpha\omega_0 t)\right] x = 0\,. \tag{2.84}$$

Here, we neglected the ϵ^2 term since we only consider small modulation amplitudes, i.e., small pump amplitudes. In a quantum-mechanical picture, the corresponding Hamiltonian in terms of the annihilation and creation operators reads

$$H = \hbar\omega_0 \left[\hat{a}^\dagger\hat{a} + \frac{1}{2} + \epsilon \cos(\alpha\omega_0 t)(\hat{a} + \hat{a}^\dagger)^2\right]. \tag{2.85}$$

After introducing a signal port and a loss port to the Hamiltonian, the Heisenberg equation of motion for the resonator field $\hat{a}$ can be solved in a frame rotating with $\alpha\omega_0/2$ and one obtains expressions for the output field of the JPA. For details on the derivation, we refer the reader to Ref. [104]. We only consider the case where the applied pump tone is twice the resonance frequency of the JPA, $\omega_\mathrm{p} = 2\omega_0$, corresponding to $\alpha = 2$. One can differentiate between two operation modes of the JPA which are discussed in the following.

Nondegenerate gain

The JPA is operated in the nondegenerate operation mode if the input signal at frequency $\omega_\mathrm{s} = \omega_\mathrm{p}/2 + \delta\omega$ has a non-zero offset to half the pump frequency, $\delta\omega \neq 0$. In the nondegenerate operation mode, every quadrature of the signal is amplified equally, and therefore, the JPA acts as a phase-preserving amplifier. For a flux-driven JPA, we can then write explicit expressions for the signal and idler power gain as [104]

$$G_\mathrm{s}(\delta\omega) = \frac{\kappa_\mathrm{int}^2\delta\omega^2 + \left[(\kappa_\mathrm{int}^2 - \kappa_\mathrm{ext}^2)/4 - \epsilon^2\omega_0^2 - \delta\omega^2\right]^2}{\kappa_\mathrm{tot}^2\delta\omega^2 + \left[\kappa_\mathrm{tot}^2/4 - \epsilon^2\omega_0^2 - \delta\omega^2\right]^2}\,, \tag{2.86}$$

$$G_\mathrm{i}(\delta\omega) = \frac{\kappa_\mathrm{ext}^2\epsilon^2\omega_0^2}{\kappa_\mathrm{tot}^2\delta\omega^2 + \left[\kappa_\mathrm{tot}^2/4 - \epsilon^2\omega_0^2 - \delta\omega^2\right]^2}\,, \tag{2.87}$$

where $\kappa_\mathrm{tot} = \kappa_\mathrm{ext} + \kappa_\mathrm{int}$ is the sum of external and internal loss rates. Equations (2.86) and (2.87) are only valid for modulation amplitudes below a certain the threshold value $\epsilon \leq \epsilon_\mathrm{c} = \kappa_\mathrm{tot}/2\omega_0$. Above this threshold, the JPA acts as a Josephson parametric phase-locked oscillator where two dynamical coherent states exist inside the oscillator [104]. The threshold appears, similar to a driven Duffing oscillator, because multiple stable states exist for a highly-driven JPA [110]. For vanishing internal losses, $\kappa_\mathrm{int} = 0$, we obtain the relation $G_\mathrm{s}(\delta\omega) - G_\mathrm{i}(\delta\omega) = 1$.

JPAs are routinely used as low-noise amplifiers of microwave signals in the gigahertz regime since they provide an excellent noise performance [4, 35, 124, 125]. According to the Haus-Caves theorem [126, 127], phase-preserving amplifiers possess a lower limit on the noise they add to the amplified signal. In order to provide a universal measure between

different amplifiers, the added noise is expressed in added noise photons A referred to the input of the amplifier and is limited by [127]

$$A \geq \frac{1}{2}\left|1 - \frac{1}{G_\mathrm{s}}\right| . \tag{2.88}$$

Consequently, for $G_\mathrm{s} \gg 1$, a phase-preserving amplifier adds at least half of a noise photon to the input signal which is known as the standard quantum limit for phase-insensitive amplification. From a theoretical point of view, this fundamental limit originates from the fact that the bosonic commutation relation of the amplified mode needs to be fulfilled [28]. The physical origin of the added noise consists in the admixture of the idler mode to the signal mode. During the parametric amplification, the noise at the idler frequency $\omega_\mathrm{i} = \omega_\mathrm{p}/2 - \delta\omega$ is converted to the signal frequency ω_s, where it is combined with the amplified original signal [123]. The limit of at least half of an added noise photon is attributed to the noise floor of the idler mode limited by the quantum fluctuations.

Degenerate gain

We now consider the case where half the pump frequency and the signal frequency are degenerate, $\omega_\mathrm{s} = \omega_\mathrm{p}/2$, which implies $\delta\omega = 0$. In this scenario, the signal and idler modes have the same frequencies which allows them to interfere with a fixed phase relation. This results in a phase-sensitive amplification where different quadratures are amplified with different gains [28]. For our case of flux-driven JPAs, the degenerate signal gain depends on the phase θ between the pump and the microwave signal and is given by [104]

$$G_\mathrm{d}(\theta) = \frac{\left(\frac{\kappa_\mathrm{ext}^2 - \kappa_\mathrm{int}^2}{4} + \epsilon^2\omega_0^2\right)^2 + \epsilon^2\kappa_\mathrm{ext}^2\omega_0^2 - 2\epsilon\kappa_\mathrm{ext}\omega_0\left(\frac{\kappa_\mathrm{ext}^2 - \kappa_\mathrm{int}^2}{4} + 4\delta^2\omega_0^2\right)\sin(2\theta)}{\left(\frac{\kappa^2}{4} - \epsilon^2\omega_0^2\right)^2} . \tag{2.89}$$

The latter equation is again only valid below the threshold $\epsilon \leq \epsilon_\mathrm{c}$. If we assume an overcoupled JPA, $\kappa_\mathrm{ext} > \kappa_\mathrm{int}$, or more precisely $(\kappa_\mathrm{ext}^2 - \kappa_\mathrm{int}^2)/4 + \epsilon^2\omega_0^2 > 0$, we can define the minimum and maximum degenerate gains

$$G_\mathrm{d}^\mathrm{min} = \left(\frac{\epsilon\omega_0 - (\kappa_\mathrm{ext} - \kappa_\mathrm{int})/2}{\epsilon\omega_0 + (\kappa_\mathrm{ext} + \kappa_\mathrm{int})/2}\right)^2 , \tag{2.90}$$

$$G_\mathrm{d}^\mathrm{max} = \left(\frac{\epsilon\omega_0 + (\kappa_\mathrm{ext} - \kappa_\mathrm{int})/2}{\epsilon\omega_0 - (\kappa_\mathrm{ext} + \kappa_\mathrm{int})/2}\right)^2 , \tag{2.91}$$

for $\theta^\mathrm{min} = \pi/4 + n\pi$ and $\theta^\mathrm{max} = 3\pi/4 + n\pi$, respectively. The difference between the phases is $\pi/2$ which means that the maximally amplified and deamplified quadratures are orthogonal to each other. Furthermore, without any internal losses, $\kappa_\mathrm{int} = 0$, we obtain

$$G_\mathrm{d}^\mathrm{min}\, G_\mathrm{d}^\mathrm{max} = 1 . \tag{2.92}$$

In the phase-sensitive regime, JPAs allow for amplification without adding any additional noise to the signal according to the Haus-Caves theorem. In fact, for a phase-sensitive amplifier, different amounts of noise can be added to each quadrature [127]

$$A_1 A_2 \geq \frac{1}{16}\left|1 - \frac{1}{\sqrt{G_1 G_2}}\right|^2 , \tag{2.93}$$

where A_1 and A_2 denote the added noise photons in orthogonal quadratures with respective gains G_1 and G_2. If we consider an amplifier for which one quadrature is amplified ($G_1 > 1$) while the orthogonal quadrature is deamplified ($G_2 < 1$), the added noise can be zero under the condition $G_1 G_2 = 1$. According to Eq. (2.92), JPAs can reach this limit in the absence of internal losses. In fact, it has been experimentally demonstrated that JPAs can phase-sensitively amplify weak microwave signals with a noise performance below the standard quantum limit [28, 29, 128].

2.2.7 Squeezing with flux-driven JPAs

In the last subsection, we discussed how JPAs can be used as nondegenerate and degenerate amplifiers of microwave signals. In addition, JPAs can also be employed as a tool to generate quantum signals in the form of squeezed states. From the discussion of single-mode squeezed (SMS) states in Sec. 2.1.2, we know that the variance along different quadrature directions varies for SMS states. In this sense, single-mode squeezing of the JPA is closely connected to the degenerate operation mode of the JPA. In order to obtain expressions for the variances of a squeezed state produced by a flux-driven JPA, we assume the fictional homodyne setup depicted in Fig. 2.11. The squeezed signal at the output of the JPA is sent to a mixer which is driven by a local oscillator (LO) with frequency $\omega_\mathrm{p}/2$ and phase ϕ_LO [129]. The mixer down-converts the squeezed input signal to zero frequency. The power spectral density P at the mixer output is directly proportional to a certain quadrature variance of the squeezed signal. This specific quadrature is determined

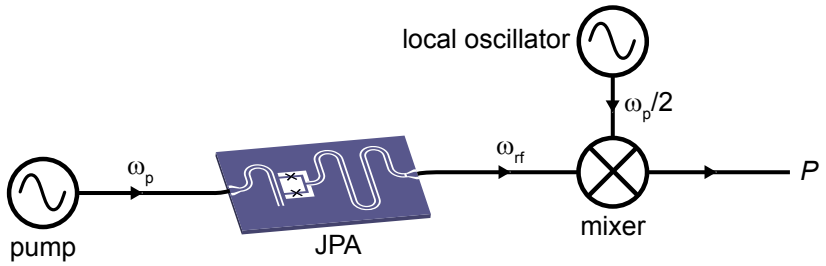

Figure 2.11: Scheme for the description of the squeezing properties of a flux-driven JPA which is pumped at a frequency ω_p. The squeezed signal around the frequency $\omega_\mathrm{rf} = \omega_\mathrm{p}/2$ is down-converted to zero frequency by a mixer which is driven by a local oscillator with frequency $\omega_\mathrm{p}/2$ and phase ϕ_LO. The power spectral density P at the mixer output is directly proportional to the variance in different quadrature directions of the squeezed signal.

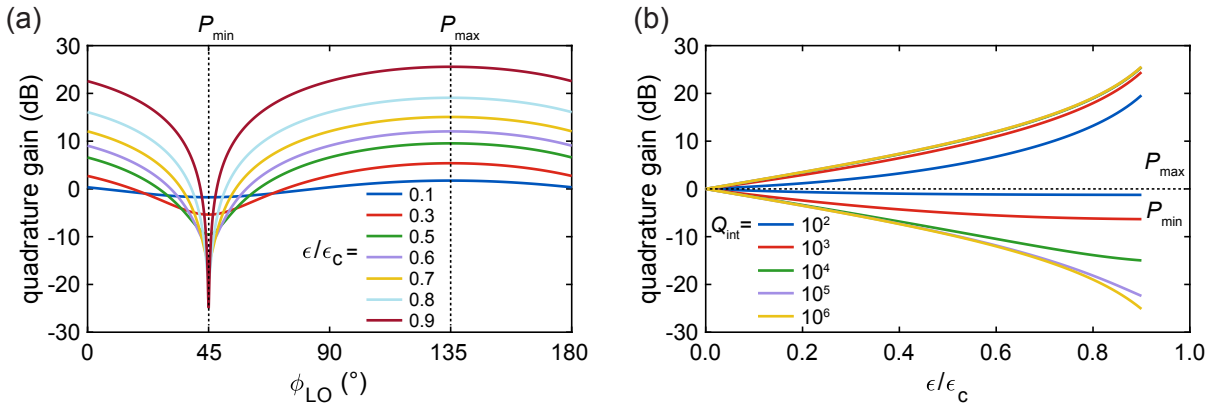

Figure 2.12: (a) Quadrature gain P as a function of the local oscillator phase ϕ_{LO} for different modulation amplitudes $\epsilon/\epsilon_{\mathrm{c}}$ and $Q_{\mathrm{int}} = 1 \cdot 10^6$. (b) Maximum gain P_{max} and minimum gain P_{min} as a function of the modulation amplitude $\epsilon/\epsilon_{\mathrm{c}}$ for different internal quality factors Q_{int}. Both panels are calculated with $Q_{\mathrm{ext}} = 300$ and $\omega_0/2\pi = 5\,\mathrm{GHz}$.

by the LO phase ϕ_{LO}. In this way, we can investigate the variance in different quadrature directions by changing ϕ_{LO}. From the theory of a flux-driven JPA presented in Ref. [104], we obtain

$$P = \left| J_{\mathrm{b}} + |K_{\mathrm{b}}| e^{i(2\phi_{\mathrm{LO}} - \pi/2)} \right|^2 + \left| J_{\mathrm{c}} + |K_{\mathrm{c}}| e^{i(2\phi_{\mathrm{LO}} - \pi/2)} \right|^2 , \tag{2.94}$$

where the first term describes the degenerate signal gain with

$$J_{\mathrm{b}} = \frac{\epsilon^2 \omega_0^2 + (\kappa_{\mathrm{ext}}^2 - \kappa_{\mathrm{int}}^2)/4}{\epsilon^2 \omega_0^2 - \kappa^2/4} \qquad \text{and} \qquad K_{\mathrm{b}} = \frac{-i\epsilon \kappa_{\mathrm{ext}} \omega_0}{\epsilon^2 \omega_0^2 - \kappa^2/4} , \tag{2.95}$$

and the second term describes the noise added by the loss channel with

$$J_{\mathrm{c}} = \frac{\kappa/2 \sqrt{\kappa_{\mathrm{ext}} \kappa_{\mathrm{int}}}}{\epsilon^2 \omega_0^2 - \kappa^2/4} \qquad \text{and} \qquad K_{\mathrm{c}} = \frac{-i\epsilon \sqrt{\kappa_{\mathrm{ext}} \kappa_{\mathrm{int}}} \omega_0}{\epsilon^2 \omega_0^2 - \kappa^2/4} . \tag{2.96}$$

For a given phase ϕ_{LO}, P provides the gain for the corresponding quadrature as shown in Fig. 2.12 (a). For $\phi_{\mathrm{LO}} = \pi/4$, we obtain the minimum gain P_{min} which corresponds to the squeezed quadrature. For the orthogonal antisqueezed quadrature at $\phi_{\mathrm{LO}} = 3\pi/4$, we obtain the maximum gain P_{max}. Since the internal quality factor $Q_{\mathrm{int}} = 1 \cdot 10^6$ is high, we observe $P_{\mathrm{max}} \cdot P_{\mathrm{min}} \simeq 1$. This observation corresponds to noiseless degenerate amplification discussed in the previous subsection, and therefore, the produced squeezed state is pure. In Fig. 2.12 (b), we show how Q_{int} influences the maximum and minimum quadrature gains. In general, the antisqueezed quadrature is only slightly affected by internal losses while the squeezed quadrature drastically depends on Q_{int}. We note that, in contrast to the degenerate signal gain in Eq. (2.89), it is important to consider the added noise due to the loss channel if the JPA is treated as a squeezer. Without consideration of the loss channel, we would obtain $P_{\mathrm{max}} \cdot P_{\mathrm{min}} < 1$ for low enough Q_{int} which would lead to a

violation of the Heisenberg uncertainty, and thus, to an unphysical state generated by the theory.

As shown in Appendix A, we can express the Hamiltonian of a pumped JPA in the interaction picture and rotating-wave approximation in the form

$$\hat{H}_{\text{int}} = i\hbar\frac{\lambda}{2}\left(\hat{a}^2 e^{-i\varphi} - (\hat{a}^\dagger)^2 e^{i\varphi}\right) , \tag{2.97}$$

where φ is the pump phase and $\lambda = \omega_0\epsilon$ is the effective nonlinearity due to the frequency modulation induced by the pump tone. As presented in Ref. [16], a direct connection of the JPA interaction Hamiltonian $\hat{H}_{\text{int}}$ to the squeezing operator can be made. For $\varphi = 0$, the Heisenberg equation of motion is

$$\frac{d}{dt}\hat{a}(t) = \frac{1}{i\hbar}[\hat{a}(t),\, \hat{H}_{\text{int}}] = -\lambda\hat{a}^\dagger(t) , \tag{2.98}$$

which is solved by $\hat{a}(t) = \hat{a}(0)\cosh(\lambda t) - \hat{a}^\dagger(0)\sinh(\lambda t)$. This solution coincides with the action of the squeeze operator on the annihilation operator, as given in Eq. (2.25). Furthermore, the unitary evolution under the action of the Hamiltonian $\hat{H}_{\text{int}}$ is given by

$$\hat{U}(t) = \exp\left[-\frac{i}{\hbar}\hat{H}_{\text{int}}t\right] = \exp\left[\frac{\lambda}{2}\left(\hat{a}^2 e^{-i\varphi} - (\hat{a}^\dagger)^2 e^{i\varphi}\right)t\right] . \tag{2.99}$$

By introducing the dimensionless interaction time $r = \lambda t$, we recreate the original squeezing operator as defined in Eq. (2.22)

$$\hat{U}(t) = \hat{S}(\xi) = \exp\left(\frac{1}{2}\xi^*\hat{a}^2 - \frac{1}{2}\xi(\hat{a}^\dagger)^2\right) , \tag{2.100}$$

with $\xi = re^{i\varphi}$.

In practice, JPAs always produce two-mode squeezed (TMS) states due to their naturally finite bandwidth. Here, correlations exist between quadratures of frequency modes which are symmetric around half the pump frequency [121, 130]. During the parametric process in the JPA, photons in these upper and lower sideband modes are generated from a single pump photon. Consequently, it is intuitively clear that these modes should be correlated. In our experimental heterodyne detection scheme (see Sec. 3.1.2 for details), we apply an analog and a digital down-conversion step to the JPA signal, as shown in Fig. 2.13. The digital down-conversion step overlaps both correlated modes to the same frequency. As a consequence, the physical TMS state is reconstructed as a SMS state in our quantum state reconstruction.

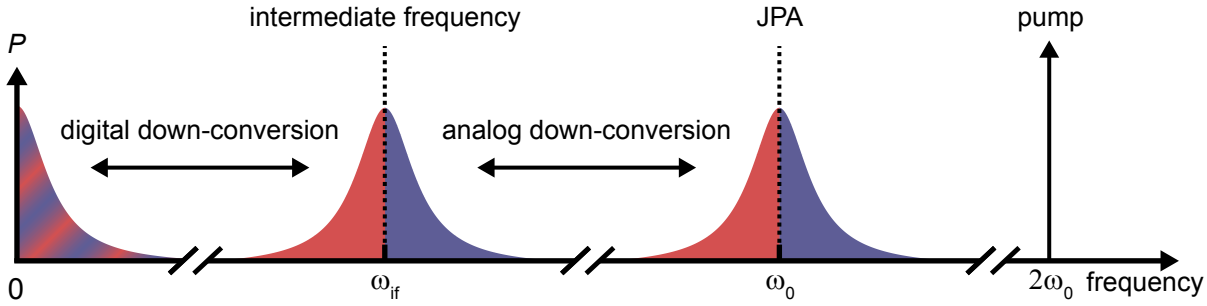

Figure 2.13: Frequency conversion in a typical heterodyne detection setup where an analog down-conversion step to an intermediate frequency ω_{if} is followed by a digital down-conversion. The bandwidth of the JPA is indicated by the red (lower sideband) and blue (upper sideband) regions. In the digital down-conversion step, both sidebands are converted to the same frequency.

2.3 Continuous-variable quantum communication

In this section, we discuss a fundamental quantum communication protocol known as remote state preparation (RSP). We give a general introduction to continuous-variable RSP and present a detailed theoretical description for our experimentally implemented RSP protocol. Finally, we compare RSP to other known quantum communication protocols.

2.3.1 Continuous-variable remote state preparation

Remote state preparation is a quantum communication protocol where nonclassical correlations are employed to realize a more efficient transfer of quantum information when compared to the best known classical methods [16, 131]. In a scenario where a quantum bit (qubit) should be sent to a receiving party and is classically known to the sender, RSP can achieve this task with only one classical bit per sent qubit. This RSP protocol was initially proposed and theoretically investigated by Pati [41], Lo [40] and Bennett *et al.* [42]. In general, it is desirable to minimize the required classical communication between parties that is needed to achieve the transfer of a certain amount of information. As depicted in Fig. 2.14, this goal is achieved in RSP by using pre-shared quantum entanglement. However, the distribution of entangled states to both parties requires certain resources and might be experimentally challenging. Therefore, a protocol in which one can choose between sending more classical communication or using more entanglement is fundamentally important. RSP exhibits such a trade-off between classical and quantum resources [42].

The RSP protocol was extended to the remote preparation of Gaussian continuous-variable states by Paris *et al.* [43]. In particular, they considered the preparation of squeezed states by employing a two-mode squeezed (TMS) state as an entangled resource which is distributed to the two communicating parties, referred to as Alice and Bob. In

order to understand the idea of RSP, we reformulate the Wigner function of a TMS state from Eq. (2.29) into the form

$$W(\mathbf{r}) = \frac{4}{\pi^2} \exp\left\{ -\frac{q_+^2 + p_-^2}{2\sigma_+^2} - \frac{q_-^2 + p_+^2}{2\sigma_-^2} \right\}, \tag{2.101}$$

where $\mathbf{r} = (q_+, q_-, p_+, p_-)$, $q_\pm = (q_1 \pm q_2)/\sqrt{2}$ and $p_\pm = (p_1 \pm p_2)/\sqrt{2}$. Also, the variances, defining the two-mode squeezing level, are given by $\sigma_+^2 = e^{2r}/4$ and $\sigma_-^2 = e^{-2r}/4$. We note that the number of photons in the TMS state is given by $N = 2\sinh r^2$. To remotely prepare a squeezed state, Alice performs an ideal homodyne detection of the q-quadrature on her part of the TMS state with a measurement outcome x. The resulting conditional Wigner function on Bob's side reads [43]

$$W_{B|x}(q_2, p_2) = \frac{2}{\pi} \exp\left\{ -\frac{(q_2 - a_x)^2}{2\Sigma_1^2} - \frac{p_2^2}{2\Sigma_2^2} \right\}, \tag{2.102}$$

where the parameters are

$$a_x = \frac{\sqrt{N(N+2)}}{1+N} x\,, \quad \Sigma_1^2 = \frac{1}{4}\frac{1}{1+N}\,, \quad \text{and} \quad \Sigma_2^2 = \frac{1}{4}(1+N)\,. \tag{2.103}$$

Consequently, the state on Bob's side is a displaced squeezed state with the displacement amplitude a_x depending on the measurement outcome of Alice. In order to deterministically prepare a squeezed state on Bob's side, Alice sends her measurement result x via the classical communication channel to Bob, where he displaces his state by $-a_x$. As a consequence, the state at Bobs side is independent of the result of the homodyne detection and reads

$$W_B(q_2, p_2) = \frac{2}{\pi} \exp\left\{ -\frac{q_2^2}{2\Sigma_1^2} - \frac{p_2^2}{2\Sigma_2^2} \right\}. \tag{2.104}$$

Since $\Sigma_1^2 \cdot \Sigma_2^2 = 1/16$, the remotely prepared state is a pure squeezed state with squeezing

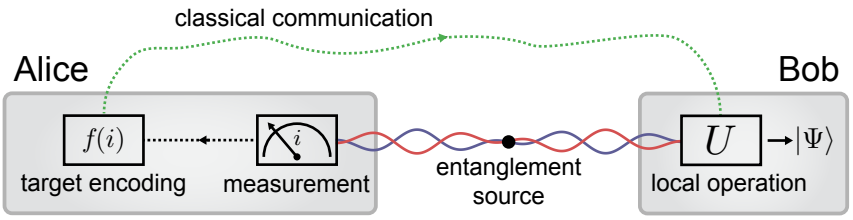

Figure 2.14: General scheme for remote state preparation. An entangled resource is shared between Alice and Bob. Alice performs a projective measurement on her part of the entangled state and encodes the known target state $|\Psi\rangle$ in a feedforward signal (classical communication) according to the measurement result. Bob performs a unitary local operation on his part of the entangled state using the feedforward signal.

in the q-direction and a squeezed variance of $\Sigma_1^2 = 1/(4\cosh 2r)$. For large two-mode squeezing, $r \gg 1$, we can approximate $\cosh 2r \simeq e^{2r}/2$ and obtain for the squeezed variance of the prepared state $\Sigma_1^2 = 2e^{-2r}/4 = 2\sigma_-^2$. Consequently, the squeezed variance of the prepared state is at least twice the initial squeezing in the TMS state.

The quantum advantage of RSP consists in a smaller amount of classical information sent through the feedforward channel in order to prepare a desired state as compared to a purely classical protocol [132, 133]. If we restrict ourselves to ideal RSP with squeezed states, we can intuitively understand the quantum advantage by considering that one remotely prepares pure squeezed states while sending only one real number to Bob. The prepared states require two real numbers, defining the squeezing level and squeezing angle, to be fully described. Consequently, in the described RSP protocol, one is able to reduce the classical communication cost by one real number when compared to a scenario where all the information about the prepared state is sent classically to Bob.

2.3.2 Remote state preparation with propagating microwaves

We now present the theory for remote state preparation of squeezed states using propagating quantum microwaves. The discussed theory allows us to describe the experiments presented in detail in chapter 5.

Full model

Figure 2.15 depicts a detailed scheme of RSP using JPAs and linear circuit elements. First, an entangled resource has to be shared between Alice and Bob. For that, we generate a symmetric TMS state by superimposing two single-mode squeezed (SMS) states at a 50:50 beam splitter. The SMS states are generated using two JPAs (JPA 1 and JPA 2) which are modeled as squeezers with the same squeezing parameter, $r_1 = r_2 = r$, but with different squeezing angles γ_1 and γ_2. The squeezing operator $\hat{S}_{12}$ for JPA 1 and JPA 2 acting on the annihilation operators $\hat{a}_i$ of path 1 (Alice) and path 2 (Bob) describes the

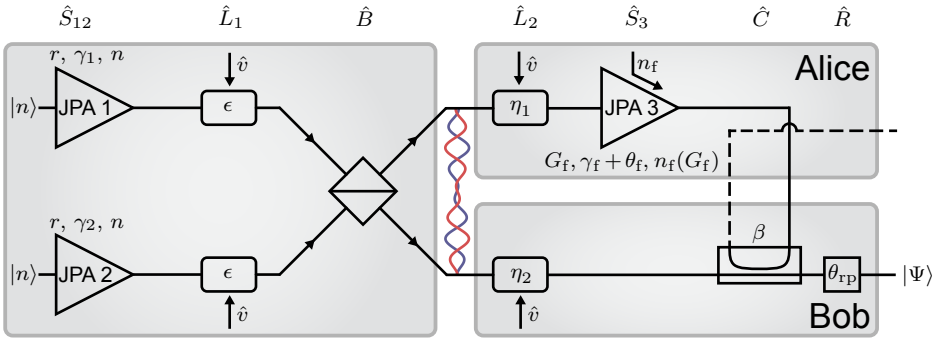

Figure 2.15: Scheme for RSP with propagating microwaves. The angles γ_1, γ_2 and γ_f are used in units of radians for all equations. Symbols are explained in the main text.

single-mode squeezing of each JPA and is given by [60]

$$\hat{S}_{12}^{\dagger}\begin{pmatrix}\hat{a}_1\\ \hat{a}_2\end{pmatrix}\hat{S}_{12}=\begin{pmatrix}\hat{a}_1\cosh r-\hat{a}_1^{\dagger}e^{-2i\gamma_1}\sinh r\\ \hat{a}_2\cosh r-\hat{a}_2^{\dagger}e^{-2i\gamma_2}\sinh r\end{pmatrix}. \tag{2.105}$$

The added noise of JPA 1 and JPA 2 is modeled by an effective thermal state $|n,\,n\rangle$ with a noise photon number $n_1=n_2=n$ incident to the JPAs such that the state after JPA 1 and JPA 2 is $\hat{S}_{12}\,|n,n\rangle$.

We assume equal losses $\epsilon_1=\epsilon_2=\epsilon$ in both paths after JPA 1 and JPA 2 and include the insertion loss of the beam splitter in ϵ. The loss is described with a beam splitter model [131]

$$\hat{L}_1^{\dagger}\begin{pmatrix}\hat{a}_1\\ \hat{a}_2\end{pmatrix}\hat{L}_1=\begin{pmatrix}\sqrt{1-\epsilon}\hat{a}_1+\sqrt{\epsilon}\hat{v}_1\\ \sqrt{1-\epsilon}\hat{a}_2+\sqrt{\epsilon}\hat{v}_2\end{pmatrix}, \tag{2.106}$$

where $\hat{v}_i$ is the operator describing the environment of path i. The environment can be reasonably well approximated to be in the vacuum state due to the millikelvin temperature of the lossy components in the experiment.

The input-output relations of the symmetric 50:50 beam splitter are given by [16]

$$\hat{B}^{\dagger}\begin{pmatrix}\hat{a}_1\\ \hat{a}_2\end{pmatrix}\hat{B}=\frac{1}{\sqrt{2}}\begin{pmatrix}\hat{a}_1+\hat{a}_2\\ -\hat{a}_1+\hat{a}_2\end{pmatrix}. \tag{2.107}$$

The beam splitter output state $\hat{B}\,\hat{L}_1\,\hat{S}_{12}\,|n,\,n\rangle$ is a symmetric TMS state if the squeezing angles of JPA 1 and JPA 2 are orthogonal to each other. This TMS state is distributed to Alice and Bob with additional losses η_i in both paths

$$\hat{L}_2^{\dagger}\begin{pmatrix}\hat{a}_1\\ \hat{a}_2\end{pmatrix}\hat{L}_2=\begin{pmatrix}\sqrt{1-\eta_1}\hat{a}_1+\sqrt{\eta_1}\hat{v}_1\\ \sqrt{1-\eta_2}\hat{a}_2+\sqrt{\eta_2}\hat{v}_2\end{pmatrix}. \tag{2.108}$$

Alice uses another JPA (JPA 3) to perform strong phase-sensitive amplification with a gain G_f on her part of the TMS state. The amplified quadrature is determined by the amplification angle γ_f. This operation models the feedforward generation in the limit of $G_\mathrm{f}\gg 1$. In order to describe the realistic actions of JPA 3, we assume that classical noise is added to the JPA input signal which is followed by ideal phase-sensitive amplification

$$\hat{S}_3^{\dagger}\begin{pmatrix}\hat{a}_1\\ \hat{a}_2\end{pmatrix}\hat{S}_3=\begin{pmatrix}(\hat{a}_1+\zeta)\cosh r_\mathrm{f}-\left(\hat{a}_1^{\dagger}+\zeta^*\right)e^{-2i(\gamma_\mathrm{f}+\gamma_\mathrm{opt})}\sinh r_\mathrm{f}\\ \hat{a}_2\end{pmatrix}, \tag{2.109}$$

where the degenerate gain G_f is related to r_f as $G_\mathrm{f}=e^{2r_\mathrm{f}}$, and γ_opt is the theoretically optimal JPA 3 amplification angle for RSP. The classical noise is described by the complex Gaussian random variable ζ with $\langle\zeta\rangle=0$, $\langle\zeta\zeta^*\rangle=n_\mathrm{f}$ and $\langle\mathrm{Re}(\zeta)^2\rangle=\langle\mathrm{Im}(\zeta)^2\rangle=n_\mathrm{f}/2$, where n_f is the effective thermal noise photon number. In general, the JPA noise is gain-dependent

which we take into account by a linear dependence on G_f. This implies $n_\mathrm{f} = n'_\mathrm{f} G_\mathrm{f}$, where n'_f is a proportionality constant determined from an experimental fit.

Finally, Alice sends the JPA 3 output signal to Bob where he uses it to displace his part of the TMS state. The displacement on Bob's side is implemented with a directional coupler and is described as a highly asymmetric beam splitter [65]

$$\hat{C}^\dagger \begin{pmatrix} \hat{a}_1 \\ \hat{a}_2 \end{pmatrix} \hat{C} = \begin{pmatrix} \sqrt{\tau}\hat{a}_1 + \sqrt{1-\tau}\hat{a}_2 \\ -\sqrt{1-\tau}\hat{a}_1 + \sqrt{\tau}\hat{a}_2 \end{pmatrix} , \tag{2.110}$$

where $\tau = 1 - 10^{\beta/10}$ is the transmissivity and β is the coupling in decibel. In order to accurately model an experimental setup, we need to take the electrical length of different components into account. The total electrical lengths as well as different path lengths after the beam splitter are compensated with a rotation $\hat{R}$ by the angle θ_rp of the final remotely prepared state on Bob's side

$$\hat{R}^\dagger \begin{pmatrix} \hat{a}_1 \\ \hat{a}_2 \end{pmatrix} \hat{R} = \begin{pmatrix} \hat{a}_1 \\ \hat{a}_2 e^{-i\theta_\mathrm{rp}} \end{pmatrix} . \tag{2.111}$$

With the operator definitions in Eqs. (2.105)–(2.111), we can write the overall RSP protocol as a sequence of operators

$$|\Psi\rangle = \hat{R}\,\hat{C}\,\hat{S}_3\,\hat{L}_2\,\hat{B}\,\hat{L}_1\,\hat{S}_{12}\,|n,\,n\rangle \ , \tag{2.112}$$

where n is the noise photon number of JPA 1 and JPA 2, and $|\Psi\rangle$ is the final bipartite state containing the remotely prepared state as a subsystem. The moment matrices for both paths of the final state are calculated as

$$\begin{pmatrix} \langle (\hat{b}_1^\dagger)^n \hat{b}_1^m \rangle \\ \langle (\hat{b}_2^\dagger)^n \hat{b}_2^m \rangle \end{pmatrix} = \langle \Psi | \begin{pmatrix} (\hat{a}_1^\dagger)^n \hat{a}_1^m \\ (\hat{a}_2^\dagger)^n \hat{a}_2^m \end{pmatrix} |\Psi\rangle \ , \tag{2.113}$$

where $\langle (\hat{b}_1^\dagger)^n \hat{b}_1^m \rangle$ are the moments of the second directional coupler output signal and $\langle (\hat{b}_2^\dagger)^n \hat{b}_2^m \rangle$ are the moments of the remotely prepared state. With the definition of the quadratures $\hat{q}_2 = (\hat{b}_2 + \hat{b}_2^\dagger)/2$ and $\hat{p}_2 = (\hat{b}_2 - \hat{b}_2^\dagger)/2i$, the moments $\langle (\hat{b}_2^\dagger)^n \hat{b}_2^m \rangle$ are used to calculate the squeezing angle γ_rp, squeezed variance σ_s^2 and antisqueezed variance σ_a^2 of the remotely prepared state as

$$\gamma_\mathrm{rp} = -\frac{1}{2}\mathrm{Arg}\left(-\langle \hat{b}_2^2 \rangle\right) , \tag{2.114}$$

$$\sigma_\mathrm{s}^2 = \frac{1}{4}\left(\langle \hat{b}_2^2 \rangle e^{2i\gamma_\mathrm{rp}} + \langle (\hat{b}_2^\dagger)^2 \rangle e^{-2i\gamma_\mathrm{rp}} + 2\langle \hat{b}_2^\dagger \hat{b}_2 \rangle + 1\right) , \tag{2.115}$$

$$\sigma_\mathrm{a}^2 = \frac{1}{4}\left(-\langle \hat{b}_2^2 \rangle e^{2i\gamma_\mathrm{rp}} - \langle (\hat{b}_2^\dagger)^2 \rangle e^{-2i\gamma_\mathrm{rp}} + 2\langle \hat{b}_2^\dagger \hat{b}_2 \rangle + 1\right) , \tag{2.116}$$

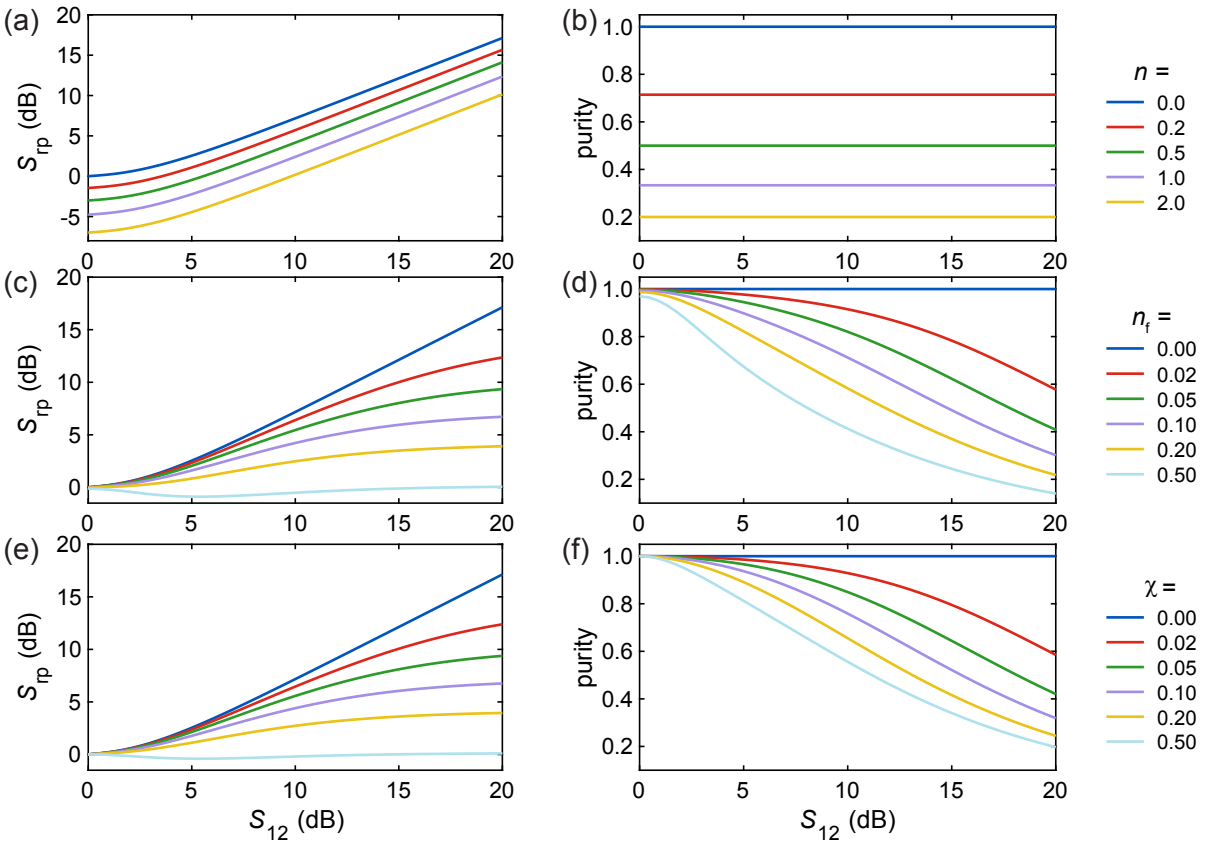

Figure 2.16: (a,c,e) Squeezing level S_{rp} and (b,d,f) purity $\mu = 1/(4\sqrt{\sigma_{\mathrm{s}}\sigma_{\mathrm{a}}})$ of remotely prepared states at the optimal point as a function of initial squeezing level S_{12} of JPA 1 and JPA 2. Panels (a,b), (c,d) and (e,f) are plotted for different JPA 1 and JPA 2 noise photon numbers n, JPA 3 noise photon numbers n_{f} and total losses χ, respectively. Except for the corresponding panels, we use $n = n_{\mathrm{f}} = \chi = 0$. The dark blue line in all panels corresponds to ideal RSP with no imperfections.

where Arg(·) is the argument of a complex number and the first order moments are taken to be zero since we only consider undisplaced states. From the moments $\langle(\hat{b}_2^\dagger)^n \hat{b}_2^m\rangle$, one can determine the full covariance matrix of the prepared state. Full expressions for the covariance matrix of the prepared states are given in Appendix B.

We can now look into the effect of possible experimental imperfections on RSP. In particular we consider non-zero JPA 1 and JPA 2 noise photon numbers n, JPA 3 noise photon numbers n_{f} and total losses χ on RSP. The total loss is defined as $\chi_1 = \chi_2 = \chi$, where $\chi_1 = 1-(1-\epsilon)(1-\eta_1) = \epsilon+\eta_1-\epsilon\eta_1$ and $\chi_2 = 1-(1-\epsilon)(1-\eta_2) = \epsilon+\eta_2-\epsilon\eta_2$. Here, we only consider the optimal point of RSP which is defined by the highest purity of the remotely prepared state when varying the gain and amplification angle of JPA 3 with otherwise fixed resources. For the optimal point, the only relevant loss is the total loss χ, i.e., the individual losses ϵ, η_1, and η_2 do not influence the prepared state as long as the total loss is χ. In Fig. 2.16, we show the squeezing level and purity of the optimally remotely prepared state as a function of the initial squeezing level S_{12} of JPA 1

and JPA 2 for various experimental imperfections. The coupling of the directional coupler is $\beta = -15\,\mathrm{dB}$. The JPAs creating the TMS state have orthogonal squeezing angles.

As shown in Fig. 2.16 (a,b), the noise photon number n of JPA 1 and JPA 2 reduces both the squeezing level as well as the purity of the prepared state. Interestingly, the purity does not depend on S_{12}. This is in contrast to the effect of added noise n_f by JPA 3 or total losses χ in the setup, where the purity decreases with increasing S_{12}, as depicted in Fig. 2.16 (d,f). Figure 2.16 (c,e) illustrates that n_f and χ have a strong effect on the optimally achievable squeezing level S_rp. Also, both n_f and χ have a similar detrimental effect on the remotely prepared state. We emphasize, that for $\tau \to 1$ and for ideal parameter settings, we reproduce the results of Paris *et al.* [43] where a state with squeezed variance $\Sigma_1 = 1/(4\cosh 2r)$ is remotely prepared. Here, r characterizes the squeezing strength of the entangled TMS state.

Simplified model

Since the full expressions for the parameters of the remotely prepared state are very lengthy, we now derive a simplified model for which we can find compact analytic expressions. For that, we choose $\gamma_1 = \gamma_\mathrm{f} = 0°$, $\gamma_2 = \gamma_\mathrm{opt} = 90°$, equal losses after the beam splitter ($\eta_1 = \eta_2$), neglect the effect of the electrical path lengths ($\theta_\mathrm{rp} = 0$), and use the total loss χ as defined above. The protocol works optimally for a fixed entangled resource if a state with the highest purity is remotely prepared. In the limit of high JPA 1 and JPA 2 squeezing level, $r \gg 1$, we reach this optimal point for a JPA 3 gain $G_\mathrm{f} = \tau/(1-\tau)$ and, by using Eqs. (2.114)–(2.116), obtain the following result for the optimally remotely prepared state

$$\tilde{\gamma}_\mathrm{rp} = \gamma_1\,, \tag{2.117}$$

$$\tilde{\sigma}_\mathrm{s}^2 = \frac{1}{4}\left[2(1+2n)e^{-2r}(1-\chi)\tau + 2(\chi+n_\mathrm{f})\tau\right]\,, \tag{2.118}$$

$$\tilde{\sigma}_\mathrm{a}^2 = \frac{(1+2n)(1-\chi)\left[e^{2r}+e^{-2r}(1-2\tau)^2\right]}{8\tau} + \frac{2n_\mathrm{f}(1-\tau)^2 + (1-2\tau+2\tau^2)\,\chi}{4\tau}\,. \tag{2.119}$$

In general, the optimal JPA 3 gain depends on r in a nontrivial manner and converges to $G_\mathrm{f} = \tau/(1-\tau)$ for $r \to \infty$. However, the latter expression offers a good approximation to the optimal JPA 3 gain even for $r \approx 1$, since the deviation of $\tilde{\gamma}_\mathrm{rp}$, $\tilde{\sigma}_\mathrm{s}^2$, and $\tilde{\sigma}_\mathrm{a}^2$ between the optimal JPA 3 gain and $G_\mathrm{f} = \tau/(1-\tau)$ is below 1% for the parameters used in our experiments (see Tab. 5.1).

We observe from Eq. (2.118) that the squeezing of the prepared state is at least two times smaller than the initially used squeezing of JPA 1 and JPA 2 which coincides with the discussion in the previous subsection. Also, we find that a squeezed state can only be remotely prepared if Alice and Bob share an entangled state, corresponding to a non-zero two-mode squeezing level, $r > 0$.

The results presented in this subsection have been published by us in Ref. [47]. Parts of the text and figures are adapted from the supplementary material of this reference.

2.3.3 Related quantum communication protocols

Until now, we only discussed remote state preparation as a fundamental quantum communication protocol. However, there exist various other protocols which have similar requirements as RSP. In this subsection, we introduce other relevant communication protocols and discuss their connection to RSP.

Quantum teleportation

One of the most well-known quantum communication protocols is quantum teleportation proposed by Bennett *et al.* [44] for discrete-variable systems. There exist several experimental realizations for teleportation with, e.g., photon polarization states [134, 135], trapped ions [136, 137], superconducting circuits [4], solid-state qubits [138] and qubit states over free-space [139, 140]. Quantum teleportation has also been extended to continuous-variables [18, 141] and experimentally realized for coherent states [17].

The aim of quantum teleportation is to communicate an unknown quantum state from one party to another. Due to the no-cloning theorem [142], obtaining full classical knowledge of an unknown quantum state is, in general, not possible and, therefore, sending purely classical information about the quantum state is not always an option. Also, directly sending the quantum state, including the physical quantum-information carrier, might not be feasible due to various technical constraints. Quantum teleportation is a quantum communication protocol where entanglement and a limited amount of classical communication can be used to communicate an unknown quantum state without directly sending it. For continuous variables, the information cost is two real numbers and one entangled EPR pair [131]. In the case of a squeezed state, the required tools for RSP and quantum teleportation are similar. For example, RSP can be implemented using one real number and one entangled EPR pair. However, in contrast to quantum teleportation, RSP transfers a known quantum state [43].

Quantum state transfer

Another possibility to deterministically transfer a quantum state from one party to another is quantum state transfer [143]. Here, an existing quantum state, stored in a stationary system at the sending node, is released to a quantum channel in the form of propagating photons. At the receiving node, these photons are captured in order to obtain the original quantum state [12, 13]. For a successful protocol, no entanglement is required since the quantum state is sent directly. This is in contrast to RSP or quantum teleportation where no direct state transfer takes place. Furthermore, we note that quantum state transfer can be used to generate, e.g., entangled qubit states [12, 13].

One-time pad

Cryptographic protocols ensure a safe transfer of information between parties. A prime example of a classical cryptographic protocol is the one-time pad [144] which allows for perfect information-theoretic security. Here, we consider a continuous version of the one-time pad where Alice possesses a message M consisting of a string of real numbers which she wants to securely communicate to Bob. To this end, she adds uniformly distributed random numbers acting as the key K to the message and obtains the cipher text $C = M + K$. The cipher is then sent to Bob via a classical (insecure) channel. In order to decrypt the cipher, Bob needs to subtract the key from the cipher $M = C - K$, and obtains the original message M. If each key is only used once and only Alice and Bob have access to the key, the protocol is secure because it is impossible to determine the actual message M from just the cipher text C. Perfect security in the protocol can be proven by using Shannon entropies. If knowledge of the cipher C does not reveal any information on the message M, the protocol is secure. This condition can be expressed using the conditional entropy $H_{\mathrm{sh}}(M|C)$ and reads [145]

$$H_{\mathrm{sh}}(M) = H_{\mathrm{sh}}(M|C)\,. \tag{2.120}$$

Kurucz *et al.* showed that continuous-variable RSP can be connected to the one-time pad [132, 146]. Here, a maximally entangled EPR state with a Wigner function $W(p_1, p_2) \propto \delta(p_1 + p_2)$ is used as a resource which provides the effective key to both parties. Consequently, the p-quadratures of both parties are perfectly correlated but locally uniformly distributed, i.e., locally the variances are infinite $\mathrm{Var}\, p_1 = \mathrm{Var}\, p_2 = \infty$. If Alice measured the q-quadrature of her EPR pair and obtains the measurement results K, she knows with certainty that a measurement of Bob's EPR pair would yield the result $-K$. Afterwards, Alice prepares a cipher text $C = M + K$ and sends it classically to Bob where he performs an appropriate displacement operation on C to obtain the message M [146]. In this protocol, the key is provided to both parties by the entangled resource. In Sec. 5.3, we present how RSP can be related to an extension of the one-time pad to the quantum regime where we consider the prepared quantum states as the message.

We note that, quantum teleportation is also secure against an eavesdropper in the classical feedforward [16]. In both RSP and quantum teleportation, the security originates from the use of the entangled resource which is essential for a successful protocol. In contrast, direct state transfer protocols [12, 13, 143] do not rely on entanglement but directly transmit quantum states between parties. Therefore, an eavesdropper in the communication channel can intercept the sent quantum state which makes direct state transfer protocols inherently insecure.

Quantum key distribution

In contrast to RSP, quantum teleportation, or quantum state transfer, where the goal is to send a quantum state, the aim of quantum key distribution (QKD) is to generate private classical keys between two parties over a public channel by utilizing quantum mechanical effects [72].

For qubits, a prominent example of a QKD protocol is BB84 named after Bennett and Brassard [147, 148]. Here, Alice encodes classical bits in qubit states with random non-orthogonal bases and sends them openly to Bob. Then, he measures the received states in a randomly chosen basis. After publicly comparing the chosen bases of both parties and performing information reconciliation and privacy amplification [72], a secret key can be generated between Alice and Bob. The generated key can later be used in, e.g., a one-time pad protocol to realize secure communication of a message [149]. The security of such a prepared key can be theoretically proven [150].

An alternative quantum key distribution protocol is E91 which relies on pre-shared entanglement and was first described by Ekert in 1991 [151]. The protocol relies on the fact that maximally entangled qubit pairs are perfectly correlated. A secret key can be obtained similar to the BB84 protocol by measuring the entangled pair in random bases on each side. After comparing the measurement results and applying a suitable post-selection, a secret classical key between Alice and Bob can be obtained. Since the E91 protocol relies on shared entanglement, a comparison to RSP can be made. Both protocols use the fact that the measurement of one part of an entangled state reveals information on the other part. In RSP this information is used to deterministically prepare a desired quantum state at the other party by sending classical information depending on the obtained measurement result. Importantly, only one part of the entangled state is measured in RSP. In the E91 protocol, both parts of the entangled state are measured which ultimately provides a classical secret key to both parties. We note that QKD protocols which do not explicitly require entanglement, such as BB84, can be equivalently viewed as entanglement-based protocols where the "virtual" entanglement plays a role in investigating security criteria for the generation of a secure key [152].

In BB84 and E91, the presence of an eavesdropper Eve can be detected by the communicating parties since Eve needs to perform measurements on the sent quantum states in order to gain any information. However, a measurement will inevitably disturb the quantum state [72]. This fact is closely connected to the no-cloning theorem which forbids to make exact copies of an arbitrary quantum state.

2.3.4 Quantum information processing with continuous and discrete variables

In this work, we focus on continuous-variable (CV) protocols where quantum information is encoded into the quadratures of a propagating electromagnetic field. Since the quadrature

operators possess continuous eigenstates, such systems are commonly referred to as CV systems and correspond to infinite-dimensional Hilbert spaces. In contrast, with discrete-variables (DV), one typically utilizes the discrete energy levels of, e.g., artificial atoms to perform quantum information processing tasks. Here, the corresponding Hilbert space possesses a finite dimension. In the following, we discuss differences between both approaches.

Many CV protocols rely on Gaussian states. Their generation and manipulation can be routinely realized with a standard experimental toolbox. For example, squeezed states are easily generated by parametric processes which require relatively low levels of nonlinearity in the system. For DVs, one typically utilizes highly nonlinear systems as central elements, which, in the simplest case, can be described as quantum two-level systems (qubits). Experimentally, it is much easier to realize systems with lower levels of nonlinearity which makes Gaussian CVs advantageous. However, the sets of logical operations required for universal CV and DV computing are also significantly different. Unitary operations and gates on the qubits are realized by applying drive pulses which lead to a controllable change of a qubit state. In general, the precise control of qubit states requires a sophisticated experimental setup which is a well-studied area nowadays [123]. The situation with CV logical gates is more involved. Some operations, such as beam-splitting, which allows for the generation of entangled states [15, 16], or displacement [64], are linear and straightforward to implement. Unfortunately, other operations, such as a non-Gaussian cubic phase gate [153] or a sum gate [154], are not. The implementation of the latter operations is still an experimental challenge. Luckily, some CV protocols do not require these complicated non-Gaussian operations at all and can be implemented by only using beam splitters and displacement operators.

The effect of losses on Gaussian CV states has various aspects. On the one hand, they do not possess a fixed number of photons so that small losses do not influence the states heavily. Consequently, Gaussian CVs can inherently tolerate limited photon losses. On the other hand, it is difficult to detect or correct for these photon losses because they change only the average observables of the states. In contrast, for certain DV protocols, where photon numbers might be strictly fixed, one can use various post-selection or conditional schemes to account, or even correct, for the photon loss. These actions will generally reduce the rate at which the protocol is successfully executed but, in turn, increase the fidelity.

Finally, there exist various types of error correction codes for both systems. For CVs, the faithful distribution of entangled states is central for many protocols. However, in practice, sharing of such entangled states between parties is imperfect and will inevitably add a finite amount of noise to the entangled states, which leads to a decrease of the entanglement strength. Such errors can be corrected in entanglement distillation protocols [155]. Also, in quantum computing with CV cluster states, errors are induced due to finite squeezing in the cluster states and proposals for correction of such errors exist [156]. In general, CV

error correction schemes are impossible to realize with only Gaussian operations [157] and, therefore, non-Gaussian operations are required [158, 159]. For quantum computing with DVs, a well-known error correction protocol is the surface code. Here, quantum information is encoded into logical qubits. The logical qubits consist of multiple physical qubits which are coupled in a specific manner so that qubit errors can be detected and corrected [160]. However, for the surface code a large number of physical qubits is required to implement a fault-tolerable logical qubit which makes the practical realization difficult. We note that also hybrid schemes exist, which combine aspects from both CVs and DVs. One prominent example is the encoding of qubits in CV Gottesman-Kitaev-Preskill (GKP) states in an oscillator [161]. The GKP states are robust against fluctuations in the quadratures and occurring errors can be corrected. However, the generation of GKP states is very demanding and requires non-Gaussian operations [162].

Both approaches to quantum information processing, either with CVs or with DVs, have their own advantages. Which system is preferable depends strongly on the task which should be achieved. Finally, we note that various hybrid protocols, which promise to overcome the individual limitations in both systems, have already been realized [14].

Chapter 3

Experimental techniques

The experimental methods and techniques presented in this chapter are the foundation for advanced experiments with propagating quantum microwaves. In general, sophisticated cryogenic and room-temperature setups combined with signal reconstruction techniques are required. In Sec. 3.1, we explain how we build our measurement setup, implement the detection of quantum microwaves, and discuss experimental challenges. In our experiments, we use Josephson parametric amplifiers (JPAs) for the generation and manipulation of quantum microwaves. The characterization of JPAs in terms of their flux tunability, nondegenerate and degenerate gains, as well as their capability to generate propagating squeezed states is discussed in Sec. 3.2. Finally, the detailed cryogenic and room temperature setups for particular measurements are introduced in Sec. 3.3.

3.1 Detection of quantum microwaves

In this section, we describe how to detect and reconstruct propagating quantum microwave signals in the frequency range of a few gigahertz. This task is associated with a number of experimental challenges. Firstly, a temperature of 50 mK corresponds to thermal radiation with a mean photon number of one at a frequency of 1 GHz. Therefore, we require temperatures around 10-20 mK to suppress thermal effects in the electromagnetic modes for the relevant frequency range of 5-6 GHz and preserve quantum coherence. Quantum information processing in general, and quantum communication in particular, require vanishingly small thermal population levels because the latter are typically very detrimental to these protocols. A second major challenge arises due to omnipresent microwave losses which lead to the decay of quantum states. Therefore, a sophisticated cryogenic setup capable of reaching millikelvin temperatures and minimized losses are imperative to realize complex protocols involving propagating quantum microwaves. Furthermore, the reliable reconstruction of quantum states is a central task in our experiments. To this end, we require a precise output line calibration which also allows us to reconstruct quantum states at different positions in the cryogenic setup.

3.1.1 Basic cryogenic setup for experiments with propagating microwaves

Experiments with propagating quantum microwaves are challenging due to the cryogenic temperatures. In our experiments, these temperatures are provided by means of a dry dilution refrigerator (cryostat) which imposes some constraints on the experimental setup. In particular, the lowest temperature stage provides a limited amount of usable experimental volume and is physically inaccessible during operation of the cryostat. Therefore, the whole cryogenic setup needs to be carefully designed, prepared, and tested before each cool-down. In the following, we describe and discuss the central parts of the cryogenic setup.

Dilution refrigerator

The experiments presented within this work are performed with a home-made dry dilution refrigerator which was designed and constructed by A. Marx, K. Uhlig, S. Höss, and T. Brenninger at the Walther-Meißner-Institute. Details on the cryostat can be found in Refs. [163, 164]. As shown in Fig. 3.1 (a), the cryostat has several temperature stages, where the first two stages are cooled by a Cryomech PT410-RM pulse-tube cryocooler to 50 K and 3 K, respectively. The third temperature stage has a temperature of 1.2 K which is cooled by a separate ^{4}He-1K-loop. The addition of the latter temperature stage allows for extra cooling power to the dilution circuit since it acts as a heat sink for output cables (lines) and pre-cooles the ^{3}He/^{4}He mixture circulating in the dilution circuit. The latter circuit composes the main part of any dilution cryostat and is based on the spontaneous phase separation of the ^{3}He/^{4}He mixture at a temperature of a few hundred millikelvin. This process happens in the so-called mixing chamber, which is the coldest part of the cryostat, and is used to cool down the cryostat to temperatures of a few millikelvin. Details on the operation principle of ^{3}He/^{4}He dilution cryostats can be found in Ref. [165].

Input and output lines

In order to perform measurements, the cryostat is equipped with multiple microwave input and output lines as shown in Fig. 3.1 (b,c). In our cryostat, eight semi-rigid coaxial cables are used as input lines. The inner and outer conductors of these cables consist of stainless steel with polytetrafluoroethylene (PTFE) as a dielectric layer (SC-219/50-SS-SS, Coax Co., Ltd.) between them. The stainless steel cables provide a good thermal isolation between the temperature stages of the cryostat but have significant microwave loss of 6 dB/m at a frequency of 6 GHz and temperature of 4 K. The inner and outer conductor of the input cables are thermalized by attenuators at four different temperature stages of the cryostat. In this way, the thermal radiation coming from room temperature is attenuated, such that, ideally, the number of thermal photons n_{th}

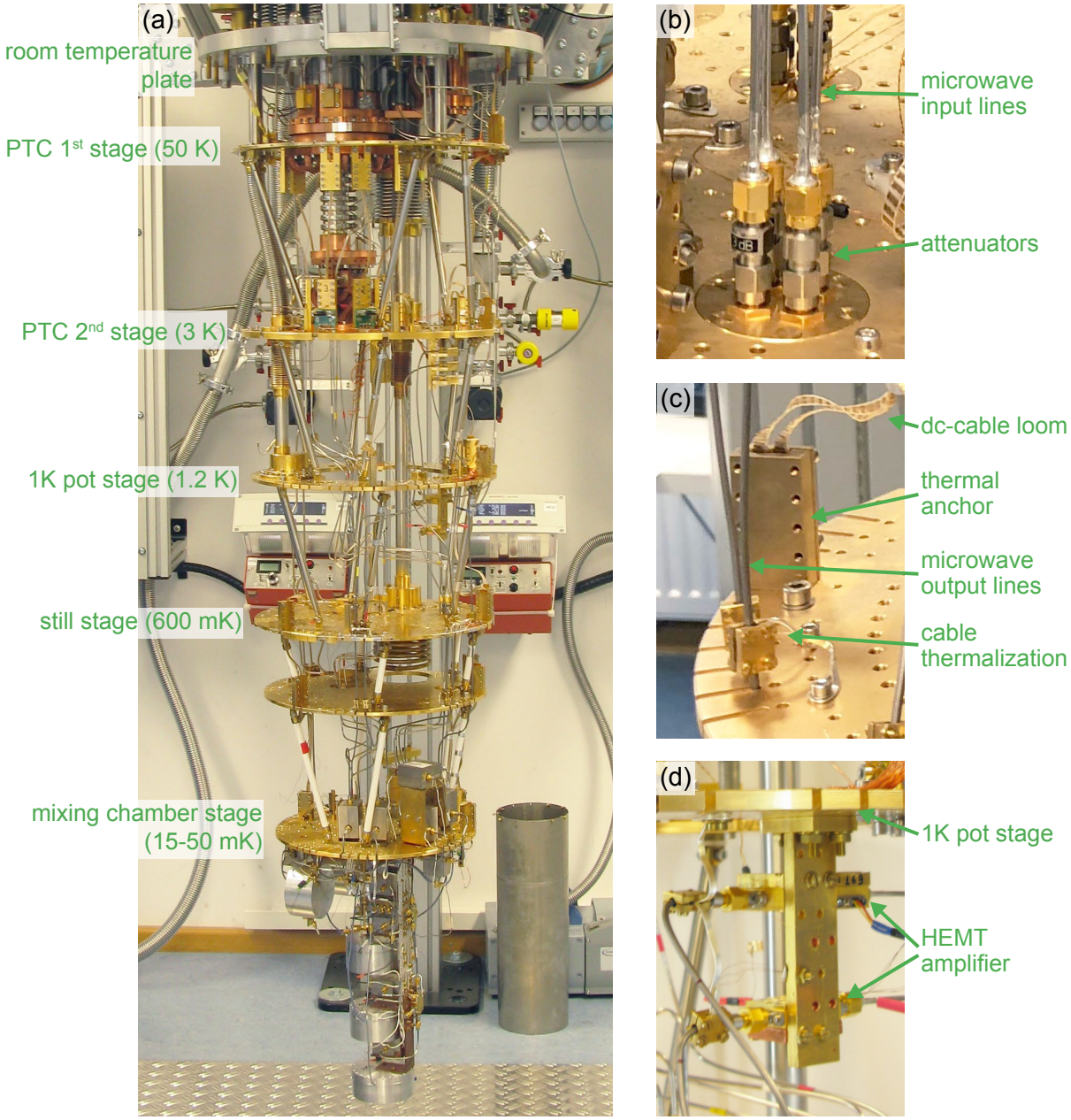

Figure 3.1: (a) Photograph of ^{3}He/^{4}He dilution refrigerator with respective temperature stages. (b) Photograph of microwave input lines with attenuators. (c) Photograph of thermal anchor for dc-cable looms and thermalization of microwave output lines. (d) Photograph of HEMT amplifiers at the 1k pot stage.

corresponds to the ambient temperature of the mixing chamber (few millikelvin), that is, $n_{\mathrm{th}} \ll 1$. For the microwave output lines, we use two types of semi-rigid coaxial cables. Since it is extremely important to minimize losses before the first amplification stage, we use superconducting cables (SC-219/50-NbTi-NbTi, Coax Co., Ltd.) from the sample stage to the first amplification stage which is located either at 1 K or 3 K cryostat stage. The superconducting cables consist of NbTi as inner and outer conductors as well as

PTFE as a dielectric layer and have microwave losses smaller than 0.3 dB/m below a temperature of 4 K. After the first amplification stage, we can tolerate minor losses, and therefore, use normal-conducting coaxial cables (SC-219/50-SSS-SS, Coax Co., Ltd.) with a silver-plated stainless steel inner conductor and stainless steel outer conductor as well as PTFE as a dielectric layer. The microwave losses for these output cables are 1.5 dB/m at a frequency of 6 GHz and temperature of 4 K. The output cables are thermalized to different temperature stages by pressing annealed silver wires or copper braids to the outer conductor of the cable. In each output line, we use two circulators (CTH1184-KS18, Quinstar and RADC-4-8-Cryo Raditek) mounted to the mixing chamber plate to isolate the cryogenic setup from noise and reflections of the following amplifiers. More details on the input and output lines can be found in Ref. [166]. We use cryogenic high electron mobility transistor (HEMT) amplifiers (LNF-LNC4_8A, Low Noise Factory) at the first amplification stages as shown in Fig. 3.1 (d). The HEMT amplifiers have a specified bandwidth from 4 GHz to 8 GHz with a noise temperature of approximately 2 K and signal gain $G = 38$ dB. Since they have a high gain $G \gg 1$, the HEMT amplifiers determine the noise temperature of the whole detection chain. In order to ensure a long-term phase and gain stability of the setup, the temperature of the HEMT power supply is stabilized by an external proportional-integral-derivative (PID) controller at $26 \pm 0.1\,^{\circ}\mathrm{C}$.

Thermometry and dc-wiring

The cryostat is equipped with multiple twisted pair wires which are employed for thermometry and experimental purposes at low frequency. We use beryllium-copper looms between the 3 K cryostat stage and the room temperature stage as well as superconducting NbTi wires below the 3 K stage. The wires are thermalized at different temperature stages of the cryostat by gently pressing them between two copper plates together with Kapton foil. We are able to measure up to 16 temperature lines with an alternating current resistance bridge (Model 370, LakeShore) in the four-wire measurement scheme. Two of the temperature lines can be used for temperature stabilization of different components in the cryogenic setup with two additional resistance bridges (AVS-47B, Picowatt) and two temperature controllers (TS-530A, Picowatt). Additional dc-wiring for experimental purposes is physically separated from the temperature lines in order to minimize crosstalk. The cryostat is equipped with additional twelve twisted-pairs which are used for applying currents to coils or heaters, and for the operation of cryogenic switches. Most of the discussed twisted pairs are filtered by low-pass filters at room temperature in order to get rid of high-frequency noise.

3.1.2 Data acquisition and processing

The heterodyne detection setup and data processing discussed in this subsection are similar to the experiments presented in Refs. [167, 168] and supplementary materials

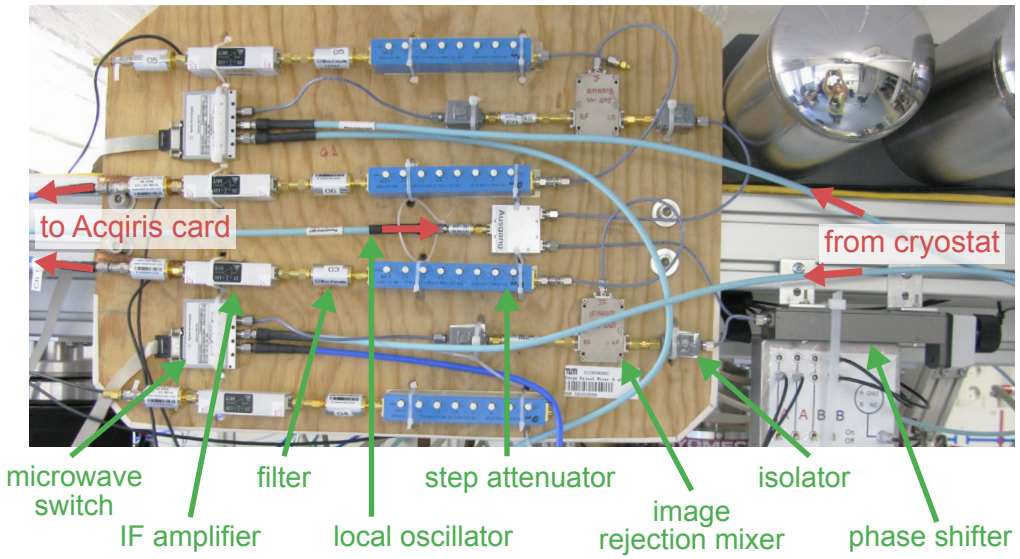

Figure 3.2: Photograph of the dual-path receiver. The top and bottom IF chains are not used.

of Ref. [39]. For tomographic measurements of quantum microwaves, we employ the dual-path receiver shown in Fig. 3.2. After amplification, the microwave signals from the cryostat are roughly filtered around the relevant frequency f_{rf} and down-converted to an intermediate frequency (IF) of $f_{\mathrm{if}} = 11\,\mathrm{MHz}$. For that, we apply a strong local oscillator (LO) signal at a frequency $f_{\mathrm{rf}} + f_{\mathrm{if}}$ to an image-rejection mixer (IRM4080B, Polyphase). The image-rejection mixer is crucial for a correct reconstruction of squeezed states since, with a normal mixer, the blue sideband at $f_{\mathrm{rf}} + 2f_{\mathrm{if}}$ would be also down-converted to f_{if} (see Fig. 3.3). However, the squeezed state is only present in a comparatively narrow bandwidth around f_{rf}. Consequently, the blue sideband would distort the squeezed signal and limit the maximal observable squeezing to 3 dB below the vacuum limit. Details can be found in Ref. [168]. After the down-conversion, the signal amplitude can be adjusted by step attenuators (ESA2-1-10/8-SFSF, EPX microwave Inc.) which are used to balance the two paths of the receiver and avoid compression effects of the following amplification. Furthermore, the step attenuators are used to fine tune the power of the amplified signals in order avoid clipping effects during the digitization of the signal at analog-to-digital converters (ADC). Before further amplification by IF-amplifiers (AU-1447-R, Miteq), the signal is band-pass filtered (Mini-Circuits, SBP-10.7+) with a passband of 9.5-11.5 MHz in order to avoid compression effects of the IF-amplifiers. Finally, the signal is low-pass filtered (Mini-Circuits, SLP-21.4+) with a bandwidth of 0-22 MHz and sent to the ADCs of the digitizer card. The relative phase difference between the two paths is adjusted to 180° with a manual phase shifter in one of the LO paths. The scheme of the full experimental setups are shown later in Figs. 3.22 and 3.24.

The dual-path receiver is the analog part of a heterodyne detection setup. In comparison to a homodyne detection of microwave signals, where a signal is down-converted to zero frequency in a single step, we use two down-conversion steps, i.e., a heterodyne detection

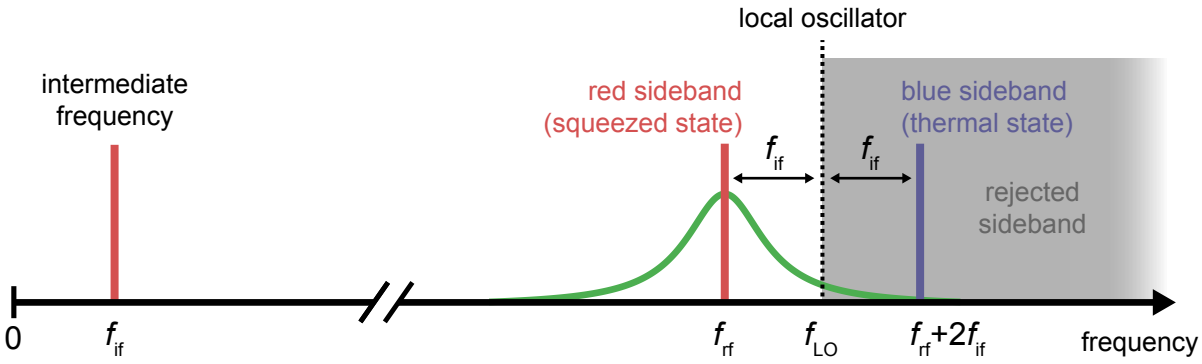

Figure 3.3: Frequency conversion scheme during analog down-conversion with image-rejection mixers. The red sideband at a frequency f_{rf} contains the squeezed signal while the blue sideband at a frequency $f_{\mathrm{rf}} + 2f_{\mathrm{if}}$ contains an unwanted weak thermal state. The gray area marks the frequency sideband which is filtered out (rejected) by the image-rejection mixer.

scheme. Here, the signal is first converted to an intermediate frequency of a few megahertz such that the $1/f$-noise before digitization of the signal is reduced. Subsequently, the signal is converted to zero frequency in a digital down-conversion (DDC) step which happens already during the data post-processing. We use an intermediate frequency of 11 MHz in order to avoid spurious signals from the 10 MHz reference signals which are used to synchronize all microwave devices.

A scheme of the employed digital signal processing is depicted in Fig. 3.4 (a). For digitization of the signals, we use an Acqiris DC440 card (Agilent). The Acqiris card has two ADCs with a 12-bit resolution and adjustable input voltage ranges between ±125 mV and ±5 V. We adjust the input voltage range such that we obtain a sufficiently high resolution but avoid clipping of the signal (events when the signal amplitude exceeds the preset voltage range). Throughout this work, we always use a sampling rate of 400 MHz. After a trigger signal is received, a timetrace of length M is recorded for each channel and saved in an internal memory of the Acqiris card. The process is repeated for N segments until the internal memory of $8 \cdot 10^6$ samples per channel is reached. Subsequently, the signal is transferred to a computer via a PXI-8570 module (ADLINK Technology Inc.) on the back-end Acqiris card. At the computer, the data is received by a PXI-to-PCI card (ADLINK Technology Inc.) and further processed by a custom `C++` code. Here, a DDC step is applied to the data where, at the same time, the signal is IQ demodulated. For that, sine and cosine timetraces at the intermediate frequency f_{if} are digitally generated and multiplied by the IF signal $A_{1,2}(t)$. This step is followed by numerical integration such that the two quadratures I and Q are obtained via

$$I = 2f_{\mathrm{if}} \int_t^{t+1/f_{\mathrm{if}}} \cos(2\pi f_{\mathrm{if}}\tau) A(\tau) d\tau \,, \tag{3.1}$$

$$Q = 2f_{\mathrm{if}} \int_t^{t+1/f_{\mathrm{if}}} \sin(2\pi f_{\mathrm{if}}\tau) A(\tau) d\tau \,. \tag{3.2}$$

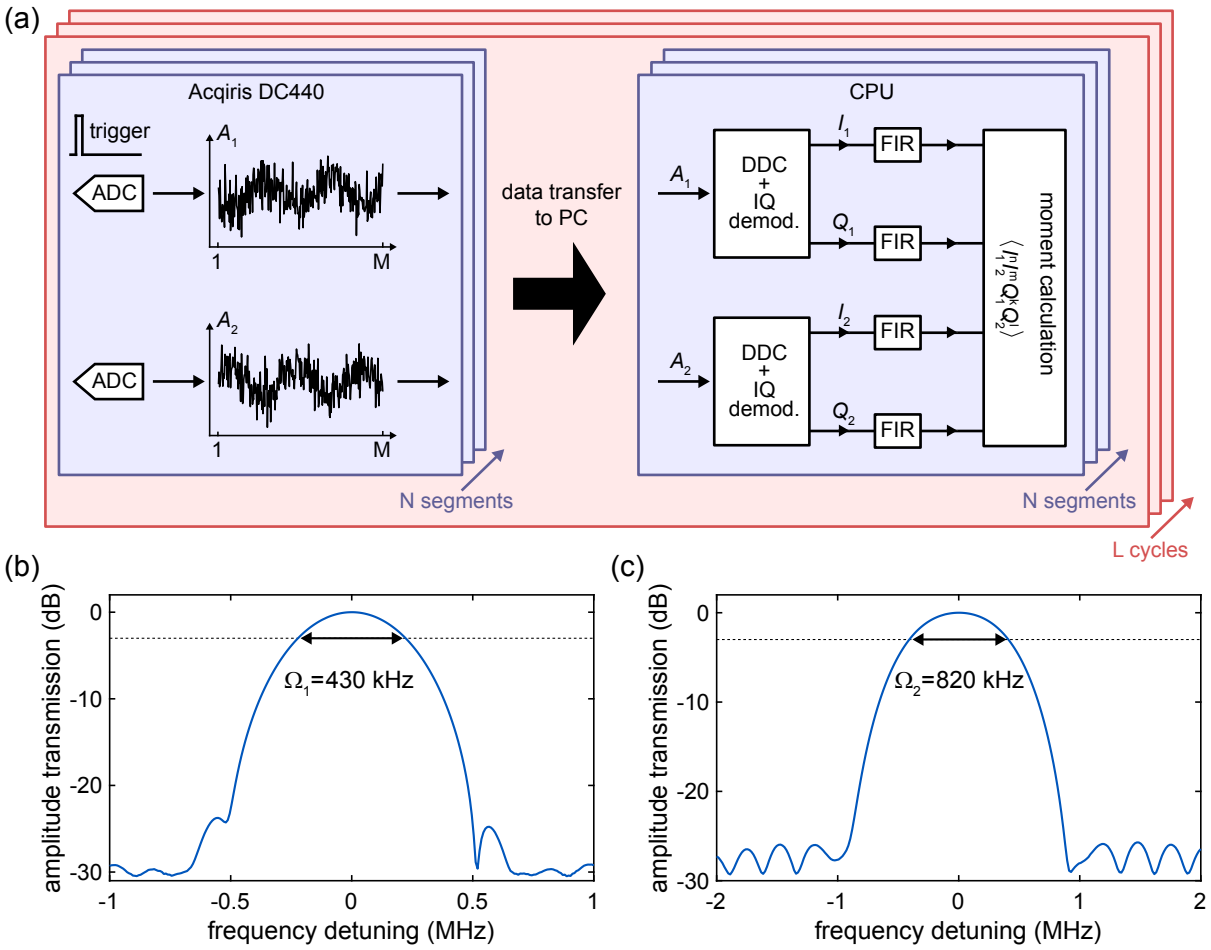

Figure 3.4: (a) Scheme of data acquisition and processing with the Acqiris digitizer card. Each segment is initiated by a separate external trigger pulse. Processing of data is performed on a PC. (b,c) Measured filter characteristics of two FIR filters with full bandwidths $\Omega_1 = 430\,\mathrm{kHz}$ and $\Omega_2 = 820\,\mathrm{kHz}$ as a function of the detuning from the center frequency at 5.323 GHz, respectively. The asymmetry in the frequency dependence is caused by artifacts from the calibration.

Subsequently, the quadratures are filtered with a digital finite-impulse response (FIR) filter. In our experiments, we use two FIR filters with different bandwidths, as shown in Fig. 3.4 (b,c). Finally, after FIR filtering, all correlation quadrature moments $\langle I_1^n I_2^m Q_1^k Q_2^l \rangle$ with $n+m+k+l \leq 4$ for $n, m, k, l \in \mathbb{N}$ are calculated and averaged over the N segments. The whole process is repeated for L cycles and the moments are saved to the PC for later analysis and reconstruction of quantum states. We note that the temporal information within each time trace is preserved during the data processing. This fact allows us to utilize a pulsed measurement scheme where different parts of the time trace correspond to different quantum states in the cryostat. The ability to pulse is crucial for the later reference-state reconstruction (see Sec. 3.1.3) and stabilization of the squeezing angles (see Sec. 3.3.3).

3.1.3 Quantum state reconstruction

The reconstruction of quantum signals in the microwave regime is a challenging task since the weak quantum signals are strongly diluted by thermal excitations at room temperature and, consequently, lose most of their quantum-mechanical properties. One possibility for the detection of quantum microwaves is to utilize single-photon detectors at cryogenic temperatures. Even though such detectors have been already experimentally realized [23, 24], they suffer from various drawbacks which render them difficult to utilize for a routine detection of quantum microwaves. In an alternative approach, one can employ linear amplifiers to amplify weak quantum signals and detect them at room temperature. However, phase-insensitive amplifiers add at least half a photon of noise to the signal [127]. In realistic scenarios, when the best available commercial HEMT amplifiers are used, the added noise is around 10 noise photons for frequencies in the range of 4-8 GHz. In order to reconstruct quantum states with this significant noise contribution, advanced signal recovery techniques need to be applied. Throughout this work, we use the so-called reference-state reconstruction and dual-path state reconstruction schemes which are introduced in the following. In both schemes, the quadrature moments $\langle I_1^n I_2^m Q_1^k Q_2^l \rangle$ are related to the moments of the complex envelopes $\hat{S}_{1,2} = (\hat{I}_{1,2} + i\hat{Q}_{1,2})/\sqrt{\kappa}$ where $\hat{I}_{1,2}$ and $\hat{Q}_{1,2}$ correspond to the measured quadratures and κ is the photon number conversion factor relating the measured voltages of the quadratures at room temperature to the number of photons of the quantum signals at the mixing chamber stage (see Sec. 3.1.4). The aim of both reconstruction schemes is to retrieve the signal moments of propagating quantum signals before the action of the amplification chain.

In the reference-state reconstruction, a well-known signal is used as a reference state which allows one to calibrate out the actions of the amplification chain [25, 26, 121]. In our experiments, the reference state is a weak thermal state with, e.g., 0.01 photons at 5 GHz and 50 mK. Due to the low thermal population, such states are also well approximated by a vacuum state. The complex envelope can be written in the form $\hat{S}_{1,2} = (\hat{a}_{1,2} + \hat{V}_{1,2}^\dagger)$ where $\hat{V}_{1,2}$ is the added noise by the respective detection chain. Here, $\hat{a}_{1,2}$ denotes the annihilation operator of the propagating quantum signal in both path 1 and 2, respectively. For the reference state, the complex envelope is given by $\hat{S}_{\mathrm{ref}} = (\hat{t}_{1,2} + \hat{V}_{1,2}^\dagger)$ where $\hat{t}_{1,2}$ describes a weak thermal state in both paths. Consequently, the signal moments $\langle (\hat{a}_1^\dagger)^n (\hat{a}_2^\dagger)^m \hat{a}_1^k \hat{a}_2^l \rangle$ can be calculated from the moments of both envelope functions, which, in turn, are related to the measured quadrature moments $\langle I_1^n I_2^m Q_1^k Q_2^l \rangle$.

In the dual-path reconstruction, the quantum signal $\hat{a}$ is sent to a 50:50 beam splitter at cryogenic temperatures. We use a 180°-hybrid ring (CPL-5850-100B, Miteq) as such a microwave beam splitter. The second input of the beam splitter needs to be a known state $\hat{v}$, i.e. a vacuum or weak thermal state. The outputs of the beam splitter are then amplified and detected, which masks the quantum signal with noise. The complex envelope function now reads $\hat{S}_{1,2} = \left(\pm\hat{a} + \hat{v} + \hat{V}_{1,2}^\dagger\right)/2$. Since the first order moment of

the noise vanishes, $\langle \hat{V}_{1,2} \rangle = 0$, and the added noise between the chains is uncorrelated, the signal moments $\langle (\hat{a}^\dagger)^n \hat{a}^k \rangle$ can be calculated from cross-moments of the envelope functions of both output paths. For more details, we refer the reader to Refs. [167, 169, 170].

In both methods, we calculate the signal moments up to the fourth order which requires measured quadrature moments up to the fourth order. For Gaussian states, only the first and second order moment are required for a full state reconstruction. However, the higher order moments are useful for verifying that our experimentally measured states are indeed Gaussian, as discussed in Sec. 3.2.6.

3.1.4 Output line calibration

As discussed in the previous subsection, both reconstruction methods of quantum microwaves require a photon number conversion factor κ (PNCF). The PNCF relates the measured quadrature voltages to the signal moments which are expressed in terms of photon numbers. Furthermore, the gain of the amplification chain is required to determine the correct amplitude of quantum signals in the cryostat. A thorough determination of the PNCF and gain is essential for our experiments since only a proper calibration allows us to obtain reproducible results.

Balancing of amplification chains

Before the output line calibration, we balance both channels in amplitude. For that, we record a histogram of the raw ADC readings from the Acqiris card for both amplification chains while no signal or pump tones are applied to the cryostat. In this way, we can correct for possibly unbalanced broadband powers of the Gaussian noise by adjusting the step attenuators in the dual-path receiver. Here, we also verify that the input voltage to the ADCs is well below the chosen maximum input voltage range. Subsequently, we apply a coherent signal through the cryostat and record an averaged timetrace of the signal. From the recorded sinusoidal oscillation, we extract a narrowband balancing factor and the phase between the channels. The amplitude of one channel is multiplied by this balancing factor during the digital moment calculation. The balancing of channels before every PNCF measurement allows us to verify if the experimental setup is functional and consistent with previous measurements. Furthermore, balanced amplitudes in both channels avoid rounding errors during the calculation of cross-moments in the digital signal processing. Finally, the relative phase between both paths is adjusted to 180° by a manual phase shifter in one local oscillator signal path. This step is required for the dual-path reconstruction since exactly this phase difference is required for the reconstructions.

Photon number conversion factor

In order to calibrate the amplification chains, we require a calibrated photon source inside the cryostat which emits a known number of photons. For that purpose, we use a 30 dB attenuator which acts as black body radiator emitting thermal radiation into the coaxial cables [171]. As shown in Fig. 3.5, the attenuator is placed in the input line of one of the JPAs. The emitted power is determined by the temperature of the attenuator which can be varied in a range $T_{\mathrm{att}} = 40 - 700\,\mathrm{mK}$ using an external PID controlled loop. For that, a heater and temperature sensor are placed on an oxygen-free high thermal conductivity (OFHC) copper holder which is fixed to the 30 dB attenuator. Since we want to change the temperature of the attenuator without heating the rest of the mixing chamber stage, the heatable attenuator is only weakly coupled to the cryostat. This is achieved by using a stainless steel input cable and a NbTi/NbTi coaxial cable after the heatable attenuator. The superconducting cable is crucial since the emitted thermal radiation from the attenuator should be transmitted with as little losses as possible to increase the precision of the output line calibration. Since the thermal conductivity of both used coaxial cables is low and can be mostly neglected, we use an additional thin silver ribbon to weakly couple the heatable attenuator to the mixing chamber plate. The additional thermal coupling ensures that the black body radiator reaches a minimal temperature of around 40 mK within a reasonable time after heating it. At the same time, the thermal coupling needs to be small enough such that the temperature of the mixing chamber stage is only negligibly affected when sweeping the temperature of the heatable attenuator.

The total detected power $P_{1,2}$ for each amplification chain at the digitizer card is given

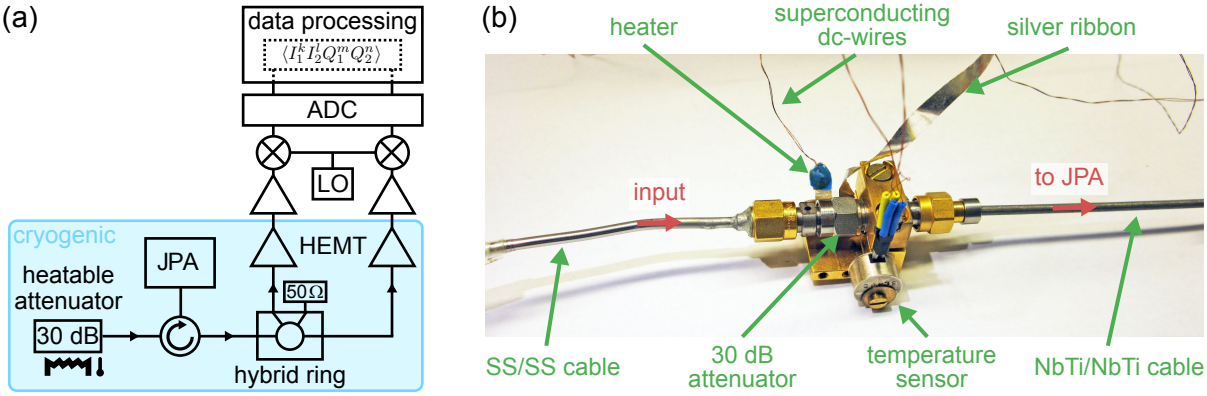

Figure 3.5: (a) Scheme for output line calibration by using a heatable attenuator as black body radiator. The thermal signal is split by a beam splitter (hybrid ring) at cryogenic temperatures and amplified before it is detected with a heterodyne detection setup. (b) Photograph of heatable attenuator setup. All components are fixed to a gold-plated OFHC copper holder. SS/SS denotes a coaxial cable with stainless steel as inner and outer conductors. NbTi is used as inner and outer conductors for NbTi/NbTi cables.

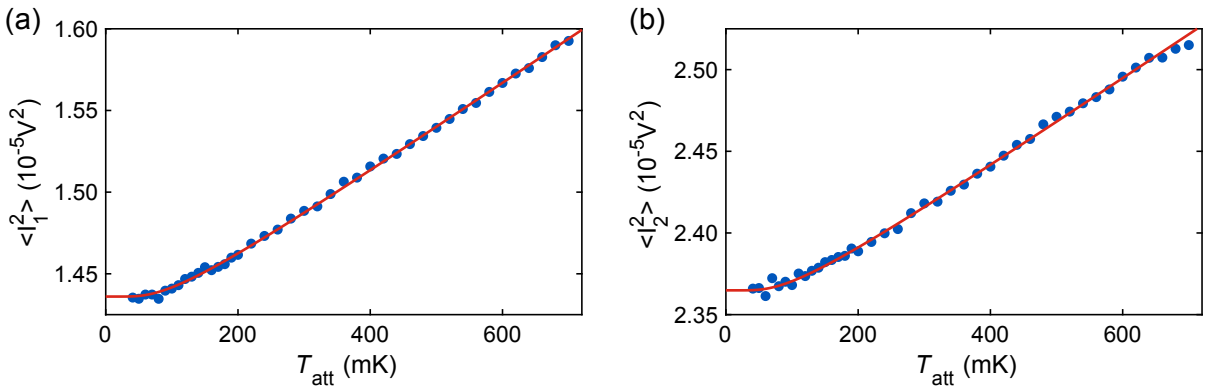

Figure 3.6: (a,b) Exemplary calibration measurement of amplification chains for path 1 and path 2, respectively. Symbols depict experimental data and solid lines are corresponding fits according to Eq. (3.3). The center frequency of the detection bandwidth is $f_0 = 5.435\,\mathrm{GHz}$ and the bandwidth is $\Omega = 430\,\mathrm{kHz}$.

by [167, 171]

$$P_{1,2}(T_{\mathrm{att}}) = \frac{\langle I_{1,2}^2 \rangle + \langle Q_{1,2}^2 \rangle}{R} = \frac{\kappa_{1,2}}{R}\left[\frac{1}{2}\coth\left(\frac{hf_0}{2k_{\mathrm{B}}T_{\mathrm{att}}}\right) + n_{1,2}\right], \tag{3.3}$$

where $R = 50\,\Omega$, h is the Planck constant, k_{B} is the Boltzmann constant, f_0 is the center frequency of the detection bandwidth, and the quantity $\kappa_{1,2}/R$ is the detected power per microwave photon. The PNCF, defined as $\kappa_{1,2} = G_{1,2} \times R \times \Omega \times hf_0$, relates the measured voltages to the photon numbers before amplification where Ω is the full detection bandwidth. The quantities $G_{1,2}$ and $n_{1,2}$ are the gain and noise photon number of both amplification chains, respectively. From Eq. (3.3) it becomes evident that a changed temperature T_{att} of the heatable attenuator leads to a different photon number and, hence, different detected powers. The PNCF and gain of the amplification chain are essentially determined by the measured slope of the measured power versus T_{att}. The offset determines the added noise photon number of the amplification chain. In Fig. 3.6, we show an exemplary calibration measurement with a corresponding fit of Eq. (3.3). From the fit, we obtain similar values of $\kappa_1 = 1.69 \pm 0.02\,(\mathrm{mV})^2$ and $\kappa_2 = 1.68 \pm 0.02\,(\mathrm{mV})^2$ due to the pre-balancing of both chains. However, the added noise photons $n_1 = 16.5 \pm 0.2$ and $n_2 = 27.7 \pm 0.4$ deviate significantly between the paths. We note that the observed noise photon numbers are roughly twice as high as expected from the datasheet values for the HEMT amplifiers. This originates from the fact that a beam splitter is placed in front of the HEMT amplifiers which reduces the signal power by a factor of two. Consequently, the noise photon number of the whole amplification chain, including the beam splitter, is doubled. Taking this effect into account, the observed n_1 fits nicely to the datasheet noise properties of the employed HEMT amplifier in path 1. For path 2, the observed noise photon number of the chain, is above the expected value due to a faulty circulator used

before the HEMT. The results of the fit for the quadrature moments $\langle Q_1^2 \rangle$ and $\langle Q_2^2 \rangle$ are similar to the ones of the corresponding I-quadratures.

Reconstruction point

If no losses are considered during the calibration of the output lines, the quantum states would be reconstructed at the noise source, i.e., the heatable attenuator. However, in the experiments, we want to reconstruct the quantum states at different positions in the setup. In order to achieve that goal, we carefully estimate the losses from the heatable attenuator to a desired reconstruction point in the experimental setup. The losses are then taken into account during determination of the PNCF factors $\kappa_{1,2}$ which are required for the quantum state reconstruction. A sketch of a simplified situation is depicted in Fig. 3.7. In order to shift the reconstruction point from the heatable attenuator (point A) to, for example, the output of the hybrid ring (point B), we carefully estimate the losses L between A and B. The total gain $G'_{1,2}$, referenced to point A, is then related to the gain $G_{1,2}$, referenced to point B, as

$$G'_{1,2} = G_{1,2} \cdot 10^{-L/10}\,, \tag{3.4}$$

where the losses are given in decibel and $L > 0$ correspond to non-zero losses between A and B. During the fitting procedure of Eq. (3.3), we also take the temperature gradient between the heatable attenuator and a circulator in front of the JPA into account which provides a small correction to the PNCFs. For that, the cable between the heatable attenuator and the circulator is discretized into 100 equal segments where each segment possesses a proportional part of the total loss of the cable. Each segment is assumed to have a temperature defined by the linear temperature gradient of the cable. The transmitted thermal photons from the heatable attenuator are then calculated with an iterative approach over all cable segments, where the loss and temperature of each segment is taken into account by a beam splitter model [131].

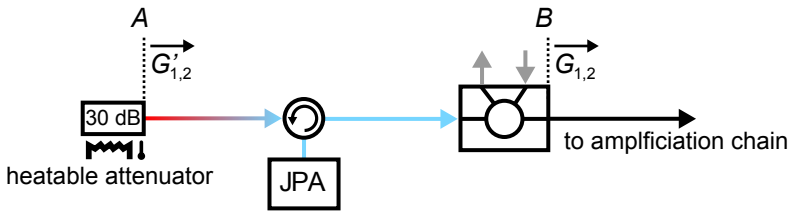

Figure 3.7: Sketch describing the procedure for shifting of the reconstruction point between different positions in the setup. $G'_{1,2}$ and $G_{1,2}$ denote the total gain of the amplification chain starting from the points A and B, respectively. Blue lines denote cold connections. A temperature gradient between the heatable attenuator and the circulator is taken into account during fitting of $\kappa_{1,2}$.

3.2 Characterization of flux-driven JPAs

Throughout this work, we employ JPAs for the generation and manipulation of propagating quantum microwaves. For these tasks, a careful characterization of the JPAs is crucial. In this section, we present how the properties and performance of each JPA are determined during our experiments. First, we probe the flux dependence of the JPA resonance frequency and the JPA nondegenerate gain. If the JPA is later employed as a phase-sensitive amplifier, we also determine its degenerate gain. Otherwise, the JPAs are typically utilized for the generation of squeezed states. Finally, we discuss Gaussianity and effect of losses on propagating squeezed microwave states.

3.2.1 JPA sample preparation and packaging

We employ JPAs as the key element in experiments with propagating quantum microwaves. Since we operate multiple JPAs in a single experiment, the bandwidth and resonant frequency of the JPAs must be compatible. Consequently, an established and reproducible fabrication routine is mandatory for advanced experiments involving JPAs. Throughout this thesis, we use JPAs designed and fabricated at NEC Smart Energy Research Laboratory, Japan and RIKEN, Japan. An optical micrograph of a JPA is shown in Fig. 3.8 where the quarter-wavelength coplanar waveguide (CPW) resonator is visible. At one end, the resonator is short-circuited to the ground plane via a dc-SQUID [108, 113]. The resonator and pump line are patterned into a 50-nm-thick Nb film which has been deposited by magnetron sputtering onto a 300-μm-thick silicon substrate covered by a thermal oxide. The dc-SQUID is fabricated using an aluminum shadow evaporation technique [172].

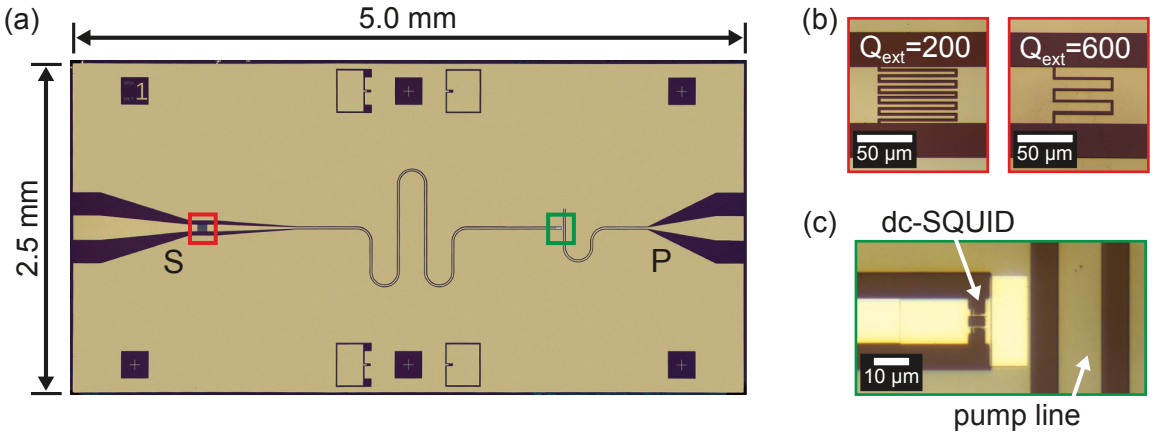

Figure 3.8: (a) Optical micrograph of a JPA sample chip. The red and green rectangles mark the coupling capacitance and dc-SQUID, respectively. The signal and pump port are marked by S and P, respectively. (b) Zoom-in to the coupling capacitance for a designed external quality factor $Q_{\mathrm{ext}} = 200$ (left panel) and $Q_{\mathrm{ext}} = 600$ (right panel). (c) Zoom-in to the dc-SQUID with adjacent pump line. The size of the dc-SQUID loop is $4.2 \times 2.4\,\mu\mathrm{m}^2$.

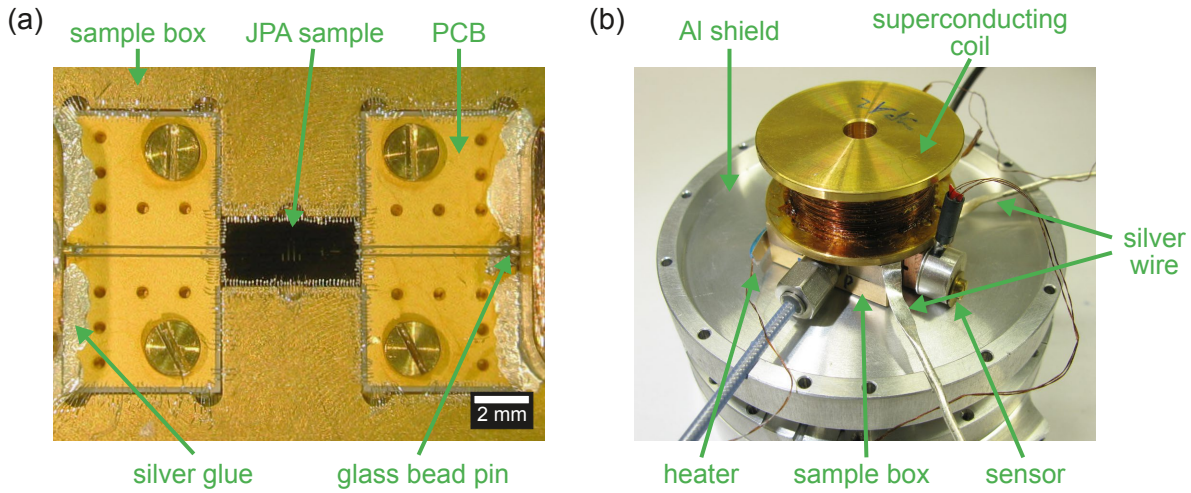

Figure 3.9: (a) Optical photograph of a JPA sample bonded in the sample box. The signal and pump ports of the JPA are coupled to RF connectors of the sample box via a PCB and glass bead. (b) Sample box mounted into a superconducting aluminum shield. The superconducting coil, temperature sensor and heater are installed on the sample holder inside the shield. Two annealed silver wires provide thermalization to all components.

The JPA samples are placed inside a sample box fabricated out of OFHC copper, as shown in Fig. 3.9 (a). In order to ensure mechanical stability and good thermalization, the JPA samples are glued with GE varnish (GE 7031, SCB) to the sample box. The JPA sample is galvanically coupled to the box ground via aluminum bonds. The signal and pump ports of the JPA are bonded to the inner conductors of CPW transmission lines on a printed circuit board (PCB). At the other ends, the inner conductors of the CPW transmission lines on the PCBs are soldered to glass bead pins (K-100, Anritsu) which serve as an interface to radio frequency (RF) K-connectors (K102F-R, Anritsu) outside of the sample box. We use silver glue in order to galvanically connect one side of the PCB to the sample box. In this way, we achieve good impedance matching to $50\,\Omega$ with a reproducible maximum mismatch of $\pm 3\,\Omega$.

The sample box with JPA is placed inside of an aluminum box which serves as a shield from external magnetic fields after the aluminum becomes superconducting at $\simeq 1\,\mathrm{K}$. An aluminum shield with removed lid is shown in Fig. 3.9 (b). In order to be able to tune the JPA resonance frequency, we place a superconducting coil on top of the sample box inside the aluminum shield. The coil body is made out of OFHC copper and we use approximately 300 m of single-filament NbTi superconducting wire (C510/NbTi, Supercon Inc.) for winding of the coil. GE varnish is used to glue, and thus, better thermalize, wire layers in the coil. Furthermore, we fix a temperature sensor and heater to the JPA sample box which are used to control the temperature with an external PID controller. The heater consists of a $100\,\Omega$ thin-film resistor which is glued to a thin silver strip. All components are thermalized with two silver wires which are clamped to the sample holder at different positions.

3.2.2 Quality factors and flux dependence

For resonators, the internal and external quality factors are important quantities. The internal quality factor Q_{int} provides information about the internal losses of the resonator, while the external quality factor Q_{ext} is mainly given by the coupling capacitance C_c which determines the coupling strength of the resonator to the signal port [107]. To determine the quality factors and the resonance frequencies for different external flux values, we record the S-parameters corresponding to a microwave signal reflected from the JPA as depicted in Fig. 3.10. The S-parameter is measured for different probe frequencies and external flux values. The measurements are performed in the low power regime with less than one photon on average inside the JPA resonator. In this subsection, we study six JPA samples (JPA 1 to JPA 6) with different screening parameters β_{L} as well as different external and internal quality factors (see Tab. 3.1). Also, no additional external pump signal is applied to the JPA during the experiments.

For a theoretical description of the reflection coefficient and corresponding S-parameters, we use the expression obtained from the input-output formalism in Eq. (2.75). For samples JPA 1 to JPA 3, we extract internal quality factors up to $Q_{\mathrm{int}} \gtrsim 3 \times 10^4$, depending on the external flux, while the external quality factors Q_{ext} decrease with increasing JPA resonance frequency ω_0. JPA 1 to JPA 3 show an overcoupled behavior. Furthermore, we observe a strongly undercoupled behavior for samples JPA 4 to JPA 6, where the external quality factor is much larger than the internal quality factor. Moreover, for these samples, Q_{ext} as well as Q_{int} are flux independent and the Q_{int} values are lower than those of samples JPA 1 to JPA 3. The low Q_{int} for the sample batch containing JPA 4 to JPA 6 is explained by intensive Ar ion milling before evaporation of the Al which degrades the quality of the metal-substrate interface leading to increased losses [173]. Furthermore, for JPA 1 to JPA 3 the extracted Q_{ext} coincide well with the design target of 200 while for JPA 4 to JPA 5 the extracted Q_{ext} deviate substantially from the design target.

In Fig. 3.11, we show the flux-dependent JPA resonance frequencies for two samples

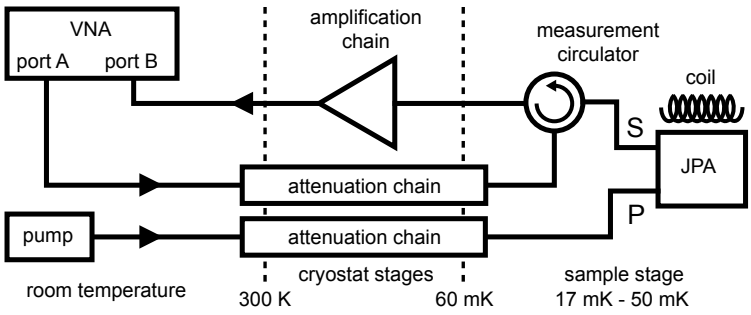

Figure 3.10: General scheme for the characterization of JPAs with a vector network analyzer (VNA). The reflected signal from the JPA is separated from the incoming signal by a measurement circulator. The flux Φ_{ext} through the dc-SQUID loop is controlled by a superconducting coil.

Table 3.1: JPA parameters extracted from fitting of the flux-dependence of the JPA resonance frequency for different JPA samples. Here, I_c is the critical current of a single Josephson junction, L_{loop} and β_{L} are the loop inductance and screening parameter of the dc-SQUID, respectively, and $\omega_r/2\pi$ is the resonance frequency of the bare resonator. The Josephson junctions of the dc-SQUID are assumed to be identical. The external quality factors Q_{ext} and internal quality factors Q_{int} are obtained from independent fits of Eq. (2.75).

Sample	I_{c} (μA)	β_{L}	L_{loop} (pH)	$\omega_{\mathrm{r}}/2\pi$ (GHz)	Q_{ext}	Q_{int}
JPA 1	2.19 ± 0.12	0.096 ± 0.008	45.4 ± 4.7	5.863 ± 0.018	265-300	>30000
JPA 2	2.34 ± 0.01	0.087 ± 0.001	38.3 ± 0.1	5.829 ± 0.001	310-380	>30000
JPA 3	2.14 ± 0.10	0.095 ± 0.005	45.9 ± 3.4	5.856 ± 0.015	280-340	>30000
JPA 4	12.16 ± 0.08	0.536 ± 0.001	45.6 ± 0.3	6.214 ± 0.001	5300 ± 100	1280 ± 30
JPA 5	9.82 ± 0.12	0.553 ± 0.001	58.2 ± 0.7	6.164 ± 0.001	12000 ± 1000	1100 ± 100
JPA 6	9.64 ± 0.27	0.557 ± 0.001	59.7 ± 1.7	6.216 ± 0.003	72000 ± 13000	1300 ± 300

together with numerical fits according to Eq. (2.82) where the critical current I_{c}, the screening parameter $\beta_{\mathrm{L}} = 2L_{\mathrm{loop}}I_c/\Phi_0$ and the bare resonator frequency $\omega_{\mathrm{r}}/2\pi$ are used as fitting parameters. In the experimentally accessed frequency range, Eq. (2.82) holds with an error of less than 0.5% compared to the exact solution from Eq. (2.78). The magnetic flux threading the dc-SQUID is controlled by applying a current through a superconducting coil mounted on the JPA sample box. As a current source, we use a source measurement unit (SourceMeter 2401, Keithley). For the investigated JPAs, the conversion factor of the coil current to the magnetic flux threading the dc-SQUID is $\simeq 6.5\,\Phi_0/\mathrm{mA}$.

Using $L_{\mathrm{r}} = 2\,\mathrm{nH}$, as estimated from the geometric design parameters and the characteristic impedance of the transmission line, $Z_0 = 50\,\Omega$, one can extract important JPA parameters from the measurement of the flux-dependent S-parameter as summarized in Tab. 3.1. In order to quantitatively model the flux dependence of JPA 1 to JPA 3, the decrease of the JPA resonance frequency with increasing absolute value of Φ_{ext} has to be taken into account. This can be achieved by considering the flux dependence of the kinetic inductance of the resonator [174], which leads to a flux dependent bare resonator frequency $\omega_{\mathrm{r}}(\Phi_{\mathrm{ext}}) = \omega_{\mathrm{r}}(0)[1 - \gamma\Phi_{\mathrm{ext}}^2]$. Here, γ is a constant depending on the material and geometry of the resonator.

For the samples JPA 1 to JPA 3, a weak hysteretic behavior is experimentally observed [see Fig. 3.11 (a,c)]. Overall, the fit describes the experimental data very well. However, the simulations of the JPA flux dependence (see Sec. 2.2.5 for details) predict a more pronounced hysteresis than observed in the experimental data. We attribute the observed deviation to a finite noise floor which causes a premature hopping of the phase particle to an adjacent minimum. Therefore, it is expected that the hysteresis is not as pronounced in the experimental data as predicted by simulations.

For the three other samples, JPA 4 to JPA 6, a strong hysteretic behavior is observed

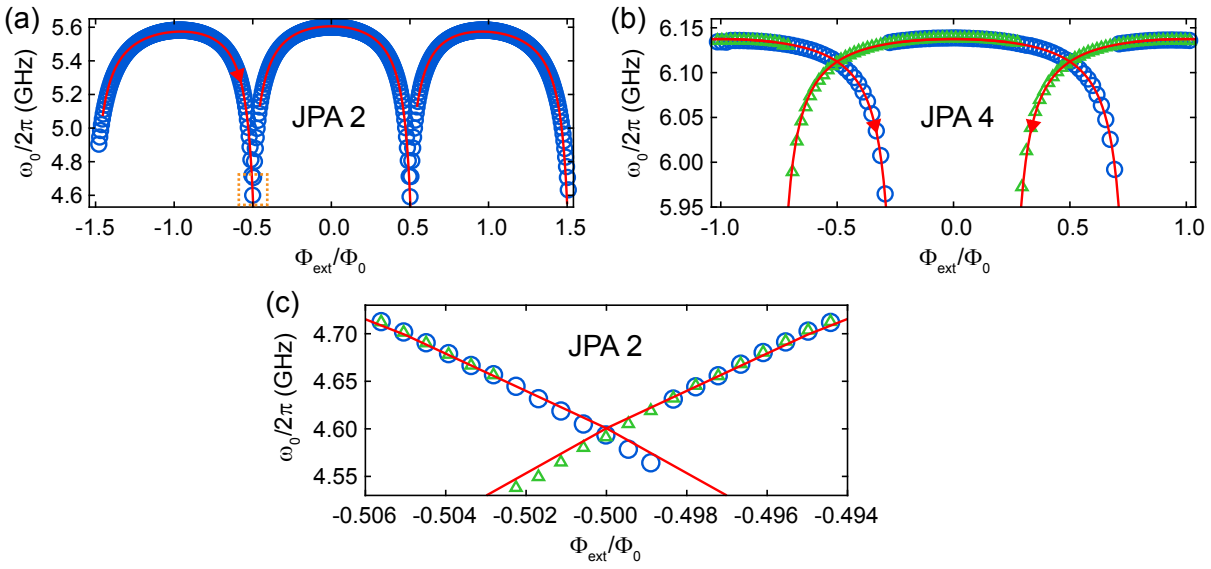

Figure 3.11: Resonance frequency of (a,c) JPA 2 and (b) JPA 4 as a function of the external magnetic flux Φ_{ext}. Blue circles and green triangles mark the data taken for increasing and decreasing values of Φ_{ext}, respectively. Symbols depict experimental data and solid lines are the corresponding fits. The errors of the ω_0 values obtained from fitting the data are smaller than the symbol size. The fit for JPA 2 is shown for $\gamma = 5.8 \times 10^{-3}\,\text{Wb}^{-2}$. The fitting results are summarized in Tab. 3.1.

in the resonance frequency versus applied flux dependence. As an example, Fig. 3.11 (c) shows an overlay of both sweep directions of the external flux for JPA 4. The flux dependence is described very well by the model calculations. The hysteresis over a large frequency window is explained by larger screening parameters β_{L} as compared to JPA 1 to JPA 3. With increasing β_{L}, the rigid coupling between the two phase differences across the junctions is lost, allowing for multiple classes of minimal energy states of the dc-SQUID for a given external flux. These different classes of minimal energy states manifest themselves in different resonance frequencies of the JPA. For the measured samples, we find only two such classes, whereas even more can exist for sufficiently large β_{L}. Depending on the history of the dc-SQUID regarding the external flux, different eligible minimal energy states are occupied by the dc-SQUID and, thus, a hysteretic behavior when changing the sweep direction of the external flux is observed.

To avoid this hysteresis, one would prefer a negligible L_{loop} which is possible by decreasing the dc-SQUID loop areas. However, to allow for an efficient coupling to the pump line, the loop area for flux-pumped parametric devices is usually chosen to be on the order of $10\,\mu\text{m}^2$ [98, 108, 128, 175]. From numerical estimations with FastHenry3 [176], we obtain the total loop inductance $L_{\text{loop}} \simeq 30\,\text{pH}$ consisting of both the geometrical inductance of the loop itself and the kinetic inductance, where the latter dominates due to the thin superconducting dc-SQUID electrodes. In order to minimize the hysteretic behavior of the JPAs while still maintaining a sufficient coupling to the pump line, one could reduce

the kinetic inductance by choosing a dc-SQUID design with thicker Al electrodes in future devices. Since all JPAs have the same dc-SQUID loop design, we attribute the spread in the extracted values of L_{loop} to variations of the kinetic inductance originating from differences during the fabrication process of the JPAs. Regarding the critical currents I_{c} for the sample batch containing JPA 1 to JPA 3, the extracted values are consistent with the design value of $2\,\mu$A. In contrast, I_{c} significantly exceeds the design values of $4\,\mu$A for the sample batch containing JPA 4 to JPA 6. The larger values of I_{c} for this sample batch are most likely caused by an excessive outgassing process of the resist mask during the Al evaporation which causes fluctuations in the Josephson junction parameters.

In addition, we find from our simulations that there is always a hysteretic behavior for any non-zero β_{L}. However, for small β_{L}, hysteretic behavior only appears at frequencies which are much smaller than the maximum resonance frequency. Furthermore, in experiments, a very small hysteresis may be hard to observe due to smearing caused by the thermally activated hopping between adjacent local energy minima of the dc-SQUID. Nevertheless, the behavior observed in our devices is markedly different from the textbook discussion of the total flux in a dc-SQUID as a function of the external flux. There, the hysteretic behavior only occurs above a certain threshold value $\beta_{\mathrm{L}} \geq 2/\pi$ of the screening parameter [97], whereas, in our devices, hysteretic behavior is already observed for $\beta_{\mathrm{L}} \ll 2/\pi$. The reason for this difference is that we take into account the full dc-SQUID potential without any simplifications.

The results presented in this subsection have been published by us in Ref. [113]. Parts of the text and figures are adapted from this reference.

3.2.3 Nondegenerate gain

We now investigate the nondegenerate gain of two JPAs, where one JPA is overcoupled ($Q_{\mathrm{ext}} < Q_{\mathrm{int}}$) and the other one is undercoupled ($Q_{\mathrm{ext}} > Q_{\mathrm{int}}$). To this end, a flux value corresponding to a certain resonance frequency ω_0 of the JPA is fixed. Then, a pump tone with the frequency $\omega_{\mathrm{p}} = 2\omega_0$ is applied to the JPA via the pump port. A scheme of the measurement setup is shown in Fig. 3.10. Regarding the input signal, the JPAs are operated in the nondegenerate mode, meaning that the frequency of the applied signal $\omega_{\mathrm{s}} = \omega_{\mathrm{p}}/2 + \delta\omega$ always has a non-zero offset from half the pump frequency, $\delta\omega \neq 0$. In order to evaluate the experimental data, we use explicit expressions of the nondegenerate gain for the case of a flux-driven JPA. As discussed in Sec. 2.2.6, the nondegenerate signal gain $G_{\mathrm{s}}(\delta\omega)$ and idler gain $G_{\mathrm{i}}(\delta\omega)$ for $\omega_{\mathrm{p}} = 2\omega_0$ are given by [104]

$$G_{\mathrm{s}}(\delta\omega) = \frac{\kappa_{\mathrm{int}}^2\delta\omega^2 + \left[(\kappa_{\mathrm{int}}^2 - \kappa_{\mathrm{ext}}^2)/4 - \epsilon^2\omega_0^2 - \delta\omega^2\right]^2}{\kappa_{\mathrm{tot}}^2\delta\omega^2 + \left[\kappa_{\mathrm{tot}}^2/4 - \epsilon^2\omega_0^2 - \delta\omega^2\right]^2}\,, \tag{3.5}$$

$$G_{\mathrm{i}}(\delta\omega) = \frac{\kappa_{\mathrm{ext}}^2\epsilon^2\omega_0^2}{\kappa_{\mathrm{tot}}^2\delta\omega^2 + \left[\kappa_{\mathrm{tot}}^2/4 - \epsilon^2\omega_0^2 - \delta\omega^2\right]^2}\,, \tag{3.6}$$

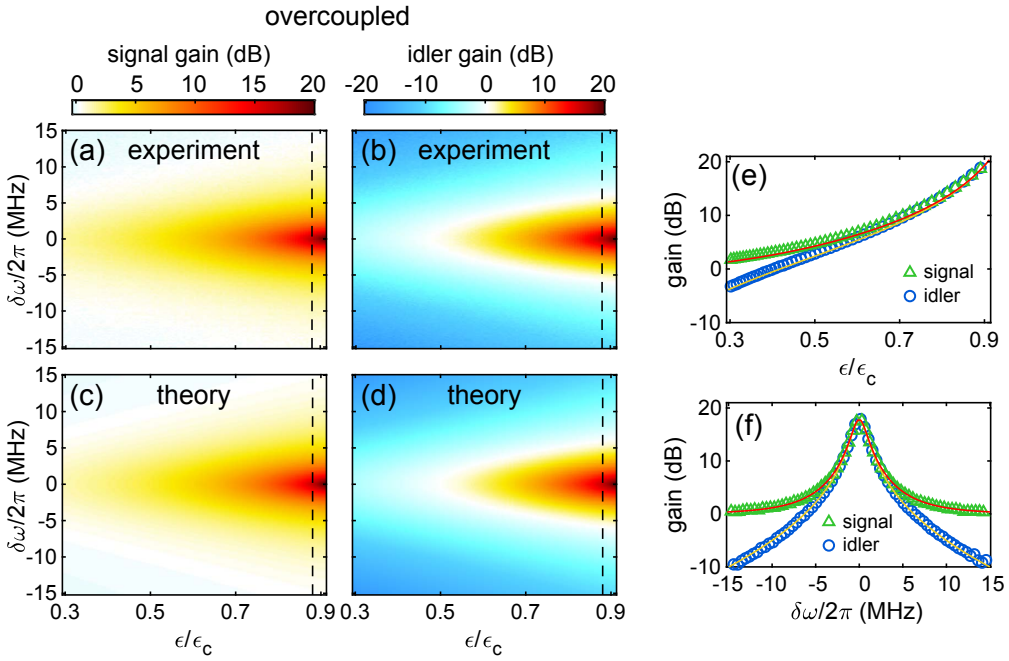

Figure 3.12: (a,b) Experimental spectra of the nondegenerate signal and idler gains as a function of ϵ and signal detuning $\delta\omega$ from half the pump frequency of $\omega_p/4\pi = 5.4\,\mathrm{GHz}$ for JPA 2. The smallest detuning is $|\delta\omega|/2\pi = 0.15\,\mathrm{MHz}$. (c,d) Theoretical calculations with $g \simeq 3.49\,\mathrm{V}^{-1}$ of the signal and idler gains computed from Eqs. (3.5) and (3.6), respectively. (e) Maximal signal and idler gains extracted from Lorentzian fits along vertical cuts in (a,b). (f) Signal and idler gains as a function of the signal frequency along the dashed lines. The symbols mark the experimental data and solid lines are fits of the data by Eqs. (3.5) and (3.6). The JPA temperature is stabilized at 50 mK.

where κ_{tot} is the total resonator loss and $\epsilon = gA_{\mathrm{pump}}$ is related to the root-mean-squared pump amplitude A_{pump} at the sample box via a coupling constant g. Eqs. (3.5) and (3.6) are only valid for $\epsilon \leq \epsilon_c = \kappa_{\mathrm{tot}}/2\omega_0$.

Figure 3.12 (a) and Fig. 3.12 (b) show the measured nondegenerate signal and idler gains as a function of ϵ for the overcoupled JPA 2. The pump frequency is fixed at $\omega_p/2\pi = 10.8\,\mathrm{GHz}$ corresponding to a flux working point of $\Phi_{\mathrm{ext}} = 0.39\,\Phi_0$ with $Q_{\mathrm{ext}} = 365$, $Q_{\mathrm{int}} \gtrsim 3 \times 10^4$ and $\epsilon_c = 1.39 \times 10^{-3}$. We measure the idler gain by comparing the generated idler mode at frequency $\omega_i = \omega_p/2 - \delta\omega$ to the applied signal at frequency $\omega_s = \omega_p/2 + \delta\omega$. Amplification can only be observed within a frequency window defined by the resonator bandwidth and centered at the resonance frequency. In this region, we observe an increased gain for both the signal and idler modes with increasing pump power. Theoretical predictions from Eqs. (3.5) and (3.6) are depicted in Fig. 3.12 (c) and Fig. 3.12 (d) for the signal and the idler mode, respectively. Only the coupling constant $g \simeq 3.49\,\mathrm{V}^{-1}$ is used as a fitting parameter, while the quality factors and the resonance frequency are fixed to previously determined experimental values. The given values for g include an additional uncertainty from the estimation of the pump line attenuation of 61 dB which is used to

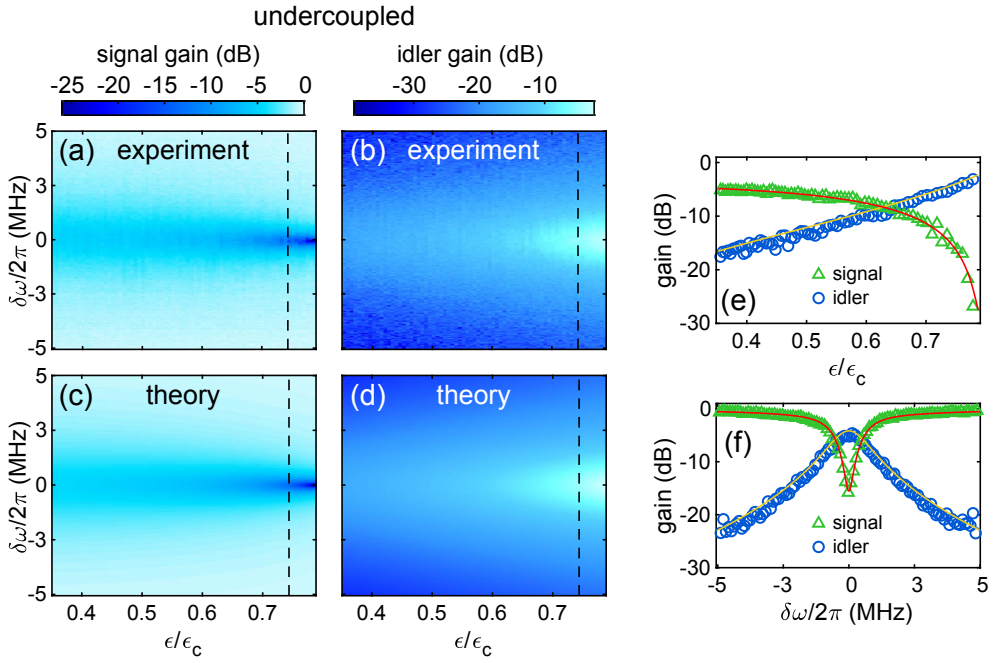

Figure 3.13: (a,b) Experimental spectra of the nondegenerate signal and idler gains as a function of ϵ and signal detuning $\delta\omega$ from half the pump frequency of $\omega_\mathrm{p}/4\pi = 6.125\,\mathrm{GHz}$ for JPA 4. The smallest detuning is $|\delta\omega|/2\pi = 25\,\mathrm{kHz}$. (c,d) Theoretical calculations with $g \simeq 0.17\,\mathrm{V}^{-1}$ of the signal and idler gains computed from Eqs. (3.5) and (3.6), respectively. (e) Maximal signal and idler gains extracted from Lorentzian fits along vertical cuts in (a,b). (f) Signal and idler gains as a function of the signal frequency along the dashed lines. The symbols mark the experimental data and solid lines are fits of the data by Eqs. (3.5) and (3.6). The JPA temperature is stabilized at 30 mK.

relate the pump power at the output of the microwave source to A_pump at the sample box. Figure 3.12 (e) shows the maximal signal and idler gains extracted from the detuning dependence and Fig. 3.12 (f) shows the signal and idler spectra at a fixed ϵ. Evidently, the model reproduces both the signal and idler modes very well.

Next, the undercoupled sample JPA 4 is investigated in the nondegenerate mode by applying a fixed pump tone at the frequency $\omega_\mathrm{p}/2\pi = 12.25\,\mathrm{GHz}$. The flux working point is $\Phi_\mathrm{ext} = -0.40\,\Phi_0$ with $Q_\mathrm{ext} = 5283$, $Q_\mathrm{int} = 1267$ and $\epsilon_c = 4.89 \times 10^{-4}$. The experimentally obtained spectra of the signal and idler as a function of the pump power are depicted in Fig. 3.13 (a) and Fig. 3.13 (b). For $\delta\omega/2\pi \simeq 50\,\mathrm{kHz}$, the incident signal is increasingly deamplified by up to $-30\,\mathrm{dB}$ with increasing pump power, while the idler gain increases. Since these undercoupled devices are described well by our parametric amplifier theory, we still call them JPAs although they do not act as amplifiers but rather as tunable attenuators. Again Fig. 3.13 (c) and Fig. 3.13 (d) depict theoretical predictions with $g \simeq 0.17\,\mathrm{V}^{-1}$ as the only fitting parameter. They reproduce the experimentally observed behavior accurately. The deamplification behavior of JPA 4 is in strong contrast to sample JPA 2 where the signal gain increases with increasing pump power. To understand this

behavior qualitatively, we simplify Eqs. (3.5) and (3.6) for $\delta\omega \to 0$ and obtain

$$G_\mathrm{s} \approx \frac{\left[(\kappa_\mathrm{int}^2 - \kappa_\mathrm{ext}^2)/4 - \epsilon^2\omega_0^2\right]^2}{\left[\kappa_\mathrm{tot}^2/4 - \epsilon^2\omega_0^2\right]^2}\,, \tag{3.7}$$

$$G_\mathrm{i} \approx \frac{\kappa_\mathrm{ext}^2\epsilon^2\omega_0^2}{\left[\kappa_\mathrm{tot}^2/4 - \epsilon^2\omega_0^2\right]^2}\,. \tag{3.8}$$

If the sample is overcoupled ($\kappa_\mathrm{ext} > \kappa_\mathrm{int}$), the numerator of Eq. (3.7) is monotonously increasing while the denominator is monotonously decreasing with increasing ϵ. However, for an undercoupled JPA ($\kappa_\mathrm{ext} < \kappa_\mathrm{int}$) the numerator crosses zero for a certain threshold value $\epsilon = \epsilon_\mathrm{crit} < \epsilon_\mathrm{c}$, meaning that the signal is increasingly deamplified with increasing ϵ until the threshold is reached. In the overcoupled regime, the JPA acts as an amplifier for an incident signal, whereas for undercoupled JPAs the incident signal is deamplified depending on the pump power. In this case, the device is no longer an amplifier but acts as a tunable microwave attenuator. In contrast, the idler gain G_i always increases for increasing ϵ independent of the fact whether the JPA is overcoupled or undercoupled.

The input-output model yielding Eqs. (3.5) and (3.6) directly relates the material and design parameters, such as internal and external quality factors, to the amplification performance of the JPAs. For example, it predicts that increasing Q_int from 10^4 to 10^5, for $Q_\mathrm{ext} = 365$, results in a similar gain-bandwidth product and an improvement of the maximal gain of 3.5 dB at a fixed pump power. Nevertheless, in the high gain limit higher-order nonlinear effects, which are not included in the model, might limit the amplification of the JPAs [110].

The results presented in this subsection have been published by us in Ref. [113]. Parts of the text and figures are based on this reference.

3.2.4 Degenerate gain

In the later experiments, we want to employ JPA 3 as phase-sensitive amplifier where one quadrature of an incoming signal is strongly amplified while the orthogonal one

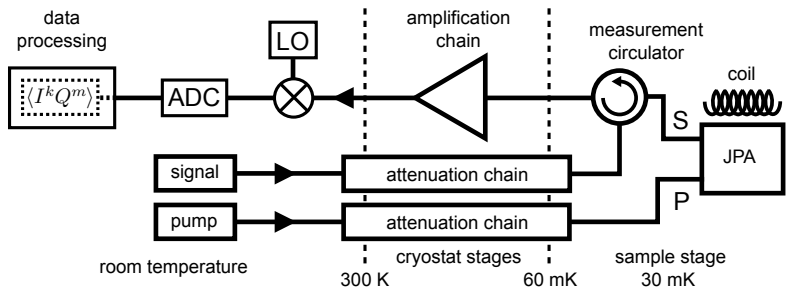

Figure 3.14: General scheme for characterization of JPAs using a heterodyne detection setup. LO denotes a local oscillator. A detailed experimental scheme is given in Fig. 3.24.

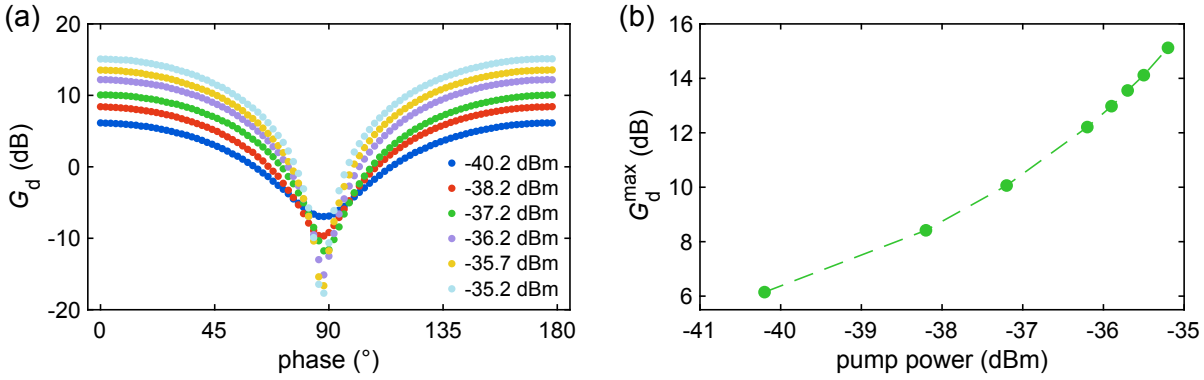

Figure 3.15: (a) Phase-dependent degenerate gain G_d and (b) maximum degenerate gain $G_\mathrm{d}^\mathrm{max}$ of JPA 3 for different values of the pump power at the pump port of the JPA. For clarity, the curves in panel (a) are shifted in phase direction such that the minima coincide. The signal at the input of the JPA has a power of $-144.8\,\mathrm{dBm}$ and a frequency of $5.43\,\mathrm{GHz}$.

is deamplified. This is in contrast to vacuum squeezing where no signal is incident to the JPA. As discussed in Sec. 2.2.6, phase-sensitive amplification allows, in theory, for noiseless amplification of one quadrature. The JPA allows for phase-sensitive amplification in the degenerate operation mode. Here, a pump signal at twice the resonance frequency $\omega_\mathrm{p} = 2\omega_0$ is applied to the JPA, similar to the case of the nondegenerate gain. However, for degenerate amplification, the signal frequency $\omega_\mathrm{s} = \omega_\mathrm{p}/2$ is exactly half the pump frequency. Thus, the idler mode is generated at the same frequency as the signal which leads to interference effects of the idler and signal. Depending on the relative phase between the pump and signal, the interference can be constructive or destructive. All pump powers are given at the input of the pump port of the JPA.

We use the dual-path receiver for the characterization of the degenerate gain as it allows for precise measurements of the signal power. A principle scheme of the setup is shown in Fig. 3.14. We apply both a coherent signal with a frequency $\omega_\mathrm{s}/2\pi = 5.43\,\mathrm{GHz}$ as well as a pump tone with a frequency $\omega_\mathrm{p} = 2\omega_\mathrm{s}$ to JPA 3. Considering the input line attenuation, the power of the incident signal to the signal port of JPA 3 is estimated to be $-145\,\mathrm{dBm}$. After amplification the phase-sensitively amplified signal is down-converted to 11 MHz and digitized as discussed in Sec. 3.1.2. The power of the amplified coherent signal $P_\mathrm{amp} = \langle I \rangle^2 + \langle Q \rangle^2$ is determined by the measured quadrature moments. As a reference measurement, we use the power P_ref recorded with no pump tone applied to the JPA. By changing the phase of the signal, we record the phase-dependent power P_amp which allows us to calculate the degenerate gain $G_\mathrm{d} = P_\mathrm{amp}/P_\mathrm{ref}$. Figure 3.15 (a) shows G_d for different pump power levels when varying the relative phase between the pump and signal tones. The extracted maximum degenerate gain $G_\mathrm{d}^\mathrm{max}$ as a function of the pump power is depicted in Fig. 3.15 (b) and serves as a calibration measurement for the experiments presented in chapter 5.

Apart from the gain, the 1 dB-compression point is another important figure of merit for

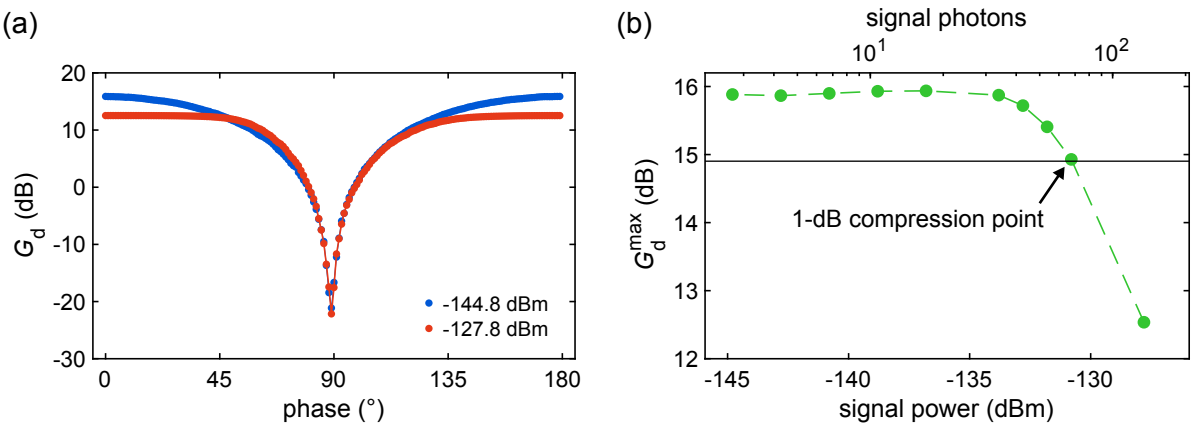

Figure 3.16: (a) Phase-dependent degenerate gain G_d and (b) maximum degenerate gain $G_\mathrm{d}^\mathrm{max}$ of JPA 3 for different values of the signal power. For clarity, the curves in panel (a) are shifted in phase direction such that the minima coincide. The pump power at the pump port of the JPA is $-35\,\mathrm{dBm}$ and the signal has a frequency of $5.43\,\mathrm{GHz}$. Top top x-axis in panel (b) corresponds to the reconstructed coherent photons in the measurement bandwidth $430\,\mathrm{kHz}$.

amplifiers. It specifies the signal input power at which the gain of the amplifier is reduced by 1 dB below its low input power value [102]. We now fix the pump power at the pump port of the JPA to $-35\,\mathrm{dBm}$, corresponding to a maximum degenerate gain of $G_\mathrm{d} \simeq 16\,\mathrm{dB}$, and increase the signal power while measuring the phase-dependent degenerate gain. Figure 3.16 (a) shows the phase dependence of G_d for two different signal powers. We observe that for the higher signal power, the amplification gain is reduced compared to lower signal powers. However, the deamplification is not influenced by this difference. This behavior is expected, as compression effects are typically caused by pump depletion or higher-order nonlinear effects [177, 178]. However, these compression mechanisms only occur if a signal is amplified which can either cause a lack of energy provided by the pump signal (pump depletion) or a high photon population in the resonator leading to higher-order nonlinear effects caused by the Josephson junctions. Neither of these effects occur when a signal is deamplified. Figure 3.16 (b) depicts the maximum degenerate gain $G_\mathrm{d}^\mathrm{max}$ for increasing signal power. For the chosen gain, the 1 dB-compression point occurs at $-131\,\mathrm{dBm}$ which corresponds to roughly 70 photons on average in the bandwidth of $430\,\mathrm{kHz}$.

3.2.5 Generation of squeezed states

A central task of the JPAs is to generate single-mode squeezed (SMS) states. The latter leak out of the JPAs and propagate along the microwave coaxial lines and components. In this work, we investigate fundamental properties of propagating microwave SMS states and apply them for the generation of path entanglement. Therefore, a routine characterization method for the squeezing properties of the JPAs is required.

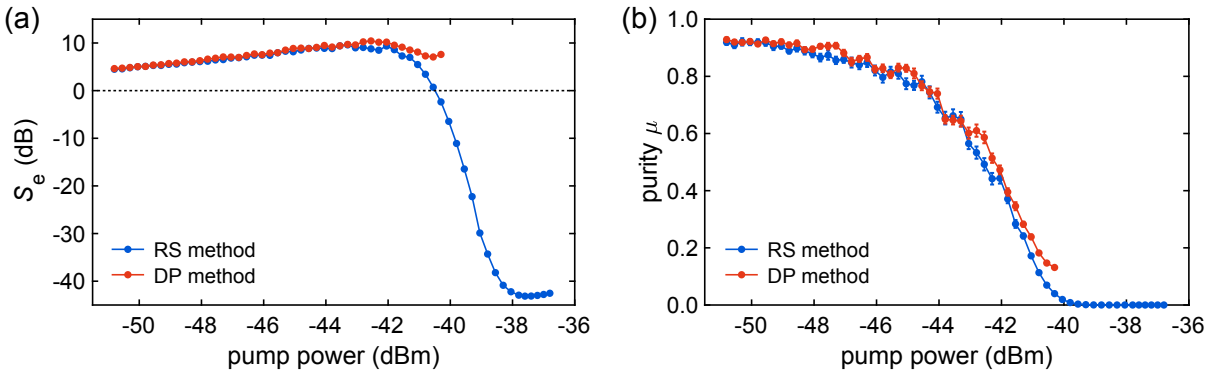

Figure 3.17: (a) Squeezing level S_e and (b) purity μ as a function of the pump power at the pump port of JPA 1. The reference-state (RS) reconstruction and dual-path (DP) reconstruction are employed for the reconstruction of the quantum states. If not shown, the standard error of the mean is smaller than the symbol size. The JPA resonance frequency is $\omega_0/2\pi = 5.435\,\text{GHz}$ and the filter bandwidth is 430 kHz.

After finding a suitable working point of the JPA, we apply a pump tone at a frequency $2\omega_0$, that is at twice the resonance frequency of the JPA. We detect the generated SMS states around the frequency ω_0 with the dual-path receiver. In this sense, the operation mode is similar to the one of the degenerate gain measurements. However, for squeezing, we do not apply any input signal to the JPA such that the JPA output consists of a weak squeezed thermal state. The photon population of the weak thermal state is determined by the temperature of the mixing chamber stage. These temperatures are typically around $30 - 50\,\text{mK}$, and therefore, the input state can be quite well approximated by a vacuum state.

As discussed in Sec. 3.1.3, we can reconstruct the quantum microwave states either by using the dual-path (DP) or the reference-state (RS) reconstruction. In Figure 3.17 (a) we have plotted the squeezing levels S_e of SMS states versus the pump powers applied to the JPA. The states are reconstructed at the input of the hybrid ring. We observe an increase of the squeezing level with increasing pump power of up to $-43\,\text{dBm}$ where both reconstruction methods coincide. Upon a further increase of the pump power, the reconstruction methods start to deviate from each other in their reconstructed S_e. Above $-40\,\text{dBm}$ pump power, all states reconstructed via the DP method become unphysical, i.e. show complex squeezing levels S_e. The RS reconstruction still yields physical states and we observe squeezing above the vacuum level of up to 40 dB. The states reconstructed with the DP method are unphysical because a central assumption for the DP method, which is that a vacuum state is incident to the second hybrid ring input, is no longer valid for high pump powers. This effect is caused by the pump signal of JPA 1 leaking through to JPA 2 which was not frequency-detuned during the measurements. Consequently, a weak squeezed state, generated by JPA 2, is incident to the second hybrid ring input. This squeezed state leads to a fact that the DP method yields unphysical results for the

state reconstructed at the first hybrid ring input. A similar cross-talk between JPAs is also observed in later experiments (see Sec. 5.1.2 for details) and originates from the fact that the hybrid ring and circulators are not designed for our pump frequencies at around 11 GHz. Consequently, the isolation of the microwave components is not sufficient to suppress the pump signal.

Figure 3.17 (b) depicts the purities μ of the produced states. For increasing pump powers, the purity decreases and coincides between the DP and RS method for a wide range of pump powers. The degradation of the squeezing level and purity is caused by nonidealities of the JPAs. On the one hand, the Josephson junctions inside the JPAs are highly nonlinear elements. The lowest-order nonlinearity is required for the parametric effects since it allows for the flux-tunability of the JPA. However, under sufficiently strong driving, e.g. by the pump tone, also higher-orders of the nonlinearity play a role in the JPA dynamics. In general, these effects lead to a deviation from an ideal parametric amplification and degrade the quality of the squeezed states [128, 177]. These higher-order nonlinear effects also lead to non-Gaussianity of the JPA output states, as discussed in detail in the next subsection. Apart from these nonidealities, the increased pump powers lead to high microwaves fields inside the JPA resonator. The high fields can lead to an increased coupling to loss channels. This causes the quantum states to become impure due to the added noise. Under the assumption of Gaussian states, both mechanisms lead to a reduced purity of the quantum states which is verified by our experimental results shown in Fig. 3.17 (b).

3.2.6 Gaussianity

All our quantum state reconstruction methods function under the assumption that the states are Gaussian, and thus, can be fully described by their signal moments up to the second order. The cumulants $\langle\langle(\hat{a}^\dagger)^n\hat{a}^m\rangle\rangle$ with order $n+m$ provide insight into the Gaussianity by characterizing, e.g., the asymmetry (third order) and sharpness (fourth order) of the characteristic function of the bosonic field operators [179]. The cumulants can be calculated from the signal moments $\langle(\hat{a}^\dagger)^n\hat{a}^m\rangle$ according to [121, 179]

$$\langle\langle(\hat{a}^\dagger)^n\hat{a}^m\rangle\rangle = \partial_x^n\partial_y^m \ln \sum_{\alpha,\beta} \frac{\langle(\hat{a}^\dagger)^\alpha\hat{a}^\beta\rangle x^\alpha y^\beta}{\alpha!\beta!}\bigg|_{x=y=0}, \tag{3.9}$$

where ∂_x^n is the n-th partial derivative with respect to x and ln is the natural logarithm. In order to check for the Gaussianity of the states, we verify that the cumulants of the third and fourth order ($n+m\geq 3$) are vanishingly small, as expected for Gaussian states [25]. Cumulants with the order $n+m\leq 2$ can be non-zero for Gaussian states.

Figure 3.18 (a,b) shows absolute values of the cumulants of squeezed states for varied pump power of JPA 1 reconstructed with the RS and DP methods, respectively. For low pump powers, we observe an increase of the cumulants $\langle\langle\hat{a}^\dagger\hat{a}\rangle\rangle$ and $\langle\langle\hat{a}\rangle\rangle$ while the other

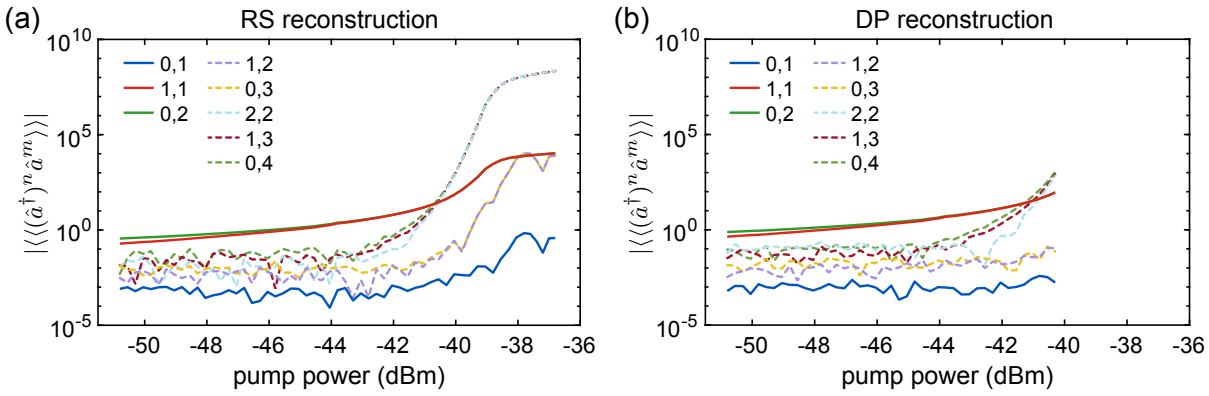

Figure 3.18: (a,b) Absolute value of cumulants $|\langle\langle(\hat{a}^\dagger)^n\hat{a}^m\rangle\rangle|$ as a function of pump power reconstructed with the RS and DP methods, respectively. Solid lines show cumulants up to second order. Third and fourth order cumulants are marked with dashed lines. The legend denotes the exponents (n, m) of the cumulants and defines the order $n+m$. The experimental data is the same as in Fig. 3.17. For better comparison, the same vertical and horizontal scales are used for both panels.

cumulants stay at much smaller constant values. Around -41 dBm pump power, the fourth order cumulants cross the second order cumulants for both reconstruction methods. Above this point the signals are clearly non-Gaussian. This finding coincides with the rapid decrease of the squeezing level observed in Fig. 3.17 (a) for the RS reconstruction. As discussed in the previous subsection, all states reconstructed with the DP method are unphysical for the pump powers above -40 dBm. For the lower pump powers, both reconstruction methods yield similar values of the cumulants.

3.2.7 Reference-state reconstruction from histograms

In our usual detection and reconstruction of quantum microwaves, we measure the quadrature moments $\langle I_1^n I_2^m Q_1^k Q_2^l\rangle$ up to the fourth order and use them to reconstruct the signal moments $\langle(\hat{a}^\dagger)^n\hat{a}^m\rangle$. This approach allows for flexible measurements with a sufficient voltage resolution in the quadrature moments, even if only a fraction of the full input range of the 12-bit ADC is used. Furthermore, the amount of required random access memory (RAM) during data processing and hard disk space for the saved data is acceptable since it is solely determined by the product of the number of calculated moments and the trace length. One drawback of this approach is that it is impossible to determine moments with orders > 4 from already processed data which might be crucial for evaluation of non-Gaussian effects.

As an alternative approach, one can record raw histograms of the quadratures I and Q and store the data on the hard drive. In principle, quadrature moments of arbitrary order can be calculated from these IQ-histograms. However, this approach requires a large amount of RAM for histograms of sufficient precision, if they are to be used for

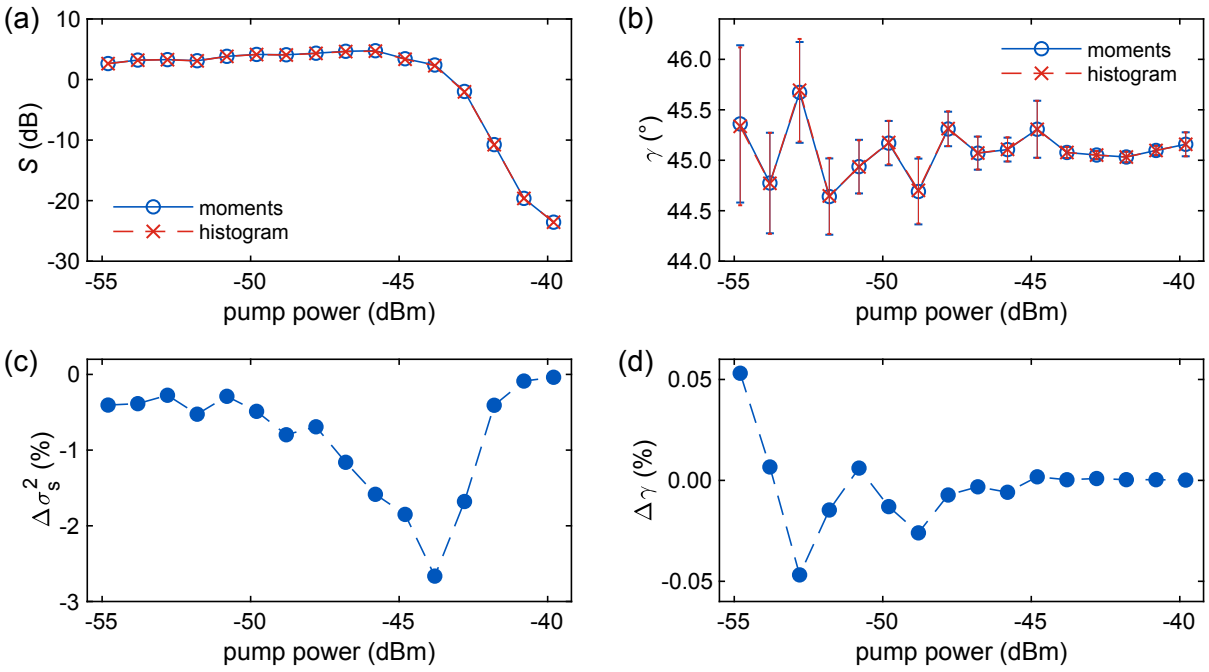

Figure 3.19: (a) Squeezing level S and (b) squeezing angle γ for different measurement approaches. Circles correspond to directly averaged quadrature moments during the raw data processing and crosses correspond to measured quadrature histograms where the quadrature moments are calculated after the measurement is finished. (c,d) Corresponding errors of the squeezed quadrature σ_s^2 and squeezing angle in percent, respectively. If not shown, the standard error of the mean is smaller than the symbol size. The JPA resonance frequency is $\omega_0/2\pi = 5.435\,\mathrm{GHz}$ and the filter bandwidth is 430 kHz.

calculations of the quadrature moments later. Consequently, the amplitude range of the histograms should be optimized for the expected signal amplitudes which requires careful estimations and calibration measurements.

In Fig. 3.19, we compare both methods of obtaining the quadrature moments. We utilize the reference-state reconstruction to obtain the squeezing level S and squeezing angle γ for varying pump powers applied to JPA 1. We observe a very good agreement between both measurement methods in both the mean values as well as the statistical standard errors of the mean. Consequently, for moments up to the second order, both methods can be applied to reconstruct quantum microwaves. However, the stored data and analysis time (after the measurement is finished) of the histogram-based approach is significantly increased when compared to directly measuring the quadrature moments. Also, as mentioned previously, for every measurement, the histogram range needs to be carefully adjusted such that no clipping effects occur if the histogram range is too small. On the other hand, if the range is to large, the resolution might be not sufficient for accurate determination of the quadrature moments. However, the measurement of the histograms have several important advantages. In particular, as already mentioned, the histograms allow for the calculation of an arbitrary order of the quadrature moments which is prohibitively difficult with direct,

real-time moment calculation. This potentially allows for a moment-based tomography of non-Gaussian states. Furthermore, the histogram-based approach gives access to a direct tomography of propagating states as their Q-function can be calculated from the histograms [125].

3.2.8 Effect of losses and physicality check on reconstructed squeezed states

Even in superconducting environments, propagating microwave states can be subject to notable losses which have detrimental effects on the quantum properties of these states. In our experiments, we utilize squeezed microwave states which are propagating along lossy components. Therefore, the understanding of the effect of losses on the squeezed states is essential for complex experiments. Since we cannot directly control losses in the experiment, we utilize the fact that we can shift the reconstruction point of the RS method by changing the PNCF of the respective amplification chain during the data post-processing (see Sec. 3.1.4). A change of the PNCF by a factor of $10^{L/10}$ corresponds to a shifted virtual RS reconstruction point after losses L. Consequently, a doubled PNCF amounts to $L = 3\,\mathrm{dB}$. Therefore, we can reconstruct the squeezed states after these virtual losses using the same dataset. Figure 3.20 (a) shows the effect of such losses on the squeezing level S and antisqueezing level A of a squeezed state. We observe that S is strongly affected by losses for high squeezing levels while A shows a weaker dependence on losses.

As discussed in Sec. 3.3.3, we separate every measurement into multiple shorter iterations in order to stabilize the squeezing angles of the JPA. In every iteration, we perform a RS reconstruction and obtain various squeezed state parameters. Some reconstructed states can be unphysical due to a lack of averaging or unlucky noise events. A squeezed state is only physical if the Heisenberg uncertainty relation

$$\sigma_\mathrm{s}^2 \sigma_\mathrm{a}^2 \geq 1/16 \tag{3.10}$$

is fulfilled. Here, σ_s and σ_a are the squeezed and antisqueezed quadrature variances, respectively. If Eq. (3.10) is violated, we call the respective state unphysical. Figure 3.20 (a) shows the mean squeezed state parameters when only physical states or all states are averaged over the iterations as a function of the losses. We note that in both cases, the mean values of σ_s^2 and σ_a^2 correspond to a physical state. We observe that for low losses, i.e., high squeezing levels S, there is a deviation between only averaging physical states and averaging all states. If all states are considered, the resulting averaged S is significantly increased. For higher losses, i.e. lower S, both cases coincide. The antisqueezing level A is only negligibly affected by the different averaging procedures.

We can theoretically model the effect of losses with an asymmetric beam splitter with

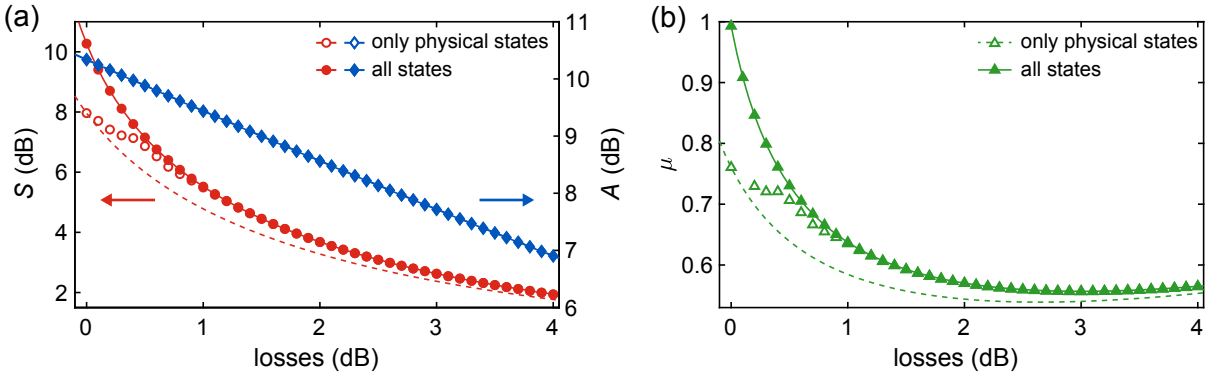

Figure 3.20: (a) Squeezing level S and antisqueezing level A as well as (b) purity μ for different losses. Symbols depict experimental data obtained from RS reconstructions with virtual losses. Lines depict the theoretically expected dependence according to Eq. (3.11). Open symbols and dashed lines correspond to averaged values where only physical states are considered. Full symbols and lines correspond to averaged values over all states. The JPA resonance frequency is $\omega_0/2\pi = 5.435\,\mathrm{GHz}$ and the filter bandwidth is 430 kHz.

transmissivity $\tau = 10^{-L/10}$, where L are the losses in units of decibel. We assume an incident vacuum state to the second input of the beam splitter due to low temperatures of the microwave components in our experiment. Consequently, we obtain the quadrature variances

$$\tilde{\sigma}_i^2 = \tau\sigma_i^2 + (1-\tau)\frac{1}{4}, \tag{3.11}$$

where $\tilde{\sigma}_i^2$ and σ_i^2 are the quadrature variances after and before losses, respectively, and $i \in \{\mathrm{s}, \mathrm{a}\}$ denotes the squeezed and antisqueezed quadrature variance, respectively. We use the experimentally reconstructed σ_i^2 for $L = 0\,\mathrm{dB}$ in order to calculate $\tilde{\sigma}_i^2$ for $L > 0\,\mathrm{dB}$ for the two different cases of averaging where (i) only physical states or (ii) all states are considered. If only physical iterations are considered, we observe a deviation between reconstructed and theoretically expected squeezing levels. In contrast, we obtain an excellent agreement if all states are considered for the averaged values of S. Again, the antisqueezed quadrature variance coincides well in both cases of averaging. The difference is explained by the finite amount of averaging in each iteration which causes a certain error in the reconstructed squeezed variances σ_s for every iteration. For highly squeezed states, σ_s is close to zero. Therefore, a small averaging fluctuation due to noise might cause a violation of Eq. (3.10) which makes the reconstructed state unphysical. However, if σ_s is increased due to this fluctuations, the state remains physical. Consequently, the physicality check of the states in every iteration yields a weaker (smaller) squeezing level on average if only physical states are considered. On the other hand, if all states are considered during averaging, weaker squeezed states are not specifically favored and the mean value is more accurate. This explanation fits nicely to the fact that nearly all reconstructed states are physical above $\simeq 1\,\mathrm{dB}$ loss and, consequently, both methods of averaging coincide.

Figure 3.20 (b) depicts the purity μ of the SMS states. Similar as for S and A, we observe that the reconstructed behavior for different losses coincides best with Eq. (3.11) if all states are considered for averaging. For increasing losses L, the purity μ decreases until $L \simeq 3\,\mathrm{dB}$. For higher L, the purity increases again because the added vacuum to the squeezed states slowly starts to dominate in the state. Since the purity of a vacuum state is unity, we expect $\mu = 1$ for $L \to \infty$ which implies that the entire signal is lost and substituted with vacuum fluctuations.

3.3 Advanced setups for experiments with propagating microwaves

In this section, we focus on the technical side of the cryogenic and room temperature setups in our experiments. A carefully designed and reliable cryogenic setup is crucial for successful experiments involving propagating microwaves. Here, we describe the key ideas behind the design of our setups and give technical details on the realization. Furthermore, we discuss how to stabilize the phases of the JPA pumps with a flexible pulse modulation scheme.

3.3.1 Setup for generation and characterization of two-mode squeezed states

In Fig. 3.21, we show a photograph of the cryogenic setup used in the experiments presented in chapter 4. Here, two JPAs inside individual aluminum shields are connected to a 180°-hybrid ring (CPL-5850-100B, Miteq). In order to separate the incoming from the outgoing signal of the JPAs, measurement circulators (CTH1184-KS18, Quinstar) are placed in the signal line of the JPAs. At one input and one output of the hybrid ring, we place a directional coupler (CPL-4000-8000-20-C, Miteq/Sirius) with a coupling of $-20\,\mathrm{dB}$ which allows to perform displacement operations (including the noise injection). All components are thermally connected to a silver rod which in turn is mounted and thermally anchored to the mixing chamber plate. In this way, all components in the cryogenic setup are thermalized to the base temperature of the cryostat. Unused ports of the microwave devices are terminated with precision $50\,\Omega$ loads which are also thermalized. For connections where low losses are essential, we either use direct connections or superconducting coaxial cables. The semi-rigid superconducting coaxial cables (SC-219/50-NbTi-NbTi, Coax Co., Ltd.) are all custom-made to fit to exact locations of the experimental setup. For the SMA connectors of the superconducting cables, we use crimp connectors (R125.052.900, Radiall) which provide good impedance matching to the $50\,\Omega$ standard with an average error of $\pm 1.5\,\Omega$. In order to preserve the quantum-mechanical properties of the propagating microwaves, the minimization of losses and environmental noise is of utmost importance.

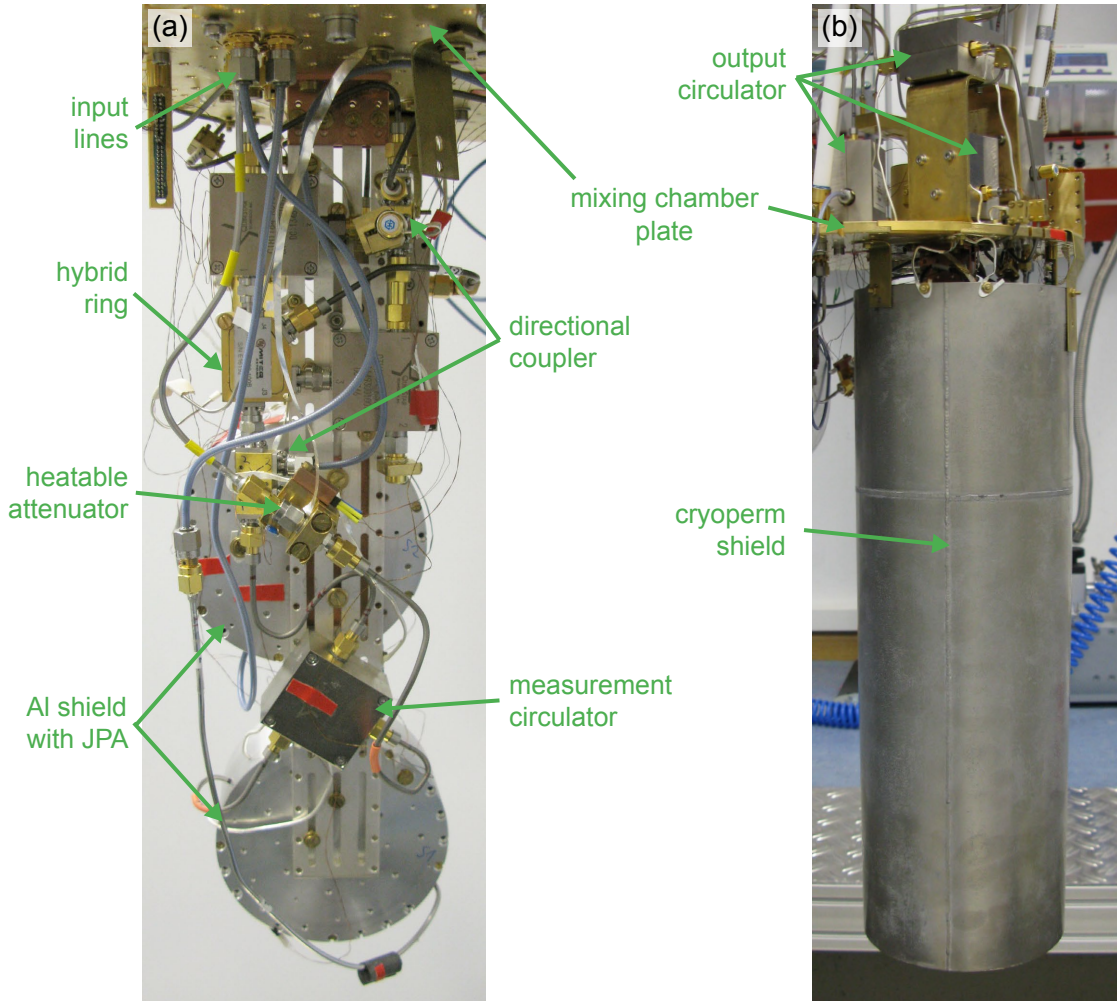

Figure 3.21: Photographs of the cryogenic setup for the experiments presented in chapter 4. Panels (a) and (b) show the setup without and with a cryoperm shield, respectively. Additional circulators of the microwave output lines are fixed at the top side of the mixing chamber plate.

The whole setup is enclosed in a cryoperm shield in order to shield the JPA samples from external magnetic fields during the cooldown. The additional magnetic shielding is required since the individual aluminum boxes for each JPA only provide magnetic shielding below the transition temperature of aluminum ($\simeq 1.2\,\mathrm{K}$) which is significantly below the one of niobium ($\simeq 9.2\,\mathrm{K}$). The latter forms the resonators and ground planes in our JPAs. We found that the probability of trapping flux in the niobium ground planes of the JPAs during the cooldown is significantly reduced when enclosing the whole setup in a cryoperm shield.

The full experimental setup is depicted in Fig. 3.22. The cryogenic setup corresponds to the previously shown photograph. The JPAs are pumped with room temperature microwave sources (SGS100A, Rohde&Schwarz). Since the relative phase stability between all microwave sources is crucial for the experiments, we reference all sources to a 10 MHz

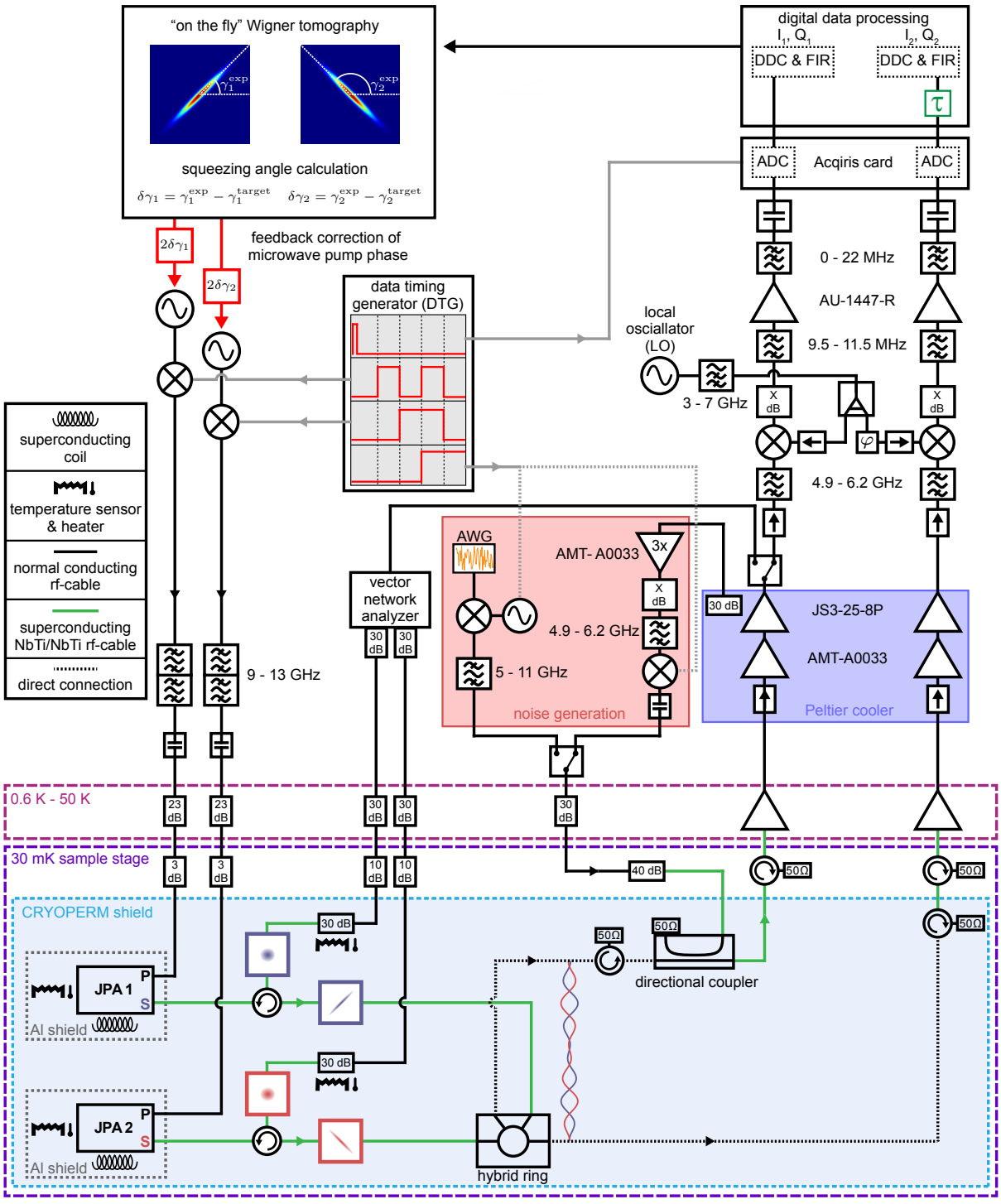

Figure 3.22: Experimental scheme for the measurements presented in chapter 4. The intertwined lines between the outputs of the hybrid ring symbolize quantum entanglement. Detailed timings of the pulses are presented later together with experimental results. The noise is generated at room temperature by either amplified thermal radiation of a 30 dB attenuator or an arbitrary-waveform generator (AWG). All microwave devices are referenced to a 10 MHz rubidium frequency standard (not shown).

rubidium frequency standard (FS725, Stanford Research Systems). The timings and trigger pulses are provided by a data timing generator (DTG 5334, Tektronix). Details on the referencing and pulse generation are given in Sec. 3.3.3. For the detection of the quantum signals, we first amplify the signals with HEMTs which are either placed at 1 K or 3 K. The first amplification stage is followed by additional RF-amplifiers (AMT-A0033, AgileMwT and JS3-25-8P, Miteq) at room temperature which are temperature stabilized with a Peltier cooler to $19.5 \pm 0.1\,^{\circ}\mathrm{C}$.

We employ room temperature switches (N1810TL, Agilent) in order to remotely switch between characterization measurements with a vector network analyzer (ZVA24, Rohde&Schwarz) and heterodyne tomographic measurements with an Acqiris card.

3.3.2 Setup for remote state preparation

In Fig. 3.23, we show a photograph of the cryogenic setup used in the experiments presented in chapter 5. The principles of designing the cryogenic setup are the same as discussed above. In particular, we use superconducting coaxial NbTi/NbTi cables at all connections where quantum signal propagate in the experiment in order to reduce the microwave losses. Due to the size constraint of the cryoperm shield, we use L-shaped copper holders to fix various components to the silver rod. For the remote state preparation (RSP) experiment, we need three JPAs each mounted in an aluminum shield. Furthermore, we employ a cryogenic 5-port switch (N1812UL, Agilent) with a specified insertion loss of 0.4 dB at 5 GHz in order to be able to switch in-situ between the actual RSP protocol or calibrating the setup. In order to toggle the cryogenic switch, a voltage pulse is applied to it. This pulse leads to a short but strong heat dissipation at the mixing chamber stage. In turn, the temperature of the sample rod increases to roughly 100 mK and relaxes to its base temperature over few tens of minutes. We note that the JPA flux working points are not affected by toggling of the microwave switch and the subsequent short increase in temperature. For the RSP experiments, we use a directional coupler (CPL-4000-8000-15-C, Miteq/Sirius) with a coupling of -15 dB. During all experiments, the temperature of the sample boxes of JPA 1 and JPA 2 is stabilized to 50 mK in order to ensure long-term stability of the JPAs and prevent an unstable temperature when the JPAs are pumped. The temperature of 50 mK is sufficiently low such that the corresponding thermal population is negligibly small. Optimally, all JPAs would be temperature stabilized. However, during the experiments only two AVS temperature bridges were available for continuous temperature stabilization of JPAs. We employ multiple heatable attenuators to calibrate all three output lines from the cryostat.

The full experimental setup is depicted in Fig. 3.24. We include an additional microwave switch at room temperature in order to switch between the direct JPA 3 measurements and measurements of the second directional coupler output. Due to a flexible architecture, we can straightforwardly measure, control, and phase stabilize the third JPA.

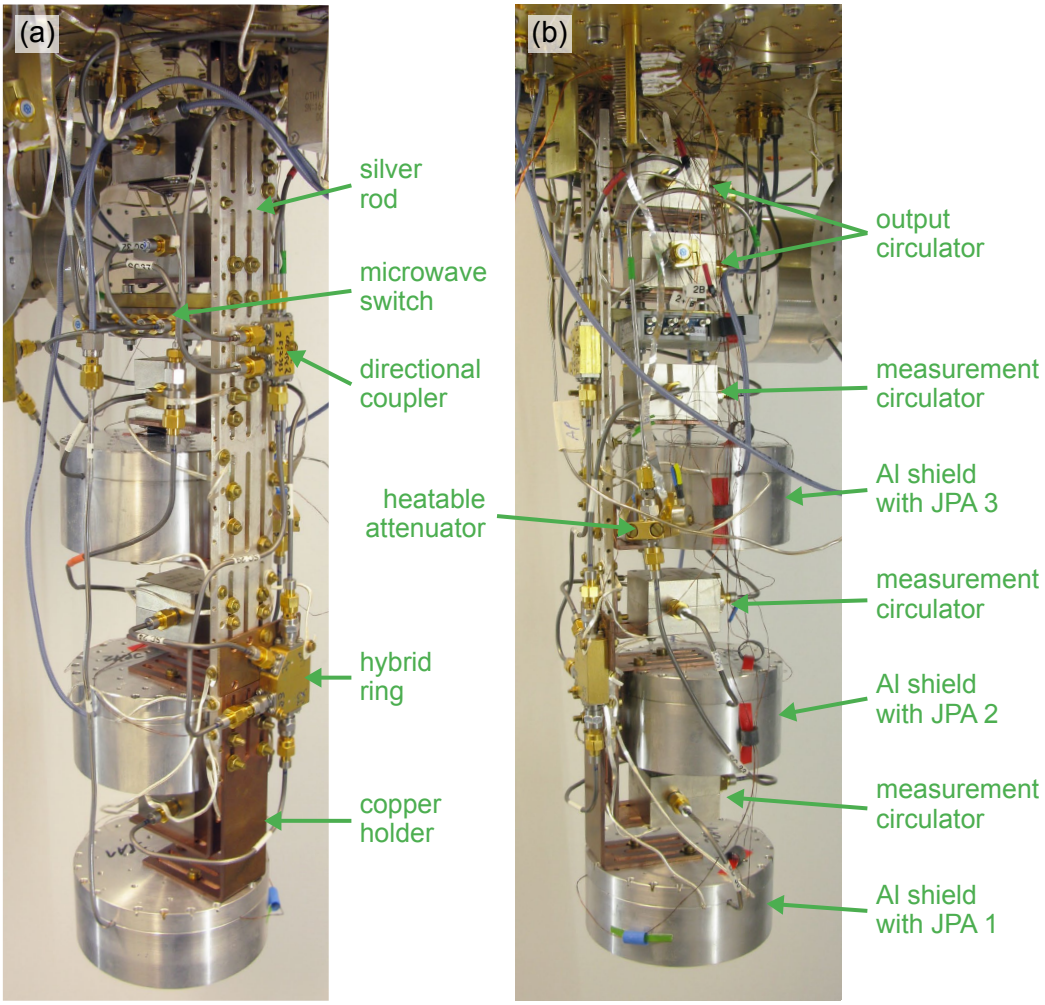

Figure 3.23: Photographs of the cryogenic setup for the remote state preparation experiments presented in chapter 5. Panels (a) and (b) depict different viewing angles on the setup. During experiments the setup is enclosed in a cryoperm shield (not shown).

3.3.3 Phase stabilization and pump modulation

For the later experiments, we require means to stabilize the squeezing angles of all JPAs to desired values. Without an active stabilization procedure, the squeezing angles of the JPAs would slowly drift over time due to phase drifts of the pump signal generated by our microwave sources. We minimize such phase drifts by synchronizing the vector network analyzer, DTG, Acqiris card and local oscillator to a 10 MHz rubidium frequency standard. The pump microwave sources are referenced to the local oscillator source with a 1 GHz signal. Without active squeezing angle stabilization, we achieve a low linear squeezing angle drift of $\simeq 0.8\,^\circ/\mathrm{h}$ with this setup.

For even better stabilization of the squeezing angles to specific target angles, we employ a flexible scheme for the pulse modulation of the JPA pumps which allows us to insert or remove certain pulses, as shown in Fig. 3.25. Here, the central element is a data

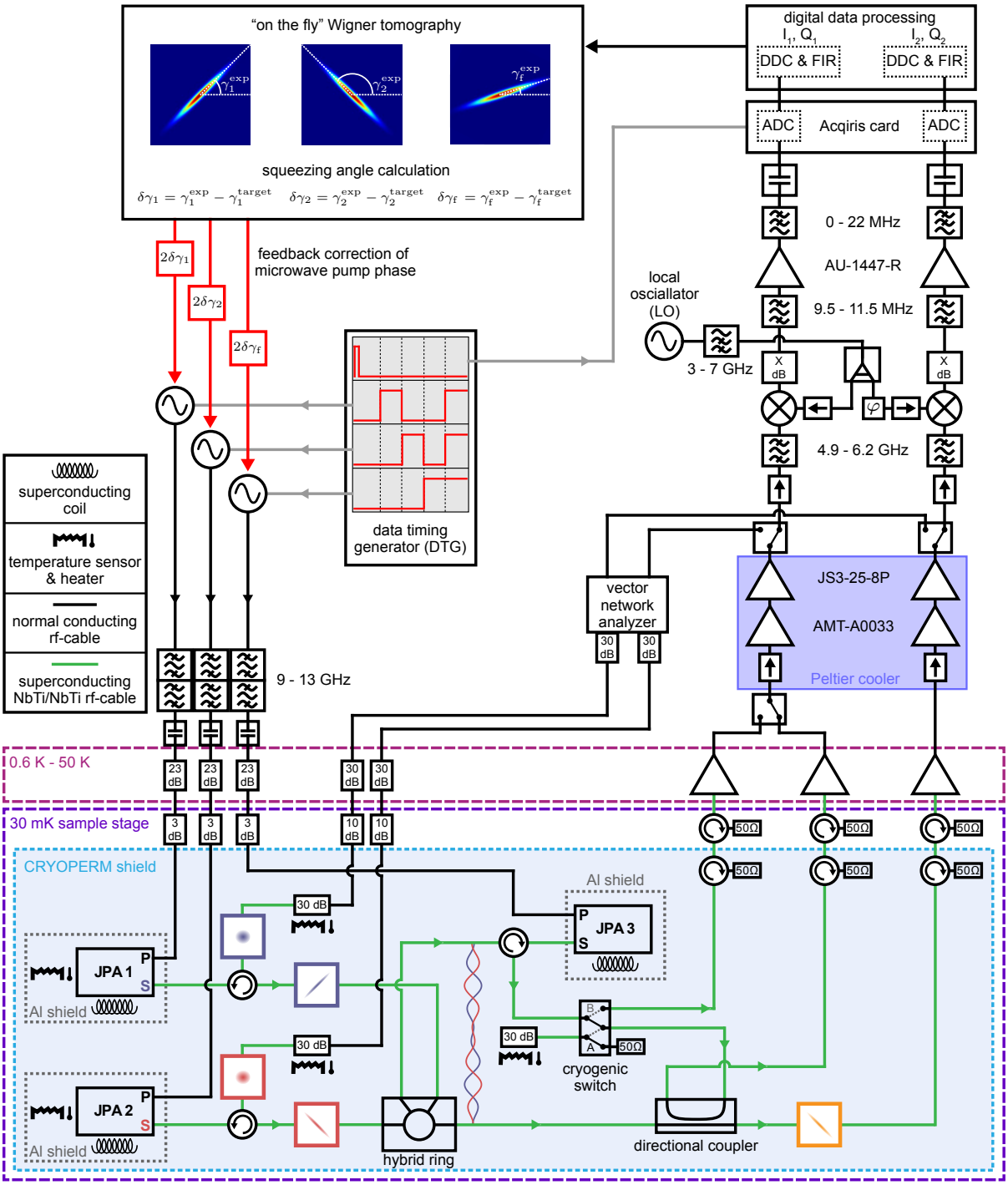

Figure 3.24: Experimental scheme for the RSP measurements presented in chapter 5. The JS3-25-8P RF-amplifiers are not used in the measurements presented in Sec. 5.2 and Sec. 5.3. The intertwined lines between the outputs of the hybrid ring symbolize quantum entanglement. JPA 3 and the directional coupler are separated by 35 cm of superconducting cable. Detailed timings of the pulses are presented later together with experimental results. All microwave devices are referenced to a 10 MHz rubidium frequency standard (not shown).

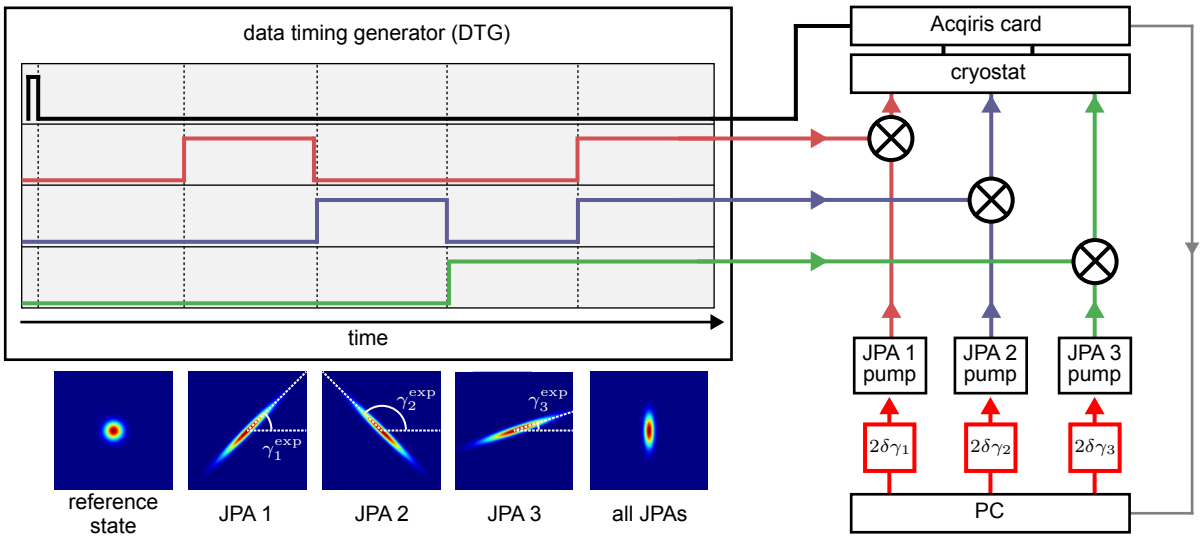

Figure 3.25: Scheme for generation of pulses and "on the fly" squeezing angle stabilization. A data timing generator generates modulation pulses and a trigger pulse for the digitizer card. The modulation pulses control the amplitude of the JPA pump tones generated by microwave sources. The squeezing angles γ_i^{exp} of all JPAs are calculated "on the fly" and utilized to obtain phase corrections $2\delta\gamma_i$ for the corresponding pump sources.

timing generator (DTG). It provides a trigger signal for the Acqiris card as well as the modulation pulses for the JPA pump microwave sources (SGS100A, Rohde&Schwarz). For the experiments presented in chapter 4, we use external mixers to modulate the continuous microwave pump tones. This method has the drawback that the mixers have 7 dB of insertion loss which limits the maximal pump power at the JPA chips. Furthermore, the mixers provide a limited on-off ratio. As an improvement, we employ the internal IQ-modulation of the SGS microwave sources to pulse the pump tones for the experiments presented in chapter 5. This approach allows for higher effective pump powers and a better on-off ratio of $\simeq 40$ dB. Together with the trigger signal, we use four channels of the DTG to allow for various combinations of three JPAs being pumped or not. In a minimal scenario, only two modulation pulses are needed for the reference-state reconstruction. The first one is the reference pulse with all JPAs turned off and for the second one all JPAs are pumped such that the actual protocol is executed. During all pulses, the JPAs are in a steady state since the pulse length of several tens of microseconds is much longer than the ring-up time of the JPAs. During the data analysis, the first $\simeq 20\,\mu$s of each pulse are discarded due to the FIR filter ring-up. The total pulse length is adjusted accordingly such that a sufficient amount of recorded data remains in each pulse. In general, the pulse length should be as long as possible in order to maximize the usable data in each pulse.

As mentioned before, we use an active method to stabilize the JPA squeezing angles. For that, we use three additional pulses in which only a single JPA is pumped. The pulses are used to perform a reference-state reconstruction for each squeezed state produced by

the JPAs. Subsequently, the obtained signal moments are used to calculate the squeezing angles γ_i^{exp} for each JPA "on the fly" in order to obtain a respective angle correction $\delta\gamma_i = \gamma_i^{\mathrm{ext}} - \gamma_i^{\mathrm{target}}$ which is then used to adjust the phase of the microwave pump tone by $2\delta\gamma_i$. Here, $\gamma_i^{\mathrm{target}}$ is the desired target squeezing angle of the i-th JPA. The factor of two originates from the fact that a phase change of the pump tone by $\delta\gamma$ translates to a squeezing angle change of $\delta\gamma/2$ due to the definition of γ. The time of averaging per reconstruction, i.e. the interval between angle corrections, varies between measurements but is around the order of 1 min.

Chapter 4

Quantum correlations in single- and two-mode squeezed microwaves

In this chapter, we focus on the experimental investigation of quantum correlations in single-mode and two-mode squeezed (TMS) propagating microwaves. In Sec. 4.1, we present our method for the generation of TMS states by superimposing two orthogonally-squeezed states at a beam splitter. We show a full tomography of the resulting states in the form of Wigner functions. The effect of finite time delays on the quantum correlations in propagating squeezed states is investigated in Sec. 4.2, which is relevant for the application of TMS states in quantum communication tasks. Finally, in Sec. 4.3, we study how noise disturbs quantum correlations in propagating TMS states. We observe the effects of sudden death of entanglement and quantum discord robustness towards noise injection.

4.1 Generation of frequency degenerate two-mode squeezed states

In the microwave regime, there exist different techniques to generate TMS states. In one approach, one utilizes Josephson junction-based superconducting circuits to generate entanglement between different frequency-nondegenerate modes. In particular, such TMS states have been generated by flux-pumping a dc-SQUID terminating a microwave transmission line [180] or current-pumped Josephson parametric amplifiers [130]. Another approach uses Josephson mixers to generate two-mode squeezing between two different physical outputs [181]. The Josephson mixer is a nonlinear superconducting circuit which allows to parametrically couple two superconducting resonators at distinct frequencies by pumping at the sum frequency of both resonators [182]. In both cases, the entangled modes of the TMS state are at different frequencies. In contrast, in our work, we use two squeezed states incident to a 50:50 beam splitter to produce path-entangled TMS states between frequency-degenerate output modes. Here, the entanglement exists between the outputs modes which are at the same frequency. In the following, we discuss the theoretical foundations for this process and present our experimental results.

4.1.1 Path entanglement via a beam splitter

In general, path entanglement can be produced by sending a nonclassical state of light to a symmetric beam splitter [183]. For example, one can use a squeezed state as such a nonclassical resource. To theoretically describe the resulting state at the beam splitter outputs, we start with two orthogonally squeezed single-mode states, with the same squeezing levels, incident to the beam splitter. Without any loss of generality, we can assume the first state to be squeezed in q direction, so that $\hat{a}_1 = \hat{v}_1 \cosh r - \hat{v}_1^\dagger \sinh r$, and the second state to be squeezed in p direction, so that $\hat{a}_2 = \hat{v}_2 \cosh r + \hat{v}_2^\dagger \sinh r$ [cf. Eq. (2.25)]. Here, $\hat{v}_i$ is the annihilation operator describing the initial state at the input of the squeezer and $\hat{a}_i$ is the annihilation operator after it. Then, the outputs of the symmetric beam splitter are given by the relation [16]

$$\begin{pmatrix} \hat{b}_1 \\ \hat{b}_2 \end{pmatrix} = \frac{1}{\sqrt{2}} \begin{pmatrix} 1 & 1 \\ -1 & 1 \end{pmatrix} \begin{pmatrix} \hat{a}_1 \\ \hat{a}_2 \end{pmatrix} . \tag{4.1}$$

The quadratures of the two beam splitter outputs states are defined as $\hat{q}_j = (\hat{b}_j + \hat{b}_j^\dagger)/2$ and $\hat{p}_j = (\hat{b}_j - \hat{b}_j^\dagger)/2i$ for $j = 1, 2$. In order to describe the squeezing in the produced TMS state, we define new collective quadratures, corresponding to the sum and difference of the original quadrature operators, $\hat{q}_\pm = (\hat{q}_1 \pm \hat{q}_2)/\sqrt{2}$ and $\hat{p}_\pm = (\hat{p}_1 \pm \hat{p}_2)/\sqrt{2}$. Finally, we obtain $\hat{q}_- = e^{-r}\hat{q}_{v1}$ and $\hat{p}_+ = e^{-r}\hat{p}_{v2}$, where $\hat{q}_{v1}$ and $\hat{p}_{v2}$ are the corresponding quadratures of the initial state incident to the squeezer. If this initial state is a vacuum state, we obtain variances of the collective quadratures $(\Delta q_-)^2 = (\Delta p_+)^2 = e^{-2r}/4$ and observe that they are squeezed for any $r > 0$ [16]. We also introduce a two-mode squeezing level S_{TMS} in decibel as the geometric mean of the two squeezed variances

$$S_{\mathrm{TMS}} = -10 \log_{10} \left[\frac{\sqrt{(\Delta q_-)^2 (\Delta p_+)^2}}{0.25} \right] . \tag{4.2}$$

In this way, for ideal TMS states, the two-mode squeezing level is equal to the initially used single-mode squeezing, $S_{\mathrm{TMS}} = S_1 = S_2$. Furthermore, under the assumption of indistinguishable local states, $S_{\mathrm{TMS}} > 0$ implies inseparability of the bipartite states [184–186].

In principle, in order to produce path entanglement, at least one state incident to the beam splitter needs to be nonclassical [183]. Therefore, it is also possible to generate path entanglement by sending only one squeezed state to the beam splitter. However, for such a scenario the resulting state will possess residual local squeezing and, consequently, will be unbalanced. In contrast, a balanced TMS state exhibits no self-correlations and locally looks like a thermal state while preserving strong entanglement between the propagation paths. Such balanced states are crucial for quantum communications as they allow to achieve perfect security.

4.1.2 Balancing of two-mode squeezed states

In order to generate the aforementioned balanced TMS states in an experiment, we use the scheme shown in Fig. 4.1 (a). Two JPAs produce squeezed states with approximately the same squeezing levels $S_1 \simeq S_2$ but orthogonal squeezing angles, $\gamma_1 = 45°$ and $\gamma_2 = 135°$. The states are sent through superconducting coaxial cables to the inputs of a hybrid ring acting as a 50:50 beam splitter. Technical details on the experimental setup are described in Sec. 3.3. We tune both JPA 1 and JPA 2 to working points with the same resonance frequency of $\omega_0/2\pi = 5.43\,\mathrm{GHz}$. We reconstruct the propagating states at the hybrid ring outputs using the reference-state method. In order to do so, we modulate the JPA pumps with pulses from a data timing generator in a four-segment scheme. All segments have a duration of $T = 64\,\mu\mathrm{s}$. Each reconstruction for each pulse is based on 5×10^9 raw samples before demodulation of the signal.

As a first step for the balancing of the TMS states, we estimate the pump powers for each JPA at which the produced squeezed states have roughly the same squeezing level. These pump powers can be found from the points at which the corresponding nondegenerate gains of both JPAs are equal. In Fig. 4.2 (a), we show a partly balanced TMS state when both JPAs are pumped such that a state with a squeezing level of approximately 7.4 dB is incident at the input of the beam splitter. In order to quantify the balancing in the TMS states, we consider the squeezed variances $\sigma^2_{\mathrm{s},i}$ and antisqueezed variances $\sigma^2_{\mathrm{a},i}$ for the local states at the beam splitter output. Here, $i = 1, 2$ denotes path 1 or path 2. For a perfectly balanced state, we expect $\sigma^2_{\mathrm{s},i} = \sigma^2_{\mathrm{a},i}$ and, therefore, define the variance ratio $\sigma^2_{\mathrm{r}} = \sigma^2_{\mathrm{a},1}/\sigma^2_{\mathrm{s},1} \cdot \sigma^2_{\mathrm{a},2}/\sigma^2_{\mathrm{s},2}$ as a measure of the imbalance. Note that σ^2_{r} is unity for a perfectly balanced state and increases with increasing imbalance. For example, we obtain $\sigma^2_{\mathrm{r}} = 1.76$ for the partly balanced state in Fig. 4.2 (a). If we slightly adjust

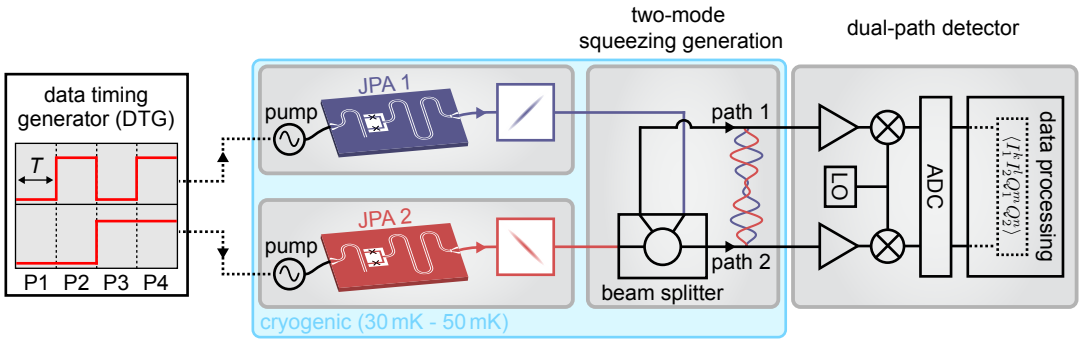

Figure 4.1: Scheme for the generation and reconstruction of TMS states. JPA 1 and JPA 2 produce squeezed states with a similar squeezing level $S_1 \approx S_2$ but orthogonal squeezing angles. The squeezed states are superimposed at a beam splitter in order to produce a TMS state at the outputs. The quantum states are reconstructed at the inputs and outputs of the bean splitter using a dual-path detector. The JPA pumps are modulated with pulses from a data timing generator in a four-segment scheme (P1-P4). Each segment has the same duration T specified in the text. The cryogenic part of the setup is marked with the blue box.

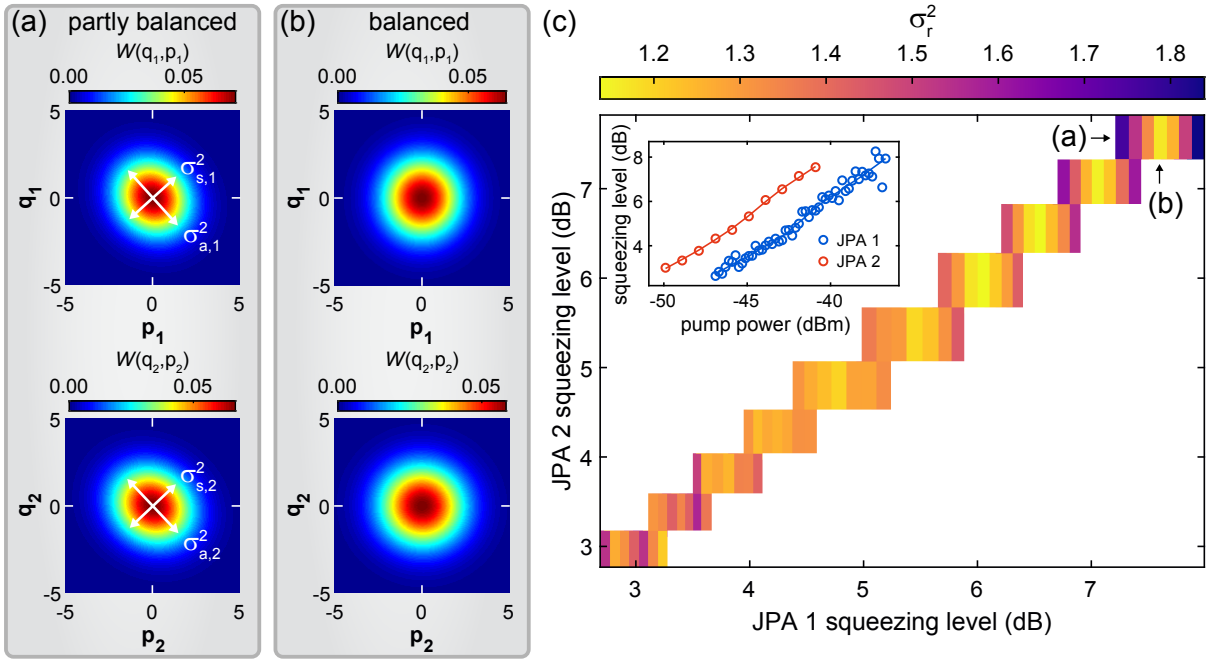

Figure 4.2: (a,b) Local marginal distributions of the Wigner function of a TMS state for path 1 (top) and path 2 (bottom). Panel (a) shows a partly balanced TMS state with residual self-correlations. Panel (b) shows the best balanced state with negligible self-correlations. (c) Variance ratio $\sigma_r^2 = \sigma_{a,1}^2/\sigma_{s,1}^2 \cdot \sigma_{a,2}^2/\sigma_{s,2}^2$ as a function of the squeezing levels of the states produced by JPA 1 and JPA 2. The TMS state is balanced if $\sigma_r^2 = 1$. The inset shows the relation between the JPA squeezing levels reconstructed at the beam splitter inputs and the corresponding pump powers. The JPA resonance frequencies are $\omega_0/2\pi = 5.43\,\mathrm{GHz}$ and the filter bandwidth is $\Omega = 430\,\mathrm{kHz}$

the squeezing level of JPA 1 by increasing the pump power, we obtain a better balancing with $\sigma_r^2 = 1.17$, as shown in Fig. 4.2 (b). In general, we experimentally balance the TMS states by fixing a specific JPA 2 squeezing level and sweep the squeezing level of JPA 1 by adjusting the corresponding pump power. At a specific pump power combination, we obtain a minimum in σ_r^2 which indicates the best balancing for the chosen JPA 2 squeezing level. A measurement for the balancing of TMS states with different squeezing levels is shown in Fig. 4.2 (c). For high squeezing levels, we observe clear minima in σ_r^2 for fixed JPA 2 squeezing. For lower squeezing levels, the minima become less pronounced because the number of photons in the states is lower, decreasing the precision of the reconstruction.

As discussed in Sec. 2.1.2, the TMS state is an entangled bipartite state closely related to the EPR state. We use the negativity kernel N_k to characterize the strength of the path entanglement. This entanglement criterion is based on a partial transpose of the covariance matrix and can be calculated from the covariance matrix of a Gaussian state. We ensure that our experimental states are Gaussian by verifying that the cumulants of order three or higher are vanishingly small. In Fig. 4.3 (a), we show N_k as a function of the initial squeezing of JPA 1 and JPA 2. As expected, the negativity kernel, and therefore the

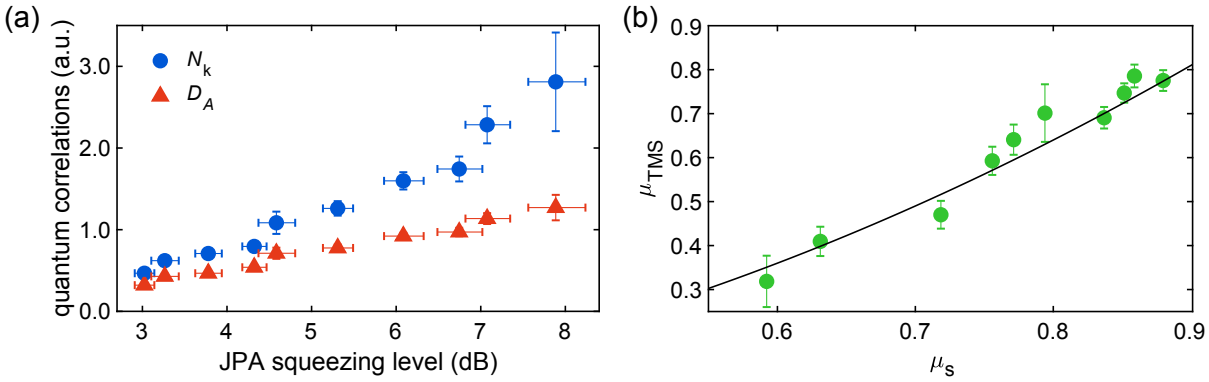

Figure 4.3: (a) Negativity kernel and quantum discord of TMS states for different initial squeezing levels of the states produced by JPA 1 and JPA 2. (b) Purity μ_{TMS} of TMS states as a function of the purity μ_{s} of the initial squeezed states used to generate the TMS state. The JPA resonance frequencies are $\omega_0/2\pi = 5.43\,\mathrm{GHz}$ and the filter bandwidth is $\Omega = 430\,\mathrm{kHz}$. Error bars give the standard error of the mean. The solid line shows $\mu_{\mathrm{TMS}} = \mu_{\mathrm{s}}^2$ expected for a lossless beam splitter.

entanglement strength, increases with increasing squeezing level. Aside from entanglement, there exist more general quantum correlations. These can be quantified by the quantum discord D_A and are particularly interesting for mixed quantum states where entanglement might vanish but other types of nonclassical correlations remain. Similar to N_{k}, quantum discord D_A increases with the squeezing level. We note that for a bipartite system, quantum discord is, in general, not symmetric and two values exist for a given quantum state, as discussed in Sec. 2.1.6. However, for our case of balanced TMS states, both values of quantum discord show the same qualitative behavior. The nonclassical correlations in the propagating TMS states are an essential resource for quantum communication protocols. Since the entangled modes are physically separate, we can straightforwardly link them to distant parties, for example, in order to distribute quantum entanglement for further use. Apart from the strength of the nonclassical correlations, the purity of the TMS states is another important quantity because it quantifies the mixedness, or the contribution of noise, in our states. For an N-mode Gaussian state, the purity is given by

$$\mu = \frac{1}{4^N \sqrt{\det \mathbf{V}}}\,, \tag{4.3}$$

where $\mathbf{V}$ is the covariance matrix of the N-mode Gaussian state. It is unity for a pure state, i.e, a state which fulfills the Heisenberg uncertainty with an equal sign. In Fig. 4.3 (b), we show the purity μ_{TMS} of the generated TMS state as a function of the purity μ_{s} of the initial squeezed states. For a lossless beam splitter, and therefore a unitary entangling operation, $\mu_{\mathrm{TMS}} = \mu_{\mathrm{s}}^2$ would be fulfilled. This dependence is nicely reproduced in our experiments. Consequently, the losses of the hybrid ring only weakly affect the purity of the TMS states.

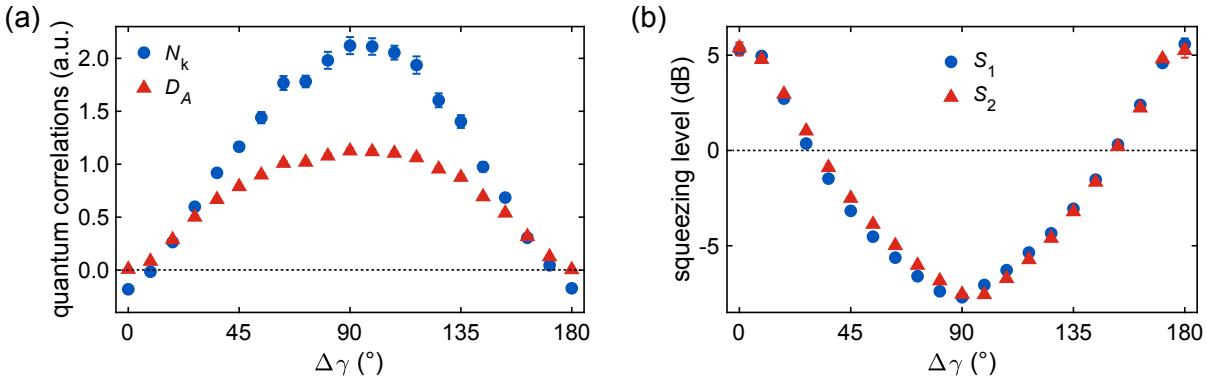

Figure 4.4: (a) Negativity kernel N_k and quantum discord D_A as a function of squeezing angle difference $\Delta\gamma$ between JPA 1 and JPA 2. The dashed line marks the threshold for entanglement ($N_\mathrm{k} > 0$). (b) Local squeezing levels S_i at the hybrid ring outputs for path 1 and path 2. The dashed line marks the threshold for squeezing below vacuum ($S_i > 0$). In both panels, the initial squeezing level is $\simeq 7.4\,\mathrm{dB}$. The squeezed states are centered at a frequency $\omega_0/2\pi = 5.323\,\mathrm{GHz}$ and the filter bandwidth is $\Omega = 820\,\mathrm{kHz}$. If not shown, the standard error of the mean is smaller than the symbol size.

In order to produce a balanced TMS state, the squeezing angles of JPA 1 and JPA 2 need to be orthogonal. If we deviate from this condition, the produced states at the beam splitter outputs are no longer ideal TMS states but exhibit residual single-mode squeezing. In Fig. 4.4 (a), we investigate the effect of a squeezing angle difference $\Delta\gamma$ between JPA 1 and JPA 2 for fixed $\gamma_2 = 135°$. Here, the JPA pumps are modulated by pulses with a duration of $T = 40\,\mu\mathrm{s}$. For $\Delta\gamma = 0$, we observe no entanglement ($N_\mathrm{k} < 0$) and nearly vanishing quantum discord D_A, as expected for parallel squeezing angles. Both N_k and D_A increase up to a maximum at $\Delta\gamma \simeq 90°$. At this squeezing angle difference, the balanced TMS states are produced. On further increasing $\Delta\gamma$, the magnitude of quantum correlations decreases. In Fig. 4.4 (b), the local squeezing levels at the hybrid ring outputs are shown. Here, we observe a maximum squeezing below the vacuum limit for $\Delta\gamma = 0°$. For the case of $\Delta\gamma = 90°$, the states, locally, do not possess any squeezing and look like thermal states. This behavior shows, that it is possible to transfer local squeezing into a nonlocal one (squeezing in collective nonlocal quadratures) and vice versa by changing the relative squeezing angle $\Delta\gamma$ between the incident squeezed state. From another perspective, one can define an invariant for general two-mode Gaussian states which captures both local nonclassicality and quantum correlations between the two modes [187]. The action of a lossless beam splitter allows for an exchange of local and nonlocal correlations while keeping the invariant constant.

4.1.3 Wigner function of two-mode squeezed states

After investigating the magnitude of quantum correlations in TMS states, we now turn to a full tomography of bipartite states at the hybrid ring outputs. For that, we reconstruct

the full Wigner function of the TMS states. The JPA pumps are modulated by pulses with a duration of $T = 40\,\mu$s. The Wigner function depends on four dimensions, corresponding to the quadratures q_1, p_1, q_2 and p_2 in the case of bipartite states, which makes it difficult to visualize. However, the Wigner function can be integrated over two certain quadratures to obtain a marginal distribution which only depends on the two other quadratures. Consequently, there exist six marginal distributions for any bipartite state. Examining the marginal distributions allows us to gain a qualitative understanding of the two-mode squeezing. Figure 4.5 (a) shows the reconstructed local states at the inputs and outputs of the hybrid ring. As expected for a balanced TMS state, we do not observe any self-correlations in the local states at the outputs if two squeezed states with squeezing levels $S_1 \simeq S_2 \simeq 7.9\,\text{dB}$ but orthogonal squeezing angles ($\gamma_1 = 45°$ and $\gamma_2 = 135°$) are incident to hybrid ring. The output states in the self-correlated subspaces $\{q_1, q_2\}$ and $\{q_2, p_2\}$ are thermal states with a mean photon number $n_{\text{th}} = 2.6$. The correlations are only visible in the cross-correlated subspaces $\{q_1, p_2\}$ and $\{p_1, q_2\}$, as depicted in Fig. 4.5 (b). The TMS state is entangled with the strength of entanglement characterized by the negativity kernel $N_{\text{k}} = 2.1$, or the two-mode squeezing level $S_{\text{TMS}} = 7.0\,\text{dB}$. It is also possible to shift the cross-correlations to the other subspaces of the bipartite state while keeping the

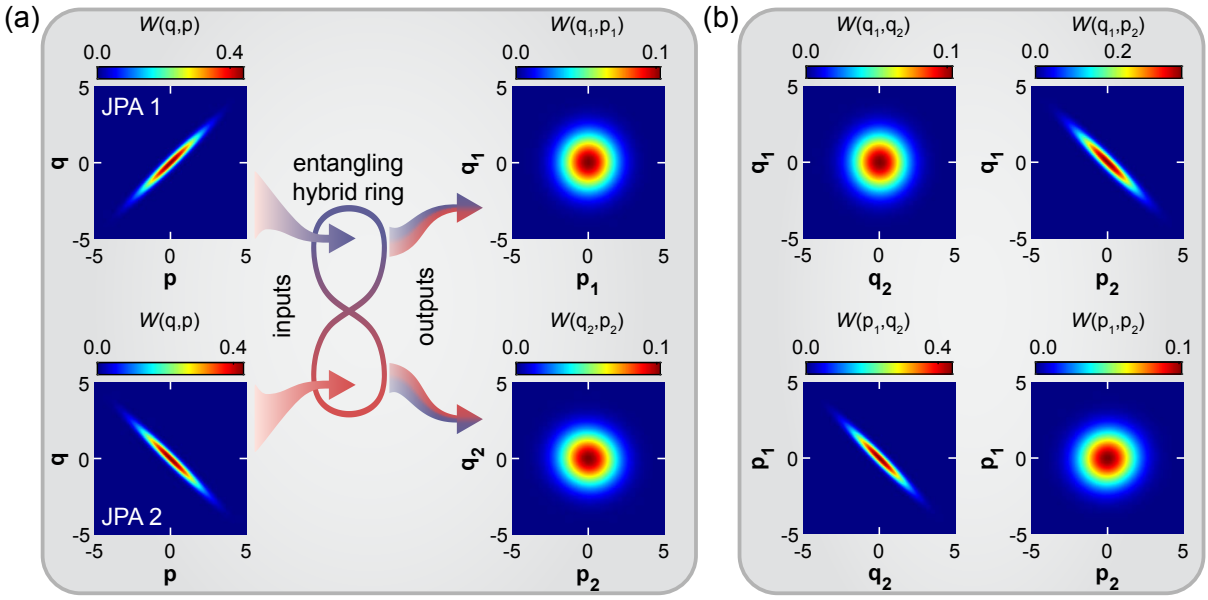

Figure 4.5: Experimental marginal distributions of the Wigner function of a balanced TMS state at the frequency $\omega_0/2\pi = 5.323\,\text{GHz}$. (a) Local states at the hybrid ring inputs and outputs. The incident squeezed states have squeezing levels $S_1 \simeq S_2 \simeq 7.9\,\text{dB}$ and orthogonal squeezing angles $\gamma_1 = \gamma_2 + 90°$. The states at the hybrid ring outputs show no local squeezing and locally correspond to thermal states with a mean photon number $n_{\text{th}} = 2.6$. (b) Marginal Wigner function distributions in the cross-correlated subspace for the TMS state with the negativity kernel $N_{\text{k}} = 2.1$ and the two-mode squeezing level $S_{\text{TMS}} = 7.0\,\text{dB}$. The filter bandwidth is $\Omega = 820\,\text{kHz}$.

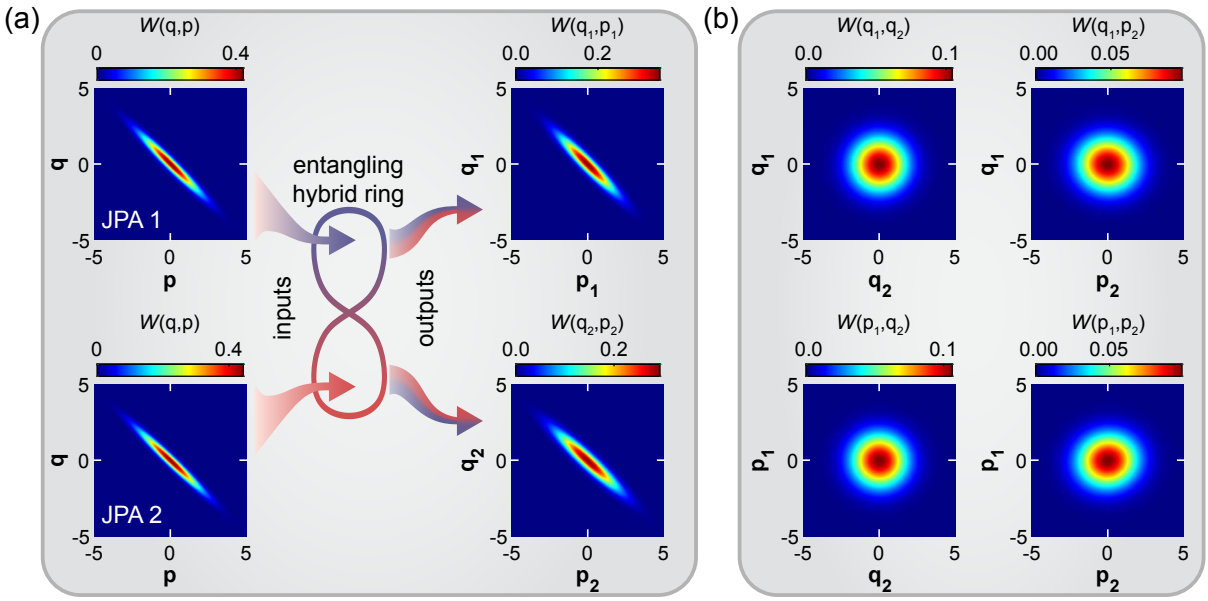

Figure 4.6: Experimental marginal distributions of the Wigner function of the state at the hybrid ring output for the case of two parallel squeezed states at the frequency $\omega_0/2\pi = 5.323\,\mathrm{GHz}$. (a) Marginal Wigner function distributions of local states at the hybrid ring inputs and outputs. The incident squeezed states have squeezing levels $S_1 \simeq S_2 \simeq 7.8\,\mathrm{dB}$ and parallel squeezing angles $\gamma_1 = \gamma_2$. The hybrid ring outputs are locally squeezed. (b) Marginal Wigner function distributions between the outputs show no squeezing in the cross-correlations. The filter bandwidth is $\Omega = 820\,\mathrm{kHz}$.

entanglement strength constant. This can be achieved by a simultaneous rotation of the squeezing angles of both JPA 1 and JPA 2 such that they stay orthogonal to each other.

If the squeezing angles of JPA 1 and JPA 2 deviate from the strict orthogonality, the produced state at the hybrid ring outputs becomes less entangled. In the extreme scenario of parallel squeezing angles $\gamma_1 = \gamma_2$, shown in Fig. 4.6, the resulting state is not entangled at all but only exhibits self-correlations in the form of local squeezing in the output paths. There is no visible correlation in the cross-correlated subspaces. Therefore, the hybrid ring output states are separable and are described by two locally squeezed states.

4.2 Finite-time quantum entanglement in propagating squeezed microwaves

If TMS states are to be used in communication or sensing protocols, it is important to investigate the fragility of their entanglement or other quantum correlations towards time delays in one of the propagating paths in respect to the other. In practice, time delays might appear due to many reasons such as a different electrical length of corresponding paths or different data processing delays at the communicating parties. The effect of

finite-time delays on propagating squeezed states is also interesting from a fundamental point of view since we can gain insight into the underlying physical processes of relative dephasing. Here, we first investigate the second-order correlation function and negativity against time delays of locally squeezed states using our dual-path detector in order to probe temporal correlations in the input states incident to the hybrid ring. Afterwards, we apply a finite-time delay in one of the paths of a propagating TMS state and observe how entanglement and quantum discord are affected by this asymmetric delay in the hybrid ring output states.

Parts of the results presented in this subsection have been published by us in Ref. [39].

4.2.1 Finite-time correlations in single-mode squeezed states

In order to measure the second-order correlation function $g^{(2)}(\tau)$ of squeezed states, we employ the dual-path detector and delay one path relative to the other by τ during the digital data processing as schematically shown in Fig. 4.7. For these measurements, we turn off JPA 2 so that only one squeezed state is incident to the hybrid ring. In this sense, our setup is similar to the Hanbury-Brown-Twiss experiment [86]. As described in Sec. 2.1.7, the second-order correlation function $g^{(2)}(\tau)$ in terms of the signal moments is given by [87]

$$g^{(2)}(\tau) = \frac{\langle \hat{a}^\dagger(0)\hat{a}^\dagger(\tau)\hat{a}(\tau)\hat{a}(0)\rangle}{\langle \hat{a}^\dagger(0)\hat{a}(0)\rangle^2} = \frac{G^{(2)}(\tau)}{G^{(1)}(0)^2}\,, \tag{4.4}$$

where we introduced the first-order correlation function $G^{(1)}(\tau) = \langle \hat{a}^\dagger(0)\hat{a}(\tau)\rangle^2$ and the unnormalized second-order correlation functions and $G^{(2)}(\tau) = \langle \hat{a}^\dagger(0)\hat{a}^\dagger(\tau)\hat{a}(\tau)\hat{a}(0)\rangle$. In order to obtain $G^{(1)}(\tau)$ and $G^{(2)}(\tau)$ from the measured quadrature moments, we apply a variant of the dual-path reconstruction [169, 170, 188]. As in the dual-path reconstruction,

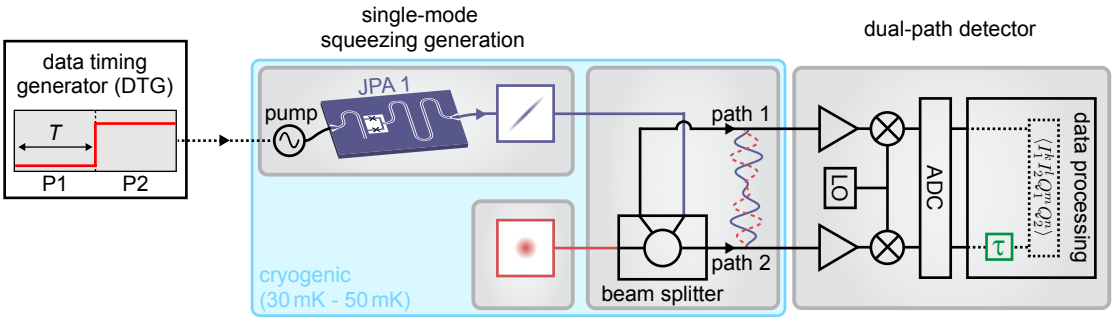

Figure 4.7: Scheme used for measurement of finite-time correlations of squeezed states. Only JPA 1 is used so that a weak thermal state is present at the second input of the hybrid ring acting as beam splitter. A time delay τ is implemented in path 2 during the digital data processing. The pump of JPA 1 is modulated with pulses from a data timing generator in a two-segments scheme (P1-P2). Both segments have the same duration $T = 40\,\mu$s. The cryogenic part of the setup is marked with the blue box.

we utilize the complex envelopes $\hat{S}_{1,2} = (\hat{I}_{1,2} + i\hat{Q}_{1,2})/\sqrt{\kappa_{1,2}}$ of path 1 and path 2, respectively, in order to reconstruct the signal moments of the quantum states in the cryostat from the measured quadrature moments $\langle I_1^n I_2^m Q_1^k Q_2^l \rangle$. Here, $\kappa_{1,2}$ is the photon number conversion factor for path 1 and path 2 referenced to the outputs of the hybrid ring, respectively (cf. Sec. 3.1.4). Then, the first-order correlation function is given by [189]

$$G^{(1)}(\tau) = 2\langle \hat{S}_1^\dagger(0)\hat{S}_2(\tau)\rangle \,. \tag{4.5}$$

Furthermore, we can write the unnormalized second-order correlation function as [189]

$$\begin{aligned} G^{(2)}(\tau) = 4\langle \hat{S}_1^\dagger(0)\hat{S}_2^\dagger(\tau)\hat{S}_2(\tau)\hat{S}_1(0)\rangle - 2G^{(1)}(0)\langle \hat{V}_2(\tau)\hat{V}_2^\dagger(\tau)\rangle - \\ 2G^{(1)}(0)\langle \hat{V}_1(0)\hat{V}_1^\dagger(0)\rangle - 4\langle \hat{V}_1(0)\hat{V}_1^\dagger(0)\rangle\langle V_2(\tau)V_2^\dagger(\tau)\rangle \,, \end{aligned} \tag{4.6}$$

where the first term is related to measured quadratures including the added noise by the amplification chains and the last three terms account for this added noise. The added noise in each path is given by

$$\hat{V}_{1,2} = \sqrt{\frac{1}{G_{1,2}}}\left(\sqrt{G_{1,2}-1}\hat{h}_{1,2} + \hat{m}_{1,2}\right) \,, \tag{4.7}$$

where $G_{1,2}$ and $\hat{h}_{1,2}$ represent the total gain and the added noise of the amplification chains, respectively, and $\hat{m}_{1,2}$ is the added noise of the IQ-mixer in both paths.

First, we set the time delay to $\tau = 0$ and use JPA 1 to produce squeezed states with different squeezing levels S, and, respectively, different photon numbers n. The JPA resonance frequency is set to $\omega_0/2\pi = 5.323\,\text{GHz}$ and the filter bandwidth is $\Omega = 820\,\text{kHz}$. The dual-path detection scheme allows us to calculate $g^{(2)}(0)$ of the input state from

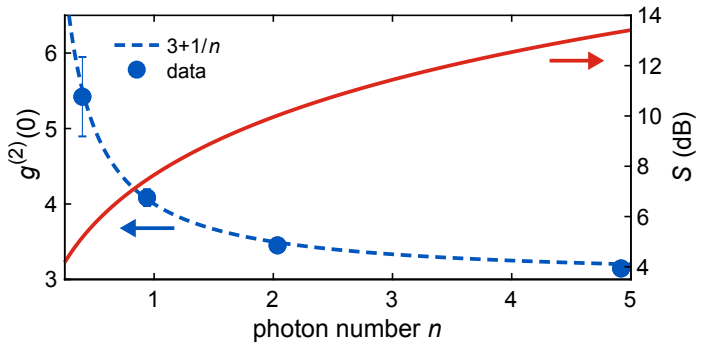

Figure 4.8: Normalized second-order correlation function $g^{(2)}(0)$ of squeezed states at the frequency $\omega_0/2\pi = 5.323\,\text{GHz}$, where n is the photon number $\langle \hat{a}^\dagger \hat{a}\rangle$ of the squeezed states. The dashed line marks the expected behavior of $g^{(2)}(0)$ for a pure squeezed state. The solid line marks the theoretical squeezing level S of a pure squeezed state with photon number n. The filter bandwidth is $\Omega = 820\,\text{kHz}$. If not shown, the standard error of the mean is smaller than the symbol size.

the auto- and cross-correlations of the output paths. Each measurement consists of 6×10^9 raw data samples. In Fig. 4.8, we plot $g^{(2)}(0)$ for a zero time delay between the paths as a function of n. We also show the theoretically expected squeezing level S of a pure squeezed state with photon number n. The dependence of $g^{(2)}(0)$ fits nicely to the expected behavior for a pure squeezed state, $g^{(2)}(0) = 3 + 1/n$ (see Tab. 2.1). In principle, the experimentally realized squeezed states are not pure and possess a non-zero thermal population. We expect $g^{(2)}(0) = 2$ for any thermal state. Therefore, we conclude that the thermal population of the experimental squeezed states only marginally affects the statistics which remains close to the one of a pure squeezed state. We note that $g^{(2)}(0)$ of squeezed states is super-Poissonian and higher than the one of a thermal state. This can be understood by recalling that photons are created in pairs during the parametric process used to generate the squeezed state. Consequently, it is likely to find two photons bunched together which is reflected by $g^{(2)}(0) > 1$.

After investigating the second-order correlation function for a zero time delay, we now proceed with finite-time delays τ in order to probe the temporal envelope of correlations in squeezed states. The experimental parameters are the same as for $\tau = 0$ and the respective results are shown in Fig. 4.9 (a). We observe a super-Poissonian and bunched character of the squeezed states indicated by $g^{(2)}(0) > 1$ and $g^{(2)}(\tau) < g^{(2)}(0)$, respectively. Squeezed states with lower squeezing possess a higher $g^{(2)}(\tau)$. In particular, we can notice a significant scatter in $g^{(2)}(\tau)$ for low squeezing levels. This is caused by low photon numbers of the signal. First, the low photon numbers lead to a low signal-to-noise ratio which increases the scatter in the measured data. Second, $g^{(2)}(\tau)$ is inversely proportional to the photon number and, thus, very sensitive to scatter in the low photon regime. We can theoretically describe our results using [88]

$$g^{(2)}(\tau) = 1 + \mathrm{sinc}^2(\Omega\tau)\frac{1 + 4\sigma_\mathrm{s}^2(2\sigma_\mathrm{s}^2 - 1) + 4\sigma_\mathrm{a}^2(2\sigma_\mathrm{a}^2 - 1)}{(1 - 2\sigma_\mathrm{s}^2 - 2\sigma_\mathrm{a}^2)^2}\,, \tag{4.8}$$

where σ_s^2 and σ_a^2 are the squeezed and antisqueezed variances, respectively, Ω is the smallest bandwidth in the setup, and $\mathrm{sinc}(x) = \sin(\pi x)/(\pi x)$. In our case, the bandwidth is defined by a low-pass FIR filter after digital down-conversion with a filter bandwidth $\Omega = 820\,\mathrm{kHz}$. We model the squeezed states realized in our experiments as single-mode squeezed thermal states, meaning that a small thermal state with a photon number n_th is squeezed. In this case, we can write [190]

$$\sigma_\mathrm{s}^2 = (1 + 2n_\mathrm{th})e^{-2r}/4 \qquad \text{and} \qquad \sigma_\mathrm{a}^2 = (1 + 2n_\mathrm{th})e^{2r}/4\,, \tag{4.9}$$

where r is the squeezing factor of the JPA and n_th is the number of noise photons added by the JPA referred to the input. Using the latter expression for the variances, we can

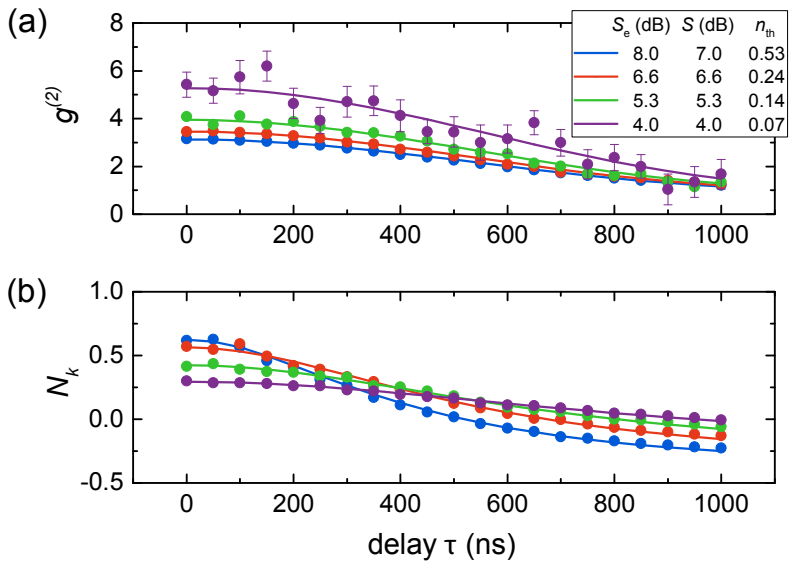

Figure 4.9: (a) Second-order correlation function $g^{(2)}(\tau)$ of squeezed states fitted with Eq. (4.10). (b) Negativity kernel $N_\mathrm{k}(\tau)$ fitted with Eq. (4.11). Symbols depict experimental data and solid lines are the corresponding fits. Fitting parameters are the same for both panels, where S is the fitted squeezing level and n_th is the fitted noise photon number. The squeezed states with experimental squeezing levels S_e are generated at the frequency $\omega_0/2\pi = 5.323\,\mathrm{GHz}$ and the experimental filter bandwidth is $\Omega = 820\,\mathrm{kHz}$. If not shown, the standard error of the mean is smaller than the symbol size. The experimental data in this figure is the same as in Ref. [39].

rewrite Eq. (4.8) as

$$g^{(2)}(\tau) = 1 + \mathrm{sinc}^2(\Omega\tau)\frac{1 - 2(1+2n_\mathrm{th})\cosh(2r) + (1+2n_\mathrm{th})^2\cosh(4r)}{\left[(1+2n_\mathrm{th})\cosh(2r) - 1\right]^2}\,. \tag{4.10}$$

From the latter equation, we observe that r and n_th do not influence the temporal shape of $g^{(2)}(\tau)$ but only define the value at zero delay $g^{(2)}(0)$. The temporal shape of $g^{(2)}(\tau)$ is solely defined by the filter bandwidth Ω. We note that we approximate the digital FIR filter with an ideal low-pass filter, i.e. a filter with a sharp cut-off frequency in Eqs. (4.8) and (4.10), which results in the sinc-dependence versus τ. From fitting of Eq. (4.10) to our experimental data, we obtain a fitted filter bandwidth $\Omega_\mathrm{fit} \simeq 750\,\mathrm{kHz}$ which coincides well with the FIR filter bandwidth $\Omega = 820\,\mathrm{kHz}$. The fits and resulting parameters are summarized in Fig. 4.9 (a).

Even though the second-order correlation function provides information about the statistics of propagating quantum microwaves, it does not reveal directly whether or not quantum correlations exist between the outputs of the hybrid ring. In order to obtain this information, we directly measure the finite-time behavior of quantum entanglement between the output paths of the hybrid ring. As before, we use the negativity kernel N_k to quantify the strength of entanglement but now include a time delay in one path to obtain $N_\mathrm{k}(\tau)$. For our general scenario of two squeezed states incident to a beam splitter,

we can write for the negativity kernel of the resulting TMS state [39]

$$N_{\mathrm{k}}(\tau) = -\frac{1}{2} + \frac{1}{2\left\{(n_1-n_2)^2 + \tilde{n}C + [\tilde{n}C - (n_1+n_2+1)^2]\mathrm{sinc}^2(\Omega\tau) - \tilde{n}D|\mathrm{sinc}(\Omega\tau)|\right\}^{1/2}}, \tag{4.11}$$

where $\tilde{n} \equiv (1+2n_1)(1+2n_2)$, $C \equiv \cosh^2(r_1+r_2)$, $D \equiv \sinh(2r_1+2r_2)$. Here, r_1 (r_2) and n_1 (n_2) are the squeezing factor and noise photon number of the squeezed state produced by JPA 1 (JPA 2), respectively. We set $r_2 = n_2 = 0$ and $n_1 = n_{\mathrm{th}}$ for the case of a single squeezed state incident to the hybrid ring. The experimentally obtained values and fits of $N_{\mathrm{k}}(\tau)$ for a single squeezed state incident to the hybrid ring are depicted in Fig. 4.9 (b). In contrast to $g^{(2)}(\tau)$, where only Ω defines the temporal shape, we observe a clear dependence of $N_{\mathrm{k}}(\tau)$ on the squeezing level $S = -10\log_{10}[(1+2n_{\mathrm{th}})e^{-2r}]$. The maximum delay τ_{d}, at which entanglement is still present in the bipartite state, decreases with increasing squeezing level. This observation can be intuitively understood by considering that the correlations in squeezed states exist between photon pairs generated during the parametric process inside the JPA. With an increased squeezing level, the number of such correlated photon pairs in the state is increased. Consequently, a time delay in one path will cause a temporal overlap of uncorrelated photons leading to vanishing entanglement. However, for states with lower squeezing, the density of photon pairs is lower. Consequently, uncorrelated photons only overlap after a bigger time delay when compared to a scenario with high density of photons. From the fit, we observe that the noise n_{th} added by the JPA increases for higher squeezing levels S_{e}. This effect can be explained by stronger required pump powers to reach these values of S_{e}. Consequently, the microwaves fields inside the JPA increase. This can cause higher-order effects [177] and lead to an increased coupling to loss channels which ultimately lead to an increase of n_{th}.

4.2.2 Entanglement strength versus delay in two-mode squeezed states

We now use both JPA 1 and JPA 2 to produce balanced TMS states after the hybrid ring, as described in Sec. 4.1. In this way, we can reach higher entanglement strengths and avoid residual local squeezing in the paths. The experimental scheme is depicted in Fig. 4.10. The experimentally measured dephasing of TMS states for different input squeezing levels and two filter bandwidths, 430 kHz and 820 kHz, is shown in Fig. 4.11. We find an excellent agreement between the experiment and fit. For fitting, we use Eq. (4.11) under the assumption of equal squeezing factors $r_1 = r_2 = r$ and equal noise photon numbers $n_1 = n_2 = n_{\mathrm{th}}$ of both JPAs. The bandwidth Ω is taken to be the corresponding FIR bandwidth, such that only the parameters r and n_{th} are fitted. We again observe a strong dependence of the dephasing time τ_{d} on the initial squeezing level, similar to the case with a single squeezed state incident to the hybrid ring. With a higher initial squeezing

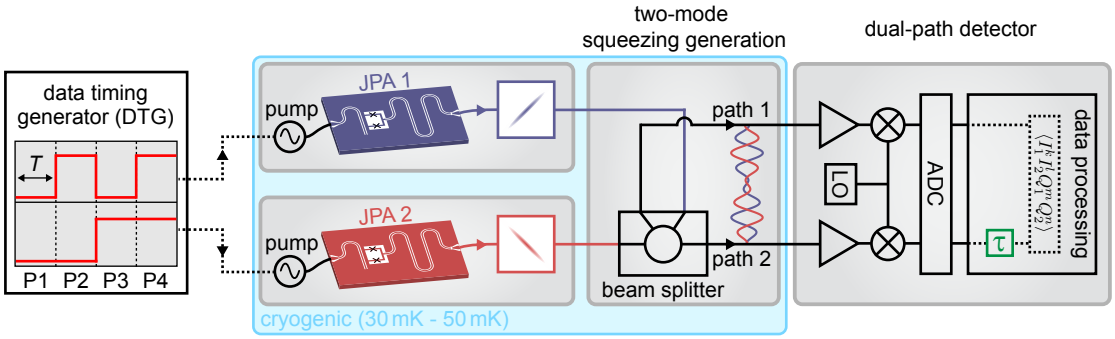

Figure 4.10: Scheme for measurement of finite-time correlations of TMS states. A time delay τ is realized in path 2 during the digital data processing. The JPA pumps are modulated with pulses from a data timing generator in a four-segment scheme (P1-P4). Each segment has the same duration $T = 40\,\mu$s. The cryogenic part of the setup is marked with the blue box.

level, and accordingly a larger negativity kernel, the entanglement vanishes faster in time corresponding to shorter τ_d. Additionally, we note that increasing the filter bandwidth Ω also leads to a decrease in the dephasing time τ_d as larger bandwidths correspond to shorter times in time domain. Both of these effects are captured by Eq. (4.11). In the extreme case of an absent digital filter, we would be limited by the JPA bandwidth which is on the order of $\Delta f \simeq 5\,$MHz in our case. These observations imply that for applications of propagating microwave TMS states in quantum communication protocols, one might need to balance the entanglement strength as well as the bandwidth against possible time delays.

Furthermore, for application scenarios, the maximal rate of transferred entangled bits (ebits) is an important quantity. We can estimate this rate by quantifying the entanglement of the TMS state in terms of the entanglement of formation E_F for which a lower bound can be calculated under the assumption of Gaussian states [191]. For $E_\mathrm{F} = 1$, the entanglement in a TMS state corresponds to one pair of maximally entangled qubits [192, 193]. Without a digital filter, we obtain $E_\mathrm{F} = 0.86$, corresponding to $N_\mathrm{k} = 1.08$, in the bandwidth Δf defined by the JPA bandwidth. Consequently, we arrive at the upper bound on the possible entangled bit-rate of $4.3 \times 10^6\,\mathrm{ebits} \cdot \mathrm{s}^{-1}$. This number sets a maximum on the information transfer capacity of any quantum communication protocol exploiting these particular propagating microwave TMS states as the entangled resource.

4.2.3 Quantum discord versus delay in two-mode squeezed states

Apart from the finite-time behavior of entanglement in TMS states, we can also investigate the temporal dependence of quantum discord. Here, we use the same measurement data as presented in the last subsection and use Eq. (2.43) to calculate quantum discord D_A from the measured covariance matrix $\mathbf{V}$ of propagating TMS states. As shown in Fig. 4.12, we observe a similar behavior of $D_A(\tau)$ when compared to $N_\mathrm{k}(\tau)$. In both

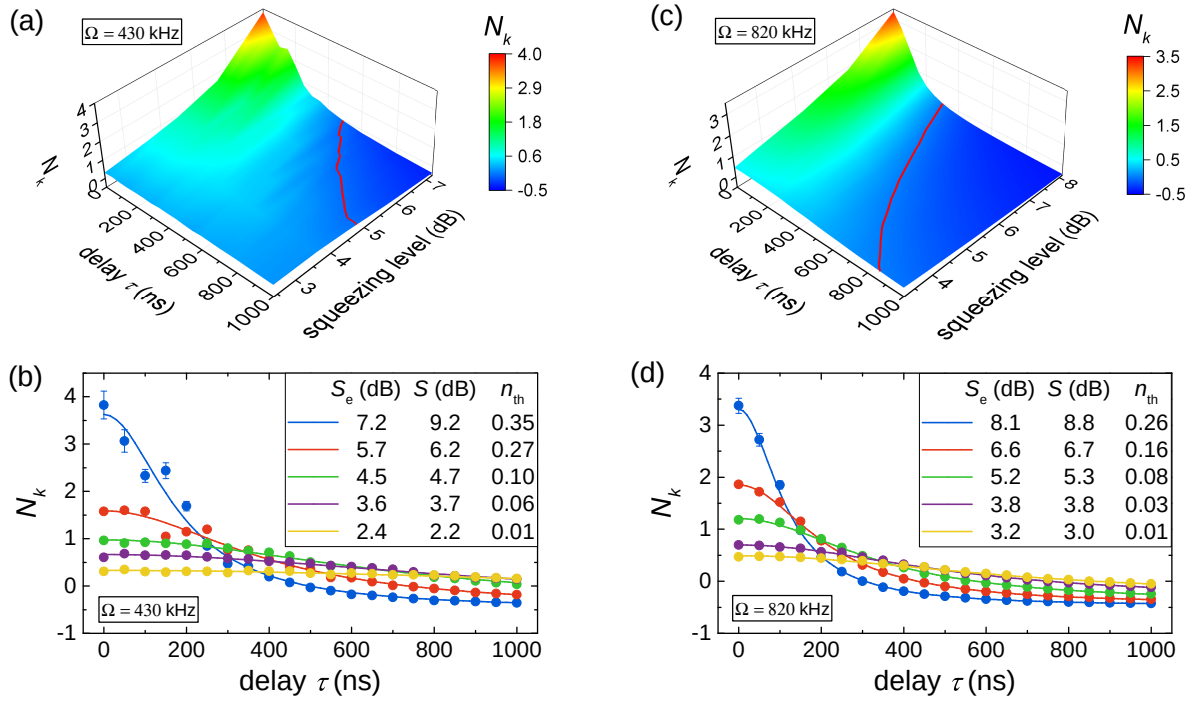

Figure 4.11: Negativity kernel $N_\mathrm{k}(\tau)$ with a finite-time delay τ in path 2 of the dual-path detector. Panels (a,b) and (c,d) show data for a filter bandwidth of $\Omega = 430\,\mathrm{kHz}$ and $\Omega = 820\,\mathrm{kHz}$, respectively. Red lines mark the boundary between entangled ($N_\mathrm{k} > 0$) and separable ($N_\mathrm{k} < 0$) regions. Symbols in panels (b,d) mark experimental data and solid lines are the corresponding fits using Eq. (4.11). S is the fitted squeezing level and n_th is the fitted noise photon number. S_e is the experimental squeezing level of JPA 1 and JPA 2 at the frequency $\omega_0/2\pi = 5.323\,\mathrm{GHz}$. If not shown, the standard error of the mean is smaller than the symbol size. The experimental data in this figure is the same as in Ref. [39].

cases, the quantum correlations decrease with increasing τ. Also, higher initial quantum correlations and a larger bandwidth cause a faster decay of the correlations. However, one important difference is that here there exists no finite dephasing time τ_d for quantum discord D_A. We observe $D_A > 0$ for all measured time delays τ. Consequently, quantum discord is asymptotically resilient to finite-time delays which makes it a promising resource in quantum communication tasks. In order to theoretically describe our results, we use the formalism described in detail in the supplementary material of Ref. [39]. Then, the covariance matrix of a TMS state with a delay of τ in one path is given by

$$\mathbf{V} = \frac{1+2n_\mathrm{th}}{4}\begin{pmatrix} \cosh 2r & 0 & \mathrm{sinc}(\Omega\tau)\sinh 2r & 0 \\ 0 & \cosh 2r & 0 & -\mathrm{sinc}(\Omega\tau)\sinh 2r \\ \mathrm{sinc}(\Omega\tau)\sinh 2r & 0 & \cosh 2r & 0 \\ 0 & -\mathrm{sinc}(\Omega\tau)\sinh 2r & 0 & \cosh 2r \end{pmatrix}, \tag{4.12}$$

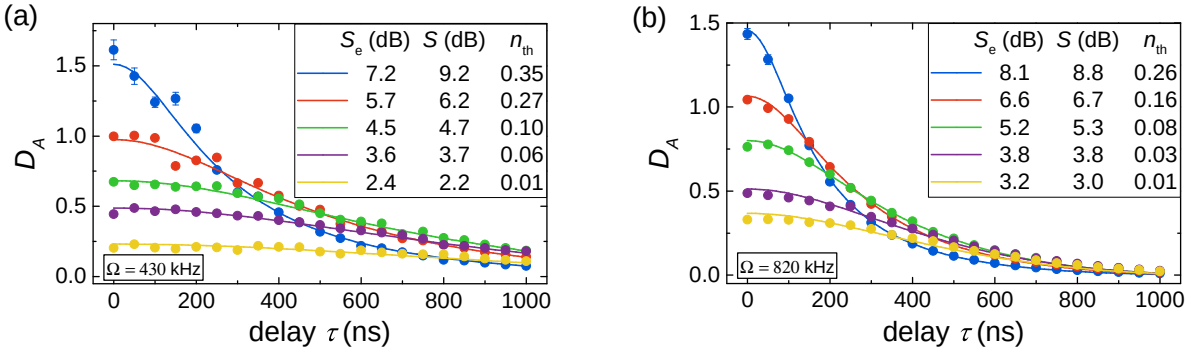

Figure 4.12: Quantum discord $D_A(\tau)$ with a finite-time delay τ in path 2. Panels (a) and (b) show data for a filter bandwidth of $\Omega = 430\,\text{kHz}$ and $\Omega = 820\,\text{kHz}$, respectively. Symbols mark experimental data and solid lines are the corresponding fits. S is the fitted squeezing level and n_{th} is the fitted noise photon number. S_e is the experimental squeezing level of JPA 1 and JPA 2 at the frequency $\omega_0/2\pi = 5.323\,\text{GHz}$. If not shown, the standard error of the mean is smaller than the symbol size. Fitting parameters are the same as for the corresponding data in Fig. 4.11.

where Ω is the bandwidth and we assume equal squeezing factors $r_1 = r_2 = r$ and noise photon numbers $n_1 = n_2 = n_{\text{th}}$ for JPA 1 and JPA 2. Furthermore, we use orthogonal squeezing angles, $\gamma_1 = 0$ and $\gamma_2 = 90°$. Note, that Eq. (4.12) is in the standard form of a covariance matrix of a Gaussian state. Any covariance matrix of a Gaussian state can be transformed into such a standard form [75]. Also, other orthogonal combinations of squeezing angles of JPA 1 and JPA 2, $\gamma_1 = \gamma_2 + 90°$, would influence the entries in the covariance matrix which encode the cross-correlations while the local states in both paths remain unchanged. However, the strength of quantum correlations is not influenced by different γ_i as long as they are orthogonal. This fact allows us to fit D_A with the generic covariance matrix given in Eq. (4.12). Again, only r and n_{th} are fitted since we set the bandwidth Ω to the FIR filter bandwidth. We observe an excellent agreement between experiment and theory for both experimental filter bandwidths. The theory confirms the asymptotic behavior of quantum discord against finite-time delays.

4.3 Two-mode squeezed states in a noisy environment

In the last subsection of this chapter, we investigate propagating microwave TMS states in noisy environments. The entanglement behavior of propagating microwave states under the effect of external noise has not been experimentally studied before. A temperature of 350 mK corresponds to a thermal population of one photon at 5 GHz. Since it is technologically demanding to achieve cryogenic temperatures around hundred millikelvin over long distances, the effect of noise on the quantum correlations in TMS states is very relevant for applications of propagating microwaves in quantum communication. Furthermore, the robustness of quantum correlations against environmental noise is

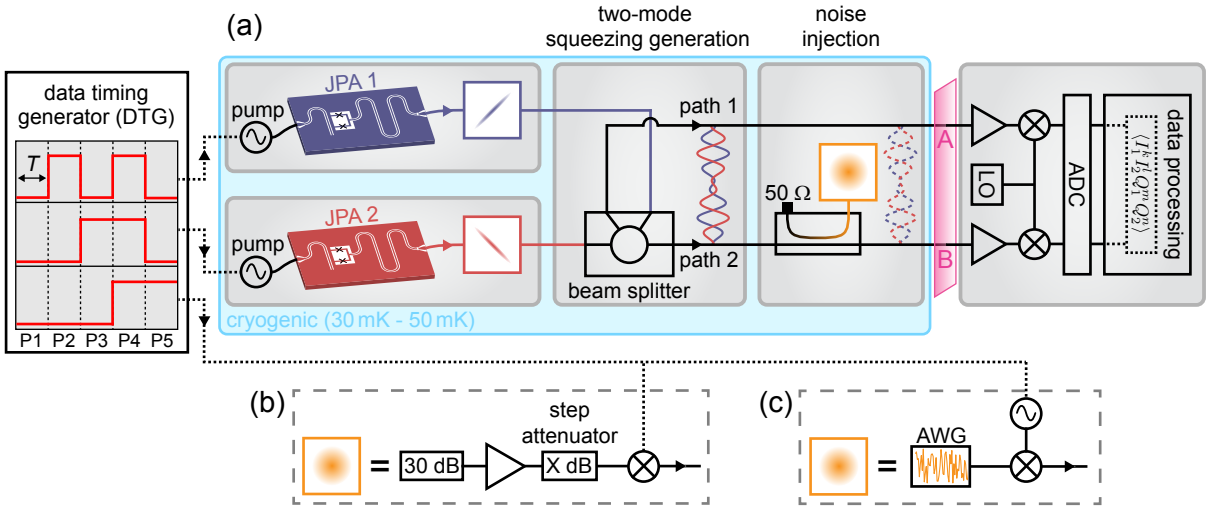

Figure 4.13: (a) Scheme for asymmetric noise injection into one path of a TMS states. The JPA pumps are modulated with pulses from a data timing generator in a five-segment scheme (P1-P5). Segments P1-P4 have the same duration $T = 40\,\mu$s and segment P5 has a duration of $T = 34\,\mu$s. The noise is generated at room temperature by either (b) amplified thermal radiation of a 30 dB attenuator or (c) an arbitrary-waveform generator (AWG). The noise is either pulsed directly with a mixer [panel (b)] or via the up-conversion signal [panel (c)]. The cryogenic part of the setup is marked with the blue box.

interesting for fundamental studies of the physical natural of quantum correlations.

We use the scheme shown in Fig. 4.13 (a) where balanced TMS states are subject to injected noise in one path. This scenario could be relevant for quantum communication protocols where one part of the TMS states is stored locally in a quantum memory and the other one is sent over a noisy channel. In our experiments, the noise is generated in two distinct ways. In the first method, we employ a 30 dB attenuator, whose temperature is stabilized to $\simeq 20\,^{\circ}$C, to act as a black body radiator. The emitted thermal radiation is subsequently amplified and filtered before it is sent into the cryostat. We control the mean number of injected noise photons n_{n} with a step attenuator after amplification at room temperature. In the second method, we use an arbitrary waveform generator (AWG) to generate synthesized noise with a specified bandwidth of 160 MHz and an approximate Gaussian amplitude distribution with a specified crest factor of 7.0. The crest factor defines the ratio of the peak amplitude to the root-mean-squared amplitude of the waveform. The noise is up-converted to our reconstruction frequency $\omega_0/2\pi = 5.323\,$GHz with a local oscillator at frequency $\omega_{\mathrm{LO}}/2\pi = 5.354\,$GHz and filtered before it is sent into the cryostat. We detune the local oscillator from ω_0 such that the spurious local oscillator signal after the mixer is filtered by the FIR filter during the digital data processing. Both methods are depicted Fig. 4.13 (b,c). In the cryostat, the noise is coupled to one path of a TMS state by a directional coupler with a coupling ratio of $\beta \simeq -20\,$dB.

First, we experimentally confirm that we can add noise to path 2 using the two described

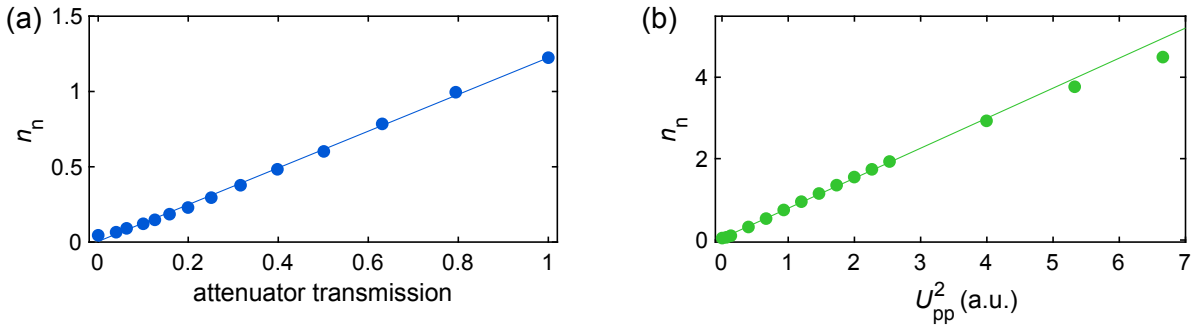

Figure 4.14: (a) Added thermal photons n_n as a function of step-attenuator transmission. (b) Added noise photons n_n from synthesized noise as a function of squared peak-to-peak voltage U^2_{pp}. Symbols mark experimental data and solid lines are linear fits.

methods above. We achieve this by applying different noise powers to the coupled port of the directional coupler and reconstructing the resulting state in path 2. In Fig. 4.14 (a), we observe a clear linear dependence of the added thermal noise photons n_n in path 2 after the directional coupler on the step attenuator transmission. Furthermore, we measure $g^{(2)}(0) = 2.06 \pm 0.08$ of the corresponding noise state which, within the error bar, coincides with the expected second-order correlation function of a thermal state, $g^{(2)}_{th}(0) = 2$ (see Tab. 2.1). Due to the strong attenuation inside the cryostat, we are only able to inject $n_n \lesssim 1.2$ noise photons to path 2. Using the AWG to generate synthesized noise, we can reach higher photon numbers, as shown in Fig. 4.14 (b). The dependence between reconstructed photons n_n and squared peak-to-peak voltage U^2_{pp} of the generated noise is linear up to $n_n \simeq 3$. For higher values, the added n_n stays below the linear trend which is most likely attributed to compression effects during the frequency up-conversion of the noise. Additionally, we find $g^{(2)}(0) = 1.92 \pm 0.02$ which is lower than the expected value for Gaussian noise. We attribute the slightly lower value of $g^{(2)}(0)$ to the fact that the synthesized noise is not perfectly Gaussian as a result of the finite crest factor of 7.0 which should be infinite for a perfect Gaussian distribution.

After confirming that we can add noise to path 2, we now use both JPA 1 and JPA 2 in order to investigate propagating microwave TMS states as a function of the mean number of injected noise photons. The filter bandwidth for these measurements is $\Omega = 430\,\mathrm{kHz}$. Figures 4.15 and 4.16 show the measured effect of added thermal noise and synthesized noise to the TMS state, respectively. We again quantify the strength of entanglement by the negativity kernel N_k. Interestingly, for any initial entanglement strength, the entanglement vanishes for $n_n \simeq 1$. This phenomenon is called sudden death of entanglement and has been originally found for qubit states [194, 195]. Later, the sudden death of entanglement has been theoretically investigated also for Gaussian states [196]. However, no experimental evidence for sudden death of entanglement in Gaussian microwave states has been reported so far. For TMS states, the entanglement manifests in strong cross-correlations between certain quadratures in both paths. In order for entanglement to occur, these correlations

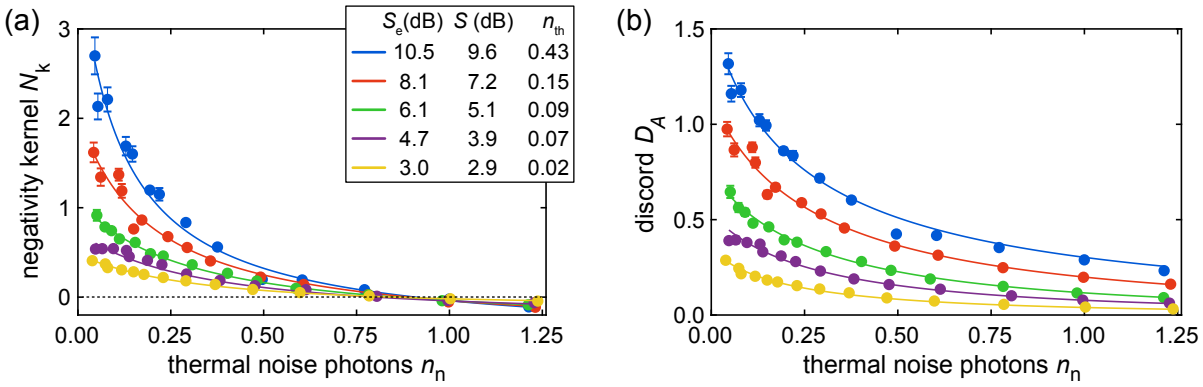

Figure 4.15: (a) Negativity kernel N_k and (b) quantum discord D_A as a function of added thermal noise to path 2 of a propagating TMS state at the frequency $\omega_0/2\pi = 5.323\,\mathrm{GHz}$. The filter bandwidth is $\Omega = 430\,\mathrm{kHz}$. Symbols mark experimental data and solid lines are fits. Fitting parameters are the same for both panels. S is the fitted squeezing level and n_th is the fitted noise photon number. If not shown, the standard error of the mean is smaller than the symbol size.

need to have a certain strength when compared to the variances of the local states. The injection of noise in one path via a directional coupler only marginally influences the strength of cross-correlations but increases the local variance in path 2 proportional to the injected noise photons. If the local variance is increased too much by the noise, when compared to the cross-correlations, entanglement vanishes. For our case of injected noise into one path of a propagating TMS state, this sudden death of entanglement occurs at $\simeq 1$ injected noise photon even though the noise is added gradually and the TMS state asymptotically loses its purity. In contrast, we find that quantum discord D_A does not vanish at a specific added noise photon number but is asymptotically resistant to noise. This property of quantum discord makes it a very intriguing resource for certain types of quantum communication protocols. This asymptotic robustness of quantum discord against environmental influences has also been predicted theoretically [196, 197] whereas experimental evidence for Gaussian microwave states is missing in literature. Furthermore, TMS states with initially higher values of D_A remain higher under the addition of noise. We also note that both investigated noise types have a similar influence on N_k and D_A.

In order to theoretically describe our results, we use a similar approach as in the derivation of Eq. (4.12). The injection of noise in path 2 after the hybrid ring is modeled by an asymmetric beam splitter with input-output relations given in Eq. (2.110). The asymmetric beam splitter describes the action of the directional coupler which is used in the experiments for the purpose of adding noise to path 2. Again, under the assumption of equal parameters of JPA 1 and JPA 2, $r_1 = r_2 = r$ and $n_1 = n_2 = n_\mathrm{th}$, but orthogonal squeezing angles, $\gamma_1 = 0$ and $\gamma_2 = \pi/2$, we obtain the covariance matrix after the injection

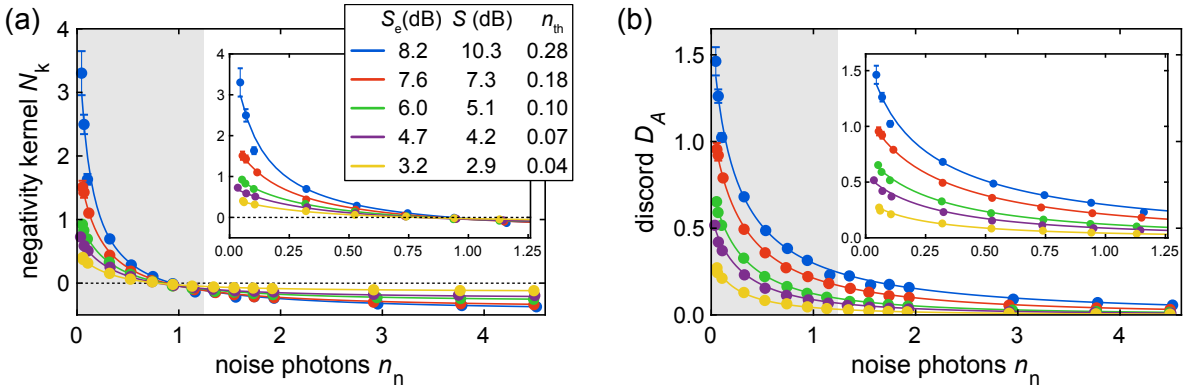

Figure 4.16: (a) Negativity kernel N_k and (b) quantum discord D_A as a function of synthesized noise added to path 2 of a propagating TMS state at the frequency $\omega_0/2\pi = 5.323\,\mathrm{GHz}$. The filter bandwidth is $\Omega = 430\,\mathrm{kHz}$. Symbols mark experimental data and solid lines are linear fits. Fitting parameters are the same for both panels. S is the fitted squeezing level and n_th is the fitted noise photon number. If not shown, the standard error of the mean is smaller than the symbol size. The insets show a zoom-in with the same range as in Fig. 4.15.

of noise in path 2 in the form

$$\mathbf{V} = \begin{pmatrix} \mathbf{A} & \mathbf{C} \\ \mathbf{C}^\mathrm{T} & \mathbf{B} \end{pmatrix}, \tag{4.13}$$

where

$$\mathbf{A} = \frac{(1+2n_\mathrm{th})\cosh 2r}{4}\,\mathbb{I}_2\,, \quad \mathbf{B} = \frac{(1+2n_\mathrm{th})\tau\cosh 2r + (1+2\tilde{n})(1-\tau)}{4}\,\mathbb{I}_2\,, \quad \mathbf{C} = \frac{(1+2n_\mathrm{th})\sqrt{\tau}\sinh 2r}{4}\,\mathbb{I}_2\,. \tag{4.14}$$

Here, $\tau = 0.99$ is the transmissivity of the directional coupler, and $\tilde{n}$ is the noise photon number at the input of the coupled port of the directional coupler. The added noise photons to path 2 are given by $n_n = (1-\tau)\tilde{n}$. We now use Eq. (4.13) to simultaneously fit the experimentally measured negativity kernel and quantum discord. We obtain a good quantitative agreement between data and theory [198]. However, in particular for the highest squeezing level, the experimental squeezing level S_e and fitted squeezing level S deviate from each other. This observation can be explained by the fact that the statistical errors of S_e, N_k and D_A are increased for increasing squeezing levels which can lead to a mismatch between experiment and theory.

Summary

In conclusion, we have studied the generation of balanced TMS states and investigated the effect of finite-time delays as well as environmental noise on the TMS states in this chapter. For the generation of TMS states, we have employed two JPAs producing squeezed states with orthogonal squeezing angles and a hybrid ring. The reconstruction of the bipartite

quantum states in terms of the signal moments, has allowed us to perform full tomography of the TMS states and determine their bipartite Wigner functions and their covariance matrices. Subsequently, one path of the TMS states is delayed by a finite time to probe the relative dephasing in propagating microwave TMS states. We discover a clear effect of the squeezing level as well as the detection bandwidth on the maximally acceptable time delay until the TMS states become disentangled. Furthermore, we have studied asymmetric noise injection in the TMS states and have found that entanglement always vanishes after injection of approximately one noise photon, independent of the initial entanglement strength. In addition, we have studied more general quantum correlations, quantified by quantum discord, under the effect of finite-time delays and injected noise. Here, an asymptotic robustness of quantum discord has been observed.

Chapter 5

Remote state preparation of squeezed microwave states

In this chapter, we focus on remote state preparation (RSP) which is a fundamental quantum communication protocol. In RSP, the goal is to prepare a known quantum state at a distant location by employing entanglement and classical communication. In Sec. 5.1, we show a successful implementation of deterministic RSP in the microwave regime with continuous variables. In our approach, we utilize propagating two-mode squeezed microwave states as the entangled resource. In Sec. 5.2, we investigate quantum correlations in RSP and present the evolution of correlations during the protocol. Finally, we connect our scheme to the secure one-time pad and show how one can securely transmit quantum states using RSP in Sec. 5.3.

5.1 Quantum remote state preparation of propagating microwaves

In this section, we realize deterministic continuous-variable RSP by creating Gaussian squeezed states with adjustable squeezing level and squeezing angle over a macroscopic distance of 35 cm. We investigate the phase space of remotely preparable squeezed states and find a good agreement with our model calculations based on the input-output formalism. Since the generation and manipulation of Gaussian states is well understood [15], they offer a viable option for building future intracity low-temperature quantum networks [199].

The results presented in this section have been published by us in Ref. [47]. Parts of the text and figures are adapted from this reference.

5.1.1 Background and experimental realization

In quantum technologies, an efficient and secure exchange of quantum information between quantum nodes in a network plays a crucial role [143] as already discussed in Sec. 2.3. One of the first protocols realizing such a task was quantum teleportation, where an unknown

quantum state is safely transferred from one party to another by using a pre-shared entangled resource and classical communication [44, 134]. In a slightly different scenario, where one party has full classical knowledge about a to-be-communicated quantum state, remote state preparation (RSP) can be used to remotely create this quantum state by employing similar tools as in quantum teleportation [40–43]. As compared to the best known classical methods, both protocols provide a quantum advantage as they require a smaller amount of classical information in the feedforward signal in order to communicate a desired quantum state [132]. However, in contrast to quantum teleportation, RSP allows for a nontrivial trade-off between the amount of classical communication and entanglement necessary for a successful protocol [42]. Furthermore, the use of an entangled resource allows RSP to operate perfectly secure [132]. RSP is already extensively investigated both theoretically and experimentally for discrete-variable systems [200–202]. However, for continuous-variable systems, only conditional schemes have been experimentally implemented [45, 46] which means that deterministic implementations with continuous-variables are still lacking. At the same time, quantum communication based on continuous-variables is a field of intense research [15, 16] investigating, e.g., quantum key distribution [20], quantum teleportation [17, 18], dense coding [21], and free-space quantum communication [22].

The majority of the previously mentioned implementations have been performed in the optical domain. On the other hand, quantum communication in the microwave domain is motivated by the tremendous progress in the area of quantum information processing with superconducting circuits. In particular, the development of superconducting multi-qubit processors [203, 204], operated at gigahertz frequencies has been highly successful. In our work, we promote an approach of quantum communication directly in the microwave regime based on propagating squeezed states. Since these states have the same frequency and are generated by technology platforms already used for superconducting quantum computers, there is no mismatch between communication and data processing units. This approach is expected to be useful for short and medium distances, where superconducting waveguides can be used.

In contrast to already demonstrated quantum state transfer protocols for discrete-variable systems with superconducting circuits [12, 13], our protocol does not directly send an existing target quantum states to a receiving party. Instead, in RSP, the final squeezed state only appears at the receiving party. Furthermore, entanglement is required for a successful remote preparation of a quantum state, whereas in quantum state transfer, the target quantum state is directly sent via a quantum channel without the requirement of any entanglement. In addition, the preshared entanglement in RSP enables the secure communication between parties.

A scheme of our experimental implementation of RSP using continuous-variable microwave states is depicted in Fig. 5.1 (see also Ref. [205]). We use flux-driven Josephson parametric amplifiers (JPAs) as the key elements for the generation and manipulation

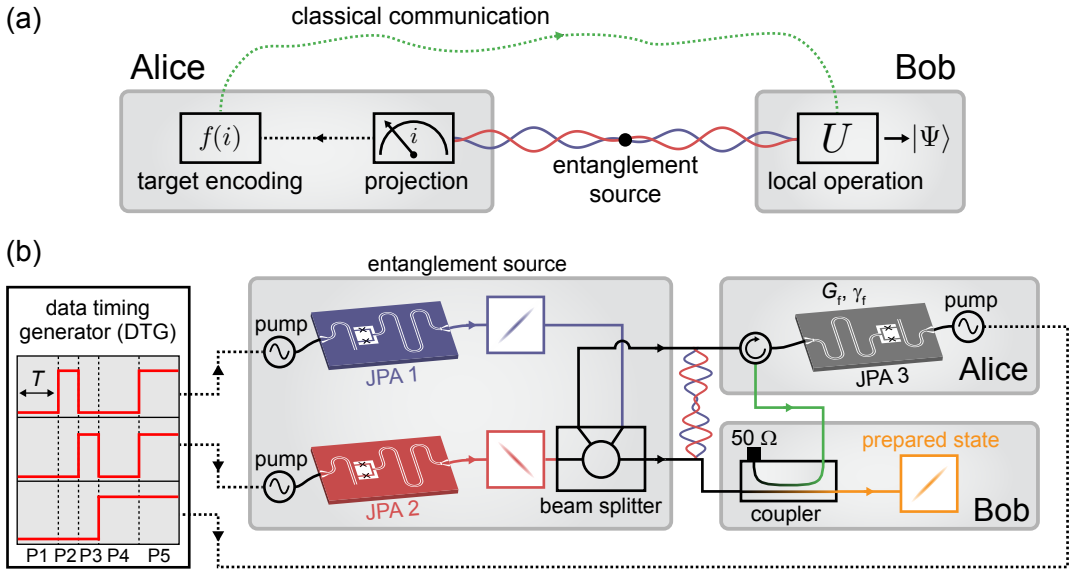

Figure 5.1: (a) General scheme for RSP. Alice performs a projective measurement on her part of an entangled state and uses the measurement result to encode the known target state $|\Psi\rangle$ in a feedforward signal (classical communication). Bob obtains the target state by applying a unitary local operation on his part of the entangled state using the feedforward signal. (b) Schematic of experimentally implemented RSP using propagating microwaves. A two-mode squeezed state serves as entangled resource. Alice decides on the prepared state by adjusting the degenerate gain G_f and amplification angle γ_f of JPA 3. The feedforward is finalized with a directional coupler on Bob's side. The JPA pumps are modulated with pulses from a data timing generator in a five-segment scheme (P1-P5). Segments P2-P4 serve for the stabilization of the squeezing angles of JPA 1-JPA 3, respectively. All JPAs are turned on in segment P5. Segments P1, P4, P5 have a duration $T = 160\,\mu$s and P2, P3 have duration $T = 80\,\mu$s.

of squeezed microwave states [107, 108, 113]. We operate all JPAs in the degenerate regime at the frequency $\omega_0/2\pi = 5.435\,$GHz with a pump frequency $\omega_\mathrm{p} = 2\omega_0$. The task of JPA 1 and JPA 2 is to generate propagating squeezed states which are incident to an entangling beam splitter. The resulting balanced two-mode squeezed (TMS) [39, 181] states have a two-mode squeezing level of $S_\mathrm{TMS} = 7.1\,$dB and an entanglement strength characterized by the negativity criterion of $N_\mathrm{k} = 2.2$. Details on the experimental generation and characterization of the TMS states are given in Sec. 4.1. The negativity kernel N_k quantifies the strength of nonlocal correlations present between field quadratures of signals propagating along different beam splitter output paths. Additionally, the balanced TMS states have negligible local squeezing within each path. In other words, the microwave signals propagating on the two paths locally look like thermal states with, nevertheless, strong entanglement between them.

In the next step, we employ the balanced propagating TMS states as a resource for remotely preparing the target squeezed microwave states. For this purpose, the

TMS states are continuously distributed between two parties, Alice and Bob, who are separated by 35 cm of superconducting cable. Alice generates a feedforward signal carrying the classical information about her choice on what quantum state is to be remotely prepared at Bob's side. Finally, Bob displaces his part of the resource state proportionally to the communicated signal by using a directional coupler with a fixed coupling of $\beta \simeq -15\,\mathrm{dB}$ [64, 131]. We experimentally generate the feedforward signal with JPA 3 operated as a phase-sensitive amplifier at Alice's side. She uses it to choose and strongly amplify a certain quadrature of the incoming TMS states. Note that, in contrast to the other JPAs, it does not matter whether the outgoing feedforward signal from JPA 3 is squeezed or not (see Sec. 5.2.2 for details). The essential classical information, as required for a successful RSP, is encoded in the large instantaneous amplitude of the phase-sensitively amplified field quadrature. For ideal RSP, the coupling β should be vanishingly small. However, since β needs to be approximately compensated by the degenerate gain of JPA 3, we are limited to a certain range of β values due to the noise performance and 1-dB compression point of JPA 3.

5.1.2 Tomography of remotely prepared states

Figure 5.2 (a) shows the experimental performance of the RSP protocol as a function of the JPA 3 degenerate gain G_f for a fixed JPA 3 amplification angle $\gamma_\mathrm{f} = 0°$. The latter is defined as the deviation from the angle of the optimal working point at which we achieve the highest purity in the remotely prepared states. We fully characterize these states in terms of their squeezing level S_rp, antisqueezing level A_rp, and squeezing angle γ_rp. We clearly observe squeezing levels of up to $S_\mathrm{rp} = 1.6 \pm 0.1\,\mathrm{dB}$ in the final states at the output

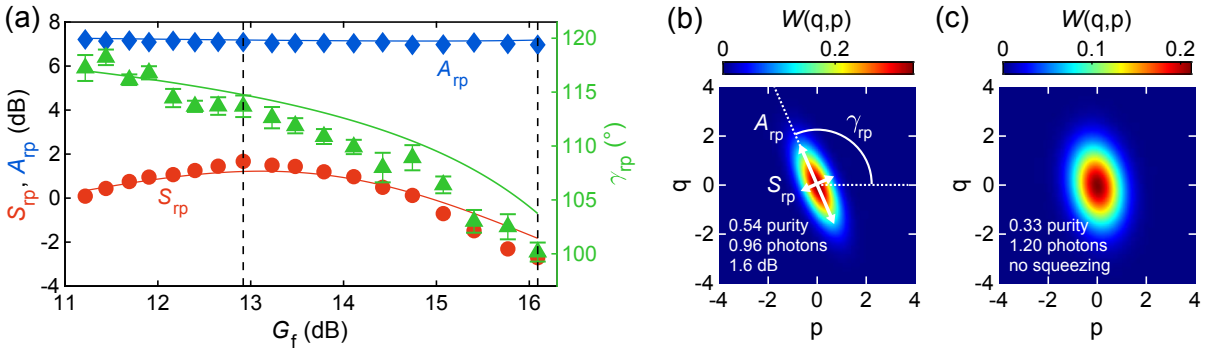

Figure 5.2: (a) Squeezing level S_rp (circles), antisqueezing level A_rp (diamonds), and squeezing angle γ_rp (triangles) of remotely prepared states as a function of the JPA 3 degenerate gain G_f at fixed angle $\gamma_\mathrm{f} = 0°$. Symbols mark experimental data and lines show the corresponding fit according to Eqs. (2.114)–(2.116). If not shown, the standard error of the mean is smaller than the symbol size. (b,c) Reconstructed Wigner functions of the remotely prepared states for the optimal and one of the non-optimal JPA 3 gains as marked by the dashed lines in panel (a).

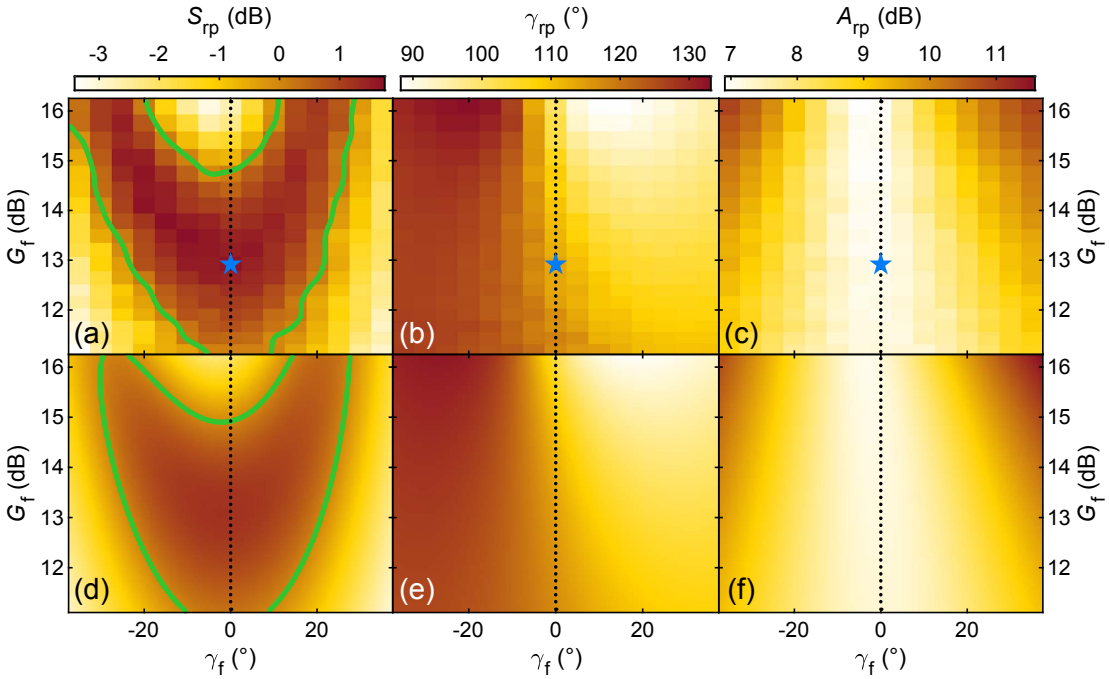

Figure 5.3: (a-c) S_{rp}, γ_{rp}, and A_{rp} of the remotely prepared states as a function of the feedforward parameters. Panels (d-f) show a joint fit of the three quantities (S_{rp}, A_{rp}, γ_{rp}) to the corresponding data in panels (a-c)as described in the text, respectively. The green lines in panel (a) mark the threshold $S_{\mathrm{rp}} \geq 0\,\mathrm{dB}$ for squeezing below the vacuum limit. The optimal point is marked by the blue star. Dotted lines show the data and fit shown in Fig. 5.2.

of the displacer near the optimal JPA 3 gain of $G_{\mathrm{f}} \simeq 13\,\mathrm{dB}$ [see Fig. 5.2 (b)]. S_{rp} decreases and the states even become non-squeezed upon moving away from the optimal JPA 3 gain as shown in Fig. 5.2 (c). The remotely prepared states can be encoded not only by varying G_{f} but also by changing γ_{f}. The latter leads to a different quadrature in the resource TMS states being projected, and accordingly, to a different state being remotely prepared. S_{rp}, γ_{rp} and A_{rp} of the remotely prepared states, obtained by sweeping both G_{f} and γ_{f}, are shown in Fig. 5.3 (a-c), respectively.

We theoretically describe our experiment by a model based on the input-output transformations for every component in the setup including transmission losses. In particular, we define χ_1 as the total loss between JPA 1 (or JPA 2) and JPA 3, and χ_2 as the total loss between JPA 1 (or JPA 2) and the directional coupler. This definition implies that all path losses between JPA 1 or JPA 2 and any component after the beam splitter are assumed to be equal. Additionally, we assume imperfect JPAs adding a certain amount of noise with mean thermal photon numbers n_i ($i \in \{1, 2, \mathrm{f}\}$) to the JPA input signal. Here, n_{f} is the noise photon number of JPA 3. From theory (cf. Sec. 2.3.2), the RSP protocol is expected to work optimally for $G_{\mathrm{f}} = \tau/(1-\tau)$ and $\gamma_{\mathrm{f}} = 0°$, where $\tau = 1 - 10^{\beta/10}$ is the transmissivity of the directional coupler. At this optimal point and under the condition

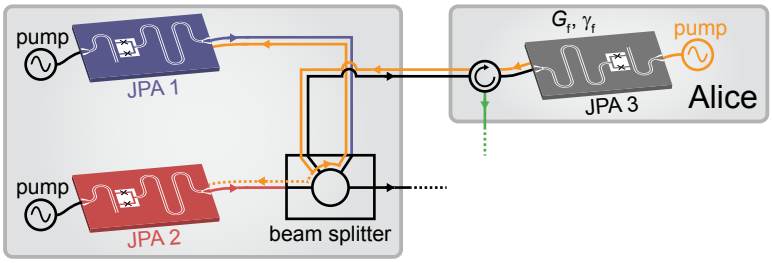

Figure 5.4: Schematic for the origin of the JPA cross-talk. The JPA 3 pump signal (orange) is leaking backwards through the setup to JPA 1 and JPA 2 since the circulator and beam splitter have only small isolation at the pump frequencies around 11 GHz. The cross-talk to JPA 1 is dominant due to worse isolation of neighboring ports in the hybrid ring..

$S_{\mathrm{TMS}} \geq 3\,\mathrm{dB}$, we obtain the squeezed variance of the remotely prepared state,

$$\sigma_{\mathrm{s}}^2 = \frac{1}{4}\left[2(1+2n)e^{-2r}(1-\chi)\tau + 2(\chi+n_{\mathrm{f}})\tau\right] . \tag{5.1}$$

In this simplified expression, we assume equal noise photon numbers $n_1 = n_2 = n$ and squeezing factors $r_1 = r_2 = r$ of JPA 1 and JPA 2 as well as equal losses $\chi_1 = \chi_2 = \chi$. More details of our theory model can be found in Sec. 2.3.2. Equation (5.1) indicates that the prepared squeezing level S_{rp} at the optimal point is approximately 3 dB lower than the squeezing level of the used resource. In order to better model the experiment, we additionally include a finite crosstalk between JPA 3 and the JPAs creating the TMS states. As depicted in Fig. 5.4, the crosstalk originates from the pump of JPA 3 leaking through to JPA 1 and JPA 2 via the beam splitter which results in a finite influence of the JPA 3 pump on the squeezing level and squeezing angle of JPA 1 and JPA 2. Since experimentally the crosstalk to JPA 1 dominates and mainly influences γ_1, we approximate the effect of the crosstalk by a linear dependence of γ_1 on the gain G_{f} and angle γ_{f} of JPA 3, $\gamma_1 = \gamma_1^{(0)} + \kappa G_{\mathrm{f}} + \lambda\gamma_{\mathrm{f}}$, where $\gamma_1^{(0)}$ is the unperturbed squeezing angle of JPA 1 incorporating a constant offset due to the crosstalk. This linear approximation is consistent with independent measurements of the crosstalk. In future experiments, the crosstalk between JPAs can be avoided by utilizing circulators and a beam splitter with better isolation at the pump frequencies around 11 GHz. In order to improve our model further, we use asymmetric losses $\chi_1 \neq \chi_2$ in the data analysis. Figure 5.3 (d-f) depicts a joint fit to the corresponding data. We observe a very good coincidence between the experimental results and our model for the following essential parameters: JPA 1,2 squeezing levels $S = 10.1\,\mathrm{dB}$, $n = 0.04$, as well as $\chi_1 = 0.22$ and $\chi_2 = 0.21$ corresponding to losses of 1.1 dB and 1.0 dB, respectively. All values nicely agree with those obtained from independent JPA characterization measurements and loss estimations. In Tab. 5.1, we summarize all parameters used for the theoretical description of our data.

We emphasize that the bare model only requires three fitting parameters (n, r, n_{f}') in order to obtain a good fit while the remaining parameters are estimated from independent

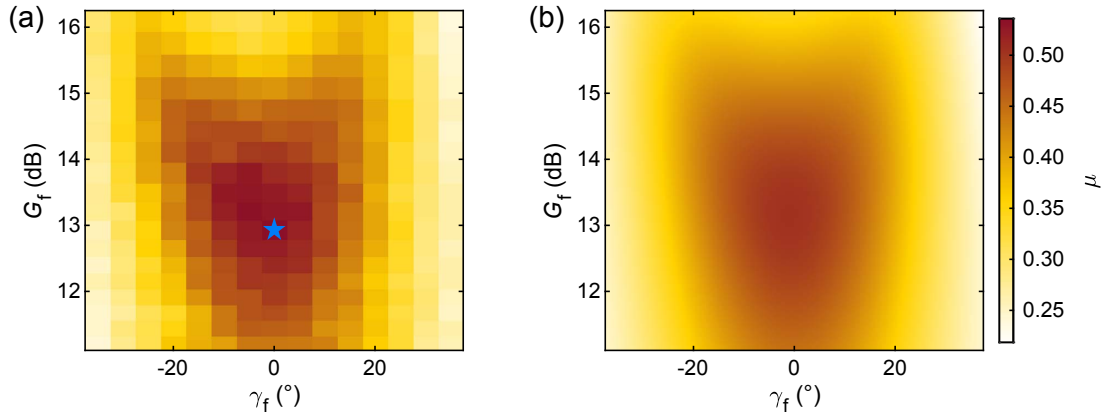

Figure 5.5: (a) Experimental and (b) theoretical purity μ of remotely prepared states as a function of the feedforward parameters. The purity in panel (b) is calculated using the fitted parameters from Tab. 5.1. The optimal point is marked by the blue star for which we obtain the purity $\mu = 0.54 \pm 0.01$.

measurements. Including β, γ_{opt}, θ_{rp}, and the crosstalk parameters ($\gamma_1^{(0)}$, κ, λ) as fitting parameters, only slightly improves the quantitative agreement between the experiment and the theory. For details on the model and parameters, we refer the reader to Sec. 2.3.2.

The purity $\mu = 1/(4\sqrt{\det \mathbf{V}})$, where $\mathbf{V}$ is the covariance matrix of the remotely prepared state, incorporates the information about the antisqueezed quadrature and is a measure of how close the state is to a pure state. It vanishes, $\mu \to 0$, for maximally mixed states and is unity, $\mu = 1$, for a pure state. The performance of RSP can be best quantified by the purity as it is unity only for an ideal RSP protocol. This is in contrast to the squeezing level of the prepared states which is fundamentally linked to the initial two-mode squeezing level. In Fig. 5.5 (a), we show the purity of the remotely prepared states for different feedforward parameters. At the optimal point, we achieve the highest uncorrected purity $\mu = 0.54 \pm 0.01$ which is sufficient for many applications of squeezed states such as entanglement generation [25], sideband cooling of optomechanical systems [31], and quantum illumination [49]. The purity decreases for increasing deviation from the optimal point. We observe a good agreement between the experimental purity and the calculated purity using the parameters in Tab. 5.1.

Table 5.1: Model parameters used to theoretically describe the RSP protocol. The total losses χ_1 and χ_2 are estimated from the individual loss of the components. γ_2 is fixed to the experimentally chosen squeezing angle of JPA 2. The JPA 3 noise photon number is $n_{\mathrm{f}} = n_{\mathrm{f}}' G_{\mathrm{f}}$, where n_{f}' is a proportionality constant. The angle γ_{opt} is the theoretically optimal JPA 3 amplification angle and θ_{rp} compensates the difference in electric path lengths.

n	r	$\gamma_1^{(0)}$ (°)	γ_2 (°)	n_{f}'	β (dB)	χ_1	χ_2	γ_{opt} (°)	θ_{rp} (°)	κ (°)	λ
0.04	1.20	49.6	135.0	0.0059	−14.6	0.22	0.21	136.5	68.5	−0.17	0.02

As mentioned above, we utilize the purity as the main quantifier for the performance of RSP instead of a fidelity criterion. The definition of a fidelity would be desired but is non-trivial as the prepared quantum state only appears on Bob's side at the final step of the protocol. Therefore, one would need to theoretically specify an ideal target state to calculate the fidelity of RSP. However, since we work with continuous variables, the corresponding Hilbert space is infinite and there is, to the best of our knowledge, no unique definition of such a target state. However, a suitable group of target states are pure states with the same squeezing level as experimentally prepared. Therefore, the purity of the prepared state quantifies the performance of the RSP protocol better than an artificially defined fidelity.

5.1.3 Phase space of remotely prepared states

The manifold of undisplaced Gaussian states we can prepare can be intuitively understood by plotting the results from Fig. 5.3 (a-c) in the phase spaces spanned by the parameters of the prepared states. In Fig. 5.6 (a,b), we show the phase spaces spanned by $\{S_{\mathrm{rp}}, \gamma_{\mathrm{rp}}\}$ and $\{S_{\mathrm{rp}}, A_{\mathrm{rp}}\}$, respectively. We can prepare states with different squeezing angles γ_{rp} between 90° and 130° while still preparing states with squeezing below the vacuum limit ($S_{\mathrm{rp}} > 0$). However, with increasing deviation from the optimal point, the purity of the

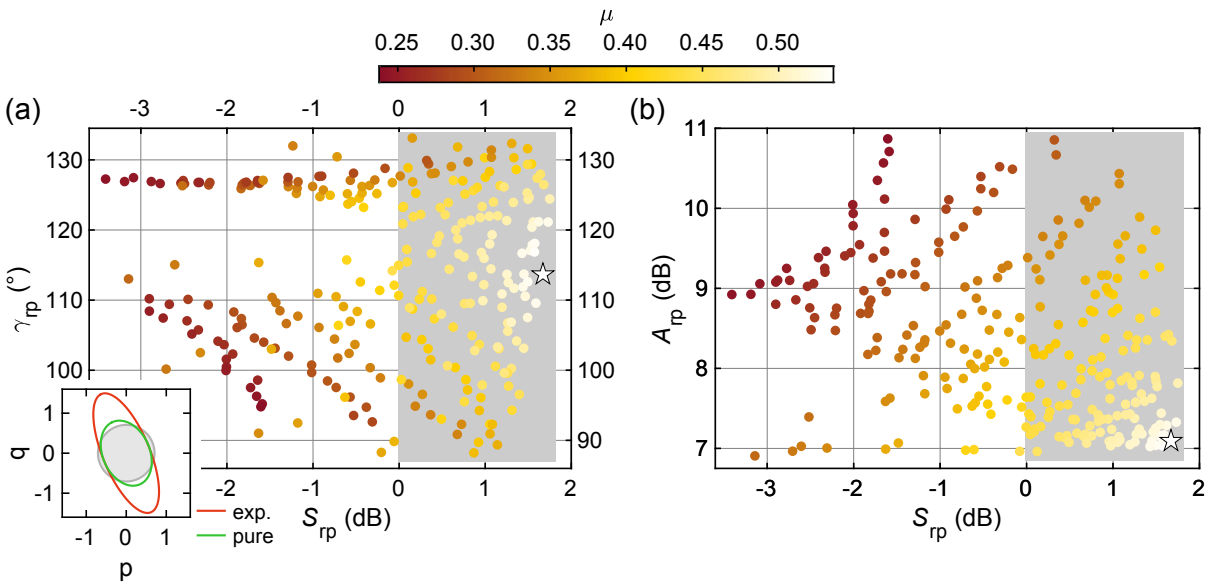

Figure 5.6: Purity of remotely prepared states in different phase spaces. (a) Phase space of the prepared states spanned by S_{rp} and γ_{rp}. (b) Phase space of the prepared states spanned by S_{rp} and A_{rp}. The grey area contains states squeezed below the vacuum limit. The color code indicates the purity μ of remotely prepared states. The optimal point is marked by the white star. The inset in panel (a) shows the Wigner function $1/e$ contours of the experimental state at the optimal point with $\mu = 0.54$ and a pure squeezed state with the same squeezing level. The vacuum $1/e$ contour is indicated in grey.

prepared states decreases. In this context, one should remember that our protocol allows for the preparation of continuous-variable squeezed states with a degree of squeezing S_{rp} that is fundamentally linked to the initial two-mode squeezing of the resource state. In the current implementation, even for a fixed resource TMS state, S_{rp} and γ_{rp} can be changed at the expense of a reduced purity μ. We note that the preparable γ_{rp} are related to which quadratures are correlated in the resource TMS state. By adding a phase shifter [206] on her side, Alice could effectively change which quadratures on her side are correlated with the ones on Bob's side. By extending our theory model with such a phase shifter, we find that the optimal JPA 3 amplification angle would be changed proportional to the phase shift which, ultimately, would lead to different γ_{rp} of the prepared states. These actions would not affect the achievable S_{rp} and μ.

Using an appropriate model of our experiment, we are able to investigate the effect of imperfections in different parts of the protocol on the purity of the prepared state at the optimal point. If the resource TMS state is pure ($\mu = 1$) and distributed ideally to Alice and Bob, the model predicts an improved purity $\mu = 0.60$ for otherwise unchanged experimental parameters. Alternatively, ideal operations of Alice and Bob (noiseless JPA 3, $n_{\mathrm{f}} = 0$, combined with no losses on Alice's and Bob's sides) together with the imperfect experimental entangled resource would yield a purity $\mu = 0.62$. Overall, the observed purity is limited by the added noise of the JPAs and the losses in the setup. Upon reducing the JPA noise photon numbers by one order of magnitude as well as the total losses to $\chi_1 = \chi_2 = 0.05$ (0.2 dB), we expect an optimized purity $\mu_{\mathrm{opt}} = 0.80$ for the prepared state at the optimal point. Such a reduction of losses could be achieved by using a superconducting hybrid ring, optimized cable connectors, and improved circulators. The latter could be realized by on-chip superconducting circulators for which various approaches for practical realizations exist. Some of the most popular approaches use mechanical oscillators [207, 208], and some others employ Josephson nonlinearities [209, 210] to realize nonreciprocal transmission of microwaves under appropriate driving of the system. However, until now, the best reported insertion losses are around 0.5 dB [209] which are notably higher than the ones of the currently employed commercial circulators (CTH1184-KS18, Quinstar). Nevertheless, it is believed that the insertion losses in these on-chip circulators can and will be brought down in the next few years, since most obstacles there have a technological nature and can be resolved. In the future, superconducting circulators could be combined with on-chip JPAs to further avoid losses due to the absence of interconnections and related reflections.

As discussed in Sec. 2.3.1, the quantum advantage of ideal RSP consists in the fact that only one real number is required to be communicated to Bob in order to prepare a desired pure squeezed state, which requires two real numbers to be fully described. However, in our implementation of RSP, we cannot avoid losses and noise added by the JPAs which results in the preparation of mixed squeezed states at Bob's side. These imperfections reduce the achievable quantum advantage in our RSP protocol. First, in the current

experiment, we utilize JPA 3 for the generation of the feedforward signal. Here, only the amplified quadrature will affect the signal at Bob's side due to the low coupling $\beta \ll 0\,\mathrm{dB}$ of the displacer. Consequently, we send two real numbers to Bob via the feedforward signal. Second, the prepared mixed squeezed states require three real numbers (S_{rp}, A_{rp}, γ_{rp}) to be fully described. It is challenging to accurately quantify the quantum advantage for our case. One reason is that all real numbers possess a certain precision in a realistic scenario and, consequently, it is not sufficient to only compare the number of real numbers alone. One would need to quantify the amount information, in bits or nats, by other means. The quantum advantage could then be obtained by comparing the amount of information sent in the feedforward signal with the one required to describe the prepared quantum state.

5.1.4 Error phase space of preparable states

We now discuss theoretically which states in the phase space are expected to be remotely preparable for our experimental parameters. According to the underlying theory model (see Sec. 2.3.2), the position of prepared states inside the phase space does not uniformly depend on G_{f} and γ_{f}. Since we select a finite and uniform step size of G_{f} and γ_{f} in the experiment, the measured remotely prepared states do not uniformly span the phase space.

In order to get a better insight into the expected phase space of remotely preparable states, we use the model of RSP discussed in Sec. 2.3.2 together with the parameters in Tab. 5.1 and calculate an expected phase space of prepared states for the experimental range of JPA 3 gains G_{f} and amplification angles γ_{f}. In Fig. 5.7 (a,b), we show the resulting expected phase spaces spanned by $\{S_{\mathrm{rp}}, \gamma_{\mathrm{rp}}\}$ and $\{S_{\mathrm{rp}}, A_{\mathrm{rp}}\}$, respectively. Additionally, in order to estimate the error of the fit, we use an iterative method to calculate the error phase space. Here, we apply a random sampling routine where a value from the 95% confidence intervals of each fitting parameter is randomly selected and the resulting error phase space is calculated. If the new error phase space lies partly or fully outside the old error phase space, the latter is expanded so that it includes the new error phase space. The process is repeated until the change of the area in the error phase space is negligible between iterations. We observe that the expected phase space does not include all experimentally prepared states but shows a good qualitative agreement. However, the error phase space of the fit includes all measured remotely prepared states.

In Fig. 5.7 (c,d), we show the expected phase spaces of the accessible prepared states under the assumption of reduced JPA noise photon numbers by one order of magnitude ($n = 4 \cdot 10^{-3}$ and $n_{\mathrm{f}} = 6 \cdot 10^{-4}$) and reduced total losses to $\chi_1 = \chi_2 = 0.05$ corresponding to a loss of 0.2 dB. Other parameters are kept as in Tab. 5.1. The range of preparable A_{rp} and γ_{rp} is only slightly affected by the optimized parameters while the accessible squeezing levels S_{rp} are significantly increased up to $\simeq 5.5\,\mathrm{dB}$ from the current experimental limit

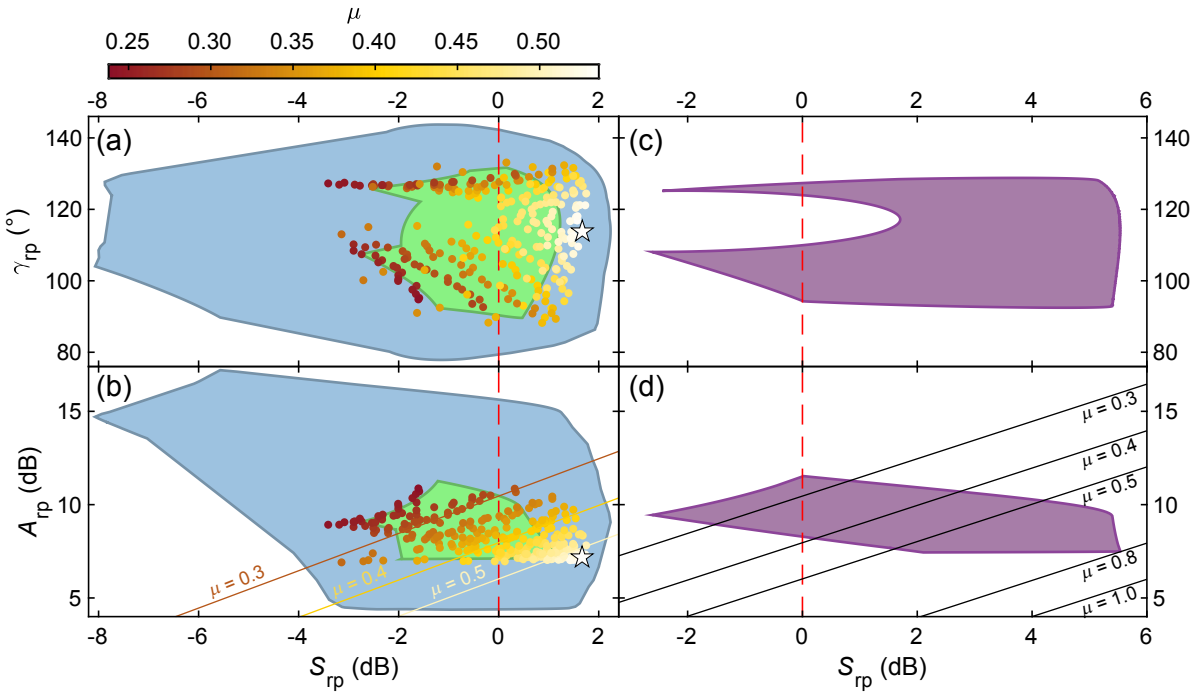

Figure 5.7: (a,b) Phase space of experimental remotely prepared states spanned by $\{S_{\mathrm{rp}}, \gamma_{\mathrm{rp}}\}$ and $\{S_{\mathrm{rp}}, A_{\mathrm{rp}}\}$, respectively. The green and blue shaded area indicate the expected phase space from the fit and the error phase space, respectively. The color code indicates the purity μ of the remotely prepared states. The optimal point is marked by the white star. (c,d) Expected theoretical phase space of preparable states for an improved setup in the phase space spanned by $\{S_{\mathrm{rp}}, \gamma_{\mathrm{rp}}\}$ and $\{S_{\mathrm{rp}}, A_{\mathrm{rp}}\}$, respectively. Here, we reduce the JPA noise photon numbers by one order of magnitude and the total losses to $\chi_1 = \chi_2 = 0.05$ with otherwise unchanged parameters from Tab. 5.1. The red dashed lines mark the threshold for squeezing below the vacuum limit. The solid lines mark states with constant purity.

of $\simeq 1.6\,\mathrm{dB}$. Consequently, it is imperative to minimize losses and JPA noise photons in future experiments in order to achieve higher squeezing levels of the prepared states.

5.1.5 Quantum Fisher information and quantum Cramér-Rao bound

Until now, we considered RSP as a quantum communication protocol where the goal is to send a known quantum state to another party. However, one can also consider to use RSP for the communication of classical information. In such a scenario, the classical parameters of the prepared squeezed state are regarded as sent information. There are multiple equivalent ways to fully describe an arbitrary single-mode squeezed state by three real numbers. Here, we will use the squeezing gain $\lambda = e^{-2r}$, the squeezing phase $\varphi = -2\gamma$, and the thermal photon number n_{th} of the squeezed state.

In order to characterize how well we can encode information in the prepared squeezed states, we use the quantum Fisher information (QFI). One way to define the QFI is via the Bures distance $d_{\mathrm{B}}^2 = 2\left(1 - \sqrt{F(\rho_1, \rho_2)}\right)$ [211] between two quantum states $\rho_{1,2}$ where we

use the Uhlmann fidelity $F(\rho_1,\rho_2)=\left(\mathrm{Tr}\sqrt{\sqrt{\rho_1}\rho_2\sqrt{\rho_1}}\right)^2$ [212]. Then, the QFI [213, 214],

$$F_\theta = 8\lim_{\epsilon\to 0}\frac{1-\sqrt{F(\rho_\theta,\rho_{\theta+\epsilon})}}{\epsilon^2} \tag{5.2}$$

quantifies how well we can distinguish between two quantum states ρ_θ and $\rho_{\theta+\epsilon}$. In other words, the QFI measures the amount of information one can gain about a parameter θ from a quantum state ρ_θ which depends on θ [215]. If the quantum state ρ_θ only weakly depends on θ, the QFI F_θ is small. On the other hand, if small changes in θ strongly alter ρ_θ, one obtains large values of F_θ. For general Gaussian states, one can find analytic expressions for F_θ in respect to various parameters of the Gaussian states [213, 216]. For the three parameters λ, φ, and n_{th}, the QFI of an arbitrary squeezed state is given by [216]

$$F_\lambda = \frac{1}{1+\mu^2}\frac{1}{\lambda^2}\,, \tag{5.3}$$

$$F_\varphi = \frac{1}{1+\mu^2}\frac{(1-\lambda^2)^2}{\lambda^2}\,, \tag{5.4}$$

$$F_{n_{\mathrm{th}}} = \frac{1}{n_{\mathrm{th}}+n_{\mathrm{th}}^2}\,, \tag{5.5}$$

where μ is the purity of the state. We obtain r and n_{th} from the experimentally measured squeezed and antisqueezed variances, which we write as $\sigma_{\mathrm{s}}^2=(1+2n_{\mathrm{th}})e^{-2r}/4$ and $\sigma_{\mathrm{a}}^2=(1+2n_{\mathrm{th}})e^{2r}/4$, respectively. The latter expressions can be rearranged to get

$$r = \frac{1}{4}\ln\frac{\sigma_{\mathrm{a}}^2}{\sigma_{\mathrm{s}}^2}\,, \tag{5.6}$$

$$n_{\mathrm{th}} = \left(\sqrt{16\sigma_{\mathrm{s}}^2\sigma_{\mathrm{a}}^2}-1\right)/2\,. \tag{5.7}$$

We now use Eqs. (5.3) – (5.5) to calculate the QFI for the prepared states during RSP. In Fig. 5.8 (a-c), we show the resulting QFI quantities for the experimentally prepared states. We observe that the optimal point in RSP, where we achieve the highest purity, is not necessarily the best point for communication of classical information encoded in the squeezed state parameters. For example, F_λ and F_φ exhibit comparatively small values at the optimal point while much larger values can be reached away from this point. Intuitively, this observation can be understood by considering the squeezing level and antisqueezing level of the prepared squeezed states [see Figs. 5.3 (a,c)]. For regions of high F_λ and F_φ, the prepared states are squeezed below the vacuum limit and possess a comparatively high antisqueezing level. This combination leads to the fact that λ and φ and can be more precisely estimated when compared to the optimal point where the antisqueezing level is lower. In contrast, $F_{n_{\mathrm{th}}}$ shows a similar behavior as the purity of the remotely prepared states and is maximal around the optimal point. This observation

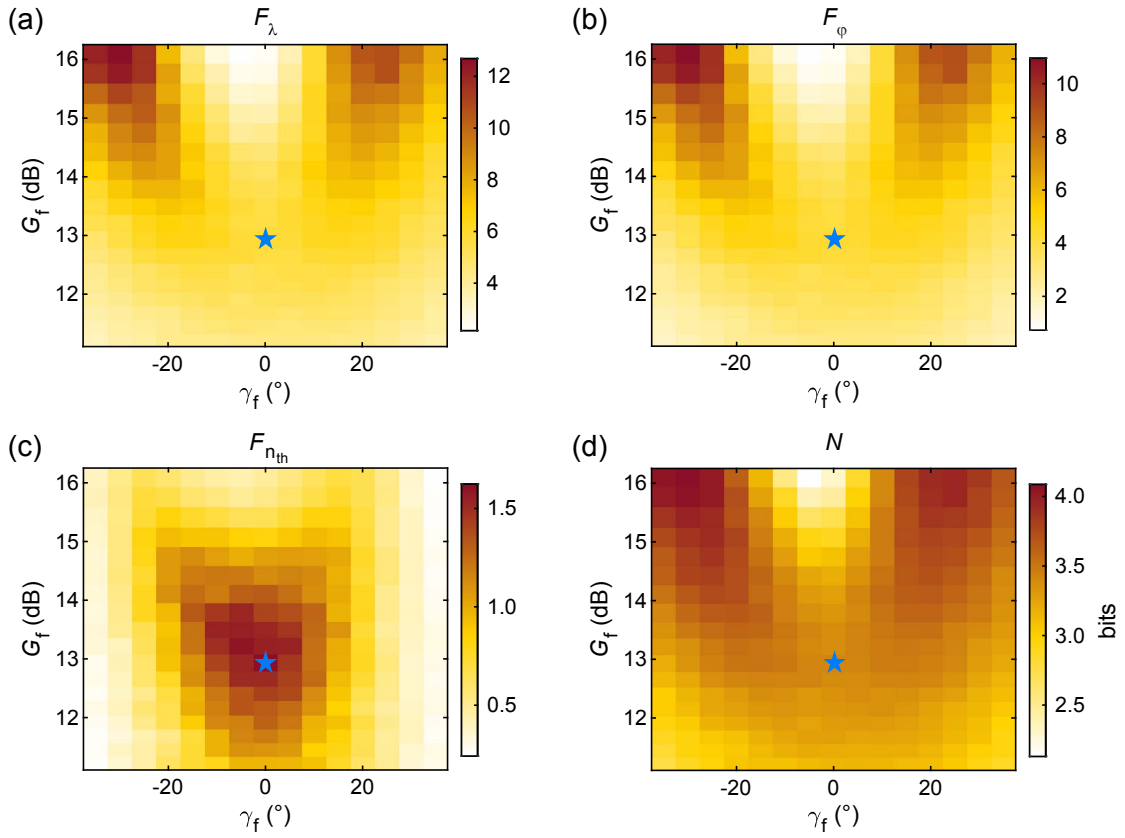

Figure 5.8: (a-c) Quantum Fisher information F_θ for different parameters $\theta = \{\lambda, \varphi, n_{\mathrm{th}}\}$, where $\lambda = e^{-2r}$ is the squeezing gain, $\varphi = -2\gamma$ is the squeezing phase, and n_{th} is the thermal photon number of the prepared squeezed states. F_θ are shown as a function of the feedforward parameters with the same range as in the RSP measurements. (d) Effective number of bits N for the squeezing phase φ of the prepared states. The optimal point of RSP is marked by the blue star.

originates from the fact that a higher purity is linked to a lower number of thermal photons n_{th} in the state. According to Eq. (5.5), $F_{n_{\mathrm{th}}}$ exhibits a similar dependence on n_{th} as the purity, which explains the similar behavior of both quantities. In addition, we observe that F_λ and F_φ are bigger than $F_{n_{\mathrm{th}}}$ for the full experimental range of JPA 3 parameters.

To quantify the amount of classical information sent via the prepared squeezed states, we can utilize the effective number of bits N of the classical parameters of the prepared states. Here, we focus only on the squeezing phase since it is most suitable for communication of classical information. We estimate N by assuming an ideal analog-to-digital converter which samples the reconstructed squeezing phase φ of the prepared state. When neglecting distortion effects of the signal, we can define $N = (SNR - 1.76\,\mathrm{dB})/6.02\,\mathrm{dB}$ [217], where $SNR = 10\log_{10}\left[\Delta\varphi^2/\sigma_\varphi^2\right]$ is the signal-to-noise ratio in decibel. Here, $\Delta\varphi = 2\pi$ is the full range of squeezing phases of a squeezed state and σ_φ is the standard deviation of φ. To obtain a lower bound for σ_φ, we use the quantum Cramér-Rao bound [218], which relates the quantum Fisher information to a lower bound of the estimation error of φ

as $\sigma_\varphi^2 \leq 1/F_\varphi$. In Fig. 5.3 (d), we show the resulting effective number of bits N for the prepared states. Similar as for F_φ, we observe the highest values of N of up to 4.1 bits away from the optimal point of RSP.

These observations do not contradict the interpretation of the optimal point in RSP. The reason is that the original purpose of RSP is the preparation of a quantum state at a remote location. There, the optimal point is defined as the point at which we are able to prepare a squeezed state with the highest obtainable purity and squeezing level. In contrast, in this subsection we investigate the QFI of the prepared states which provides insight into the question of how good we can estimate the classical squeezed state parameters. The optimal operational points for both tasks is not necessarily the same. For example, according to Eqs. (5.3) and (5.3), F_λ and F_φ are bigger for lower purity of the squeezed states.

5.1.6 Effect of entanglement strength on remote state preparation

Until now, we kept the entanglement strength in the TMS states fixed in the RSP measurements. However, as previously discussed, the highest achievable squeezing level of the prepared state is closely linked to the two-mode squeezing level of the resource state. TMS states with varying entanglement strength are produced by changing the pump powers of JPA 1 and JPA 2 in such a way that the resulting TMS states stay well balanced, as presented in Sec. 4.1. The TMS states are then used in RSP as the entangled resource. Here, we only investigate the optimal point of RSP with the JPA 3 parameters fixed to the optimal values of $G_\mathrm{f} \simeq 13\,\mathrm{dB}$ and $\gamma_\mathrm{f} = 0°$. With an increasing two-mode squeezing level, i.e. stronger entanglement, the prepared states in RSP show an increasing squeezing level.

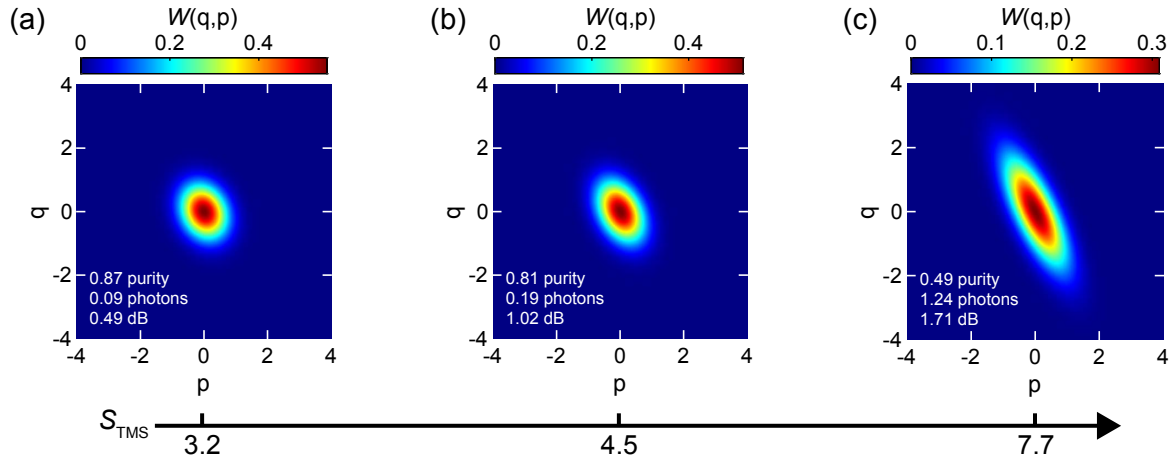

Figure 5.9: (a-c) Wigner functions of remotely prepared states during RSP for different TMS states with increasing entanglement strength quantified by the two-mode squeezing level S_TMS. All three states are shown for the optimal working point of RSP with the JPA 3 parameters $G_\mathrm{f} \simeq 13\,\mathrm{dB}$ and $\gamma_\mathrm{f} = 0°$. The text inside the panels provides the purity, photon number, and squeezing level of the prepared states from top to bottom, respectively.

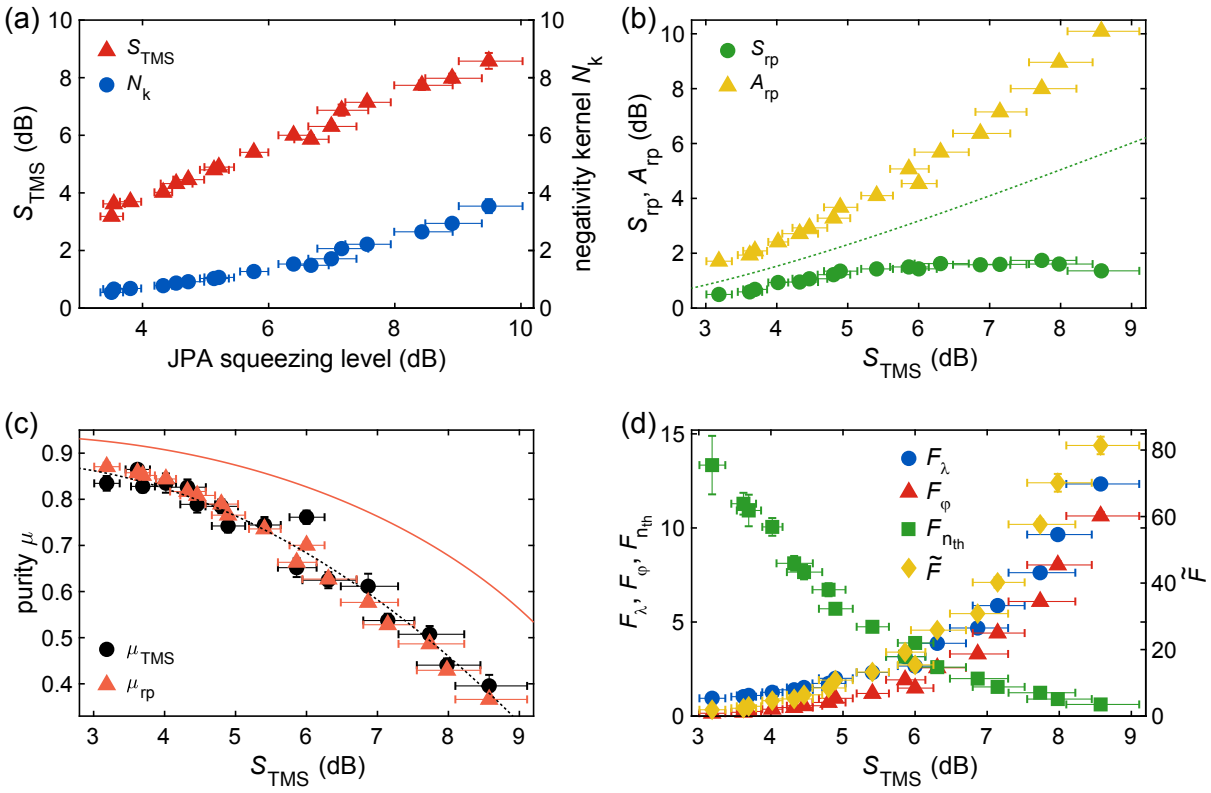

Figure 5.10: (a) Two-mode squeezing level S_{TMS} and negativity kernel N_{k} as a function of the squeezing levels of the states produced by JPA 1 and JPA 2. (b) Squeezing level S_{rp} and antisqueezing level A_{rp} of remotely prepared states. The green dashed line marks maximum achievable S_{rp} for the experimental TMS states under ideal operations on Alice's and Bob's side (noiseless JPA 3 and no losses). (c) Purity of TMS states and remotely prepared states. The solid orange line marks maximum achievable purity $\tilde{\mu}_{\mathrm{rp}} = \sqrt{\tilde{\mu}_{\mathrm{TMS}}}$ of remotely prepared states when using the TMS states with purity $\tilde{\mu}_{\mathrm{TMS}}$ given by the dashed black line and corresponding S_{TMS}. The operations on Alice's and Bob's side are assumed to be ideal for this estimation. (d) Quantum Fisher information (QFI) F_θ for different parameters $\theta = \{\lambda, \varphi, n_{\mathrm{th}}\}$, where $\lambda = e^{-2r}$ is the squeezing gain, $\varphi = -2\gamma$ is the squeezing phase, and n_{th} are the thermal photons of the prepared squeezed states. Here, $\tilde{F} = F_\lambda F_\varphi F_{n_{\mathrm{th}}}$ is the product of different QFI quantities. If not shown, the standard error of the mean is smaller than the symbol size.

This behavior is well visible in the Wigner functions of the prepared states, as shown in Fig. 5.9. We also observe a strong increase of the antisqueezed quadrature which is connected to a larger number of noise photons in the TMS states with larger two-mode squeezing, corresponding to stronger entanglement.

In Fig. 5.10, we summarize the relevant quantities of RSP as a function of the entanglement strength. Upon increasing the squeezing levels of the states produced by JPA 1 and JPA 2, the negativity kernel N_{k} and two-mode squeezing level S_{TMS} of the resulting TMS states increase, as shown in Fig. 5.10 (a). The corresponding squeezing levels S_{rp} and antisqueezing levels A_{rp} of the remotely prepared states are shown in Fig. 5.10 (b)

and generally increase for increasing S_{TMS}. However, S_{rp} saturates to a constant value around $S_{\mathrm{TMS}} \simeq 6\,\mathrm{dB}$. From Fig. 5.10 (c), we observe that the dependence of μ_{rp} and μ_{TMS} on S_{TMS} is similar. However, we emphasize that μ_{rp} does not solely depend on μ_{TMS} but also on the losses on Alice's and Bob's side as well as the added noise by JPA 3. If these imperfections are negligible, one can even achieve $\tilde{\mu}_{\mathrm{rp}} = \sqrt{\tilde{\mu}_{\mathrm{TMS}}} = \tilde{\mu}_{\mathrm{s}}$, where $\tilde{\mu}_{\mathrm{s}}$ is the purity of the squeezed states produced by JPA 1 and JPA 2. The latter relation is explained by the fact that a TMS state with purity $\tilde{\mu}_{\mathrm{TMS}}$ is produced by two squeezed states with purity $\tilde{\mu}_{\mathrm{s}}$ (see Sec. 4.1.2). It is then intuitive to understand that, in the absence of imperfections during RSP, the purities of the initial squeezed states and remotely prepared states are identical, i.e., $\tilde{\mu}_{\mathrm{rp}} = \tilde{\mu}_{\mathrm{s}}$.

Finally, we determine the QFI of the remotely prepared states depending on the two-mode squeezing level S_{TMS}. For that, we use Eqs. (5.3)–(5.5) to calculate the QFI for the different parameters λ, φ and n_{th} and show the result in Fig. 5.10 (d). We observe a decrease in $F_{n_{\mathrm{th}}}$ for increasing S_{TMS}. This behavior is expected since $F_{n_{\mathrm{th}}}$ inversely depends on the thermal population n_{th} of the prepared squeezed state. The latter increases for prepared squeezed states with increasing squeezing level. The dependence is inverted for F_λ and F_φ which increase for higher S_{TMS}, and therefore, higher squeezing of the prepared squeezed state. This fact can be intuitively understood by considering that the squeezing gain λ and the squeezing phase φ can be easier estimated for a high antisqueezed quadrature. Consequently, we observe a cross-over for the best parameter to estimate from the prepared states in RSP at the optimal point. For low S_{TMS}, i.e. low squeezing levels and high purities of the prepared states, n_{th} can be best estimated while it is easier to determine λ and φ for high $S_{\mathrm{TMS}} > 6.5\,\mathrm{dB}$, i.e., higher squeezing levels and lower purities of the prepared states. In addition, we calculate the product $\tilde{F} = F_\lambda\, F_\varphi\, F_{n_{\mathrm{th}}}$ of the different QFI quantities and observe increasing $\tilde{F}$ for increasing S_{TMS}. The previous conclusions are only fully valid for the optimal point of RSP. As we have seen in Fig. 5.8, $F_{n_{\mathrm{th}}}$ decreases upon moving away from the optimal point of RSP and λ as well as F_φ can substantially increase for high G_{f}. Therefore, when considering non-optimally prepared states, it can be advantageous to estimate λ and φ even for low S_{TMS}. In conclusion, we find a cross-over of which single parameter can be best estimated from the prepared states while the product $\tilde{F}$ increases with stronger entanglement.

5.2 Quantum correlations in remote state preparation

In the previous section, we mainly discussed the preparable states during RSP. This section focuses on studying classical and quantum correlations during different stages of the protocol. In particular, we investigate quantum entanglement, quantified by the negativity kernel N_{k}, and quantum discord D which is a more general quantifier for quantum correlations. Quantum correlations are necessary for successful RSP. For remote state preparation of qubit states, geometric discord has been shown to be a sufficient

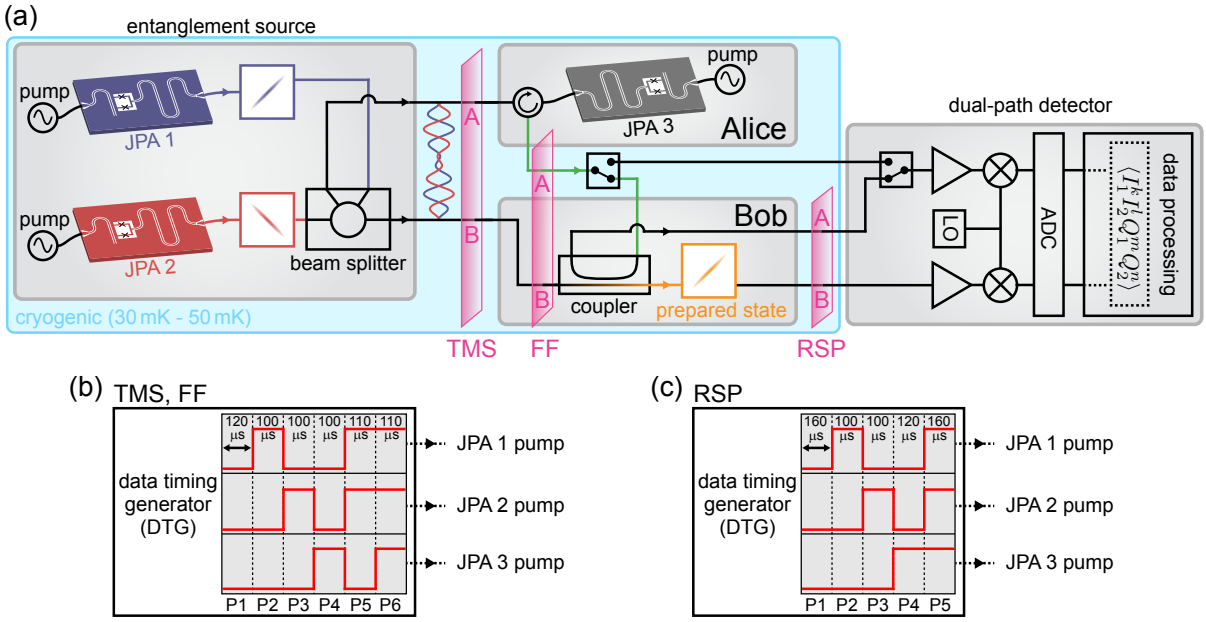

Figure 5.11: (a) Schematic of RSP with different key stages during the protocol. The first stage (TMS) corresponds to the distribution of entanglement to Alice and Bob, the second stage (FF) corresponds to the bipartite state after generation of the feedforward signal, and the third stage (RSP) corresponds to the final state after the remote preparation of a squeezed state. The two paths of the bipartite states are marked with A and B. (b) Pump modulation scheme employed for measurements of the TMS stage and FF stage. (c) Pump modulation scheme employed for measurements of the RSP stage. The cryogenic part of the setup is marked with the blue box.

resource in Ref. [200]. However, it has been argued that entangled states still could yield higher efficiencies if compared to separable resource states [219]. In our particular implementation of RSP, we cannot prepare squeezed states with squeezing below the vacuum limit without an entangled resource. Intuitively, this property can be explained by considering that TMS states are locally thermal states. To obtain a squeezed state by a local displacement operation, one needs to rely on correlations with a strength that allows for a reduction of the antisqueezed variance of the local TMS state below the vacuum variance. In our case, this is only possible with entangled resource states.

As shown in Fig. 5.11, we will focus on three different key stages of RSP and, in this way, investigate how correlations are consumed or transformed during the protocol [220]. The first stage (TMS) is the entanglement distribution to Alice and Bob. The second stage (FF) is after the phase-sensitive amplification of JPA 3. The final stage (RSP) is after the local operation on Bob's side. In all stages, we can experimentally probe classical and quantum correlations between the two paths. We note that, due to a modified cryogenic setup, the experimental results in this section quantitatively slightly differ but show the same qualitative behavior when compared to the previous section.

5.2.1 Entanglement distribution

The entanglement distribution stage (TMS stage) is essential for RSP since it provides the entangled resource to both parties. We use propagating microwave TMS states as such entangled states. Details on the generation of TMS states are provided in Sec. 4.1. Experimentally, we are able to investigate the TMS and feedforward stages by utilizing a cryogenic switch at Alice's side after JPA 3. In one position of the switch, we perform RSP by sending the feedforward signal to Bob (the directional coupler). In the other position of the switch, we send the feedforward signal to one path of the dual-path receiver for detection. Technical details on the cryogenic and room-temperature setups are provided in Sec. 3.3.2.

Different characteristic quantities of the TMS state, later serving as entangled resource in RSP, are shown in Tab. 5.2. Here, we choose a TMS state for which we are able to obtain high purities and squeezing levels in the RSP protocol. Apart from the negativity kernel N_k, negative conditional entropies $H(A|B) \simeq H(B|A) < 0$ also reveal entanglement in the TMS state. Furthermore, we can calculate a lower bound on the entanglement of formation E_F, which is a commonly used quantifier for the entanglement strength [191]. Additionally, the two-mode squeezing level S_TMS shows that field quadratures in the two paths are strongly correlated. From the von Neumann entropies, one can gain insight into the local properties of the state. The joint entropy of the TMS state is smaller than the entropies of the local states, $H(A,B) < H(A)$ and $H(A,B) < H(B)$. This observation coincides with the fact that TMS states are locally thermal states while the joint entropy of the whole quantum state can be zero in the limit of pure states with $\mu = 1$. In our experiments, the joint entropy is non-zero due to a finite noise in the TMS states which results in a purity $\mu < 1$. Finally, the TMS state possesses a non-zero mutual information $I(A:B)$ encompassing both classical and quantum correlations. The quantum correlations can be quantified by the quantum discord D_A and D_B. Furthermore, the similar values of $D_A \approx D_B$, $H(A|B) \approx H(B|A)$ and $H(A) \approx H(B)$ indicate that the TMS states are symmetric upon exchanging A and B.

Table 5.2: Different characteristic quantities of a particular TMS states. The errors are the standard error of the mean. The quantities are described in detail in the main text.

N_k	E_F	$H(A\|B)$	$H(B\|A)$	S_TMS (dB)	μ
1.84 ± 0.04	1.16 ± 0.02	-0.80 ± 0.02	-0.79 ± 0.02	6.5 ± 0.1	0.55 ± 0.01
D_A	D_B	$H(A,B)$	$H(A)$	$H(B)$	$I(A:B)$
1.04 ± 0.01	1.05 ± 0.01	0.97 ± 0.02	1.768 ± 0.001	1.770 ± 0.001	2.56 ± 0.02

5.2.2 Feedforward signal

In theory, the feedforward signal sent to Bob should be fully classical for ideal RSP. Therefore, we now turn to the feedforward (FF) stage and investigate the bipartite states after the phase-sensitive amplification of JPA 3 at A. Similar to the entanglement distribution stage, we can calculate different quantifiers for correlations in the bipartite states at the FF stage. However, now the properties of the bipartite states depend also on the amplification parameters of JPA 3. In the case of ideal phase-sensitive amplification, the correlations between A and B would not be affected by the unitary action of JPA 3. However, in the experiments, JPA 3 inevitably adds a finite amount of noise to state A due to its imperfections. Consequently, the correlations between A and B are affected by the amplification by JPA 3.

First, we only consider how the amplification by JPA 3 affects the quantum correlations, as shown in Fig. 5.12 (a) for fixed $\gamma_\mathrm{f} = 0°$. For low values of the JPA 3 gain G_f, there still exists entanglement between A and B. However, the negativity kernel N_k is significantly reduced in comparison to the one of the initial TMS state. The negativity kernel further decreases with increasing G_f until the states become and stay separable ($N_\mathrm{k} < 0$) above a certain G_f. This observation is related to an increased number of added noise photons of JPA 3 to A which ultimately leads to a sudden death of entanglement (see Sec. 4.3) at $G_\mathrm{f} = 12.5\,\mathrm{dB}$. Since we cannot directly determine the JPA 3 noise photon number n_f referenced to the JPA input, we use the fitted proportionality constant $n'_\mathrm{f} = 0.0059$ from Tab. 5.1 to determine the JPA noise photon number via the relation $n_\mathrm{f} = n'_\mathrm{f} G_\mathrm{f}$. Furthermore, we can express the noise photon number in the amplified quadrature after JPA 3 as $N_\mathrm{f} = n_\mathrm{f} G_\mathrm{f} = 1.9$ for the JPA gain of vanishing entanglement. However, as discussed in Sec. 4.3, we expect that the sudden death of entanglement appears at $\simeq 1$ added noise photon to one path. We attribute the difference to a changed noise performance of JPA 3

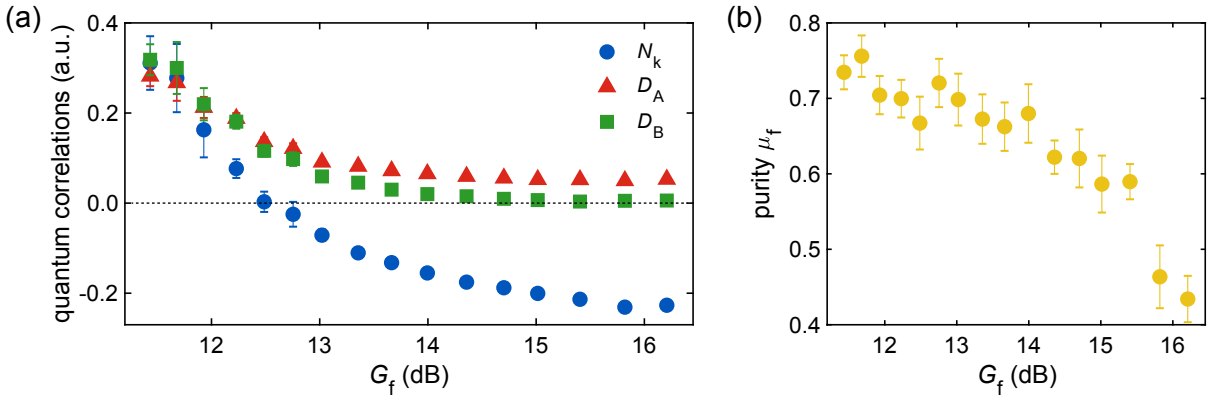

Figure 5.12: (a) Negativity kernel N_k and quantum discord $D_{A,B}$ in the FF stage as a function of G_f for $\gamma_\mathrm{f} = 0°$. (b) Purity μ_f of states produced by JPA 3 with the other JPAs turned off. The data point for $G_\mathrm{f} \simeq 12\,\mathrm{dB}$ is averaged over two adjacent γ_f values around $\gamma_\mathrm{f} = 0°$. If not shown, the standard error of the mean is smaller than the symbol size.

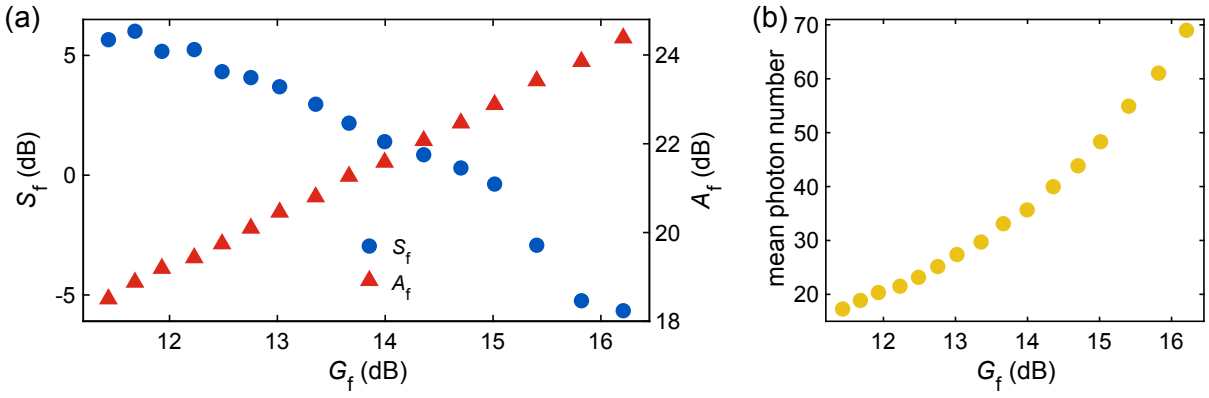

Figure 5.13: (a) Squeezing level S_f and antisqueezing level A_f as well as (b) mean photon number in the FF stage for $\gamma_\mathrm{f} = 0°$. The data point for $G_\mathrm{f} \simeq 12\,\mathrm{dB}$ is averaged over two adjacent γ_f values around $\gamma_\mathrm{f} = 0°$. If not shown, the standard error of the mean is smaller than the symbol size.

between measurement runs such that the value of n_f' is not fully accurate for the results presented in this section. The noise photon number of JPA 3 can be indirectly evaluated by the purity μ_f of the state produced by JPA 3, as shown Fig. 5.12 (b). Here, JPA 1 and JPA 2 are turned off (segment P4 in Fig. 5.11), meaning that, in good approximation, a vacuum state is incident to JPA 3. The purity μ_f decreases with increasing G_f which indicates an increasing thermal population of the state produced by JPA 3.

Quantum discord is affected in a similar way as N_k as it decreases for increasing G_f. For low G_f, both D_A and D_B coincide but start to deviate with increasing G_f. For $G_\mathrm{f} > 15\,\mathrm{dB}$, quantum discord D_B is approximately zero while $D_A \simeq 0.05$. From the observation $D_B \simeq 0$ for high G_f, we can gain insight into the classicality of the feedforward signal. As discussed in Sec. 2.1.6, quantum discord D_B only vanishes for fully distinguishable states, i.e. classical states, on A. Consequently, we can treat the feedforward signal classically for high G_f. Since $D_A > 0$, the states at B are not fully distinguishable due to their remaining quantum mechanical properties. Consequently, the bipartite state at the FF stage is approximately a classical-quantum state [see Eq. (2.42)] for high G_f.

To further investigate the classicality of the feedforward signal, we show the squeezing level S_f and antisqueezing level A_f in the FF stage in Fig. 5.13 (a). The feedforward signal is squeezed below the vacuum for low G_f and becomes non-squeezed for $G_\mathrm{f} \geq 15\,\mathrm{dB}$ while $A_\mathrm{f} > 18\,\mathrm{dB}$ for all G_f. Our theory model and experimental evidence show that the deamplified, and at times squeezed, quadrature has a negligible effect on the prepared state during RSP. This can be understood by considering that the feedforward signal is only weakly coupled to Bob's part of the entangled state by the directional coupler. Therefore, only the strongly amplified quadrature in the feedforward signal will affect the prepared state on Bob's side.

We consider the feedforward signal as classical if it (i) has a positive Wigner function, (ii) is not squeezed below the vacuum, and (iii) is not entangled with the signal on Bob's side. Therefore, under these criteria, all feedforward signals for $G_\mathrm{f} \geq 15\,\mathrm{dB}$ are classical.

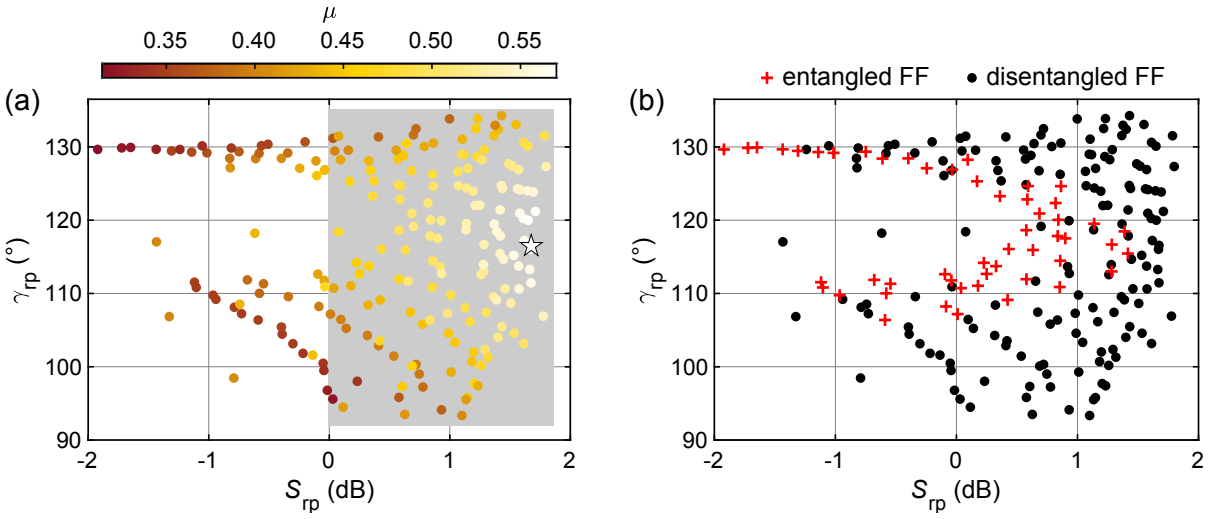

Figure 5.14: (a) Purity of remotely prepared states in the phase space spanned by S_{rp} and γ_{rp}. The gray area marks squeezing below the vacuum limit. The color code indicates the purity μ of the remotely prepared states. The optimal point is marked by the white star. (b) Phase space of remotely prepared states with separable (black dots) and entangled (red crosses) bipartite states during the feedforward.

In Fig. 5.13 (b), we show the mean photon number of the feedforward signal. The high mean photon numbers together with the observation $A_{\mathrm{f}} > 18\,\mathrm{dB}$ support our conclusion that the feedforward signal can be treated classically.

In the previous discussion, we stated that the prepared state at Bob's side is dominantly affected by the amplified quadrature of JPA 3. Therefore, entanglement between A and B after the action of JPA 3 should have no considerable effect on the range of preparable states. In Fig. 5.14 (a), we show the full phase space spanned by S_{rp} and γ_{rp} of the prepared states in RSP. In order to check for the impact of entanglement on the RSP protocol, we exclude points with non-zero entanglement during the feedforward from the phase space of prepared states, as shown in Fig. 5.14 (b). The range of states which we can prepare is only negligibly reduced. In particular, the states with high squeezing level S_{rp} are not influenced when only considering separable states during the FF stage. Consequently, entanglement in the FF stage does not play a role for successful RSP. We note that the data in this subsection is obtained in a different measurement run as compared to Sec. 5.1. Nevertheless, the qualitative behavior between the runs is the same and we observe also a good quantitative agreement.

5.2.3 Correlation consumption in remote state preparation

We now summarize and compare different types of correlations in the three stages of RSP, as shown in Fig. 5.15. We restrict the analysis to the optimal JPA 3 amplification angle $\gamma_{\mathrm{f}} = 0°$. As shown previously in Tab. 5.2, we start with a correlated TMS state

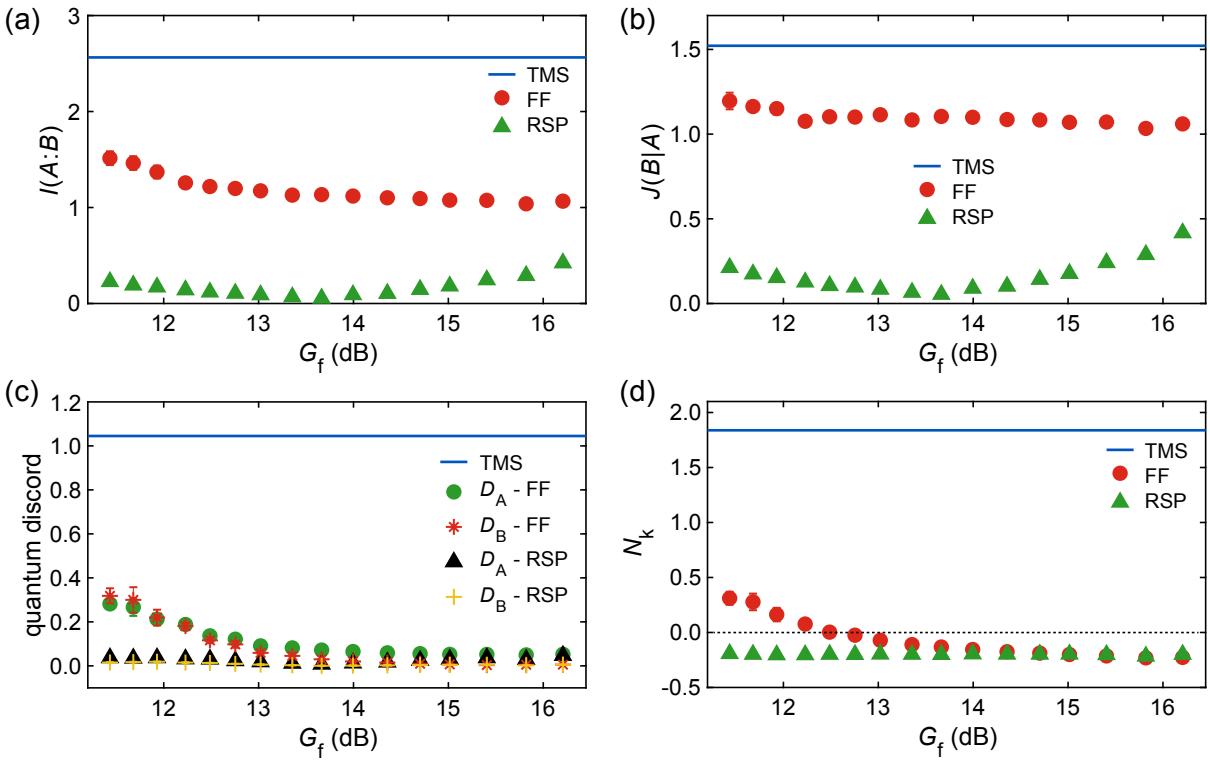

Figure 5.15: (a) Mutual information $I(A:B)$, (b) one-way classical correlations $J(B|A)$, (c) quantum discord, and (d) negativity kernel N_k at different stages of the RSP protocol. The data point for $G_\mathrm{f} \simeq 12\,\mathrm{dB}$ for the FF stage is averaged over two adjacent γ_f values around $\gamma_\mathrm{f} = 0°$.

serving as the entangled resource for RSP. After the local phase-sensitive amplification by JPA 3 on Alice's side, we observe a reduced $I(A:B)$ which further decreases with increasing G_f. The mutual information $I(A:B)$ consists both of classical and quantum correlations between A and B. Notably, the one-way classical correlation $J(B|A)$ is much less affected by the amplification of JPA 3 than the quantum correlations quantified by quantum discord. The latter is drastically reduced in the FF stage and nearly vanishes for high G_f. Quantum entanglement, quantified by the negativity kernel N_k, is also strongly affected by the action of JPA 3. The reduced classical and quantum correlations can be attributed to the added noise by JPA 3 during the amplification process and path losses of the propagating signals.

Finally, the RSP stage is considered, where we perform the RSP protocol as described in Sec. 5.1 while simultaneously detecting the second output of the directional coupler on Bob's side. Here, A is the path corresponding to the second output of the directional coupler, which mainly consists of the feedforward signal, and B denotes the path of the prepared state in RSP. For all feedforward parameters G_f and γ_f, the states at the RSP stage are separable with $N_\mathrm{k} < 0$. Furthermore, most correlations are consumed, resulting in comparatively small $I(A:B)$ if compared to the other two stages. At the optimal JPA 3 gain $G_\mathrm{f} \simeq 13.7\,\mathrm{dB}$, we observe nearly vanishing classical and quantum correlations.

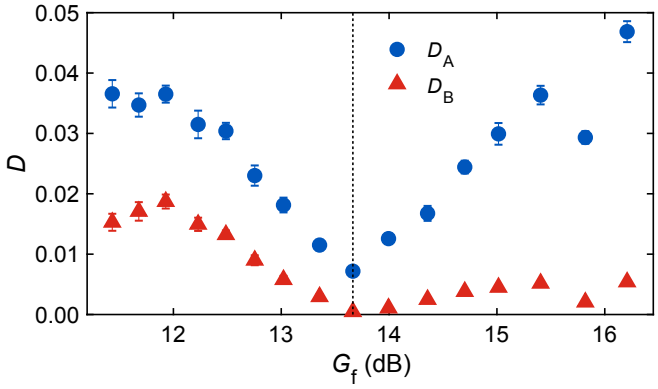

Figure 5.16: Quantum discord as a function of G_f at the optimal amplification angle $\gamma_f = 0°$ at the RSP stage. The dashed line marks the optimal JPA 3 gain $G_f = 13.7\,\mathrm{dB}$. If not shown, the standard error of the mean is smaller than the symbol size.

This observation indicates the operational meaning of $I(A:B)$ since a larger correlation consumption during RSP leads to more optimally prepared states. For non-optimal G_f, the quantum discord D_B is nearly completely consumed while some classical correlations remain in the RSP stage. In Fig. 5.16, we show both values of quantum discord in the RSP stage at the optimal amplification angle $\gamma_f = 0°$ (see Appendix C for the full dependence of quantum discord on G_f and γ_f). Similar to the FF stage, we observe $D_A > D_B$ for the same feedforward parameters indicating that the states at A are better distinguishable than the states at B. Towards optimal G_f, the values of both D_A and D_B decrease. At the optimal point, D_B is vanishingly small while D_A is roughly one order of magnitude larger than D_B. Consequently, the initial correlations are most efficiently used at the optimal operation point of RSP where squeezed state with the highest squeezing level and purity are remotely prepared. This observation illustrates that correlations are essential for RSP. In our current implementation of RSP, we can only optimally utilize the correlations for $\gamma_f = 0°$ since the correlated quadratures in the TMS resource state are fixed during the experiments. Consequently, only one JPA 3 amplification angle exists at which a correlated quadrature at Alice's side is amplified optimally in respect to the corresponding quadrature at Bob's side. Then, Bob's local displacement, which is proportional to the feedforward signal, allows for a reduction of the variance below the vacuum limit in one particular quadrature direction.

5.2.4 Bit-rates in remote state preparation

Finally, we discuss different types of bit-rates in the RSP protocol. First, we calculate the entangled bit-rate during the TMS stage. As discussed in Sec. 4.2.2, the entanglement of formation E_F can be utilized for that task since $E_F \simeq 1$ corresponds to one pair of maximally entangled qubits. From the measurement bandwidth $\Omega = 430\,\mathrm{kHz}$ and $E_f = 1.16$, we obtain the upper bound on the entangled bit-rate of $5.0 \times 10^5\,\mathrm{ebits} \cdot \mathrm{s}^{-1}$.

The maximal classical bit rate of the feedforward channel and remotely prepared state channel can be estimated using the Shannon-Hartley theorem [221]

$$C = \Omega \log_2 \left(1 + \frac{S}{N}\right) , \tag{5.8}$$

where C is the channel capacity in bits/s, Ω is the bandwidth, S is the signal power, and N is the average noise power of Gaussian white noise. The theorem provides an upper limit for the maximal bit-rate transmitted over a channel under Gaussian white noise. In our scenario, we assume that the signals are detected with the amplification chains utilized in our experiments. The noise in the amplification chain is dominated by the noise added during the amplification by the cryogenic HEMT amplifiers and is typically around $n_{\mathrm{amp}} \simeq 10$ photons. During the FF stage, the feedforward signal has a mean photon number $n_{\mathrm{f}} \simeq 33$ at the optimal point. By using $n_{\mathrm{f}}/n_{\mathrm{amp}} = S/N$, we find a channel capacity of the feedforward $C_{\mathrm{f}} = 9.1 \times 10^5\,\mathrm{bits} \cdot \mathrm{s}^{-1}$. We calculate the channel capacity corresponding to the final prepared state at the optimal point with $n_{\mathrm{rp}} = 0.8$ in the same way and obtain $C_{\mathrm{rp}} = 4.8 \times 10^4\,\mathrm{bits} \cdot \mathrm{s}^{-1}$. Consequently, the channel capacity of the feedforward is higher than the one of the final state, which is expected due to the higher mean photon numbers in the feedforward signal.

In an alternative approach, we directly estimate the classical bit-rate of RSP from the reconstructed quantum states. As discussed previously, the prepared squeezed states are described by three real parameters. For the following analysis, we will use the squeezed variance σ_{s}, antisqueezed variance σ_{a}, and the squeezing angle γ_{rp} of the remotely prepared states at the optimal point. In contrast to Sec. 5.1.5, here, we use a direct approach to estimate the number of classical bits encoded in the parameters of the prepared states. For that, we consider that the three parameters are only reconstructed with a certain precision during our experiments. In order to estimate the precision, we repeat the preparation of a squeezed state at the optimal point multiple times and calculate the mean and standard error of the mean for every parameters. In a simple approach, the precision is given by the significant digits of the three parameters up to the digit limited by the standard error of the mean. Consecutively, we calculate the number of bits required to express the three truncated parameters and obtain a number of 22 bits. Every respective reconstruction takes 125 s which leads us to an uncorrected bit-rate of $0.2\,\mathrm{bits} \cdot \mathrm{s}^{-1}$. We note that the latter bit-rate is directly estimated without any corrections or optimization of the measurement procedure. Higher rates could be easily achieved by optimizing the measurement scheme in a way that only the remotely prepared states are measured. If, in addition, the data transfer and processing are improved such that we are limited by the sampling rate of the digitizer card of 400 MHz, we expect bit-rates of $23\,\mathrm{bits} \cdot \mathrm{s}^{-1}$. Nevertheless, the direct estimate of the bit-rate is much lower than the one from the channel capacities since our implementation of RSP has not been yet optimized for transmission of classical information.

5.3 Quantum one-time pad

Secure communication between parties is a permanently relevant subject. Nowadays commonly-used classical encryption techniques typically rely on a so-called computational complexity to provide security [222]. With the steady progress towards building large-scale quantum processors, new ways for secure communication are required since some classically complex problems can be efficiently solved on a quantum computer [223]. One prominent example of secure protocols against the computing power of quantum computers is quantum key distribution (QKD), as discussed in Sec. 2.3.3. The security in QKD protocols stems from the fact that they are not based on computational complexity but rather on unique properties of quantum-mechanical systems such as superposition or entanglement [147]. Also, in QKD protocols, the no-cloning theorem plays a central role as it ensures that an eavesdropper can only gain a certain amount of information on the publicly communicated quantum states from which the secret keys are generated. However, QKD is only one class of applications in the broader field of quantum cryptography which encompasses a variety of protocols. In the following, we investigate how the RSP scheme can be applied to securely send information from one party to another.

We now relate our experimental RSP scheme to the cryptographic protocol known as the one-time pad [144] by extending the latter to the quantum regime [132, 224]. Both the classical and quantum version of the one-time pad allow for information-theoretic security. In our case, Alice aims to securely send a quantum state M to Bob over an insecure channel. We identify the transmitted message M as the remotely prepared state on Bob's side and the openly communicated cipher C as the feedforward signal (see Fig. 5.17). The entangled TMS state provides the random key K in the form of correlated quantum fluctuations to both parties. Note that K is essential for the one-time pad since it is used by Alice and Bob to encode and decode M. For secure communication, K needs to be a uniform random variable, such that an eavesdropper with knowledge about C does not gain any information about M [145]. Formally, we can write this security criterion in the

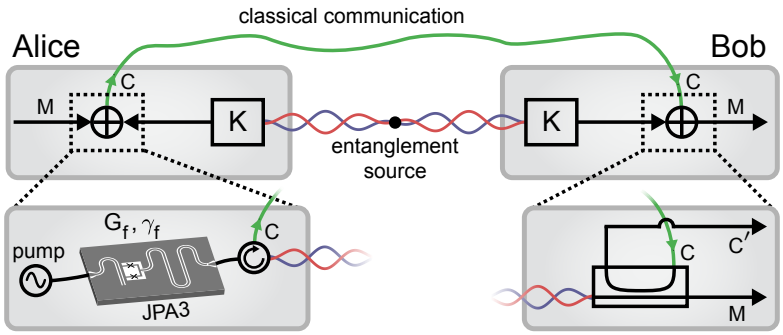

Figure 5.17: Interpretation of the RSP setup in terms of the one-time pad. Here, the message M is a prepared squeezed state, the cipher C is the classical communication, and the key K is provided by an entangled resource. Intertwined red-blue lines symbolize the entanglement.

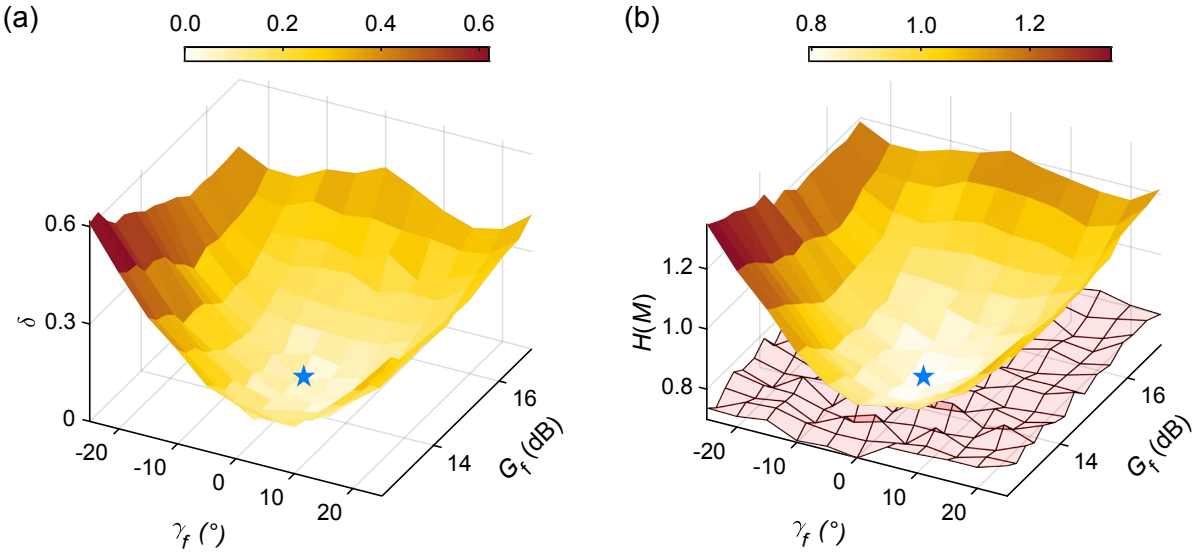

Figure 5.18: (a) Entropy difference $\delta = H(M) - H(M|C')$ as a function of the feedforward gain G_f and angle γ_f. (b) Entropy $H(M)$ of remotely prepared states. The red shaded area is the conditional entropy $H(M|C')$. The optimal point is marked by the blue star.

following form

$$H(M) - H(M|C) = 0\,, \tag{5.9}$$

where $H(M)$ is the von Neumann entropy of the remotely prepared state and $H(M|C)$ is the conditional entropy of M given the feedforward signal. The conditional entropy is defined as $H(M|C) = H(M,C) - H(C)$, where $H(M,C)$ is the joint entropy and $H(C)$ is the entropy of the cipher (see Sec. 2.1.4 for details). We experimentally investigate the quantum one-time pad by measuring the prepared states as a function of the JPA 3 parameters while additionally detecting the signal C' from the second output of the directional coupler. Otherwise, the experimental setup and pulse modulation are the same as in Sec. 5.1. We compute $\delta = H(M) - H(M|C')$ to verify Eq. (5.9) under the approximation $C' \approx C$ using state tomography. The latter relation is justified by the high transmissivity of the directional coupler $\tau \simeq 1$. In Fig. 5.18 (a), we observe a decrease in δ when moving towards the optimal point where the smallest value $\delta = 0.06 \pm 0.04$ is reached and the entropy of the prepared state is $H(M) = 0.80 \pm 0.02$. The observation $\delta \ll H(M)$ indicates that the remote preparation of a quantum state on Bob's side is close to perfect security when approaching the optimal point. Upon a deviation from the optimal point, the entropy of the prepared state increases, as shown in Fig. 5.18 (b). However, $H(M|C')$ is approximately constant for the experimental range of G_f and γ_f which results in increasing δ when moving away from the optimal point. Consequently, there is a trade-off between the security and range of prepared states. We do not reach $\delta = 0$ inside the statistical error in the experiment. The biggest contribution to this deviation is caused by non-optimal JPA 3 parameters. From model calculations, we expect

to obtain $\delta \simeq 2 \times 10^{-3}$ upon fine-tuning the JPA 3 gain and amplification angle. In order to approach the perfect secrecy scenario ($\delta = 0$), the protocol needs to be ideal, i.e., no losses and vanishing JPA noise. As mentioned in Sec. 5.1, a straightforward extension of the optimal working range of RSP can be realized by adding a phase shifter on Alice's side. Then, all optimally prepared states would correspond to minimal δ for arbitrary squeezing angles while the accessible squeezing level and purity stay unaffected. However, also in this scenario, the protocol needs to be ideal in order to reach $\delta = 0$.

Equation (5.9) only ensures security against an eavesdropper (Eve) who has access solely to the cipher C. However, other types of attacks are also possible. In general, an eavesdropper who exclusively listens to the two-mode squeezed resource state (random key K), will not be able to gain any information about the desired prepared state (message M) since the latter is encoded by Alice. To gain information about the prepared state, Eve would need to additionally intercept the feedforward signal. Also, Eve's interaction with the entangled resource would most probably reduce the entanglement between Alice and Bob which reduces the purity and squeezing level of the prepared states. The reduction of the latter quantities under the actions of the eavesdropper on the TMS states potentially allows Bob to detect the presence of Eve. For example, Eve could be detected in a scenario where Alice and Bob arrange to only prepare squeezed states with squeezing below the vacuum level. It is only possible to remotely prepare states with squeezing below the vacuum limit if Alice and Bob share at least some finite entanglement. Therefore, Bob can directly notice the presence of an entanglement-breaking eavesdropper from a suddden change of the squeezing level of prepared states on his side.

The results presented in this section have been published by us in Ref. [47]. Parts of the text and figures are adapted from this reference.

Summary

We have successfully implemented a deterministic RSP protocol over a distance of 35 cm in the microwave regime with continuous variables and explored the influence of different parameters on the remotely prepared states. We have demonstrated the remote preparation of squeezed states with a squeezing level of up to 1.6 dB below the vacuum limit and a purity of 0.54. By increasing the entanglement strength, we have been able to achieve squeezing levels up to 1.7 dB while reducing the purity to 0.49. Furthermore, in our specific RSP implementation and for fixed entanglement strength, Alice can control the squeezing level and, to some extent, the squeezing angle of the remotely prepared state at the expense of a reduced purity. Additionally, we demonstrate that the protocol can be interpreted as a secure one-time pad near the optimal point. The operational range of both the RSP and quantum one-time pad protocols can be extended to any angle γ_{rp} by an additional phase shifter on Alice's side. The demonstrated protocol opens up new possibilities for a multitude of intriguing experiments with quantum microwaves such as probing the Holevo bound limits [225], studying the role of quantum discord in quantum

communication protocols [226], exploring hybrid continuous-discrete schemes of quantum information processing [14], and implementing quantum illumination protocols [49]. Squeezing operations can further be exploited for the preparation of Gottesman-Kitaev-Preskill (GKP) states for continuous-variable quantum error correction [161, 162]. Our experiment proves that prototypical local quantum networks using continuous-variable quantum microwaves are within experimental reach.

Chapter 6

Conclusion and outlook

In this thesis, we develop fundamental concepts and techniques for quantum communication with propagating quantum microwaves. In our experimental approach, we use superconducting quantum circuits operated in the microwave regime which presently are considered the most promising technology platform for building a scalable quantum computer. Therefore, the development of efficient techniques for communication between such future quantum processors become a necessity. We utilize superconducting quantum circuits and linear circuit elements to generate propagating two-mode squeezed (TMS) states which serve as an entangled resource for advanced experiments. In particular, we successfully apply them as a resource in a fundamental quantum communication protocol, namely, remote state preparation.

In our experiments, superconducting Josephson parametric amplifiers (JPA) play a central role. We employ them for the generation and manipulation of propagating quantum microwaves. During this thesis, we have developed routine methods for the characterization and calibration of multiple JPAs in a single experiment. These developments are essential as they allow us to utilize multiple JPAs for advanced quantum communication protocols. If employed as generators of squeezed states, the JPAs can routinely produce squeezed states with squeezing levels up to 10 dB below the vacuum limit.

As a first main result, we have successfully demonstrated the generation of propagating TMS microwave states. We have achieved this task by superimposing two squeezed states with the same squeezing level but orthogonal squeezing angles at a microwave hybrid ring acting as a 50:50 beam splitter. The resulting TMS states possess path entanglement between the hybrid ring outputs manifesting itself in nonlocal correlations between quadratures in different paths. We have produced balanced TMS states with nearly vanishing self-correlations. This clearly demonstrates our ability to precisely control the properties of the squeezed states. We have reached record entanglement strengths quantified by the negativity of up to 3.9 which corresponds to a two-mode squeezing level of 9.4 dB.

Furthermore, we have systematically characterized the properties of the TMS states as a prerequisite for their application in future experiments. First, the behavior against finite-time delays between the propagation paths of the TMS states has been clarified. We

have found that, for low squeezing levels, the TMS states remain entangled for asymmetric time delays of up to 1 μs, whereas the maximally acceptable delay, until the entanglement disappears, decreases for increasing squeezing level. We also found that a wider detection bandwidth decreases the tolerable time delays. Second, we have investigated the influence of environmental noise on the propagating TMS states in detail. This is crucial for practical implementations of quantum communication protocols. We have discovered a sudden death of entanglement when adding roughly one noise photon to one path of the TMS state. This sudden death of entanglement is found to be independent of the initial entanglement strength. Third, we have studied quantum discord which quantifies quantum correlations beyond entanglement. Interestingly, quantum discord in our TMS states is found to be asymptotically robust against both finite-time delays and environmental noise.

A key result of this thesis is the first successful realization of deterministic remote state preparation (RSP) with continuous-variable quantum microwaves. To this end, we have employed the TMS states as an entangled resource and an additional JPA as a phase-sensitive low-noise amplifier for the generation of a feedforward signal. In this way, party A can remotely prepare a known quantum state at a distant location B. In our prototypical experiment, the distance between A and B was set to be 35 cm, and thus, the propagation distance of the feedforward signal encompasses multiple signal wavelengths. We have remotely prepared squeezed states with squeezing levels of up to 1.7 dB below the vacuum limit and a purity of $\simeq 0.50$ at the optimal operation point. We have found good agreement between our experimental results and a theoretical model description based on the input-output formalism. In addition, we have explored how the entanglement strength influences the range of preparable states in RSP. As predicted by our theoretical model, the squeezing level of the prepared states increases for increasing entanglement strengths. Also, the classical and quantum correlations in different stages of the RSP protocol have been studied where we have observed that, at the optimal point of RSP, most correlations are used up after the protocol. Finally, we have clarified the relation of the RSP scheme to an extension of the one-time pad cryptographic protocol into the quantum regime. We have succeeded to implement close-to-perfectly secure communication of a quantum state in the vicinity of the optimal point of RSP.

The fundamental studies and technical developments achieved in this thesis lay the foundations for further research on propagating quantum microwaves and their application on advanced quantum communication protocols. In future experiments, different technical details can be optimized. First, the generation of the path-entangled TMS resource states can be simplified by integrating two JPAs and a hybrid ring on a single chip. This approach would avoid additional connection losses between the different components, resulting in TMS states with a higher purity and squeezing level. Towards the fabrication of quantum circuits with a higher degree of integration, recently a JPA and a superconducting qubit have been integrated on a single chip in order to provide a more efficient qubit readout [124]. Second, the measurement times can be significantly reduced by utilizing a modern field

programmable gate array (FPGA) for data processing. With an increased measurement efficiency, the phase stability of squeezed states between measurements will be improved and states with high squeezing levels can be reconstructed more reliably. We also note that, FPGAs are essential for experiments with digital feedforward as the time delays for state tomography must not exceed a few hundred nanoseconds. Third, the reduction of path losses will increase the purity and fidelity of quantum states in future experiments. The detailed analysis of the RSP protocol shows that presently we are limited to a large extent by connection and insertion losses of different components in the current experimental setup. The reduction of losses can be achieved by using optimized cable connectors, superconducting hybrid rings, and superconducting on-chip circulators.

In the near future, we plan to utilize the same toolbox as in RSP to realize deterministic quantum teleportation of squeezed microwave states [131]. Assuming similar losses and JPA performances as in the current RSP implementation, we expect fidelities of the teleported state of around 0.85. This fidelity could be further improved by reducing microwave losses and optimizing the noise performance of the JPAs. Furthermore, it is interesting to consider the application of propagating quantum microwaves in continuous-variable quantum key distribution schemes. Here, a key challenge is the efficient detection of microwave signals in order to achieve high key rates.

On a longer timescale, we envision a realization of a small local quantum network using propagating microwaves where quantum information can be communicated via teleportation or RSP schemes. Here, a central element is the realization of a cryogenic link between nodes in the quantum network which would enable the realization of such schemes.

Appendix A

JPA Hamiltonian in the interaction picture

In order to illustrate the connection of a JPA to a degenerate parametric amplifier, we write the JPA Hamiltonian in the interaction picture. Doing so, we start with the Hamiltonian $\hat{H}$ of a flux-driven JPA given in Eq. (2.85) and assume a flux pump with phase $\tilde{\varphi}$ at twice the resonance frequency ω_0. Then, the Hamiltonian takes the form

$$\hat{H} = \hbar\omega_0 \left[\hat{a}^\dagger\hat{a} + \frac{1}{2} + \epsilon\cos(2\omega_0 t - \tilde{\varphi})(\hat{a} + \hat{a}^\dagger)^2\right] = \hat{H}_0 + \hat{H}_1(t)\,, \tag{A.1}$$

where $\hat{H}_0 = \hbar\omega_0\hat{a}^\dagger\hat{a} + 1/2$, $\hat{H}_1(t) = \hbar\omega_0\epsilon\cos(2\omega_0 t - \tilde{\varphi})(\hat{a} + \hat{a}^\dagger)^2$, and $\epsilon/2$ is the amplitude of the frequency modulation which depends on the pump strength. The transformation of a Hamiltonian to the interaction picture is a unitary transformation with the unitary operator $\hat{U} = e^{iH_0 t/\hbar}$. The JPA Hamiltonian in the interaction picture then reads

$$\hat{H}_I = \hat{U}\hat{H}\hat{U}^\dagger - i\hbar\hat{U}\left(\frac{\partial}{\partial t}\hat{U}^\dagger\right) = \hat{U}\hat{H}_1(t)\hat{U}^\dagger\,, \tag{A.2}$$

where we used

$$\hat{U}\hat{H}\hat{U}^\dagger = \hat{H}_0 + \hat{U}\hat{H}_1(t)\hat{U}^\dagger\,, \tag{A.3}$$

$$i\hbar\hat{U}\left(\frac{\partial}{\partial t}\hat{U}^\dagger\right) = -H_0\,. \tag{A.4}$$

By using the relations

$$\hat{U}\,\hat{a}^2\,\hat{U}^\dagger = \hat{a}^2 e^{-2i\omega_0 t}\,, \tag{A.5}$$

$$\hat{U}\,(\hat{a}^\dagger)^2\,\hat{U}^\dagger = (\hat{a}^\dagger)^2 e^{2i\omega_0 t}\,, \tag{A.6}$$

$$\hat{U}\,\hat{a}^\dagger\hat{a}\,\hat{U}^\dagger = \hat{a}^\dagger\hat{a}\,, \tag{A.7}$$

and the commutation relation $[\hat{a}, \hat{a}^\dagger] = 1$, we arrive at

$$\hat{H}_I = \hbar \frac{\omega_0 \epsilon}{2} \left(e^{2i\omega_0 t - i\tilde{\varphi}} + e^{-2i\omega_0 t + i\tilde{\varphi}} \right) \left(\hat{a}^2 e^{-2i\omega_0 t} + (\hat{a}^\dagger)^2 e^{2i\omega_0 t} + 2\hat{a}^\dagger \hat{a} + 1 \right) , \tag{A.8}$$

where we additionally express the cosine in terms of exponential functions. We are only interested in slowly oscillating terms. Therefore, we apply the rotating wave approximation where we neglect terms oscillating with frequencies $\omega \gg \omega_0$ and obtain

$$\hat{H}_I = \hbar \frac{\omega_0 \epsilon}{2} \left(\hat{a}^2 e^{-i\tilde{\varphi}} + (\hat{a}^\dagger)^2 e^{i\tilde{\varphi}} \right) . \tag{A.9}$$

Finally, we introduce the effective frequency modulation $\lambda = \omega_0 \epsilon$ and shift the pump phase by $\pi/2$ such that $\tilde{\varphi} = \varphi - \pi/2$. The resulting Hamiltonian

$$\hat{H}_I = i\hbar \frac{\lambda}{2} \left(\hat{a}^2 e^{-i\varphi} - (\hat{a}^\dagger)^2 e^{i\varphi} \right) \tag{A.10}$$

is equivalent to the Hamiltonian of a degenerate parametric amplifier [16, 177].

Appendix B

Full model for remote state preparation

Here, we present the full analytic expressions for the prepared state during remote state preparation (RSP) calculated in `Mathematica`. The expressions depend on the noise photon number n, squeezing factor r, and squeezing angles (γ_1 and γ_2) of JPA 1 and JPA 2 as well as the degenerate gain G_f, amplification angle γ_f, and noise photon number n_f of JPA 3. Furthermore, the prepared state is affected by the losses ϵ, η_1, and η_2. Details on the model are given in Sec. 2.3.2.

The final state is a single-mode squeezed state with a covariance matrix

$$\mathbf{V} = \begin{pmatrix} V_{11} & V_{12} \\ V_{12} & V_{22} \end{pmatrix}, \tag{B.1}$$

where

$$\begin{aligned}
V_{11} = \frac{e^{-2r}}{64\,G_\mathrm{f}}\Big\{ & 2n\epsilon\cos(2\gamma_2-4\gamma_\mathrm{f})\eta_1-2n\epsilon\tau\cos(2\gamma_2-4\gamma_\mathrm{f})\eta_1-\epsilon\tau\cos(2\gamma_2-4\gamma_\mathrm{f})\eta_1-16\tau e^{2r}G_\mathrm{f}- \\
& 8(e^{4r}-1)(1+2n)\sin(\gamma_1-\gamma_2)\sin(\gamma_1+\gamma_2-2\gamma_\mathrm{f})\lambda G_\mathrm{f}-4(\tau-1)e^{2r}\sin^2(\gamma_\mathrm{f})(8n_\mathrm{f}+4)- \\
& 4(\tau-1)\sin^2(\gamma_\mathrm{f})\epsilon\left[2(2n-2e^{2r}+e^{4r}(1+2n)+1)+(e^{4r}-1)(1+2n)(C_{13}+C_{23})\right]\eta_1 G_\mathrm{f}^2- \\
& 8(e^{4r}-1)(1+2n)\epsilon(\tau-1)G_\mathrm{f}\cos(\gamma_1-\gamma_2)\sin(2\gamma_\mathrm{f})\sin(\gamma_1+\gamma_2-2\gamma_\mathrm{f})\eta_1+ \\
& 4\tau\epsilon G_\mathrm{f}\left[-2(2n-2e^{2r}+e^{4r}(1+2n)+1)+(e^{4r}-1)(1+2n)(\cos(2\gamma_1)+\cos(2\gamma_2))\right]\eta_2+ \\
& 8e^{2r}-8e^{2r}\tau+8e^{2r}\cos(2\gamma_\mathrm{f})-8e^{2r}\tau\cos(2\gamma_\mathrm{f})-4e^{4r}\cos(2\gamma_1)\lambda-8e^{4r}n\cos(2\gamma_1)\lambda+8n\cos(2\gamma_1)\lambda+ \\
& 4\cos(2\gamma_1)\lambda+4e^{4r}\cos(2\gamma_2)\lambda+8e^{4r}n\cos(2\gamma_2)\lambda-8n\cos(2\gamma_2)\lambda-4\cos(2\gamma_2)\lambda- \\
& 4e^{4r}C_{13}\lambda-8e^{4r}nC_{13}\lambda+8nC_{13}\lambda+4C_{13}\lambda+4e^{4r}C_{23}\lambda+8e^{4r}nC_{23}\lambda-8nC_{23}\lambda-4C_{23}\lambda- \\
& 4e^{4r}\cos(2\gamma_1)\lambda G_\mathrm{f}-8e^{4r}n\cos(2\gamma_1)\lambda G_\mathrm{f}+8n\cos(2\gamma_1)\lambda G_\mathrm{f}+4\cos(2\gamma_1)\lambda G_\mathrm{f}+4e^{4r}\cos(2\gamma_2)\lambda G_\mathrm{f}+ \\
& 8e^{4r}n\cos(2\gamma_2)\lambda G_\mathrm{f}-8n\cos(2\gamma_2)\lambda G_\mathrm{f}-4\cos(2\gamma_2)\lambda G_\mathrm{f}-32e^{2r}(\tau-1)\cos^2(\gamma_\mathrm{f})n_\mathrm{f}-8e^{2r}\epsilon\eta_1+ \\
& 4e^{4r}\epsilon\eta_1+8e^{4r}n\epsilon\eta_1+8n\epsilon\eta_1+4\epsilon\eta_1+8e^{2r}\epsilon\tau\eta_1-4e^{4r}\epsilon\tau\eta_1-8e^{4r}n\epsilon\tau\eta_1-8n\epsilon\tau\eta_1-4\epsilon\tau\eta_1- \\
& e^{4r}\epsilon\cos(2\gamma_1)\eta_1-2e^{4r}n\epsilon\cos(2\gamma_1)\eta_1+2n\epsilon\cos(2\gamma_1)\eta_1+\epsilon\cos(2\gamma_1)\eta_1+e^{4r}\epsilon\tau\cos(2\gamma_1)\eta_1+ \\
& 2e^{4r}n\epsilon\tau\cos(2\gamma_1)\eta_1-2n\epsilon\tau\cos(2\gamma_1)\eta_1-\epsilon\tau\cos(2\gamma_1)\eta_1-e^{4r}\epsilon\cos(2\gamma_2)\eta_1-2e^{4r}n\epsilon\cos(2\gamma_2)\eta_1+ \\
& 2n\epsilon\cos(2\gamma_2)\eta_1+\epsilon\cos(2\gamma_2)\eta_1+e^{4r}\epsilon\tau\cos(2\gamma_2)\eta_1+2e^{4r}n\epsilon\tau\cos(2\gamma_2)\eta_1-2n\epsilon\tau\cos(2\gamma_2)\eta_1-
\end{aligned}$$

$$\epsilon\tau\cos(2\gamma_2)\eta_1 - 8e^{2r}\epsilon\cos(2\gamma_\mathrm{f})\eta_1 + 4e^{4r}\epsilon\cos(2\gamma_\mathrm{f})\eta_1 + 8e^{4r}n\epsilon\cos(2\gamma_\mathrm{f})\eta_1 + 8n\epsilon\cos(2\gamma_\mathrm{f})\eta_1 +$$
$$4\epsilon\cos(2\gamma_\mathrm{f})\eta_1 + 8e^{2r}\epsilon\tau\cos(2\gamma_\mathrm{f})\eta_1 - 4e^{4r}\epsilon\tau\cos(2\gamma_\mathrm{f})\eta_1 - 8e^{4r}n\epsilon\tau\cos(2\gamma_\mathrm{f})\eta_1 - 8n\epsilon\tau\cos(2\gamma_\mathrm{f})\eta_1 -$$
$$4\epsilon\tau\cos(2\gamma_\mathrm{f})\eta_1 - 2e^{4r}\epsilon C_{13}\eta_1 - 4e^{4r}n\epsilon C_{13}\eta_1 + 4n\epsilon C_{13}\eta_1 + 2\epsilon C_{13}\eta_1 + 2e^{4r}\epsilon\tau C_{13}\eta_1 + 4e^{4r}n\epsilon\tau C_{13}\eta_1 -$$
$$4n\epsilon\tau C_{13}\eta_1 - 2\epsilon\tau C_{13}\eta_1 - 2e^{4r}\epsilon C_{23}\eta_1 - 4e^{4r}n\epsilon C_{23}\eta_1 + 4n\epsilon C_{23}\eta_1 + 2\epsilon C_{23}\eta_1 + 2e^{4r}\epsilon\tau C_{23}\eta_1 +$$
$$4e^{4r}n\epsilon\tau C_{23}\eta_1 - 4n\epsilon\tau C_{23}\eta_1 - 2\epsilon\tau C_{23}\eta_1 - e^{4r}\epsilon\cos(2\gamma_1 - 4\gamma_\mathrm{f})\eta_1 - 2e^{4r}n\epsilon\cos(2\gamma_1 - 4\gamma_\mathrm{f})\eta_1 +$$
$$2n\epsilon\cos(2\gamma_1 - 4\gamma_\mathrm{f})\eta_1 + \epsilon\cos(2\gamma_1 - 4\gamma_\mathrm{f})\eta_1 + e^{4r}\epsilon\tau\cos(2\gamma_1 - 4\gamma_\mathrm{f})\eta_1 + 2e^{4r}n\epsilon\tau\cos(2\gamma_1 - 4\gamma_\mathrm{f})\eta_1 -$$
$$2n\epsilon\tau\cos(2\gamma_1 - 4\gamma_\mathrm{f})\eta_1 - \epsilon\tau\cos(2\gamma_1 - 4\gamma_\mathrm{f})\eta_1 - e^{4r}\epsilon\cos(2\gamma_2 - 4\gamma_\mathrm{f})\eta_1 - 2e^{4r}n\epsilon\cos(2\gamma_2 - 4\gamma_\mathrm{f})\eta_1 +$$
$$\epsilon\cos(2\gamma_2 - 4\gamma_\mathrm{f})\eta_1 + e^{4r}\epsilon\tau\cos(2\gamma_2 - 4\gamma_\mathrm{f})\eta_1 + 2e^{4r}n\epsilon\tau\cos(2\gamma_2 - 4\gamma_\mathrm{f})\eta_1\Big\}, \quad \text{(B.2)}$$

$$V_{22} = \frac{e^{-2r}}{32\,G_\mathrm{f}}\Big\{2\epsilon\tau\sin(\gamma_2)\sin(\gamma_2 - 2\gamma_\mathrm{f})\eta_1 + 4n\epsilon\tau\sin(\gamma_2)\sin(\gamma_2 - 2\gamma_\mathrm{f})\eta_1 +$$
$$8(1+2n)\cos(\gamma_\mathrm{f})\sin(\gamma_1 - \gamma_2)\sin(\gamma_1 + \gamma_2 - \gamma_\mathrm{f})\lambda G_\mathrm{f} - 2(\tau-1)e^{2r}\cos^2(\gamma_\mathrm{f})(8n_\mathrm{f} + 4) -$$
$$2(\tau-1)\cos^2(\gamma_\mathrm{f})\epsilon\left[2(2n - 2e^{2r} + e^{4r}(1+2n) + 1) + (e^{4r}-1)(1+2n)(C_{13} + C_{23})\right]\eta_1 G_\mathrm{f}^2 +$$
$$4(-1+e^{4r})(1+2n)\epsilon(\tau-1)G_\mathrm{f}\cos(\gamma_1 - \gamma_2)\sin(2\gamma_\mathrm{f})\sin(\gamma_1 + \gamma_2 - 2\gamma_\mathrm{f})\eta_1 +$$
$$2\tau G_\mathrm{f}\epsilon\left[2(2n - 2e^{2r} + e^{4r}(1+2n) + 1) + (e^{4r}-1)(1+2n)(\cos(2\gamma_1) + \cos(2\gamma_2))\right]\eta_2 +$$
$$4e^{2r} + 8e^{2r}\sin^2(\gamma_\mathrm{f}) - 8e^{2r}\tau\sin^2(\gamma_\mathrm{f}) + 4e^{4r}\cos^2(\gamma_1)\lambda + 8e^{4r}n\cos^2(\gamma_1)\lambda - 4e^{4r}\cos^2(\gamma_2)\lambda -$$
$$8e^{4r}n\cos^2(\gamma_2)\lambda + 8n\sin^2(\gamma_1)\lambda + 4\sin^2(\gamma_1)\lambda - 8n\sin^2(\gamma_2)\lambda - 4\sin^2(\gamma_2)\lambda - 4e^{4r}\cos(\gamma_1)\tilde{C}_{13}\lambda -$$
$$8e^{4r}n\cos(\gamma_1)\tilde{C}_{13}\lambda + 4e^{4r}\cos(\gamma_2)\tilde{C}_{23}\lambda + 8e^{4r}n\cos(\gamma_2)\tilde{C}_{23}\lambda - 8n\sin(\gamma_1)\sin(\gamma_1 - 2\gamma_\mathrm{f})\lambda -$$
$$4\sin(\gamma_1)\sin(\gamma_1 - 2\gamma_\mathrm{f})\lambda + 8n\sin(\gamma_2)\sin(\gamma_2 - 2\gamma_\mathrm{f})\lambda + 4\sin(\gamma_2)\sin(\gamma_2 - 2\gamma_\mathrm{f})\lambda + 4e^{4r}\cos^2(\gamma_1)\lambda G_\mathrm{f} +$$
$$8e^{4r}n\cos^2(\gamma_1)\lambda G_\mathrm{f} - 4e^{4r}\cos^2(\gamma_2)\lambda G_\mathrm{f} - 8e^{4r}n\cos^2(\gamma_2)\lambda G_\mathrm{f} + 4e^{4r}\cos(\gamma_1)\tilde{C}_{13}\lambda G_\mathrm{f} +$$
$$8e^{4r}n\cos(\gamma_1)\tilde{C}_{13}\lambda G_\mathrm{f} - 4e^{4r}\cos(\gamma_2)\tilde{C}_{23}\lambda G_\mathrm{f} - 8e^{4r}n\cos(\gamma_2)\tilde{C}_{23}\lambda G_\mathrm{f} - 16e^{2r}(\tau-1)\sin^2(\gamma_\mathrm{f})n_\mathrm{f} +$$
$$e^{4r}\epsilon\cos^2(\gamma_1)\eta_1 + 2e^{4r}n\epsilon\cos^2(\gamma_1)\eta_1 - e^{4r}\epsilon\tau\cos^2(\gamma_1)\eta_1 - 2e^{4r}n\epsilon\tau\cos^2(\gamma_1)\eta_1 + e^{4r}\epsilon\cos^2(\gamma_2)\eta_1 +$$
$$2e^{4r}n\epsilon\cos^2(\gamma_2)\eta_1 - e^{4r}\epsilon\tau\cos^2(\gamma_2)\eta_1 - 2e^{4r}n\epsilon\tau\cos^2(\gamma_2)\eta_1 + e^{4r}\epsilon\tilde{C}_{13}^2\eta_1 + 2e^{4r}n\epsilon\tilde{C}_{13}^2\eta_1 -$$
$$e^{4r}\epsilon\tau\tilde{C}_{13}^2\eta_1 - 2e^{4r}n\epsilon\tau\tilde{C}_{13}^2\eta_1 + e^{4r}\epsilon\tilde{C}_{23}^2\eta_1 + 2e^{4r}n\epsilon\tilde{C}_{23}^2\eta_1 - e^{4r}\epsilon\tau\tilde{C}_{23}^2\eta_1 - 2e^{4r}n\epsilon\tau\tilde{C}_{23}^2\eta_1 +$$
$$2n\epsilon\sin^2(\gamma_1)\eta_1 + \epsilon\sin^2(\gamma_1)\eta_1 - 2n\epsilon\tau\sin^2(\gamma_1)\eta_1 - \epsilon\tau\sin^2(\gamma_1)\eta_1 + 2n\epsilon\sin^2(\gamma_2)\eta_1 + \epsilon\sin^2(\gamma_2)\eta_1 -$$
$$2n\epsilon\tau\sin^2(\gamma_2)\eta_1 - \epsilon\tau\sin^2(\gamma_2)\eta_1 - 8e^{2r}\epsilon\sin^2(\gamma_\mathrm{f})\eta_1 + 8e^{2r}\epsilon\tau\sin^2(\gamma_\mathrm{f})\eta_1 + 2n\epsilon\sin^2(\gamma_1 - 2\gamma_\mathrm{f})\eta_1 +$$
$$\epsilon\sin^2(\gamma_1 - 2\gamma_\mathrm{f})\eta_1 - 2n\epsilon\tau\sin^2(\gamma_1 - 2\gamma_\mathrm{f})\eta_1 - \epsilon\tau\sin^2(\gamma_1 - 2\gamma_\mathrm{f})\eta_1 + 2n\epsilon\sin^2(\gamma_2 - 2\gamma_\mathrm{f})\eta_1 +$$
$$\epsilon\sin^2(\gamma_2 - 2\gamma_\mathrm{f})\eta_1 - 2n\epsilon\tau\sin^2(\gamma_2 - 2\gamma_\mathrm{f})\eta_1 - \epsilon\tau\sin^2(\gamma_2 - 2\gamma_\mathrm{f})\eta_1 - 2e^{4r}\epsilon\cos(\gamma_1)\tilde{C}_{13}\eta_1 -$$
$$4e^{4r}n\epsilon\cos(\gamma_1)\tilde{C}_{13}\eta_1 + 2e^{4r}\epsilon\tau\cos(\gamma_1)\tilde{C}_{13}\eta_1 + 4e^{4r}n\epsilon\tau\cos(\gamma_1)\tilde{C}_{13}\eta_1 - 2e^{4r}\epsilon\cos(\gamma_2)\tilde{C}_{23}\eta_1 -$$
$$4e^{4r}n\epsilon\cos(\gamma_2)\tilde{C}_{23}\eta_1 + 2e^{4r}\epsilon\tau\cos(\gamma_2)\tilde{C}_{23}\eta_1 + 4e^{4r}n\epsilon\tau\cos(\gamma_2)\tilde{C}_{23}\eta_1 - 4n\epsilon\sin(\gamma_1)\sin(\gamma_1 - 2\gamma_\mathrm{f})\eta_1 -$$
$$2\epsilon\sin(\gamma_1)\sin(\gamma_1 - 2\gamma_\mathrm{f})\eta_1 + 4n\epsilon\tau\sin(\gamma_1)\sin(\gamma_1 - 2\gamma_\mathrm{f})\eta_1 + 2\epsilon\tau\sin(\gamma_1)\sin(\gamma_1 - 2\gamma_\mathrm{f})\eta_1 -$$
$$4n\epsilon\sin(\gamma_2)\sin(\gamma_2 - 2\gamma_\mathrm{f})\eta_1 - 2\epsilon\sin(\gamma_2)\sin(\gamma_2 - 2\gamma_\mathrm{f})\eta_1\Big\}, \quad \text{(B.3)}$$

$$V_{12} = \frac{e^{-2r}}{64\,G_\mathrm{f}}\Big\{\epsilon\sin(2\gamma_2-4\gamma_\mathrm{f})\eta_1 - 2n\epsilon\tau\sin(2\gamma_2-4\gamma_\mathrm{f})\eta_1 - \epsilon\tau\sin(2\gamma_2-4\gamma_\mathrm{f})\eta_1 +$$
$$2e^{4r}n\epsilon\tau\sin(2\gamma_2-4\gamma_\mathrm{f})\eta_1 + e^{4r}\epsilon\tau\sin(2\gamma_2-4\gamma_\mathrm{f})\eta_1 - 2(\tau-1)e^{2r}\sin(2\gamma_\mathrm{f})(8n_\mathrm{f}+4) -$$
$$2(\tau-1)\sin(2\gamma_\mathrm{f})\epsilon\left[2(2n-2e^{2r}+e^{4r}(1+2n)+1)+(e^{4r}-1)(1+2n)(C_{13}+C_{23})\right]\eta_1 G_f^2 -$$
$$4(-1+e^{4r})(1+2n)\epsilon\cos(\gamma_1-\gamma_2)(2(\tau-1)\cos(2\gamma_\mathrm{f})\sin(\gamma_1+\gamma_2-2\gamma_\mathrm{f})\eta_1 - 2\tau\sin(\gamma_1+\gamma_2)\eta_2)G_f -$$
$$8e^{2r}\sin(2\gamma_\mathrm{f}) + 8e^{2r}\tau\sin(2\gamma_\mathrm{f}) + 4e^{4r}\sin(2\gamma_1)\lambda + 8e^{4r}n\sin(2\gamma_1)\lambda - 8n\sin(2\gamma_1)\lambda - 4\sin(2\gamma_1)\lambda -$$
$$4e^{4r}\sin(2\gamma_2)\lambda - 8e^{4r}n\sin(2\gamma_2)\lambda + 8n\sin(2\gamma_2)\lambda + 4\sin(2\gamma_2)\lambda + 4e^{4r}\sin(2\gamma_1)\lambda G_\mathrm{f} +$$
$$8e^{4r}n\sin(2\gamma_1)\lambda G_\mathrm{f} - 8n\sin(2\gamma_1)\lambda G_\mathrm{f} - 4\sin(2\gamma_1)\lambda G_\mathrm{f} - 4e^{4r}\sin(2\gamma_2)\lambda G_\mathrm{f} - 8e^{4r}n\sin(2\gamma_2)\lambda G_\mathrm{f} +$$
$$8n\sin(2\gamma_2)\lambda G_\mathrm{f} + 4\sin(2\gamma_2)\lambda G_\mathrm{f} + 16e^{2r}(\tau-1)\sin(2\gamma_\mathrm{f})n_\mathrm{f} + e^{4r}\epsilon\sin(2\gamma_1)\eta_1 + 2e^{4r}n\epsilon\sin(2\gamma_1)\eta_1 -$$
$$2n\epsilon\sin(2\gamma_1)\eta_1 - \epsilon\sin(2\gamma_1)\eta_1 - e^{4r}\epsilon\tau\sin(2\gamma_1)\eta_1 - 2e^{4r}n\epsilon\tau\sin(2\gamma_1)\eta_1 + 2n\epsilon\tau\sin(2\gamma_1)\eta_1 +$$
$$\epsilon\tau\sin(2\gamma_1)\eta_1 + e^{4r}\epsilon\sin(2\gamma_2)\eta_1 + 2e^{4r}n\epsilon\sin(2\gamma_2)\eta_1 - 2n\epsilon\sin(2\gamma_2)\eta_1 - \epsilon\sin(2\gamma_2)\eta_1 -$$
$$e^{4r}\epsilon\tau\sin(2\gamma_2)\eta_1 - 2e^{4r}n\epsilon\tau\sin(2\gamma_2)\eta_1 + 2n\epsilon\tau\sin(2\gamma_2)\eta_1 + \epsilon\tau\sin(2\gamma_2)\eta_1 + 8e^{2r}\epsilon\sin(2\gamma_\mathrm{f})\eta_1 -$$
$$4e^{4r}\epsilon\sin(2\gamma_\mathrm{f})\eta_1 - 8e^{4r}n\epsilon\sin(2\gamma_\mathrm{f})\eta_1 - 8n\epsilon\sin(2\gamma_\mathrm{f})\eta_1 - 4\epsilon\sin(2\gamma_\mathrm{f})\eta_1 - 8e^{2r}\epsilon\tau\sin(2\gamma_\mathrm{f})\eta_1 +$$
$$4e^{4r}\epsilon\tau\sin(2\gamma_\mathrm{f})\eta_1 + 8e^{4r}n\epsilon\tau\sin(2\gamma_\mathrm{f})\eta_1 + 8n\epsilon\tau\sin(2\gamma_\mathrm{f})\eta_1 + 4\epsilon\tau\sin(2\gamma_\mathrm{f})\eta_1 -$$
$$e^{4r}\epsilon\sin(2\gamma_1-4\gamma_\mathrm{f})\eta_1 - 2e^{4r}n\epsilon\sin(2\gamma_1-4\gamma_\mathrm{f})\eta_1 + 2n\epsilon\sin(2\gamma_1-4\gamma_\mathrm{f})\eta_1 + \epsilon\sin(2\gamma_1-4\gamma_\mathrm{f})\eta_1 +$$
$$e^{4r}\epsilon\tau\sin(2\gamma_1-4\gamma_\mathrm{f})\eta_1 + 2e^{4r}n\epsilon\tau\sin(2\gamma_1-4\gamma_\mathrm{f})\eta_1 - 2n\epsilon\tau\sin(2\gamma_1-4\gamma_\mathrm{f})\eta_1 - \epsilon\tau\sin(2\gamma_1-4\gamma_\mathrm{f})\eta_1 -$$
$$e^{4r}\epsilon\sin(2\gamma_2-4\gamma_\mathrm{f})\eta_1 - 2e^{4r}n\epsilon\sin(2\gamma_2-4\gamma_\mathrm{f})\eta_1 + 2n\epsilon\sin(2\gamma_2-4\gamma_\mathrm{f})\eta_1\Big\}. \quad \text{(B.4)}$$

Here, we use $\lambda = \epsilon\sqrt{(1-\tau)\tau G_\mathrm{f}\eta_1\eta_2}$, $C_{13} = \cos(2\gamma_1 - 2\gamma_\mathrm{f})$, $C_{23} = \cos(2\gamma_2 - 2\gamma_\mathrm{f})$, $\tilde{C}_{13} = \cos(\gamma_1 - 2\gamma_\mathrm{f})$, and $\tilde{C}_{23} = \cos(\gamma_2 - 2\gamma_\mathrm{f})$ in order to simplify the expressions. In order to describe our experimental results, the total electrical lengths as well as different path lengths are taken into account by the parameters γ_opt and θ_rp. For that, we substitute $\gamma_\mathrm{f} \to \gamma_\mathrm{f} + \gamma_\mathrm{opt}$ in Eqs. (B.2) to (B.4) and rotate the final state by an angle θ_rp according to Eq. (2.4).

Appendix C

Quantum discord at RSP stage

In Fig. C.1, we show the values of quantum discord, D_A and D_B, as a function of the feedforward parameters in the RSP protocol. The latter parameters are the JPA 3 gain G_f and amplification angle γ_f. As discussed in Sec. 5.2.3, we observe nearly vanishing quantum discord around the optimal point of RSP while $D_A > D_B$. However, for both D_A and D_B, we find a shift to negative γ_f in the characteristic "V-shape" which is observed in the squeezing level S_rp of the remotely prepared states. Also, there is no symmetry around a certain γ_f value which we observe in, e.g., the prepared squeezing level S_rp, antisqueezing level A_rp, or the purity μ. For the RSP parameters discussed in Sec. 5.1 (including the cross-talk), the shift and asymmetry are not reproduced by our theory model. However, they might be explained by a stronger cross-talk which, in general, causes an asymmetry in respect to the optimal γ_f. Furthermore, in the current model, we only consider a cross-talk to the squeezing angle of JPA 1. However, the squeezing level of JPA 1, and possibly JPA 2, is weakly affected by the cross-talk as well.

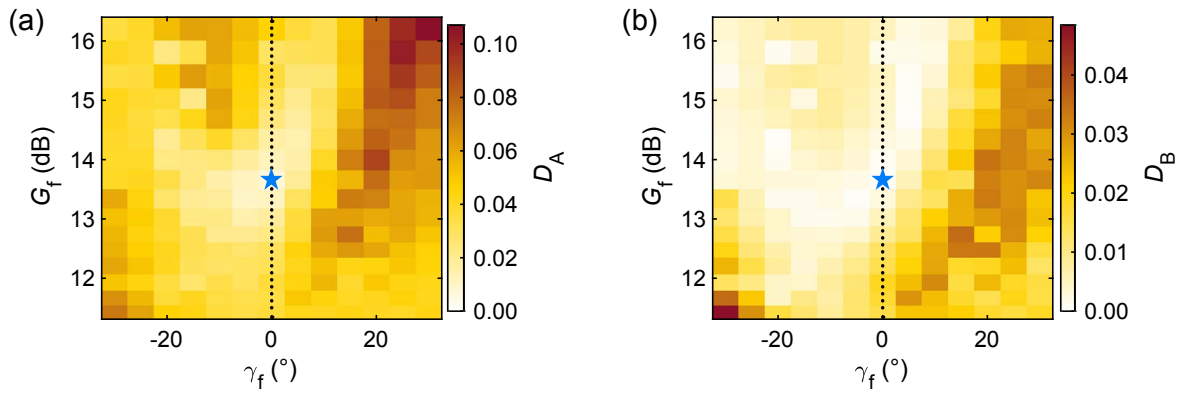

Figure C.1: Quantum discord (a) D_A and (b) D_B as a function of the feedforward parameters at the RSP stage. The optimal point is marked by the blue star. The dashed line marks the optimal amplification angle $\gamma_\mathrm{f} = 0°$.

Bibliography

[1] M. H. Devoret and R. J. Schoelkopf, "Superconducting Circuits for Quantum Information: An Outlook", Science **339**, 1169 (2013).

[2] N. Gisin, G. Ribordy, W. Tittel, and H. Zbinden, "Quantum cryptography", Rev. Mod. Phys. **74**, 145 (2002).

[3] N. Gisin and R. Thew, "Quantum communication", Nat. Photonics **1**, 165 (2007).

[4] L. Steffen, Y. Salathe, M. Oppliger, P. Kurpiers, M. Baur, C. Lang, C. Eichler, G. Puebla-Hellmann, A. Fedorov, and A. Wallraff, "Deterministic quantum teleportation with feed-forward in a solid state system", Nature **500**, 319 (2013).

[5] C. Gross and I. Bloch, "Quantum simulations with ultracold atoms in optical lattices", Science **357**, 995 (2017).

[6] S. Pirandola, B. R. Bardhan, T. Gehring, C. Weedbrook, and S. Lloyd, "Advances in photonic quantum sensing", Nat. Photonics **12**, 724 (2018).

[7] S. Lloyd, "Enhanced Sensitivity of Photodetection via Quantum Illumination", Science **321**, 1463 (2008).

[8] R. J. Schoelkopf and S. M. Girvin, "Wiring up quantum systems", Nature **451**, 664 (2008).

[9] A. Wallraff, D. I. Schuster, A. Blais, L. Frunzio, R. S. Huang, J. Majer, S. Kumar, S. M. Girvin, and R. J. Schoelkopf, "Strong coupling of a single photon to a superconducting qubit using circuit quantum electrodynamics", Nature **431**, 162 (2004).

[10] T. Niemczyk, F. Deppe, H. Huebl, E. P. Menzel, F. Hocke, M. J. Schwarz, J. J. Garcia-Ripoll, D. Zueco, T. Hümmer, E. Solano, A. Marx, and R. Gross, "Circuit quantum electrodynamics in the ultrastrong-coupling regime", Nat. Phys. **6**, 772 (2010).

[11] F. Arute et al., "Quantum supremacy using a programmable superconducting processor", Nature **574**, 505 (2019).

[12] P. Kurpiers, P. Magnard, T. Walter, B. Royer, M. Pechal, J. Heinsoo, Y. Salathé, A. Akin, S. Storz, J.-C. Besse, S. Gasparinetti, A. Blais, and A. Wallraff, "Deterministic quantum state transfer and remote entanglement using microwave photons", Nature **558**, 264 (2018).

[13] C. J. Axline, L. D. Burkhart, W. Pfaff, M. Zhang, K. Chou, P. Campagne-Ibarcq, P. Reinhold, L. Frunzio, S. M. Girvin, L. Jiang, M. H. Devoret, and R. J. Schoelkopf, "On-demand quantum state transfer and entanglement between remote microwave cavity memories", Nat. Phys. **14**, 705 (2018).

[14] U. L. Andersen, J. S. Neergaard-Nielsen, P. van Loock, and A. Furusawa, "Hybrid discrete- and continuous-variable quantum information", Nat. Phys. **11**, 713 (2015).

[15] C. Weedbrook, S. Pirandola, R. García-Patrón, N. J. Cerf, T. C. Ralph, J. H. Shapiro, and S. Lloyd, "Gaussian quantum information", Rev. Mod. Phys. **84**, 621 (2012).

[16] S. L. Braunstein and P. van Loock, "Quantum information with continuous variables", Rev. Mod. Phys. **77**, 513 (2005).

[17] A. Furusawa, J. L. Sørensen, S. L. Braunstein, C. A. Fuchs, H. J. Kimble, and E. S. Polzik, "Unconditional Quantum Teleportation", Science **282**, 706 (1998).

[18] S. L. Braunstein and H. J. Kimble, "Teleportation of Continuous Quantum Variables", Phys. Rev. Lett. **80**, 869 (1998).

[19] F. Grosshans, G. Van Assche, J. Wenger, R. Brouri, N. J. Cerf, and P. Grangier, "Quantum key distribution using gaussian-modulated coherent states", Nature **421**, 238 (2003).

[20] P. Jouguet, S. Kunz-Jacques, A. Leverrier, P. Grangier, and E. Diamanti, "Experimental demonstration of long-distance continuous-variable quantum key distribution", Nat. Photonics **7**, 378 (2013).

[21] K. Mattle, H. Weinfurter, P. G. Kwiat, and A. Zeilinger, "Dense Coding in Experimental Quantum Communication", Phys. Rev. Lett. **76**, 4656 (1996).

[22] B. Heim, C. Peuntinger, N. Killoran, I. Khan, C. Wittmann, C. Marquardt, and G. Leuchs, "Atmospheric continuous-variable quantum communication", New J. Phys. **16**, 113018 (2014).

[23] A. Narla, S. Shankar, M. Hatridge, Z. Leghtas, K. M. Sliwa, E. Zalys-Geller, S. O. Mundhada, W. Pfaff, L. Frunzio, R. J. Schoelkopf, and M. H. Devoret, "Robust Concurrent Remote Entanglement Between Two Superconducting Qubits", Phys. Rev. X **6**, 031036 (2016).

[24] K. Inomata, Z. Lin, K. Koshino, W. D. Oliver, J.-S. Tsai, T. Yamamoto, and Y. Nakamura, "Single microwave-photon detector using an artificial Λ-type three-level system", Nat. Commun. **7**, 12303 (2016).

[25] E. P. Menzel, R. Di Candia, F. Deppe, P. Eder, L. Zhong, M. Ihmig, M. Haeberlein, A. Baust, E. Hoffmann, D. Ballester, K. Inomata, T. Yamamoto, Y. Nakamura, E. Solano, A. Marx, and R. Gross, "Path Entanglement of Continuous-Variable Quantum Microwaves", Phys. Rev. Lett. **109**, 250502 (2012).

[26] C. Eichler, D. Bozyigit, C. Lang, L. Steffen, J. Fink, and A. Wallraff, "Experimental State Tomography of Itinerant Single Microwave Photons", Phys. Rev. Lett. **106**, 220503 (2011).

[27] B. Yurke, P. G. Kaminsky, R. E. Miller, E. A. Whittaker, A. D. Smith, A. H. Silver, and R. W. Simon, "Observation of 4.2-K equilibrium-noise squeezing via a Josephson-parametric amplifier", Phys. Rev. Lett. **60**, 764 (1988).

[28] B. Yurke, L. R. Corruccini, P. G. Kaminsky, L. W. Rupp, A. D. Smith, A. H. Silver, R. W. Simon, and E. A. Whittaker, "Observation of parametric amplification and deamplification in a Josephson parametric amplifier", Phys. Rev. A **39**, 2519 (1989).

[29] R. Movshovich, B. Yurke, P. G. Kaminsky, A. D. Smith, A. H. Silver, R. W. Simon, and M. V. Schneider, "Observation of zero-point noise squeezing via a Josephson-parametric amplifier", Phys. Rev. Lett. **65**, 1419 (1990).

[30] M. A. Castellanos-Beltran, K. D. Irwin, G. C. Hilton, L. R. Vale, and K. W. Lehnert, "Amplification and squeezing of quantum noise with a tunable Josephson metamaterial", Nat. Phys. **4**, 929 (2008).

[31] J. B. Clark, F. Lecocq, R. W. Simmonds, J. Aumentado, and J. D. Teufel, "Sideband cooling beyond the quantum backaction limit with squeezed light", Nature **541**, 191 (2017).

[32] A. Bienfait, P. Campagne-Ibarcq, A. H. Kiilerich, X. Zhou, S. Probst, J. J. Pla, T. Schenkel, D. Vion, D. Esteve, J. J. L. Morton, K. Moelmer, and P. Bertet, "Magnetic Resonance with Squeezed Microwaves", Phys. Rev. X **7**, 041011 (2017).

[33] A. Eddins, S. Schreppler, D. M. Toyli, L. S. Martin, S. Hacohen-Gourgy, L. C. G. Govia, H. Ribeiro, A. A. Clerk, and I. Siddiqi, "Stroboscopic Qubit Measurement with Squeezed Illumination", Phys. Rev. Lett. **120**, 040505 (2018).

[34] R. Vijay, D. H. Slichter, and I. Siddiqi, "Observation of Quantum Jumps in a Superconducting Artificial Atom", Phys. Rev. Lett. **106**, 110502 (2011).

[35] Z. R. Lin, K. Inomata, W. D. Oliver, K. Koshino, Y. Nakamura, J. S. Tsai, and T. Yamamoto, "Single-shot readout of a superconducting flux qubit with a flux-driven Josephson parametric amplifier", Appl. Phys. Lett. **103**, 132602 (2013).

[36] A. Einstein, B. Podolsky, and N. Rosen, "Can Quantum-Mechanical Description of Physical Reality Be Considered Complete?", Phys. Rev. **47**, 777 (1935).

[37] N. Lee, H. Benichi, Y. Takeno, S. Takeda, J. Webb, E. Huntington, and A. Furusawa, "Teleportation of Nonclassical Wave Packets of Light", Science **332**, 330 (2011).

[38] J.-W. Pan, D. Bouwmeester, H. Weinfurter, and A. Zeilinger, "Experimental Entanglement Swapping: Entangling Photons That Never Interacted", Phys. Rev. Lett. **80**, 3891 (1998).

[39] K. G. Fedorov, S. Pogorzalek, U. Las Heras, M. Sanz, P. Yard, P. Eder, M. Fischer, J. Goetz, E. Xie, K. Inomata, Y. Nakamura, R. Di Candia, E. Solano, A. Marx, F. Deppe, and R. Gross, "Finite-time quantum entanglement in propagating squeezed microwaves", Sci. Rep. **8**, 6416 (2018).

[40] H.-K. Lo, "Classical-communication cost in distributed quantum-information processing: A generalization of quantum-communication complexity", Phys. Rev. A **62**, 012313 (2000).

[41] A. K. Pati, "Minimum classical bit for remote preparation and measurement of a qubit", Phys. Rev. A **63**, 014302 (2000).

[42] C. H. Bennett, D. P. DiVincenzo, P. W. Shor, J. A. Smolin, B. M. Terhal, and W. K. Wootters, "Remote State Preparation", Phys. Rev. Lett. **87**, 077902 (2001).

[43] M. G. A. Paris, M. Cola, and R. Bonifacio, "Remote state preparation and teleportation in phase space", J. Opt. B **5**, S360 (2003).

[44] C. H. Bennett, G. Brassard, C. Crépeau, R. Jozsa, A. Peres, and W. K. Wootters, "Teleporting an unknown quantum state via dual classical and Einstein-Podolsky-Rosen channels", Phys. Rev. Lett. **70**, 1895 (1993).

[45] H. Le Jeannic, A. Cavaillès, J. Raskop, K. Huang, and J. Laurat, "Remote preparation of continuous-variable qubits using loss-tolerant hybrid entanglement of light", Optica **5**, 1012 (2018).

[46] J. Laurat, T. Coudreau, N. Treps, A. Maître, and C. Fabre, "Conditional Preparation of a Quantum State in the Continuous Variable Regime: Generation of a sub-Poissonian State from Twin Beams", Phys. Rev. Lett. **91**, 213601 (2003).

[47] S. Pogorzalek, K. G. Fedorov, M. Xu, A. Parra-Rodriguez, M. Sanz, M. Fischer, E. Xie, K. Inomata, Y. Nakamura, E. Solano, A. Marx, F. Deppe, and R. Gross, "Secure quantum remote state preparation of squeezed microwave states", Nat. Commun. **10**, 2604 (2019).

[48] S.-H. Tan, B. I. Erkmen, V. Giovannetti, S. Guha, S. Lloyd, L. Maccone, S. Pirandola, and J. H. Shapiro, "Quantum Illumination with Gaussian States", Phys. Rev. Lett. **101**, 253601 (2008).

[49] U. Las Heras, R. Di Candia, K. G. Fedorov, F. Deppe, M. Sanz, and E. Solano, "Quantum illumination reveals phase-shift inducing cloaking", Sci. Rep. **7**, 9333 (2017).

[50] D. F. Walls and G. J. Milburn, *Quantum Optics* (Springer, Berlin Heidelberg, 2008).

[51] U. Leonhardt and H. Paul, "Measuring the quantum state of light", Prog. Quantum Electron. **19**, 89 (1995).

[52] W. Heisenberg, "Über den anschaulichen Inhalt der quantentheoretischen Kinematik und Mechanik", Z. Phys. **43**, 172 (1927).

[53] A. Wünsche, "Reconstruction of operators from their normally ordered moments for a single boson mode", Quantum Opt. **2**, 453 (1990).

[54] V. Bužek, G. Adam, and G. Drobný, "Quantum state reconstruction and detection of quantum coherences on different observation levels", Phys. Rev. A **54**, 804 (1996).

[55] A. Serafini, F. Illuminati, and S. D. Siena, "Symplectic invariants, entropic measures and correlations of Gaussian states", J. Phys. B **37**, L21 (2004).

[56] G. Adesso, A. Serafini, and F. Illuminati, "Determination of Continuous Variable Entanglement by Purity Measurements", Phys. Rev. Lett. **92**, 087901 (2004).

[57] G. Adesso and F. Illuminati, "Gaussian measures of entanglement versus negativities: Ordering of two-mode Gaussian states", Phys. Rev. A **72**, 032334 (2005).

[58] R. J. Glauber, "Coherent and Incoherent States of the Radiation Field", Phys. Rev. **131**, 2766 (1963).

[59] E. C. G. Sudarshan, "Equivalence of Semiclassical and Quantum Mechanical Descriptions of Statistical Light Beams", Phys. Rev. Lett. **10**, 277 (1963).

[60] M. O. Scully and M. S. Zubairy, *Quantum optics* (Cambridge University Press, Cambridge, 1997).

[61] E. Wigner, "On the Quantum Correction For Thermodynamic Equilibrium", Phys. Rev. **40**, 749 (1932).

[62] V. Bužek, G. Adam, and G. Drobný, "Reconstruction of Wigner Functions on Different Observation Levels", Ann. Phys. **245**, 37 (1996).

[63] H. Nyquist, "Thermal Agitation of Electric Charge in Conductors", Phys. Rev. **32**, 110 (1928).

[64] K. G. Fedorov, L. Zhong, S. Pogorzalek, P. Eder, M. Fischer, J. Goetz, E. Xie, F. Wulschner, K. Inomata, T. Yamamoto, Y. Nakamura, R. Di Candia, U. Las Heras, M. Sanz, E. Solano, E. P. Menzel, F. Deppe, A. Marx, and R. Gross, "Displacement of Propagating Squeezed Microwave States", Phys. Rev. Lett. **117**, 020502 (2016).

[65] M. G. Paris, "Displacement operator by beam splitter", Phys. Lett. A **217**, 78 (1996).

[66] N. N. Bogoliubov, "On a new method in the theory of superconductivity", Nuovo Cim. **7**, 794 (1958).

[67] J. G. Valatin, "Comments on the theory of superconductivity", Nuovo Cim. **7**, 843 (1958).

[68] W. G. Unruh, "Notes on black-hole evaporation", Phys. Rev. D **14**, 870 (1976).

[69] S. Caracciolo, F. Palumbo, and G. Viola, "Bogoliubov transformations and fermion condensates in lattice field theories", Ann. Phys. **324**, 584 (2009).

[70] M. Bamba, K. Inomata, and Y. Nakamura, "Superradiant Phase Transition in a Superconducting Circuit in Thermal Equilibrium", Phys. Rev. Lett. **117**, 173601 (2016).

[71] C. E. Shannon, "A Mathematical Theory of Communication", Bell Syst. Tech. J. **27**, 379 (1948).

[72] M. A. Nielsen and I. L. Chuang, *Quantum Computation and Quantum Information* (Cambridge University Press, Cambridge, 2010).

[73] R. Jozsa and B. Schumacher, "A New Proof of the Quantum Noiseless Coding Theorem", J. Mod. Opt. **41**, 2343 (1994).

[74] B. Schumacher, "Quantum coding", Phys. Rev. A **51**, 2738 (1995).

[75] A. Serafini, F. Illuminati, M. G. A. Paris, and S. De Siena, "Entanglement and purity of two-mode Gaussian states in noisy channels", Phys. Rev. A **69**, 022318 (2004).

[76] H. Ollivier and W. H. Zurek, "Quantum Discord: A Measure of the Quantumness of Correlations", Phys. Rev. Lett. **88**, 017901 (2001).

[77] K. Modi, A. Brodutch, H. Cable, T. Paterek, and V. Vedral, "The classical-quantum boundary for correlations: Discord and related measures", Rev. Mod. Phys. **84**, 1655 (2012).

[78] M. Gessner, E.-M. Laine, H.-P. Breuer, and J. Piilo, "Correlations in quantum states and the local creation of quantum discord", Phys. Rev. A **85**, 052122 (2012).

[79] P. Giorda and M. G. A. Paris, "Gaussian Quantum Discord", Phys. Rev. Lett. **105**, 020503 (2010).

[80] G. Adesso, T. R. Bromley, and M. Cianciaruso, "Measures and applications of quantum correlations", J. Phys. A **49**, 75 (2016).

[81] G. Adesso, M. Cianciaruso, and T. R. Bromley, "An introduction to quantum discord and non-classical correlations beyond entanglement", ArXiv e-prints:1611.01959 (2016).

[82] G. Adesso and A. Datta, "Quantum versus Classical Correlations in Gaussian States", Phys. Rev. Lett. **105**, 030501 (2010).

[83] S. Pirandola, G. Spedalieri, S. L. Braunstein, N. J. Cerf, and S. Lloyd, "Optimality of Gaussian Discord", Phys. Rev. Lett. **113**, 140405 (2014).

[84] A. Bera, T. Das, D. Sadhukhan, S. Singha Roy, A. Sen(De), and U. Sen, "Quantum discord and its allies: a review of recent progress", Rep. Prog. Phys. **81**, 024001 (2018).

[85] P. Marian, I. Ghiu, and T. a. Marian, "Decay of Gaussian correlations in local thermal reservoirs", Phys. Scr. **90**, 074041 (2015).

[86] R. Hanbury Brown and R. Q. Twiss, "A Test of a New Type of Stellar Interferometer on Sirius", Nature **178**, 1046 (1956).

[87] M. Alexanian, "Temporal second-order coherence function for displaced-squeezed thermal states", J. Mod. Opt. **63**, 961 (2016).

[88] N. B. Grosse, T. Symul, M. Stobińska, T. C. Ralph, and P. K. Lam, "Measuring Photon Antibunching from Continuous Variable Sideband Squeezing", Phys. Rev. Lett. **98**, 153603 (2007).

[89] B. D. Josephson, "Possible new effects in superconductive tunnelling", Phys. Lett. **1**, 251 (1962).

[90] P. E. Schmidt, "Widerstand zwecklos: Die makroskopische Wellenfunktion als Grundlage der Theorie von Supraleitung und Suprafluidität", Junge Wissenschaft **84**, 38 (2009).

[91] W. Buckel and R. Kleiner, *Superconductivity* (Wiley, Weinheim, 2004).

[92] R. Gross and A. Marx, *Festkörperphysik* (Oldenbourg Verlag, München, 2012).

[93] J. Clarke and A. I. Braginski, *The SQUID Handbook: Fundamentals and Technology of SQUIDs and SQUID Systems* (Wiley, Weinheim, 2004).

[94] G. Wendin and V. S. Shumeiko, "Superconducting Quantum Circuits, Qubits and Computing", in *Handbook of Theoretical and Computational Nanotechnology*, edited by M. Rieth and W. Schommers (American Scientific Publishers, Los Angeles, 2006), pp. 223–309.

[95] S. M. Girvin, M. H. Devoret, and R. J. Schoelkopf, "Circuit QED and engineering charge-based superconducting qubits", Phys. Scr. **T137**, 014012 (2009).

[96] G. Wendin, "Quantum information processing with superconducting circuits: a review", Rep. Prog. Phys. **80**, 106001 (2017).

[97] M. Tinkham, *Introduction to Superconductivity* (McGraw-Hill Inc., New York, 1996).

[98] M. Sandberg, C. M. Wilson, F. Persson, T. Bauch, G. Johansson, V. Shumeiko, T. Duty, and P. Delsing, "Tuning the field in a microwave resonator faster than the photon lifetime", Appl. Phys. Lett. **92**, 203501 (2008).

[99] V. Lefevre-Seguin, E. Turlot, C. Urbina, D. Esteve, and M. H. Devoret, "Thermal activation of a hysteretic dc superconducting quantum interference device from its different zero-voltage states", Phys. Rev. B **46**, 5507 (1992).

[100] M. Mariantoni, H. Wang, T. Yamamoto, M. Neeley, R. C. Bialczak, Y. Chen, M. Lenander, E. Lucero, A. D. O'Connell, D. Sank, M. Weides, J. Wenner, Y. Yin, J. Zhao, A. N. Korotkov, A. N. Cleland, and J. M. Martinis, "Implementing the Quantum von Neumann Architecture with Superconducting Circuits", Science **334**, 61 (2011).

[101] E. Xie, F. Deppe, M. Renger, D. Repp, P. Eder, M. Fischer, J. Goetz, S. Pogorzalek, K. G. Fedorov, A. Marx, and R. Gross, "Compact 3D quantum memory", Appl. Phys. Lett. **112**, 202601 (2018).

[102] D. M. Pozar, *Microwave Engineering* (Wiley, Hoboken, 2012).

[103] M. Göppl, A. Fragner, M. Baur, R. Bianchetti, S. Filipp, J. M. Fink, P. J. Leek, G. Puebla, L. Steffen, and A. Wallraff, "Coplanar waveguide resonators for circuit quantum electrodynamics", J. Appl. Phys. **104**, 113904 (2008).

[104] T. Yamamoto, K. Koshino, and Y. Nakamura, "Parametric Amplifier and Oscillator Based on Josephson Junction Circuitry", in *Principles and Methods of Quantum Information Technologies*, edited by Y. Yamamoto and K. Semba (Springer Japan, Tokyo, 2016), pp. 495–513.

[105] D. S. Wisbey, J. Gao, M. R. Vissers, F. C. S. da Silva, J. S. Kline, L. Vale, and D. P. Pappas, "Effect of metal/substrate interfaces on radio-frequency loss in superconducting coplanar waveguides", J. Appl. Phys. **108**, 093918 (2010).

[106] C. L. Holloway and E. F. Kuester, "Edge shape effects and quasi-closed form expressions for the conductor loss of microstrip lines", Radio Sci. **29**, 539 (1994).

[107] J. Goetz, F. Deppe, M. Haeberlein, F. Wulschner, C. W. Zollitsch, S. Meier, M. Fischer, P. Eder, E. Xie, K. G. Fedorov, E. P. Menzel, A. Marx, and R. Gross, "Loss mechanisms in superconducting thin film microwave resonators", J. Appl. Phys. **119**, 015304 (2016).

[108] T. Yamamoto, K. Inomata, M. Watanabe, K. Matsuba, T. Miyazaki, W. D. Oliver, Y. Nakamura, and J. S. Tsai, "Flux-driven Josephson parametric amplifier", Appl. Phys. Lett. **93**, 042510 (2008).

[109] M. Wallquist, V. S. Shumeiko, and G. Wendin, "Selective coupling of superconducting charge qubits mediated by a tunable stripline cavity", Phys. Rev. B **74**, 224506 (2006).

[110] W. Wustmann and V. Shumeiko, "Parametric resonance in tunable superconducting cavities", Phys. Rev. B **87**, 184501 (2013).

[111] J. Bourassa, F. Beaudoin, J. M. Gambetta, and A. Blais, "Josephson-junction-embedded transmission-line resonators: From Kerr medium to in-line transmon", Phys. Rev. A **86**, 013814 (2012).

[112] P. Bhupathi, P. Groszkowski, M. P. DeFeo, M. Ware, F. K. Wilhelm, and B. L. T. Plourde, "Transient Dynamics of a Superconducting Nonlinear Oscillator", Phys. Rev. Appl. **5**, 024002 (2016).

[113] S. Pogorzalek, K. G. Fedorov, L. Zhong, J. Goetz, F. Wulschner, M. Fischer, P. Eder, E. Xie, K. Inomata, T. Yamamoto, Y. Nakamura, A. Marx, F. Deppe, and R. Gross, "Hysteretic Flux Response and Nondegenerate Gain of Flux-Driven Josephson Parametric Amplifiers", Phys. Rev. Appl. **8**, 024012 (2017).

[114] F. Balestro, J. Claudon, J. P. Pekola, and O. Buisson, "Evidence of two-dimensional macroscopic quantum tunneling of a current-biased dc SQUID", Phys. Rev. Lett. **91**, 158301 (2003).

[115] E. Hoskinson, F. Lecocq, N. Didier, A. Fay, F. W. J. Hekking, W. Guichard, O. Buisson, R. Dolata, B. Mackrodt, and A. B. Zorin, "Quantum Dynamics in a Camelback Potential of a dc SQUID", Phys. Rev. Lett. **102**, 097004 (2009).

[116] W. H. Louisell, A. Yariv, and A. E. Siegman, "Quantum Fluctuations and Noise in Parametric Processes. I.", Phys. Rev. **124**, 1646 (1961).

[117] J. P. Gordon, W. H. Louisell, and L. R. Walker, "Quantum Fluctuations and Noise in Parametric Processes. II", Phys. Rev. **129**, 481 (1963).

[118] M. A. Castellanos-Beltran and K. W. Lehnert, "Widely tunable parametric amplifier based on a superconducting quantum interference device array resonator", Appl. Phys. Lett. **91**, 083509 (2007).

[119] N. Bergeal, F. Schackert, M. Metcalfe, R. Vijay, V. E. Manucharyan, L. Frunzio, D. E. Prober, R. J. Schoelkopf, S. M. Girvin, and M. H. Devoret, "Phase-preserving amplification near the quantum limit with a Josephson ring modulator", Nature **465**, 64 (2010).

[120] M. Hatridge, R. Vijay, D. H. Slichter, J. Clarke, and I. Siddiqi, "Dispersive magnetometry with a quantum limited SQUID parametric amplifier", Phys. Rev. B **83**, 134501 (2011).

[121] C. Eichler, Y. Salathe, J. Mlynek, S. Schmidt, and A. Wallraff, "Quantum-Limited Amplification and Entanglement in Coupled Nonlinear Resonators", Phys. Rev. Lett. **113**, 110502 (2014).

[122] C. Macklin, K. O'Brien, D. Hover, M. E. Schwartz, V. Bolkhovsky, X. Zhang, W. D. Oliver, and I. Siddiqi, "A near-quantum-limited Josephson traveling-wave parametric amplifier", Science **350**, 307 (2015).

[123] A. A. Clerk, M. H. Devoret, S. M. Girvin, F. Marquardt, and R. J. Schoelkopf, "Introduction to quantum noise, measurement, and amplification", Rev. Mod. Phys. **82**, 1155 (2010).

[124] A. Eddins, J. M. Kreikebaum, D. M. Toyli, E. M. Levenson-Falk, A. Dove, W. P. Livingston, B. A. Levitan, L. C. G. Govia, A. A. Clerk, and I. Siddiqi, "High-Efficiency Measurement of an Artificial Atom Embedded in a Parametric Amplifier", Phys. Rev. X **9**, 011004 (2019).

[125] W. Pfaff, C. J. Axline, L. D. Burkhart, U. Vool, P. Reinhold, L. Frunzio, L. Jiang, M. H. Devoret, and R. J. Schoelkopf, "Controlled release of multiphoton quantum states from a microwave cavity memory", Nat. Phys. **13**, 882 (2017).

[126] H. A. Haus and J. A. Mullen, "Quantum Noise in Linear Amplifiers", Phys. Rev. **128**, 2407 (1962).

[127] C. M. Caves, "Quantum limits on noise in linear amplifiers", Phys. Rev. D **26**, 1817 (1982).

[128] L. Zhong, E. P. Menzel, R. Di Candia, P. Eder, M. Ihmig, A. Baust, M. Haeberlein, E. Hoffmann, K. Inomata, T. Yamamoto, Y. Nakamura, E. Solano, F. Deppe, A. Marx, and R. Gross, "Squeezing with a flux-driven Josephson parametric amplifier", New J. Phys. **15**, 125013 (2013).

[129] B. Yurke and E. Buks, "Performance of cavity-parametric amplifiers, employing Kerr nonlinearites, in the presence of two-photon loss", J. Light. Technol. **24**, 5054 (2006).

[130] C. Eichler, D. Bozyigit, C. Lang, M. Baur, L. Steffen, J. M. Fink, S. Filipp, and A. Wallraff, "Observation of Two-Mode Squeezing in the Microwave Frequency Domain", Phys. Rev. Lett. **107**, 113601 (2011).

[131] R. Di Candia, K. Fedorov, L. Zhong, S. Felicetti, E. Menzel, M. Sanz, F. Deppe, A. Marx, R. Gross, and E. Solano, "Quantum teleportation of propagating quantum microwaves", EPJ Quantum Technol. **2**, 25 (2015).

[132] Z. Kurucz, P. Adam, Z. Kis, and J. Janszky, "Continuous variable remote state preparation", Phys. Rev. A **72**, 052315 (2005).

[133] N. Killoran, D. N. Biggerstaff, R. Kaltenbaek, K. J. Resch, and N. Lütkenhaus, "Derivation and experimental test of fidelity benchmarks for remote preparation of arbitrary qubit states", Phys. Rev. A **81**, 012334 (2010).

[134] D. Bouwmeester, J.-W. Pan, K. Mattle, M. Eibl, H. Weinfurter, and A. Zeilinger, "Experimental quantum teleportation", Nature **390**, 575 (1997).

[135] D. Boschi, S. Branca, F. De Martini, L. Hardy, and S. Popescu, "Experimental Realization of Teleporting an Unknown Pure Quantum State via Dual Classical and Einstein-Podolsky-Rosen Channels", Phys. Rev. Lett. **80**, 1121 (1998).

[136] M. Riebe, H. Häffner, C. F. Roos, W. Hänsel, J. Benhelm, G. P. T. Lancaster, T. W. Körber, C. Becher, F. Schmidt-Kaler, D. F. V. James, and R. Blatt, "Deterministic quantum teleportation with atoms", Nature **429**, 734 (2004).

[137] M. D. Barrett, J. Chiaverini, T. Schaetz, J. Britton, W. M. Itano, J. D. Jost, E. Knill, C. Langer, D. Leibfried, R. Ozeri, and D. J. Wineland, "Deterministic quantum teleportation of atomic qubits", Nature **429**, 737 (2004).

[138] W. Pfaff, B. J. Hensen, H. Bernien, S. B. van Dam, M. S. Blok, T. H. Taminiau, M. J. Tiggelman, R. N. Schouten, M. Markham, D. J. Twitchen, and R. Hanson, "Unconditional quantum teleportation between distant solid-state quantum bits", Science **345**, 532 (2014).

[139] X.-M. Jin, J.-G. Ren, B. Yang, Z.-H. Yi, F. Zhou, X.-F. Xu, S.-K. Wang, D. Yang, Y.-F. Hu, S. Jiang, T. Yang, H. Yin, K. Chen, C.-Z. Peng, and J.-W. Pan, "Experimental free-space quantum teleportation", Nat. Photonics **4**, 376 (2010).

[140] X.-S. Ma, T. Herbst, T. Scheidl, D. Wang, S. Kropatschek, W. Naylor, B. Wittmann, A. Mech, J. Kofler, E. Anisimova, V. Makarov, T. Jennewein, R. Ursin, and A. Zeilinger, "Quantum teleportation over 143 kilometres using active feed-forward", Nature **489**, 269 (2012).

[141] L. Vaidman, "Teleportation of quantum states", Phys. Rev. A **49**, 1473 (1994).

[142] W. K. Wootters and W. H. Zurek, "A single quantum cannot be cloned", Nature **299**, 802 (1982).

[143] J. I. Cirac, P. Zoller, H. J. Kimble, and H. Mabuchi, "Quantum State Transfer and Entanglement Distribution among Distant Nodes in a Quantum Network", Phys. Rev. Lett. **78**, 3221 (1997).

[144] G. S. Vernam, "Cipher Printing Telegraph Systems For Secret Wire and Radio Telegraphic Communications", Trans. Am. Inst. Electr. Eng. **XLV**, 295 (1926).

[145] C. E. Shannon, "Communication Theory of Secrecy Systems", Bell Syst. Tech. J. **28**, 656 (1949).

[146] Z. Kurucz, P. Adam, and J. Janszky, "Remote State Preparation in Quadrature Basis", Acta Phys. Hung. B **26**, 319 (2006).

[147] C. H. Bennett and G. Brassard, "Quantum cryptography: Public key distribution and coin tossing", in *Proceedings of the Conference on Computers, Systems and Signal Processing* (IEEE, New York, 1984), p. 175.

[148] C. H. Bennett and G. Brassard, "Quantum cryptography: Public key distribution and coin tossing", Theor. Comput. Sci. **560**, 7 (2014).

[149] S.-K. Liao, W.-Q. Cai, J. Handsteiner, B. Liu, J. Yin, L. Zhang, D. Rauch, M. Fink, J.-G. Ren, W.-Y. Liu, Y. Li, Q. Shen, Y. Cao, F.-Z. Li, J.-F. Wang, Y.-M. Huang,

L. Deng, T. Xi, L. Ma, T. Hu, L. Li, N.-L. Liu, F. Koidl, P. Wang, Y.-A. Chen, X.-B. Wang, M. Steindorfer, G. Kirchner, C.-Y. Lu, R. Shu, R. Ursin, T. Scheidl, C.-Z. Peng, J.-Y. Wang, A. Zeilinger, and J.-W. Pan, "Satellite-Relayed Intercontinental Quantum Network", Phys. Rev. Lett. **120**, 030501 (2018).

[150] P. W. Shor and J. Preskill, "Simple Proof of Security of the BB84 Quantum Key Distribution Protocol", Phys. Rev. Lett. **85**, 441 (2000).

[151] A. K. Ekert, "Quantum cryptography based on Bell's theorem", Phys. Rev. Lett. **67**, 661 (1991).

[152] F. Grosshans, N. J. Cerf, J. Wenger, R. Tualle-Brouri, and P. Grangier, "Virtual Entanglement and Reconciliation Protocols for Quantum Cryptography with Continuous Variables", Quantum Inf. Comput. **3**, 535 (2003).

[153] S. Ghose and B. C. Sanders, "Non-Gaussian ancilla states for continuous variable quantum computation via Gaussian maps", J. Mod. Opt. **54**, 855 (2007).

[154] J.-i. Yoshikawa, Y. Miwa, A. Huck, U. L. Andersen, P. van Loock, and A. Furusawa, "Demonstration of a Quantum Nondemolition Sum Gate", Phys. Rev. Lett. **101**, 250501 (2008).

[155] H. Takahashi, J. S. Neergaard-Nielsen, M. Takeuchi, M. Takeoka, K. Hayasaka, A. Furusawa, and M. Sasaki, "Entanglement distillation from Gaussian input states", Nat. Photonics **4**, 178 (2010).

[156] D. Su, C. Weedbrook, and K. Brádler, "Correcting finite squeezing errors in continuous-variable cluster states", Phys. Rev. A **98**, 042304 (2018).

[157] J. Niset, J. Fiurášek, and N. J. Cerf, "No-Go Theorem for Gaussian Quantum Error Correction", Phys. Rev. Lett. **102**, 120501 (2009).

[158] J. Fiurášek, "Gaussian Transformations and Distillation of Entangled Gaussian States", Phys. Rev. Lett. **89**, 137904 (2002).

[159] G. Giedke and J. Ignacio Cirac, "Characterization of Gaussian operations and distillation of Gaussian states", Phys. Rev. A **66**, 032316 (2002).

[160] A. G. Fowler, M. Mariantoni, J. M. Martinis, and A. N. Cleland, "Surface codes: Towards practical large-scale quantum computation", Phys. Rev. A **86**, 032324 (2012).

[161] D. Gottesman, A. Kitaev, and J. Preskill, "Encoding a qubit in an oscillator", Phys. Rev. A **64**, 012310 (2001).

[162] K. Fukui, A. Tomita, A. Okamoto, and K. Fujii, "High-Threshold Fault-Tolerant Quantum Computation with Analog Quantum Error Correction", Phys. Rev. X **8**, 021054 (2018).

[163] K. Uhlig, "Dry dilution refrigerator with ^{4}He-1K-loop", Cryogenics **66**, 6 (2015).

[164] A. Marx, J. Hoess, and K. Uhlig, "Dry Dilution Refrigerator for Experiments on Quantum Effects in the Microwave Regime", ArXiv e-prints:1412.3619 (2014).

[165] F. Pobell, *Matter and Methods at Low Temperatures* (Springer, Berlin Heidelberg, 2007).

[166] L. Zhong, "Generation and Reconstruction of Propagating Quantum Microwaves", Phd thesis, Technische Universität München (2015), URL http://www.wmi.badw.de/publications/theses/Zhong,Ling_Doktorarbeit_2015.pdf.

[167] E. P. Menzel, "Propagating quantum microwaves: dual-path state reconstruction and path entanglement", Phd thesis, Technische Universität München (2013), URL http://www.wmi.badw.de/publications/theses/Menzel_Doktorarbeit_2013.pdf.

[168] S. Pogorzalek, "Displacement of squeezed propagating microwave states", Master's thesis, Technische Universität München (2015), URL http://www.wmi.badw.de/publications/theses/Pogorzalek,Stefan_Masterarbeit_2015.pdf.

[169] R. Di Candia, E. P. Menzel, L. Zhong, F. Deppe, A. Marx, R. Gross, and E. Solano, "Dual-path methods for propagating quantum microwaves", New J. Phys. **16**, 015001 (2014).

[170] E. P. Menzel, F. Deppe, M. Mariantoni, M. Á. Araque Caballero, A. Baust, T. Niemczyk, E. Hoffmann, A. Marx, E. Solano, and R. Gross, "Dual-Path State Reconstruction Scheme for Propagating Quantum Microwaves and Detector Noise Tomography", Phys. Rev. Lett. **105**, 100401 (2010).

[171] M. Mariantoni, E. P. Menzel, F. Deppe, M. Á. Araque Caballero, A. Baust, T. Niemczyk, E. Hoffmann, E. Solano, A. Marx, and R. Gross, "Planck Spectroscopy and Quantum Noise of Microwave Beam Splitters", Phys. Rev. Lett. **105**, 133601 (2010).

[172] G. J. Dolan, "Offset masks for lift-off photoprocessing", Appl. Phys. Lett. **31**, 337 (1977).

[173] C. M. Quintana, A. Megrant, Z. Chen, A. Dunsworth, B. Chiaro, R. Barends, B. Campbell, Y. Chen, I.-C. Hoi, E. Jeffrey, J. Kelly, J. Y. Mutus, P. J. J. O'Malley, C. Neill, P. Roushan, D. Sank, A. Vainsencher, J. Wenner, T. C. White, A. N.

Cleland, and J. M. Martinis, "Characterization and reduction of microfabrication-induced decoherence in superconducting quantum circuits", Appl. Phys. Lett. **105**, 062601 (2014).

[174] J. E. Healey, T. Lindström, M. S. Colclough, C. M. Muirhead, and A. Y. Tzalenchuk, "Magnetic field tuning of coplanar waveguide resonators", Appl. Phys. Lett. **93**, 043513 (2008).

[175] M. Simoen, C. W. S. Chang, P. Krantz, J. Bylander, W. Wustmann, V. Shumeiko, P. Delsing, and C. M. Wilson, "Characterization of a multimode coplanar waveguide parametric amplifier", J. Appl. Phys. **118**, 154501 (2015).

[176] M. Kamon, M. Ttsuk, and J. White, "FASTHENRY: a multipole-accelerated 3-D inductance extraction program", IEEE Trans. Microw. Theory Tech. **42**, 1750 (1994).

[177] S. Boutin, D. M. Toyli, A. V. Venkatramani, A. W. Eddins, I. Siddiqi, and A. Blais, "Effect of Higher-Order Nonlinearities on Amplification and Squeezing in Josephson Parametric Amplifiers", Phys. Rev. Appl. **8**, 054030 (2017).

[178] D. Arweiler, "Multi-SQUID Josephson Parametric Amplifiers", Master's thesis, Technische Universität München (2018), URL `http://www.wmi.badw.de/publications/theses/Arweiler,Daniel_Masterarbeit_2018.pdf`.

[179] S.-H. Xiang, W. Wen, Y.-J. Zhao, and K.-H. Song, "Evaluation of the non-Gaussianity of two-mode entangled states over a bosonic memory channel via cumulant theory and quadrature detection", Phys. Rev. A **97**, 042303 (2018).

[180] C. M. Wilson, G. Johansson, A. Pourkabirian, M. Simoen, J. R. Johansson, T. Duty, F. Nori, and P. Delsing, "Observation of the dynamical Casimir effect in a superconducting circuit", Nature **479**, 376 (2011).

[181] E. Flurin, N. Roch, F. Mallet, M. H. Devoret, and B. Huard, "Generating Entangled Microwave Radiation Over Two Transmission Lines", Phys. Rev. Lett. **109**, 183901 (2012).

[182] N. Roch, E. Flurin, F. Nguyen, P. Morfin, P. Campagne-Ibarcq, M. H. Devoret, and B. Huard, "Widely Tunable, Nondegenerate Three-Wave Mixing Microwave Device Operating near the Quantum Limit", Phys. Rev. Lett. **108**, 147701 (2012).

[183] M. S. Kim, W. Son, V. Bužek, and P. L. Knight, "Entanglement by a beam splitter: Nonclassicality as a prerequisite for entanglement", Phys. Rev. A **65**, 032323 (2002).

[184] L.-M. Duan, G. Giedke, J. I. Cirac, and P. Zoller, "Inseparability Criterion for Continuous Variable Systems", Phys. Rev. Lett. **84**, 2722 (2000).

[185] S. Mancini, V. Giovannetti, D. Vitali, and P. Tombesi, "Entangling Macroscopic Oscillators Exploiting Radiation Pressure", Phys. Rev. Lett. **88**, 120401 (2002).

[186] W. P. Bowen, R. Schnabel, P. K. Lam, and T. C. Ralph, "Experimental Investigation of Criteria for Continuous Variable Entanglement", Phys. Rev. Lett. **90**, 043601 (2003).

[187] I. I. Arkhipov, J. Perina, J. Svozilík, and A. Miranowicz, "Nonclassicality Invariant of General Two-Mode Gaussian States", Sci. Rep. **6**, 26523 (2016).

[188] P. Yard, "Noncommutation and Finite-time Correlations with Propagating Quantum Microwave States", Master's thesis, Technische Universität München (2016), URL http://www.wmi.badw.de/publications/theses/Yard,Patrick_Masterarbeit_2016.pdf.

[189] R. Di Candia, M. Sanz, and E. Solano (2013), private communication.

[190] H. Fearn and M. Collett, "Representations of Squeezed States with Thermal Noise", J. Mod. Opt. **35**, 553 (1988).

[191] S. Tserkis and T. C. Ralph, "Quantifying entanglement in two-mode Gaussian states", Phys. Rev. A **96**, 062338 (2017).

[192] W. K. Wootters, "Entanglement of Formation of an Arbitrary State of Two Qubits", Phys. Rev. Lett. **80**, 2245 (1998).

[193] W. K. Wootters, "Entanglement of formation and concurrence for mixed states", Quantum Inf. Comput. **1**, 27 (2001).

[194] M. P. Almeida, F. de Melo, M. Hor-Meyll, A. Salles, S. P. Walborn, P. H. S. Ribeiro, and L. Davidovich, "Environment-Induced Sudden Death of Entanglement", Science **316**, 579 (2007).

[195] T. Yu and J. H. Eberly, "Sudden Death of Entanglement", Science **323**, 598 (2009).

[196] A. Isar, "Entanglement and discord in two-mode Gaussian open quantum systems", Phys. Scr. **T147**, 014015 (2012).

[197] T. Werlang, S. Souza, F. F. Fanchini, and C. J. Villas Boas, "Robustness of quantum discord to sudden death", Phys. Rev. A **80**, 024103 (2009).

[198] S. Trattnig, "Quantum correlations beyond entanglement", Bachelor's thesis, Technische Universität München (2017), URL http://www.wmi.badw.de/publications/theses/Trattnig,Stephan%20Bachelor%20Thesis%202017.pdf.

[199] Z.-L. Xiang, M. Zhang, L. Jiang, and P. Rabl, "Intracity Quantum Communication via Thermal Microwave Networks", Phys. Rev. X **7**, 011035 (2017).

[200] B. Dakić, Y. O. Lipp, X. Ma, M. Ringbauer, S. Kropatschek, S. Barz, T. Paterek, V. Vedral, A. Zeilinger, Č. Brukner, and P. Walther, "Quantum discord as resource for remote state preparation", Nat. Phys. **8**, 666 (2012).

[201] N. A. Peters, J. T. Barreiro, M. E. Goggin, T.-C. Wei, and P. G. Kwiat, "Remote State Preparation: Arbitrary Remote Control of Photon Polarization", Phys. Rev. Lett. **94**, 150502 (2005).

[202] M.-Y. Ye, Y.-S. Zhang, and G.-C. Guo, "Faithful remote state preparation using finite classical bits and a nonmaximally entangled state", Phys. Rev. A **69**, 022310 (2004).

[203] C. Neill, P. Roushan, K. Kechedzhi, S. Boixo, S. V. Isakov, V. Smelyanskiy, A. Megrant, B. Chiaro, A. Dunsworth, K. Arya, R. Barends, B. Burkett, Y. Chen, Z. Chen, A. Fowler, B. Foxen, M. Giustina, R. Graff, E. Jeffrey, T. Huang, J. Kelly, P. Klimov, E. Lucero, J. Mutus, M. Neeley, C. Quintana, D. Sank, A. Vainsencher, J. Wenner, T. C. White, H. Neven, and J. M. Martinis, "A blueprint for demonstrating quantum supremacy with superconducting qubits", Science **360**, 195 (2018).

[204] A. D. Corcoles, E. Magesan, S. J. Srinivasan, A. W. Cross, M. Steffen, J. M. Gambetta, and J. M. Chow, "Demonstration of a quantum error detection code using a square lattice of four superconducting qubits", Nat. Commun. **6**, 6979 (2015).

[205] S. B. Ghaffari, "Remote State Preparation of Propagating Quantum Microwaves", Master's thesis, Technische Universität München (2018), URL http://www.wmi.badw.de/publications/theses/Ghaffari,Seyed%20Behdad_Masterarbeit_2018.pdf.

[206] R. Kokkoniemi, T. Ollikainen, R. E. Lake, S. Saarenpää, K. Y. Tan, J. I. Kokkala, C. B. Dağ, J. Govenius, and M. Möttönen, "Flux-tunable phase shifter for microwaves", Sci. Rep. **7**, 14713 (2017).

[207] S. Barzanjeh, M. Wulf, M. Peruzzo, M. Kalaee, P. B. Dieterle, O. Painter, and J. M. Fink, "Mechanical on-chip microwave circulator", Nat. Commun. **8**, 953 (2017).

[208] N. R. Bernier, L. D. Tóth, A. Koottandavida, M. A. Ioannou, D. Malz, A. Nunnenkamp, A. K. Feofanov, and T. J. Kippenberg, "Nonreciprocal reconfigurable microwave optomechanical circuit", Nat. Commun. **8**, 604 (2017).

[209] F. Lecocq, L. Ranzani, G. A. Peterson, K. Cicak, R. W. Simmonds, J. D. Teufel, and J. Aumentado, "Nonreciprocal Microwave Signal Processing with a Field-Programmable Josephson Amplifier", Phys. Rev. Appl. **7**, 024028 (2017).

[210] B. J. Chapman, E. I. Rosenthal, J. Kerckhoff, B. A. Moores, L. R. Vale, J. A. B. Mates, G. C. Hilton, K. Lalumière, A. Blais, and K. W. Lehnert, "Widely Tunable On-Chip Microwave Circulator for Superconducting Quantum Circuits", Phys. Rev. X **7**, 041043 (2017).

[211] D. Bures, "An extension of Kakutani's theorem on infinite product measures to the tensor product of semifinite w*-algebras", Trans. Am. Math. Soc. **135**, 199 (1969).

[212] A. Uhlmann, "The 'transition probability' in the state space of a *-algebra", Rep. Math. Phys. **9**, 273 (1976).

[213] D. Šafránek, A. R. Lee, and I. Fuentes, "Quantum parameter estimation using multi-mode Gaussian states", New J. Phys. **17**, 073016 (2015).

[214] L. Rigovacca, A. Farace, L. A. M. Souza, A. De Pasquale, V. Giovannetti, and G. Adesso, "Versatile Gaussian probes for squeezing estimation", Phys. Rev. A **95**, 052331 (2017).

[215] D. Petz and C. Ghinea, "Introduction to quantum Fisher information", in *Quantum Probability and Related Topics* (World Scientific, 2011), pp. 261–281.

[216] O. Pinel, P. Jian, N. Treps, C. Fabre, and D. Braun, "Quantum parameter estimation using general single-mode Gaussian states", Phys. Rev. A **88**, 040102 (2013).

[217] W. Kester, *Data Conversion Handbook* (Elsevier, Oxford, 2005).

[218] S. L. Braunstein and C. M. Caves, "Statistical distance and the geometry of quantum states", Phys. Rev. Lett. **72**, 3439 (1994).

[219] P. Horodecki, J. Tuziemski, P. Mazurek, and R. Horodecki, "Can Communication Power of Separable Correlations Exceed That of Entanglement Resource?", Phys. Rev. Lett. **112**, 140507 (2014).

[220] M. Xu, "Quantum Correlations in Remote State Preparation", Master's thesis, Technische Universität München (2018).

[221] C. E. Shannon, "Communication in the Presence of Noise", Proc. IRE **37**, 10 (1949).

[222] A. Menezes, P. Oorschot, and V. S.A., *Handbook of Applied Cryptography* (CRC Press, Boca Raton, 1996).

[223] S. Hallgren and U. Vollmer, "Quantum computing", in *Post-Quantum Cryptography*, edited by D. J. Bernstein, J. Buchmann, and E. Dahmen (Springer Berlin, Heidelberg, 2009), pp. 15–34.

[224] D. W. Leung, "Quantum Vernam Cipher", Quantum Inf. Comput. **2**, 14 (2002).

[225] M. Zwolak and W. H. Zurek, "Complementarity of quantum discord and classically accessible information", Sci. Rep. **3**, 1729 (2013).

[226] M. Gu, H. M. Chrzanowski, S. M. Assad, T. Symul, K. Modi, T. C. Ralph, V. Vedral, and P. K. Lam, "Observing the operational significance of discord consumption", Nat. Phys. **8**, 671 (2012).

List of publications

- S. Pogorzalek, K. G. Fedorov, M. Xu, A. Parra-Rodriguez, M. Sanz, M. Fischer, E. Xie, K. Inomata, Y. Nakamura, E. Solano, A. Marx, F. Deppe, R. Gross, "Secure quantum remote state preparation of squeezed microwave states", Nat. Commun. **10**, 2604 (2019).

- P. Eder, T. Ramos, J. Goetz, M. Fischer, S. Pogorzalek, J. Puertas Martínez, E. P. Menzel, F. Loacker, E. Xie, J.-J. Garcia-Ripoll, K. G. Fedorov, A. Marx, F. Deppe, R. Gross, "Quantum probe of an on-chip broadband interferometer for quantum microwave photonics", Supercond. Sci. Technol. **31**, 115002 (2018).

- J. Goetz, F. Deppe, K. G. Fedorov, P. Eder, M. Fischer, S. Pogorzalek, E. Xie, A. Marx, R. Gross, "Parity-Engineered Light-Matter Interaction", Phys. Rev. Lett. **121**, 060503 (2018).

- E. Xie, F. Deppe, M. Renger, D. Repp, P. Eder, M. Fischer, J. Goetz, S. Pogorzalek, K. G. Fedorov, A. Marx, R. Gross, "Compact 3D quantum memory", Appl. Phys. Lett. **112**, 202601 (2018).

- K. G. Fedorov, S. Pogorzalek, U. Las Heras, M. Sanz, P. Yard, P. Eder, M. Fischer, J. Goetz, E. Xie, K. Inomata, Y. Nakamura, R. Di Candia, E. Solano, A. Marx, F. Deppe, R. Gross, "Finite-time quantum entanglement in propagating squeezed microwaves", Sci. Rep. **8**, 6416 (2018).

- S. Pogorzalek, K. G. Fedorov, L. Zhong, J. Goetz, F. Wulschner, M. Fischer, P. Eder, E. Xie, K. Inomata, T. Yamamoto, Y. Nakamura, A. Marx, F. Deppe, R. Gross, "Hysteretic Flux Response and Nondegenerate Gain of Flux-Driven Josephson Parametric Amplifiers", Phys. Rev. Appl. **8**, 024012 (2017).

- J. Goetz, S. Pogorzalek, F. Deppe, K. G. Fedorov, P. Eder, M. Fischer, F. Wulschner, E. Xie, A. Marx, R. Gross, "Photon Statistics of Propagating Thermal Microwaves," Phys. Rev. Lett. **118**, 103602 (2017).

- J. Goetz, F. Deppe, P. Eder, M. Fischer, M. Müting, J. Puertas Martínez, S. Pogorzalek, F. Wulschner, E. Xie, K. G. Fedorov, A. Marx, R. Gross, "Second-order decoherence mechanisms of a transmon qubit probed with thermal microwave states", Quant. Sci. Tech. **2**, 025002 (2017).

- K. G. Fedorov, L. Zhong, S. Pogorzalek, P. Eder, M. Fischer, J. Goetz, E. Xie, F. Wulschner, K. Inomata, T. Yamamoto, Y. Nakamura, R. Di Candia, U. Las Heras, M. Sanz, E. Solano, E. P. Menzel, F. Deppe, A. Marx, R. Gross, "Displacement of Propagating Squeezed Microwave States", Phys. Rev. Lett. **117**, 020502 (2016).

Acknowledgments

This work would not have been possible without the support, knowledge, and guidance of many people whom I would like to thank in the following:

My doctoral advisor, *Prof. Dr. Rudolf Gross*, for giving me the opportunity to join the qubit group at the Walther-Meißner-Institute for my Master's thesis and afterwards my dissertation. Your vast knowledge and persistent dedication as a scientist inspire me.

Kirill G. Fedorov as day-to-day advisor during my work at WMI. I enjoyed plenty scientific and non-scientific discussions during work and lunch time (including the talks during closing of the cryostat). I could always come to you for help, ideas, and various questions. Also, thanks for teaching me how to do lab-work and all the help in the lab. The constant and valuable support enabled the results in this work. I admire your enthusiasm and scientific curiosity. Thank you for your support and I wish you all the best!

Frank Deppe for leading the qubit group and valuable input concerning the analysis and interpretation of the measurement data. Despite your full schedule, you always found the time to discuss about our results in detail. *Achim Marx* for managing various issues concerning the cryostat and, thus, allowing for smooth measurements without much downtime. Also, thanks to you, our experiments were only minimally affected during the reconstruction works at WMI.

My office colleagues for the great atmosphere in the office and for plenty of interesting chit-chat about various topics. I specifically want to thank *Philip* for our various work-related as well as private discussions and also for a few "feuchtfröhliche" evenings. We shared some long evenings at WMI when writing our theses. I wish you all the best in Vienna! *Michael R.* for continuing my project and putting up with a few quick-and-dirty solutions in the lab. Thanks for the nice times in Freiburg or Augustiner. *Michael F.* for his calm and friendly nature. I always enjoyed talking to you and our bouldering visits. *Peter* for his direct attitude and various nice conversations.

All current and former members of WMI - especially the qubit group - for the great working atmosphere. Thank you *Daniel S.*, *Friedrich*, *Qiming*, *Stefan W.*, and *Yuki* for the help and being always available for questions. Working together with you when sharing equipment or instruments was never a hurdle. In particular, I would like thank *Jan G.* for valuable discussions and developing as well as maintaining our measurement

program. *Alexander*, *Edwin*, *Ling*, and *Peter* for your previous work concerning the operation and measurement of JPAs. Without your groundwork, this thesis would not have been possible.

The bachelor and master students who worked together with me on various topics over the last years. *Patrick* implemented the code for measurements with a time delay and measured first two-mode squeezed states. *Behdad* contributed to building the RSP setup and helped measuring and analyzing the first RSP results. *Daniel A.* fabricated JPAs at WMI. *Minxing* optimized RSP and explored the connection of RSP to information theoretic measures. *Stephan* investigated the topic of quantum discord.

Enrique Solano and all of his group for the fruitful theory collaboration. In particular, I want to thank *Adrian Parra-Rodriguez* for his time in many Skype calls concerning central parts in our work. Also, *Mikel Sanz* for many inspiring discussion. I enjoyed the visit in Bilbao.

Our Japanese collaborators, *Tsuyoshi Yamamoto*, *Kunihiro Inomata*, and *Yasunobu Nakamura*, for providing us with the JPA samples and the efficient collaboration. Also, the theory concerning the flux-driven JPAs is very valuable for understanding the JPA dynamics.

The workshop team consisting of *Helmut*, *Alexander*, *Georg*, *Christian*, and *Mario* for always being friendly and helpful. You constructed various important pieces for the project and I am thankful for their effort. Also *Emel*, *Ludwig*, *Andrea*, and *Carola* deserve a special thanks for the administrative work and shielding me from too much bureaucracy.

Sebastian, *Karen*, *Astrid*, *Christoph*, and *Andreas* for efficient help regarding chemicals, electronics, and other technical issues. *Maria* and *Sybilla* for keeping the office, the lab and WMI clean. It was always a pleasure talking to you. The IT-crowd consisting of *Matthias O.*, *Andreas B.*, *Daniel S.*, *Dieter*, *Michael R.*, and *Peter* for their helpfulness and many hours of commitment in various computer-related problems.

My parents for their constant support throughout my studies and dissertation. Without your support this work would not have been possible. I am grateful for your understanding and your encouragement. Your doors are always open for me and I can always rely on you if I need help. Also special thanks go to my good friends which are always a pleasant distraction from work.

Finally, I thank *Alexandra* for being there for me over the last years and supporting me. Thank you for your patience when I stayed late at WMI because the measurements were not going as planned or urgent things came up. I'm very glad to have you in my life!